Université des Sciences et Technologies de Lille

Travaux présentés par

M. Olivier Boucher

en vue de l'obtention de

L'HABILITATION A DIRIGER DES RECHERCHES EN SCIENCES PHYSIQUES

Effets radiatifs direct et indirect des aérosols

devant le jury composé de :

François-Marie Bréon	Rapporteur
Maurice Herman	Examinateur
Yoram Kaufman	Rapporteur
Hervé Le Treut	Président
Gérard Mégie	Examinateur
Jean-Jacques Morcrette	Rapporteur
Didier Tanré	Examinateur

U.F.R de Physique Fondamentale

Laboratoire d'Optique Atmosphérique

Remerciements

Je tiens à remercier chaleureusement toutes les personnes qui ont participé directement ou indirectement à ce travail. C'est le cas, en particulier, des nombreux coauteurs des manuscrits présentés dans ce document : Jim Haywood (chapitre 2 et annexe A), Mai Pham (chapitres 3, 4, 5 et 6), Chandra Venkataraman (chapitres 3 et 5), Cyril Moulin (chapitre 5), Sauveur Belviso (chapitres 5 et 6), Olivier Aumont (chapitres 5 et 6), Laurent Bopp (chapitres 5 et 6), Emmanuel Cosme (chapitre 5), Rolf von Kuhlmann (chapitre 5), Mark Lawrence (chapitre 5), Shekar Reddy (chapitre 5), Jean Sciare (chapitre 5), Jean-Louis Dufresne (chapitre 6), Patrick Monfray (chapitre 6), Didier Tanré (chapitre 8 et annexe B), Jean-Claude Buriez (chapitre 8), Marie Boucher (chapitre 8), Isabelle Chiapello (chapitre 8), Geneviève Sèze (chapitre 8) et Yoram Kaufman (annexe B). Shekar Reddy, Nicolas Bellouin, Michèle Vesperini, Gunnar Myhre et Paola Formenti ont aussi largement contribué aux résultats non encore publiés qui ont été présentés lors de la soutenance.

Je remercie le Laboratoire d'Optique Atmosphérique dans son ensemble et ses directeurs successifs pour les conditions de travail, tant humaines que matérielles, qui ont permis l'accomplissement de ces recherches. L'Institut Max Planck de Mayence (qui m'a gentiment accueilli pendant deux ans) et le CNRS (qui m'a gentiment laissé partir !) m'ont permis de tisser d'autres collaborations et d'explorer d'autres aspects de la recherche sur les aérosols.

Gérard Mégie, Hervé Le Treut, Jean-Jacques Morcrette, François-Marie Bréon, Yoram Kaufman, Maurice Herman et Didier Tanré m'ont fait l'amitié d'accepter de faire partie du jury, je les remercie également.

A mes parents, Marie, Léa et Eulalie

Résumé

Les aérosols atmosphériques exercent un effet radiatif direct par diffusion et absorption du rayonnement ondes courtes et diffusion, absorption et émission du rayonnement ondes longues. Ils sont aussi responsables d'un effet radiatif indirect par modification des propriétés microphysiques et optiques des nuages, avec des rétroactions possibles sur le cycle hydrologique. La perturbation du bilan radiatif de la planète (aussi appelé forçage radiatif) due aux aérosols d'origine anthropique représente une des incertitudes majeures dans la problématique du changement climatique. Nous avons développé une représentation du cycle des aérosols soufrés dans le modèle de circulation générale LMDZT, qui a été largement évaluée avec les mesures disponibles. L'historique des concentrations et des forçages radiatifs depuis le début de l'ère industrielle a ainsi pu être reconstitué. Le diméthylsulfide est un composant clé du cycle du soufre naturel qui est émis par certaines espèces de phytoplancton marine. Nous avons étudié la sensibilité du cycle du soufre naturelle et de l'effet indirect des aérosols soufrés aux incertitudes liées à la climatologie de DMS marin, la paramétrisation des échanges entre l'océan et l'atmosphère, et le rôle de chemins d'oxydation habituellement non pris en compte dans les modèles globaux. Nous avons ensuite estimé avec une suite de modèles quelle pouvait être la réponse du DMS atmosphérique et de l'albédo des nuages au réchauffement climatique. Les données satellitaires des propriétés optiques des aérosols complètent très utilement les modèles globaux. Nous avons utilisé les données POLDER pour estimer l'effet radiatif direct des aérosols et tenter de discriminer les aérosols naturels des aérosols anthropiques. L'effet indirect des aérosols est plus difficile à détecter car l'impact de la morphologie des nuages prime sur celui induit par les aérosols sur la microphysique. Des résultats plus récents concernant le rôle des aérosols carbonés et la campagne INDOEX, ainsi qu'une réflexion sur le concept de forçage radiatif ont également été présentés lors de la soutenance.

Table des matières

Chapitre 1

Introduction

1 Généralités

L'intérêt pour les sciences atmosphériques a considérablement grandi au cours des dernières années en raison de la possibilité d'une influence anthropique sur le climat. Les modèles de circulation générale ont été largement utilisés pour tenter de quantifier l'effet sur le climat de l'augmentation de la concentration des gaz à effet de serre. La sensibilité du climat prédite par ces différents modèles (mesurée en °C d'augmentation de température globale à l'équilibre pour un doublement de la concentration de CO_2) varie entre 1.5 et 4.5°C, soit un facteur 3 d'incertitude (IPCC, 1996, 2001). Aucune de ces valeurs n'est en contradiction avec les variations de température du siècle dernier car les forçages radiatifs autres que celui des gaz à effet de serre, restent sujets à la plus grande incertitude. En utilisant un modèle de complexité intermédiaire, Knutti et al. (2002) ont pu estimer la distribution statistique du paramètre de sensibilité climatique. Les auteurs ont réalisé un grand nombre de simulations pour des sensibilités climatiques différentes et un large éventail de perturbations climatiques (dues aux gaz à effet de serre anthropiques, à l'ozone stratosphérique ou aux aérosols) dont les amplitudes varient à l'intérieur de leurs intervalles de confiance respectifs. La distribution statistique de la sensibilité climatique a ensuite été obtenue en ne conservant que les simulations réalistes en terme d'évolution de la température de surface et du contenu en chaleur de l'océan sur la période instrumentale. Les auteurs ont ainsi montré que des valeurs élevées du paramètre de sensibilité climatique ne sont pas à exclure, ce qui implique une probabilité non négligeable d'un réchauffement climatique plus important que prévu à la fin du XXIe siècle. La sensibilité du climat ne pourra donc pas être déterminée à partir de l'utilisation conjointe de modèles et d'observations des températures tant que les différents forçages radiatifs, parmi lesquels ceux dus aux aérosols, ne seront pas connus avec précision.

2 Rappels sur les effets des aérosols et le forçage radiatif

On appelle "effet direct des aérosols" l'extinction (diffusion et absorption) par les aérosols en ciel clair, "effet semi-direct des aérosols" l'impact de l'absorption par les aérosols en ciel clair sur le profil de température et d'humidité et indirectement sur la formation des nuages, "premier effet indirect des aérosols" (ou parfois effet Twomey) l'augmentation de l'épaisseur optique des nuages suite à l'augmentation du nombre et à la diminution de la taille des gouttelettes d'eau nuageuse (à contenu en eau liquide fixé), et "second effet indirect des aérosols" l'augmentation du contenu en eau liquide, de la hauteur ou de la durée de vie des nuages due à une efficacité à précipiter moindre du nuage induite par la plus petite taille des gouttelettes (Figure 1).

On appelle "forçage radiatif" la perturbation du bilan radiatif à la tropopause après ajustement des températures stratosphériques, mais avec les profils de température et d'humidité de la troposphère (et de la surface) maintenus fixes. Le concept de forçage radiatif est intéressant car un grand nombre d'expériences à l'aide de modèles uni- et tri-dimensionnels montrent que le changement de température de la surface (en moyenne globale et à l'équilibre) est proportionnel au forçage radiatif, soit :

$$\Delta Ts = \lambda \, \Delta F \tag{1}$$

Figure 1: Schéma expliquant les premier et second effets indirects des aérosols. On suspecte également la possibilité d'un effet indirect sur les nuages de glace.

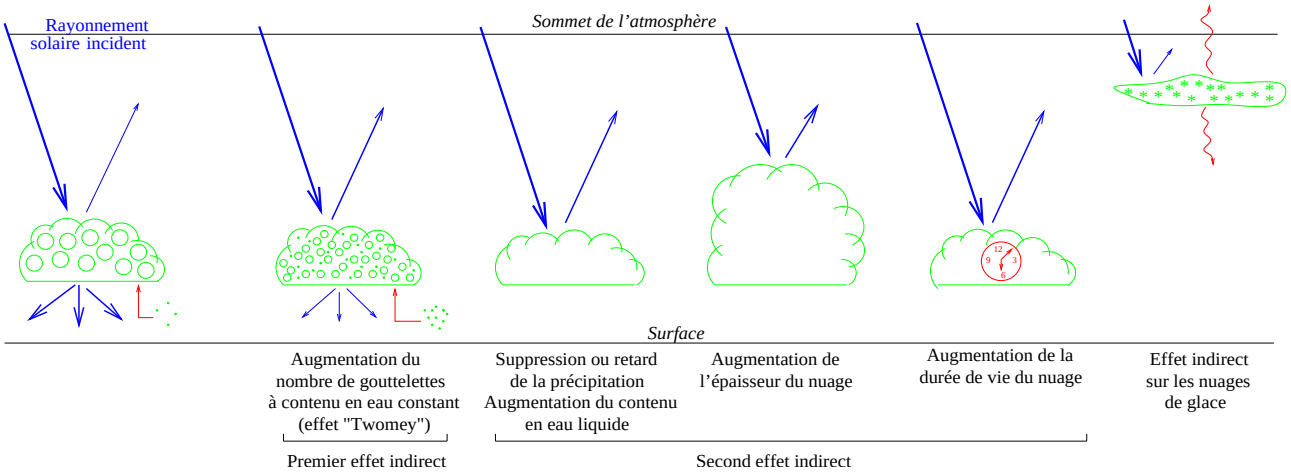

où le paramètre de sensibilité climatique, λ, est dépendant du modèle en question mais relativement indépendant (de l'ordre de $\pm$ 20%) du signe, de l'ordre de grandeur et de la distribution spatiale du forçage radiatif (Hansen et al., 1998; Le Treut et al., 1998).

La notion de forçage radiatif ne s'applique strictement qu'à une perturbation radiative due à un agent climatique EXTERNE qu'il soit naturel ou anthropique (modification de la concentration en gaz à effet de serre due aux activités anthropiques, aérosols anthropiques, modification de la constante solaire, changement de l'albédo de surface, etc...). On fait donc une différence entre le "forçage radiatif des aérosols" qui représente la perturbation radiative due aux aérosols anthropiques, et la "perturbation radiative des aérosols" qui représente celle due à tous les aérosols. Cette convention est cependant loin d'être appliquée uniformément dans la littérature. On se méfiera donc des affirmations comparant la "perturbation radiative de(tous le)s aérosols" au "forçage radiatif des gaz à effet de serre (anthropique)".

Le concept de forçage radiatif a toutefois des limitations (voir Ramaswamy et al. (2001) pour une discussion complète du concept). On notera que le paramètre de sensibilité du climat λ peut dévier significativement de sa valeur moyenne pour le forçage radiatif par des aérosols très absorbants (en raison de l'effet semi-direct impliquant des rétroactions sur les nuages, Hansen et al., 1998). On ne peut définir strictement le forçage radiatif pour le second effet indirect des aérosols (Rotstayn et Penner, 2001)ou l'effet de l'irrigation sur la vapeur d'eau atmosphérique et le climat (Myhre et al., 2002). Comme indiqué plus haut, la définition de forçage radiatif implique un calcul à profil constant de température et d'humidité, ce qui n'est clairement pas possible pour le second effet indirect qui ne peut être défini de manière instantanée mais nécessite une évolution temporelle d'un certain nombre de paramètres impliquant le cycle de l'eau.

En conclusion, on peut utiliser, en prenant quelques précautions, le concept de forçage radiatif pour comparer plusieurs mécanismes de changement climatique (Figure 2). Les forçages radiatifs dus aux aérosols sont parmi ceux présentant la plus grande incertitude. Les aérosols soufrés ne sont bien évidemment pas le seul type d'aérosols responsable de forçage radiatif. Il faut également tenir compte des aérosols carbonés, que l'on sépare en général en carbone-suie (*black carbon* ou BC) et carbone organique (*organic carbon* ou OC) et qui proviennent à la fois de la combustion des combustibles fossiles et des feux de biomasse. Jouent aussi un rôle les poussières désertiques dont une fraction des émissions pourrait être la conséquence des activités humaines. On a l'habitude de classer les aérosols en fonction de leur composition chimique car i) il y a une spéciation des émissions d'aérosols et de leurs précurseurs, ii) la spéciation chimique de l'aérosol est un aspect important de la mesure de l'aérosol ambient. C'est donc également par composé chimique que l'on modélise l'aérosol.

Figure 2 : Forçages radiatifs depuis le début de l'ère industrielle jusqu'à la période actuelle. On a également indiqué le niveau de compréhension scientifique pour chaque agent climatique. Le nombre d'agents climatiques, qu'ils soient ou non liés aux aérosols, a augmenté significativement entre les deux rapports successifs du GIEC (Groupe Intergouvernemental d'Experts sur l'Evolution du Climat ou IPCC en anglais) de 1995 (IPCC, 1996) et 2001 (IPCC, 2001). D'après Ramaswamy et al. (2001).

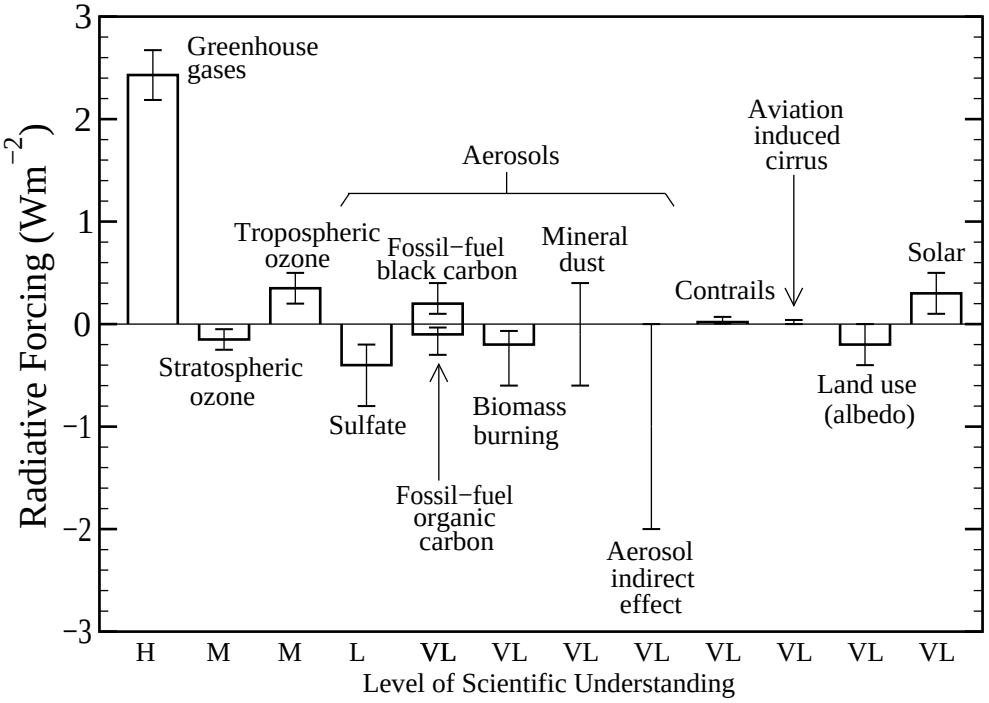

3 Les mesures POLDER

Les mesures satellitaires permettent d'inverser plusieurs paramètres liés aux aérosols en condition de ciel clair. L'algorithme de classe 1 de l'instrument POLDER permet de mesurer l'épaisseur optique des aérosols et leur coefficient d'Angström au-dessus des océans (Goloub et al., 1999; Deuzé et al., 2000). Le modèle d'aérosol utilisé pour l'inversion (non validé) est également disponible. L'algorithme de classe 2, basé sur une sélection différente de modèles, fournit également le rapport entre le mode d'accumulation et le mode grossier au-dessus des océans. Au-dessus des continents, les nouveaux algorithmes basés essentiellement sur l'analyse de la lumière polarisée fournissent une estimation de l'épaisseur optique et du coefficient d'Angström du mode d'accumulation (comportant les particules les plus polarisantes).

Les mesures satellitaires ne permettent malheureusement pas de discriminer la composition chimique de l'aérosol. Au mieux, une analyse conjointe de l'épaisseur optique et du coefficient d'Angström donne une indication sur le type de l'aérosol dominant. Ainsi une épaisseur optique élevée associée à un coefficient d'Angström faible indique plutôt la présence de poussières désertiques. A l'inverse un coefficient d'Angström élevé indique la présence d'aérosols du mode d'accumulation, particules sulfatées ou carbonées. Des épaisseurs optiques élevées de particules de petites tailles sont probablement d'origine humaine (feux de biomasse provoqué par l'homme ou aérosols de pollution industrielle). On peut donc faire une discrimination grossière de l'aérosol en supposant au premier ordre que les particules les plus petites sont majoritairement d'origine anthropique. Cela reste néanmoins à quantifier à partir de mesures sol ou in-situ et en combinant l'information radiométrique avec celle d'autres instruments spatiaux.

4 Organisation du manuscrit

Le travail présenté dans cette habilitation reprend un certain nombre d'études réalisées depuis mon travail de thèse (Boucher, 1995) se rapportant aux effets radiatifs direct et indirect des aérosols. Il tente de répondre aux questions posées en conclusion de ce travail de thèse à partir d'un travail de modélisation globale en ligne des aérosols et d'analyse des données POLDER. L'ensemble des sujets abordés dans les différents chapitres vise à former un tout cohérent et récent. Pour cette raison, certains aspects annexes ou plus techniques sur lesquels j'ai également travaillés sont volontairement laissés de côté : comparaison de codes de transfert radiatif simulant le forçage radiatif des aérosols (Boucher et al., 1998), impact du choix de la fonction de phase sur le calcul du forçage radiatif des aérosols (Boucher, 1998), transfert radiatif tri-dimensionnel dans un panache d'aérosols provenant d'un feu de forêt (Trentmann et al., 2002), expérience de clôture sur les flux radiatifs en présence d'aérosols (Formenti et al., 2002b), méthode itérative d'estimation de l'indice de réfraction complexe des aérosols à partir de mesures optiques de diffusion et d'absorption (Guyon et al., 2002), ou encore intercomparaison de modèles uni-colonnes issus de modèles de circulation générale avec les données de la campagne ACE-2 (Menon et al., 2002).

Ce manuscrit est donc divisé en chapitres qui reprennent différents développements de ma recherche sur les aérosols. Le chapitre 2 s'appuie sur les conclusions de l'IPCC (2001) pour estimer les distributions probabilistiques du forçage radiatif total et de ses composantes liées ou non aux aérosols. Ce travail a ouvert la voie à une interprétation probabilistique du changement climatique (par exemple, Knutti et al., 2002). Les autres chapitres visent directement à diminuer l'incertitude des forçages radiatifs des aérosols ainsi mise en évidence. Cela passe par le développement et l'évaluation d'un modèle simulant les différentes composantes chimiques de l'aérosol atmosphérique. La description et l'évaluation pour l'aérosol soufré sont données dans le chapitre 3. L'évolution temporelle du cycle du soufre et des forçages radiatifs associés est estimée dans le chapitre 4 ; cette information est nécessaire pour mener au mieux les études de détection et d'attribution du changement climatique à partir des séries temporelles d'observation et des simulations climatiques. La sensibilité du cycle du soufre à la représentation de la source et de l'oxydation du diméthylsulfide (DMS) est discutée dans le chapitre 5. Le chapitre 6 examine l'hypothèse d'une rétroaction climatique impliquant le diméthylsulfide en réponse au changement climatique. L'utilisation des données satellitaires POLDER pour la détection et la quantification des effets climatiques des aérosols donne lieu aux chapitres 7 et 8. Enfin un exercice de prospective qui concerne plus particulièrement les effets des aérosols à l'échelle globale est présenté dans le chapitre 9. La conclusion est axée sur mes projets futurs de recherche. Deux articles de synthèses sont également présentés en annexes.

Chapitre 2

Sommation des forçages radiatifs et incertitudes dues aux aérosols

Ce chapitre reprend l'article de *Boucher et Haywood* [2001] paru dans le journal *Climate Dynamics*.

On summing the components of radiative forcing of climate change

Olivier Boucher
Laboratoire d'Optique Atmosphrique,
U.F.R. de Physique, Btiment P5,
Universit des Sciences et Technologies de Lille,
59655 Villeneuve d'Ascq Cedex, France
On sabbatical leave at the Max Planck Institute for Chemistry, Mainz, Germany.
E-mail: boucher@loa.univ-lille1.fr

Jim Haywood
Met Office, London Road,
Bracknell, England
E-mail: jim.haywood@metoffice.com

Abstract. Radiative forcing is a useful concept in determining the potential influence of a particular mechanism of climate change. However, due to the increased number of forcing agents identified over the past decade, the total radiative forcing is difficult to assess. By assigning a range of probability distribution functions to the individual radiative forcings and using a Monte-Carlo approach, we estimate the total radiative forcing since pre-industrial times including all quantitative radiative forcing estimates to date. The resulting total radiative forcing has a 75–97% probability of being positive (or similarly a 3–25% probability of being negative), with mean radiative forcing ranging from +0.68 to +1.34 Wm^{-2}, and median radiative forcing ranging from +0.94 to +1.39 Wm^{-2}.

1 Introduction

Radiative forcing (RF) enables estimation of the potential climatic effect of a particular perturbation to the energy balance of the Earth/atmosphere system. Many modelling studies of varying complexity indicate that the global mean temperature response, ΔT, to a global mean RF, ΔF, may be estimated using the relationship:

$$\Delta T = \lambda \, \Delta F \qquad (1)$$

where λ is the climate sensitivity of the particular model in K/(Wm^{-2}). While the climate sensitivity parameter varies between models, it appears approximately independent of the sign, magnitude, and spatial distribution of the RF (Ramaswamy and Chen 1997a; Le Treut et al 1998; Hansen et al 1998; Forster et al 2000).

There have been significant advances in our understanding of RF mechanisms. IPCC (1990) and IPCC (1994) presented estimates for well-mixed greenhouse gases (CO_2, CH_4, N_2O, and the halocarbons), stratospheric and tropospheric ozone, the direct and indirect effect of anthropogenic aerosols, and solar activity. Shine et al (1996) in IPCC (1996) separated the direct effect of aerosols into sulphate, fossil-fuel soot, and biomass burning. Ramaswamy et al (2001) in IPCC (2001) added fossil-fuel organic carbon, mineral dust, contrails, aircraft induced cirrus, and the effects of land-use change upon the albedo of the Earth. Note that Ramaswamy et al (2001) only considered the first indirect aerosol effect (an increase in cloud albedo due to an increase in cloud droplet number concentration at fixed liquid water content) and not the second one (a possible increase in cloud liquid water content and cloud cover associated with a decrease in precipitation efficiency). In Fig. 1, best estimates of the RF from pre-industrial ($\tilde{1}750$) to present (late 1990s; $\tilde{2}000$) times are shown by the rectangular bars, with vertical lines indicating the uncertainty which is guided for the most part by the range of published estimates. Exceptions are for mineral dust, aviation induced cirrus, and the first indirect effect of tropospheric aerosols. For mineral dust and the first aerosol indirect effect, no best estimate is presented owing to the large uncertainties associated with the mechanisms. The range given for the first aerosol indirect effect is broader than the range of model results to account for uncertainties in model parameterisations and neglect of in-cloud absorption by black carbon aerosols (Ramaswamy et al 2001). Note that Shine and Forster (1999) did not account for uncertainties related to in-cloud absorption, and suggested a best estimate of –1 Wm^{-2} and a factor of two uncertainty. For aviation-induced cirrus, the range represents a range of best estimates and does not involve uncertainties which could not be quantified (IPCC 1999). We ignore the RF due to stratospheric volcanic aerosols because of its episodic and transient nature. A qualitative Level of Scientific Understanding (LOSU) was included for each mechanism to provide a subjective judgement of the scientific grounding on which each of the estimates is made (Ramaswamy et al 2001).

Fig. 1: Global, annual-mean radiative forcing (Wm^{-2}) due to a number of agents from pre- industrial (1750) to present (late 1990s; 2000) times. H, M, L, and VL are the different LOSU and stand for "high", "medium", "low", and "very low", respectively. Adapted from Ramaswamy et al (2001).

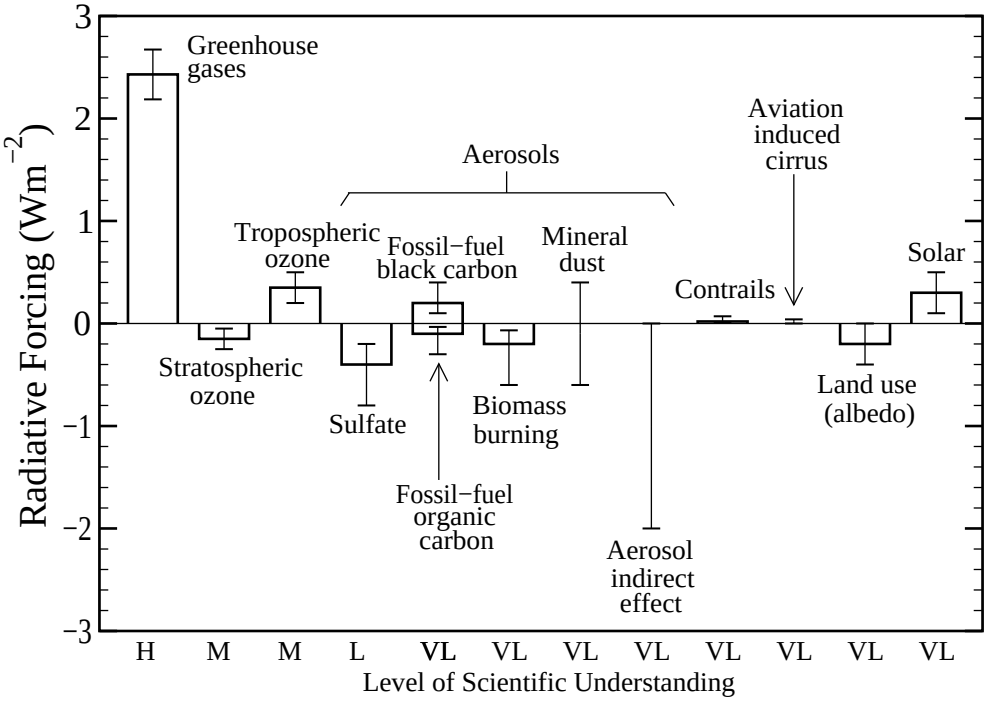

The total RF since pre-industrial times and its sign are of central importance to climate modelling studies because, according to equation (1), a negative net RF leads to a surface cooling while a positive net RF leads to a surface warming. Models have been used to combine different RFs and simulate the past temperature change, the complexity of the models ranging from simple energy balance models (e.g., Raper and Cubasch 1996) to fully coupled atmosphere-ocean general circulation models (e.g., Meehl et al 2000). While Shine et al (1996) and Ramaswamy et al (2001) did not derive a 'best estimate' of the total RF, Schwartz and Andreae (1996) provided a 'best estimate' RF by summing the individual best estimates, and an uncertainty range by summing the upper and lower ends of the individual uncertainty ranges. This study extends the study of Schwartz and Andreae (1996) by including all RF agents identified by Ramaswamy et al (2001). We assume probability density functions (PDFs) for each RF mechanism and a total probability density function (TPDF) is obtained by combining these PDFs using a Monte-Carlo modelling technique. The mean and median of the TPDF, as well as the probability that the total RF is negative, are computed.

2 Method

As summarized in Table 1, the uncertainties in Ramaswamy et al (2001) are given either as a range (e.g., for greenhouse gases, stratospheric and tropospheric ozone) or as an uncertainty factor (e.g., for sulphate aerosols or contrails). Three basic functions are used in this study to represent the PDF of the individual RF component: the normal PDF, the log-normal PDF, and the equally probable or 'flat' PDF. Fig. 2 shows these PDFs for the RF of sulphate aerosols which is given a best estimate of –0.4 Wm^{-2} and an uncertainty factor of 2 in Ramaswamy et al (2001). The solid line on Fig. 2 shows a normal PDF centred on –0.5 Wm^{-2} with 2 standard deviations encompassing the range –0.2 to –0.8 Wm^{-2} (i.e., 2 σ = 0.3 Wm^{-2}). The dashed line shows a log-normal PDF which expresses the fact that the logarithm of the (magnitude of the) RF is normally distributed around ln(0.4) with a standard deviation verifying 2 σ = ln(0.4)–ln(0.2) = ln(0.8)–ln(0.4) = ln(2). The dotted line shows a flat PDF encompassing the range –0.2 to –0.8 Wm^{-2}. Note here that, although the ranges are constrained in a consistent way, the means of the normal and log-normal PDFs shown in Figure 2 are not identical. They are –0.5 and –0.425 Wm^{-2} for the normal and the log-normal PDFs, respectively, and differ from the best estimate. The log-normal PDF is probably the best representation of the mean and range of those RFs quoted by Ramaswamy et al (2001) 'as uncertain by a factor of y'. It also constrains the sign of the forcing, which is not the case when a (broad) normal PDF is used.

Table 1: Radiative forcings (Wm^{-2}) from pre-industrial (1750) to present (late 1990s; 2000) times as given in Ramaswamy et al (2001) and used in this study.

Forcing agent	IPCC best estimate (Wm^{-2})	Uncertainty or range (Wm^{-2})	Mean value (normal PDF) (Wm^{-2})	Mean values (log-normal PDFs) x=1.0/x=1.5/x=2.0	Mean value (flat PDF) (Wm^{-2})
Greenhouse gases	+2.43	± 10%	+2.43	NA	NA
Stratospheric ozone	−0.15	± 0.10	−0.15	NA	NA
Tropospheric ozone	+0.35	± 0.15	+0.35	NA	NA
Sulphate aerosols	−0.40	x 2	−0.50	−0.508/−0.445/−0.425	NA
Fossil-fuel organic carbon	−0.10	x 3	−0.167	−0.183/−0.131/−0.116	NA
Fossil-fuel black carbon	+0.20	x 2	+0.25	+0.254/+0.222/+0.212	NA
Biomass burning aerosols	−0.20	x 3	−0.333	−0.365/−0.261/−0.233	NA
Mineral dust	NA	−0.6 to +0.4	−0.10	NA	−0.10
Aerosol indirect effect	NA	−2.0 to 0	−1.00	−1.220/−0.872/−0.776 *	−1.00
Contrails	+0.02	x 3.5	+0.038	+0.044/+0.028/+0.024	NA
Aviation-induced cirrus	NA	0 to +0.04 #	+0.02	NA	+0.02
Land-use (albedo)	-0.20	± 100%	−0.20	NA	NA
Solar	+0.30	± 0.20	+0.30	NA	NA

NA means "Not Applicable". The mean radiative forcing, RFmean, assuming a log-normal PDF is related to the best estimate radiative forcing, $RF_{\text{best estimate}}$, the uncertainty factor, and x through the relationship:
$RF_{\text{mean}} = RF_{\text{best estimate}} \exp ((\ln(\text{uncertainty factor}) / x)^2 / 2)$
The range 0 to 0.04 Wm^{-2} given in IPCC (1999, 2001) is a range of best estimate, but we use it here as a range of uncertainty. * For the log-normal PDF of the aerosol indirect effect, we assume a best estimate value of −0.667 Wm^{-2} and a factor of 3 uncertainty.

Fig. 2: Illustration of the three basic probability distribution functions (PDFs) used for the direct aerosol radiative forcing by sulphate aerosols. The normal (solid line) and log-normal (dashed line) PDFs are for x=2.0. The flat PDF (dotted line) is shown for completeness but is not used in the present study for sulphate aerosols.

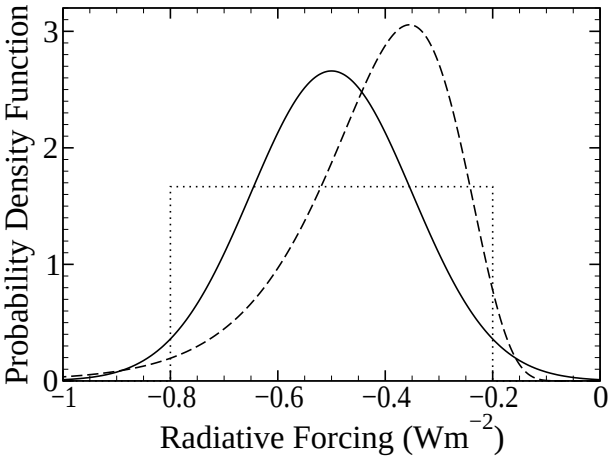

We restrict ourselves to the forcing agents identified by Ramaswamy et al (2001) and to the period from pre-industrial to present times. A similar analysis could be conducted for the past time history of RFs (Myhre et al 2001) and for the future RFs estimated from the IPCC emission scenarios (Ramaswamy et al 2001). Different scenarios are set up where one of the three PDFs is assigned to each RF component shown in Fig. 1. The normal and log-normal PDFs are set up so that the range given by Ramaswamy et al (2001) encompasses the mean $\pm$ x standard deviations (Table 1). As Ramaswamy et al (2001) state that the range is based on values in the published literature, our calculations assume x values of 1.0, 1.5, and 2.0. Thus when normal and log-normal PDFs are used, the ranges in Ramaswamy et al (2001) are interpreted as representing the 68%, 87%, or 95% confidence intervals, respectively. The flat PDF assumes an equally probable likelihood that the RF lies within the range given by Ramaswamy et al (2001). A Monte-Carlo simulation is performed, where we generate 1 million vectors composed of the 13 RF components of Fig. 1. As mentioned above, each RF component is treated as a random variable which follows an assumed PDF (as defined in Tables 1 and 2). A new random variable (the total RF) is defined as the sum of the 13 RF components, for which we obtain a PDF (called the TPDF). In this procedure, we assume that the different RFs can be considered as independent, which may not be entirely valid.

Three simulations (referred to as 1.0, 1.5, and 2.0 corresponding to x values of 1.0, 1.5, and 2.0, respectively) are performed for each of four scenarios. In scenario A, all the RFs are assumed to follow normal PDFs (Table 2). Scenario B is as scenario A, but those RFs quoted by Ramaswamy et al (2001) as 'uncertain by a factor of y' (the RF by contrails and the direct aerosol RFs, except that due to mineral dust) are modelled by log-normal PDFs. Implementation of these scenarios skews the PDF for each component toward the best guess of Ramaswamy et al (2001). Scenario C is as scenario B, but RFs with no best estimate (first indirect aerosol effect, mineral dust, and aviation induced cirrus) are modelled by flat PDFs. Scenario D is as scenario C, but with the first indirect aerosol RF being modelled by a log-normal PDF.

3 Results

Fig. 3a–c shows the results of the simulations for x=1.0, x=1.5, and x=2.0, respectively. The TPDF curves in Fig. 3 are not entirely smooth due to the use of a statistical Monte-Carlo model in determining each PDF. However, multiple computations with the Monte-Carlo model suggest that the mean, median, and probability

Table 2: Summary of the PDFs for individual RFs in scenarios A to D.

	Greenhouse gases land-use and solar			Direct aerosol effect (except mineral dust) and contrails			Mineral dust and aviation-induced cirrus			First aerosol indirect effect		
Scenario	N	LN	F	N	LN	F	N	LN	F	N	LN	F
A	X			X			X			X		
B	X				X		X			X		
C	X				X				X			X
D	X				X				X		X	

N, LN, and F stand for 'normal', 'log-normal', and 'flat' PDF, respectively.

of negative forcing shown in Table 3 are accurate to 0.005 Wm^{-2}, 0.01 Wm^{-2}, and 0.1%, respectively. We have verified that the Monte-Carlo approach yields the expected results for simulations A, where the TPDF can be computed analytically, and that for each simulation the mean total RF obtained with the Monte-Carlo calculations is identical to the sum of the individual mean RFs.

Fig. 3: Probability distribution functions of the total radiative forcing for the 12 simulations described in the text: a) x=1.0, b) x=1.5, and c) x=2.0.

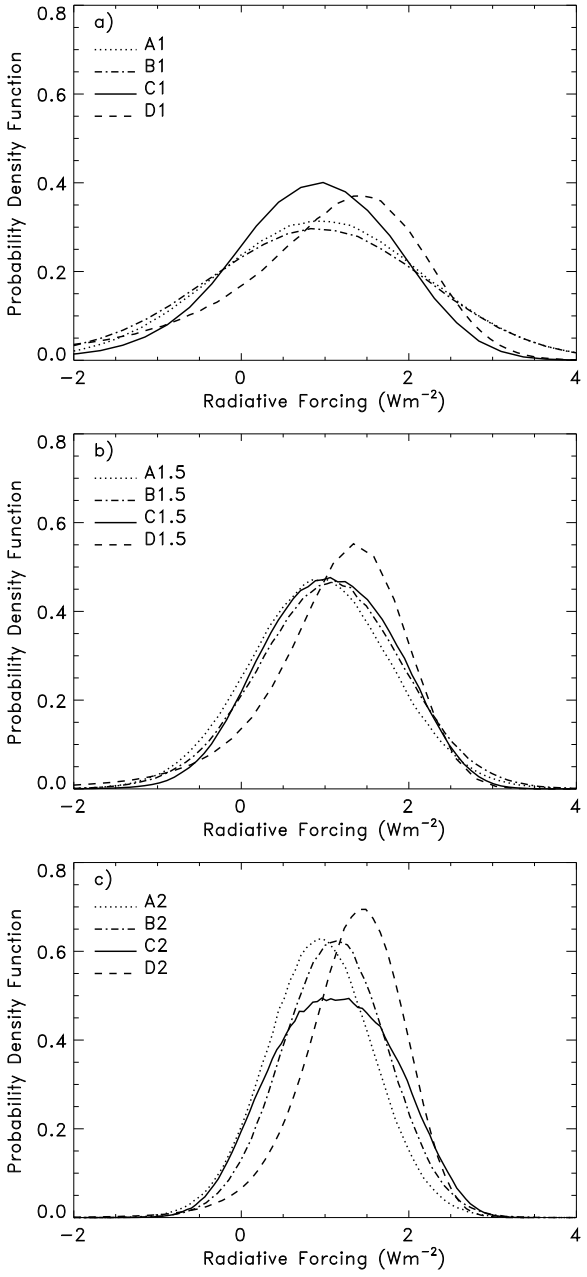

Table 3: Mean and median total radiative forcing (RF in Wm^{-2}) and probability that the total radiative forcing is negative (%) for the 12 simulations presented in the text.

Simulation	Mean RF (Wm^{-2})	Median RF (Wm^{-2})	Probability that RF is negative (%)
A1.0	0.94	0.94	23.0
B1.0	0.89	0.94	24.7
C1.0	0.89	0.96	17.7
D1.0	0.67	1.10	22.7
A1.5	0.94	0.94	13.5
B1.5	1.06	1.07	10.9
C1.5	1.06	1.07	8.9
D1.5	1.19	1.32	8.5
A2.0	0.94	0.94	7.1
B2.0	1.11	1.11	4.2
C2.0	1.11	1.11	6.0
D2.0	1.34	1.39	2.8

The mean total RF is very sensitive to the assumed value for x (Table 3). It ranges among the scenarios from 0.68 to 0.94 Wm^{-2}, 0.94 to 1.19 Wm^{-2}, and 0.94 to 1.34 Wm^{-2}, for x values of 1.0, 1.5, and 2.0, respectively. Except for simulations of scenario A, the median is larger than the mean total RF because the log-normal PDFs are primarily applied to RFs that are negative, which skews the TPDFs to larger RFs. Note that the median, which may be more relevant than the mean, is never smaller than 0.94 Wm^{-2}.

The only difference between the simulations from the C and D scenarios is that the PDF for the first aerosol indirect effect is changed from a flat PDF (range –2 to 0 Wm^{-2}) to a log-normal PDF (with 68%, 87, or 95% confidence intervals for the range -0.22 to -2.0 Wm^{-2}). While both PDFs appear reasonable, the effects upon the TPDF are significant. The median total RF is much larger in the D compared to the C simulations. Also the probability for negative total RF is either much larger (when x=1.0) or much smaller (when x=2.0) in the D compared to the C scenario.

We compute the probability that the total RF is negative to range between 2.8% and 24.7%. Similarly the total RF has a 75.3 to 97.2% probability of being positive. If we follow IPCC (2001) to indicate confidence estimates, this means that the total RF is unlikely (10–33% chance) or very unlikely (1–10% chance) to be negative.

4 Discussion and conclusion

The arguments for not summing the radiative forcings from the different forcing mechanisms rely on the following arguments:-

a) The uncertainty range given for each RF is not a statistically rigorous quantity. The ranges are for the most part guided by the spread in the published estimates of RFs, but in some cases (e.g., anthropogenic mineral dust, or first aerosol indirect effect) they also reflect a subjective assessment of the uncertainties. Performing rigorous statistical analysis of the results from the models is difficult because of the small number of studies, and because several of the modelling studies are not truly independent. Attempts to estimate the uncertainty in the aerosol RF using simplified expressions (e.g., Charlson et al 1992; Penner et al 2001) make simplifying assumptions which may limit their applicability.

b) The presence of RF estimates where no best estimate is provided such as for aviation induced cirrus, anthropogenic mineral dust, and the first aerosol indirect effect makes such a summation difficult.

c) The different LOSU afforded to each of the forcing mechanisms complicate the issue. It may be argued that RFs with very low LOSU should be given a lower weighting than those with a high LOSU.

d) Because of a complex spatial distribution, the global-mean total RF does not give sufficient information on the spatial response of the climate system. Thus even for a global mean RF of zero, there may be significant local changes in climate (Cox et al 1995; Ramaswamy and Chen 1997b).

e) The additivity of the climate responses to different RFs, which is the central justification for a summation of RF, has been shown for some but not all of the RF mechanisms (e.g., Ramaswamy and Chen 1997a; Hansen et al 1998).

By performing a set of simulations using different PDFs (as discussed in section 2) and presenting an ensemble of results we circumvent arguments a) and b). While we temporarily add a level of complexity by choosing different sets of PDFs, we can draw in the end more robust conclusions because they apply to the whole set of simulations. It is difficult to justify argument c) as if a forcing mechanism is identified as scientifically valid and assigned a very low LOSU, it should not simply be discarded or assigned a reduced weighting, but should be treated in a manner consistent with the rest of the RF mechanisms (Penner and Rotstayn 2000). Argument d) may be rebuffed as RF has never been intended to be an indicator of regional climate change. If the climate sensitivity parameter λ varies for different RFs, or combinations of RFs (argument e), then the whole concept of RF as an indicator of potential climate change is flawed. While some studies show that the climate sensitivity parameter may differ for some RF mechanisms such as absorption by black carbon aerosols (e.g., Hansen et al 1998), these forcing mechanisms should currently be considered as exceptions to the rule, given the number of studies that have shown the relationship between global mean temperature response and global mean RF as being relatively robust.

Some simulations represent a better interpretation of the conclusions of Ramaswamy et al (2001) than others. Simulations A and B assume a normal distribution for the first aerosol indirect RF. One consequence is that it allows positive values for this forcing, which becomes more probable as x decreases. This is not realistic and we believe that the C and D simulations are better representations of Ramaswamy et al (2001). It is difficult to select a best value for x, but there are some limited indications that values of 1.5 or 2.0 are more appropriate than a value of 1.0. Analysis of the published estimates of the direct sulphate aerosol RF, as compiled by Ramaswamy et al (2001), reveals a mean of 0.45 Wm^{-2} and a standard deviation of 0.18 Wm^{-2} (n=19), which would roughly correspond to x=1.7. A similar analysis for the tropospheric ozone RF yields a mean of 0.35 Wm^{-2} and a standard deviation of 0.05 Wm^{-2} (n=11), corresponding to x=3.0. These simple statistics cannot be carried out for the other RF agents because of the lack of suitably large samples. If one rejects (somewhat subjectively) an x value of 1.0 and select the C and D scenarios, the probability of a negative total RF is always less than 9% (i.e., the total RF is very unlikely negative – or very likely positive). While analysis of climate variability and of temperature records suggests that the total RF is indeed positive (IPCC 2001), such arguments involve a degree of circular reasoning (Rodhe et al 2000) and assume that our understanding of RF mechanisms, climate sensitivity, and climate response is complete.

Finally it should be noted that we only account for known RF mechanisms. In particular, we have excluded the second aerosol indirect effect from our analysis because too little is known about it (Ramaswamy et al 2001). Since this RF is believed to be negative, its inclusion would increase the probability for a total negative RF and would correspondingly decrease the mean and median total RF. We plotted in Fig. 4 the PDF of the

Fig. 4: Probability distribution functions of the total aerosol and non-aerosol radiative forcings for a) scenarios C1.5 and D1.5 and b) scenarios C2.0 and D2.0.

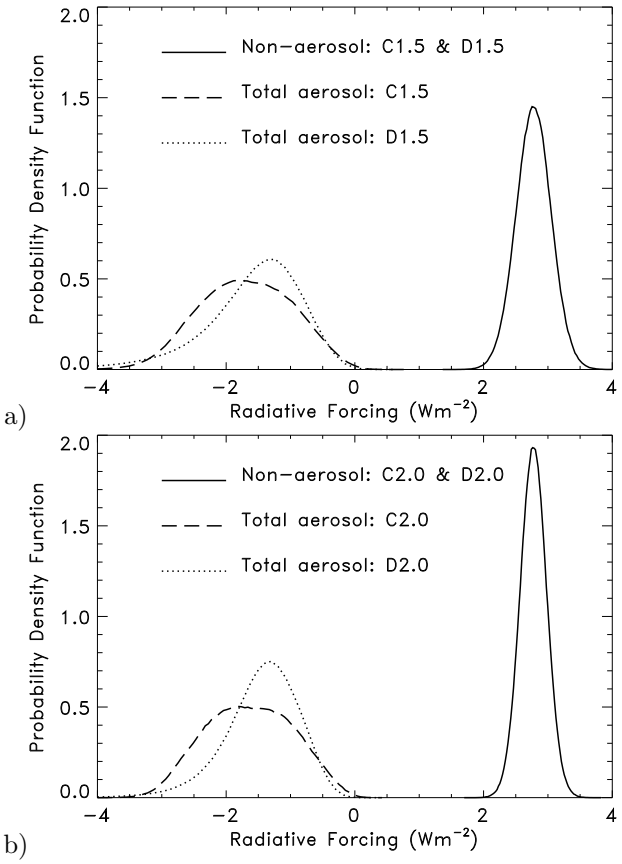

total aerosol and non-aerosol RFs for a subset of our scenarios (C1.5, D1.5, C2.0, and D2.0). It is clear that it is to a large extent the uncertainties in the aerosol RF which drive the large uncertainty in the total RF. We reiterate the conclusions of previous studies (Schwartz and Andreae 1996; Haywood and Boucher 2000) emphasizing that reducing these uncertainties should be a priority in order to improve climate change scenarios . It has been shown, for instance, that the determination of the climate sensitivity parameter, λ, is highly sensitive to the magnitude of the aerosol RF (Schlesinger et al 1992). One possible direction for reducing the uncertainties could consist in a thorough analysis and comparison to observations of the different model estimates in order to select the most reliable ones.

Acknowledgements. The authors are grateful to V. Ramaswamy and S. Schwartz for interesting discussions. Olivier Boucher thanks P. J. Crutzen, J. Lelieveld, and the MPI for Chemistry in Mainz for hospitality. We acknowledge K. Shine and the anonymous referees for their constructive remarks.

References

Charlson RJ, Schwartz SE, Hales JM, Cess RD, Coakley JA, Hansen JE, Hofmann DJ (1992) Climate forcing by anthropogenic aerosols. Science 255: 423–430

Cox SJ, Wang W-C, Schwartz SE (1995) Climate response to forcings by sulfate aerosols and greenhouse gases. Geophys Res Lett 22: 2509–2512

Forster PM de F, Blackburn M, Glover R, Shine KP (2000) An examination of climate sensitivity for idealised climate change experiments in an intermediate general circulation model. Clim Dyn 16: 833–849

Hansen JE., Sato M, Lacis A, Ruedy R, Tegen I, Matthews E (1998) Climate forcings in the Industrial era. Proc Natl Acad Sci USA 95: 12753–12758

Haywood J., Boucher O (2000) Estimates of the direct and indirect radiative forcing due to tropospheric aerosols: A review. Rev Geophys 38: 513–543

IPCC (1990) Climate Change 1990: The Intergovernmental Panel on Climate Change Scientific Assessment, JT Houghton et al (Eds.), Cambridge University Press, New York, USA

IPCC (1994) Climate Change 1994: Radiative Forcing of Climate Change and an Evaluation of the IPCC IS92 Emission Scenarios, JT Houghton et al (Eds.), Cambridge University Press, New York, USA

IPCC (1996) Climate Change 1995: The Science of Climate Change, Contribution of Working Group I to the Second Assessment Report of the Intergovernmental Panel on Climate Change, JT Houghton et al (Eds.), Cambridge University Press, New York, NY, USA, 572 pp

IPCC (1999) Intergovernmental Panel on Climate Change Special Report on Aviation and the Global Atmosphere, JE Penner et al (Eds.), Cambridge University Press, New York, USA, 373 pp

IPCC (2001) Climate Change 2001, The Scientific Basis, Contribution of Working Group I to the Third Assessment Report of the Intergovernmental Panel on Climate Change. JT Houghton et al (Eds.), Cambridge University Press, New York, USA, 881 pp

Le Treut H, Forichon, M, Boucher O, Li Z-X (1998) Sulfate aerosol, indirect effect and CO2 greenhouse forcing: Equilibrium response of the LMD GCM and associated feedbacks. J Climate 11: 1673–1684

Meehl GA, Collins WD, Boville BA, Kiehl JT, Wigley TML, Arblaste JM (2000) Response of the NCAR climate system model to increased CO2 and the role of physical processes. J Climate 13: 1879–1898

Myhre G, Myhre A, Stordal F (2001) Historical evolution of radiative forcing of climate. Atmos Env 35: 2361–2373

Penner JE, Andreae M, Annegarn H, Barrie L, Feichter J, Hegg D, Jayaraman A, Leaitch R, Murphy D, Nganga J,

Pitari G (2001) Aerosols, their Direct and Indirect Effects, In: Climate Change 2001, Contribution of Working Group I to the Third Assessment Report of the Intergovernmental Panel on Climate Change. JT Houghton et al (Eds.), Cambridge University Press, New York, USA, pp. 289–348

Penner JE, Rotstayn LD (2000) Indirect aerosol forcing. Science 290: 407

Ramaswamy V, Chen C-T (1997a) Climate forcing-response relationships for greenhouse and shortwave radiative perturbations. Geophys Res Lett 24: 667–670

Ramaswamy V, Chen C-T (1997b) Linear additivity of climate response for combined albedo and greenhouse perturbations. Geophys Res Lett 24: 567–570

Ramaswamy V, Boucher O, Haigh J, Hauglustaine D, Haywood J, Myhre G, Nakajima T, Shi GY, Solomon S (2001) Radiative Forcing of Climate Change, In: Climate Change 2001, Contribution of Working Group I to the Third Assessment Report of the Intergovernmental Panel on Climate Change. JT Houghton et al (Eds.), Cambridge University Press, New York, USA, pp. 349–416

Raper, SCB, Cubasch U (1996) Emulation of the results from a coupled general circulation model using a simple climate model. Geophys Res Lett 23: 1107–1110

Rodhe H, Charlson RJ, Anderson TL (2000) Avoiding circular logic in climate modelling. Climate Change 44: 419–422

Schlesinger ME, Jiang, X, Charlson, RJ (1992) Implication of anthropogenic atmospheric sulphate for the sensitivity of the climate system, In: Climate Change and Energy Policy, L. Rosen and R. Glasser (Eds), American Institute of Physics, New-York, pp 75–108

Schwartz SE, Andreae MO (1996) Uncertainty in climate change caused by aerosols. Science 272: 1121–1122

Shine KP, Fouquart Y, Ramaswamy V, Solomon S, Srinivasan J (1996) Radiative Forcing of Climate Change, In: Climate Change 1995: The Science of Climate Change, Contribution of Working Group I to the Second Assessment Report of the Intergovernmental Panel on Climate Change, JT Houghton et al (Eds.), Cambridge University Press, New York, USA, pp. 108–118

Shine KP, Forster PM de F (1999) The effect of human activity on radiative forcing of climate change: a review of recent developments. Global Planet Change 20: 205–225

Chapitre 3

Simulation du cycle du soufre

Ce chapitre reprend la note scientifique de l'IPSL de *Boucher et al.* [2002a].

Simulation of the atmospheric sulfur cycle in the Laboratoire de Météorologie Dynamique General Circulation Model. Model Description, Model Evaluation, and Global and European Budgets.

O. Boucher, Laboratoire d'Optique Atmosphérique, Bâtiment P5, Université des Sciences et Technologies de Lille, 59655 Villeneuve d'Ascq Cedex, France. (e-mail: boucher@loa.univ-lille1.fr)

M. Pham, Service d'Aéronomie, Boîte 102, Université Pierre et Marie Curie, 4 Place Jussieu, 75252 Paris Cedex 05, France. (e-mail: mai.pham@aero.jussieu.fr)

C. Venkataraman, Aerosol Research Laboratory, Centre for Environmental Science and Engineering, Indian Institute of Technology Bombay, Powai, Mumbai-400 076, India. (e-mail: chandra@cc.iitb.ac.in)

Abstract. We have used the Laboratoire de Météorologie Dynamique (LMD) general circulation model to simulate the global sulfur cycle. Processes incorporated in the model include emissions, boundary layer mixing, advective and convective transport, dry and wet scavenging, gaseous- and aqueous-phase chemistry. The model predicts the atmospheric fate of hydrogen peroxide (H_2O_2) and six sulfur species: dimethylsulfide (DMS), dimethylsulfoxide (DMSO), hydrogen sulfide (H_2S), sulfur dioxide (SO_2), sulfate (SO_4^{2-}), and methanesulfonic acid (MSA). The model is evaluated through extensive comparisons to measurements. The model represents many features of the observed concentrations of sulfur species. At remote locations, the agreement with observations is generally good. The surface mixing ratios of sulfur dioxide and sulfate aerosols are underestimated over Europe in winter, and overestimated over North America in summer and autumn. At first order, these discrepancies may be explained by biases in the simulated cloud cover and precipitation fields. A sensitivity run, where H_2O_2 is not depleted upon oxidation of SO_2, exhibits a large increase in H_2O_2 concentration in wintertime over polluted regions. This indicates that under these conditions this chemical reaction may represent an important sink for H_2O_2.

1 Introduction

Several sulfur gases are emitted at the Earth's surface from anthropogenic and biogenic activities. Once in the atmosphere, they are transported, oxidized in gas and aqueous phase, and removed by dry and wet deposition. In particular, a large fraction of the gas-phase sulfur dioxide is converted into particulate sulfate. In the seventies, the main concern about the tropospheric sulphur cycle was on the environmental consequences of the man-made sulfur emissions, and particularly the issue of acid rain, since anthropogenic emissions account for more than 60% of the global emissions of sulfur gases (e.g., Rodhe, 1999). In the last ten years, it has been recognized that sulfate aerosols may also affect the climate system (e.g., Charlson et al., 1992). Sulfate aerosols affect the radiation balance, directly through scattering of solar radiation (Boucher and Anderson, 1995), and indirectly by serving as cloud condensation nuclei (CCN), thereby modifying the cloud microphysical and optical properties (Boucher and Lohmann, 1995). Sulfate aerosols also interact chemically with other aerosol types and may play a role in heterogeneous chemistry (Dentener and Crutzen, 1993). In order to assess the climate forcing due to sulfate aerosols, it is necessary to compute the four-dimensional distribution of sulfate concentration, and thus, to simulate the emissions, transport, and transformation of its precursors.

Although there now exist many model studies on the regional or global sulfur cycle (Langner and Rodhe, 1991; Benkovitz et al., 1994; Pham et al., 1995a, 1995b; Feichter et al., 1996; Chin et al., 1996; Chuang et al., 1997; Kasibhatla et al., 1997; Roelofs et al., 1998; Koch et al., 1999; Adams et al., 1999; Barth et al., 2000; Rasch et al., 2000; Chin et al., 2000a, 2000b), there are still areas of uncertainties. The representation of wet scavenging and aqueous-phase chemistry is generally crude in large-scale models. In particular the relative importances of the different oxidation pathways for SO_2 are not well established. Also many models underpredict wintertime sulfate concentrations over Europe and North-East United States (e.g., Barth et al., 2000; Chuang et al., 2002). The reason for this is uncertain. Some authors believe that there is a missing pathway for SO_2 oxidation in models (Kasibhatla et al., 1997; Roelofs et al., 1998), heterogeneous oxidation of SO_2 onto aerosols (Kasibhatla et al., 1997) and aqueous-phase oxidation of SO_2 by peroxynitric acid (HNO_4) (Warneck, 1999; Dentener et al., 2002) being some candidates. Chin et al. (2000b) suggested that contamination by sea-salt of the EMEP measurements could partly explain the discrepancy over Europe. Another possibility is that the concentration of one of the oxidants of SO_2 is underestimated in global models. In particular, this could be the case for H_2O_2 if ozonolysis of alkenes –which is usually not considered in global models– turns out to be an important production term for H_2O_2 in wintertime conditions as suggested by Ariya et al. (2000). The discrepancy between observed and simulated sulfate concentrations may also simply be due to deficiencies in the parameterizations of aqueous-phase chemistry and/or wet scavenging, or in the efficiency of the convective transport (Barth et al., 2000).

Here we present a description of the global sulfur cycle as it was introduced in the General Circulation Model (GCM) of the Laboratoire de Météorologie Dynamique (LMD-ZT). The model is thoroughly evaluated against available measurements. The budgets of sulfur species and H_2O_2 – and their coupling to each other – are discussed. We favored an on-line, in contrast to off-line, approach because we are interested in studying climate-chemistry interactions. By doing so, it is possible to represent to a high degree of consistency the physical and chemical processes of the sulfur cycle. However it is clear that inaccuracies in the simulation of the hydrological cycle (e.g., cloudiness, precipitation) can result in significant biases in the simulated concentrations of the sulfur species. LMD-ZT can also be nudged to meteorological analyses so that comparison with observations at a specific place and time is possible (Hourdin and Issartel, 2000). In the simulations presented in this study, the radiative impact of sulfate aerosols does not feedback on the meteorology. Work is in progress to include a full interactive gas-phase chemistry, as well as carbonaceous, sea-salt, and dust aerosols in the same version of the model. We will then have a useful tool to study the chemical interactions among the different aerosol species. The model will also be used to compute the aerosol radiative forcing and to run scenarios of climate change with the forcings from greenhouse gases and aerosols included.

2 Description of the Model

2.1 LMD-ZT

In LMD-ZT, atmospheric transport is computed with a finite volume transport scheme for large-scale advection (van Leer, 1977; Hourdin and Armangaud, 1999), a scheme for turbulent mixing in the boundary layer, and a mass flux scheme for convection (Tiedtke, 1989). The

Fig. 1: Annual-mean precipitation rate (mm/day) in LMD-ZT (left panel) and the Legates and Willmott (1990) climatology (right panel).

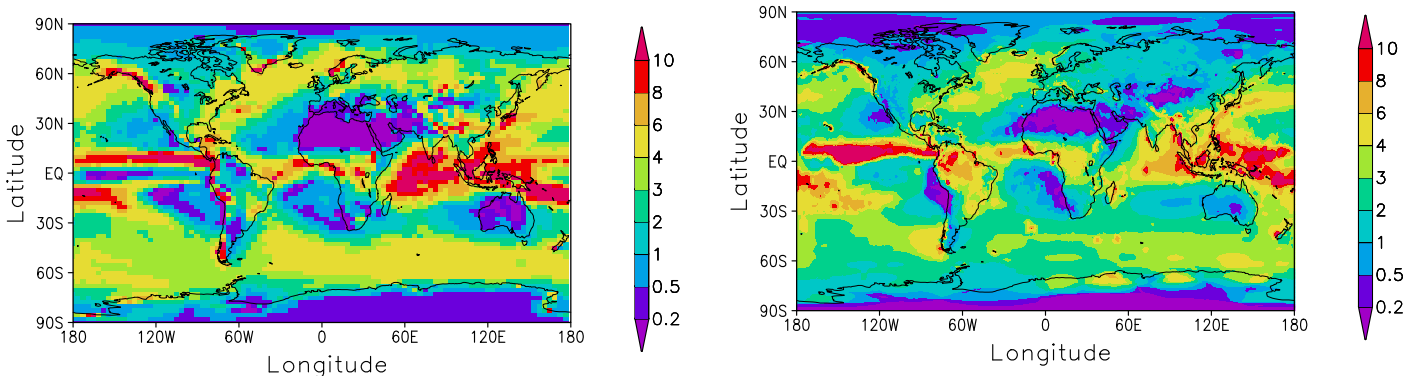

resolution is 3.75° in longitude, 2.5° in latitude (corresponding roughly to the resolution of a T48 spectral model, Hourdin, personal communication) and 19 layers on the vertical. In this version (referred to as 3.3), a hybrid σ-pressure coordinate on the vertical is used, with 5 layers below about 850 hPa and 9 layers above about 250 hPa. The time step is 3 min for resolving the dynamical part of the primitive equations. Mass fluxes are cumulated over 5 time steps so that large-scale advection is applied every 15 min. The physical and chemical parametrizations are applied every 10 time steps or 30 min. The different processes are handled through operator splitting.

In its present version, the model exhibits a too low precipitation rate and cloud cover over continental areas in summertime, and a too large precipitation rate and cloud cover over Europe in wintertime. The precipitation field is shown on Fig. 1 in annual mean along with observations from Legates and Willmott (1990).

Six sulfur species are considered in the model: dimethylsulfide (DMS), dimethylsulfoxide (DMSO), hydrogen sulfide (H_2S), sulfur dioxide (SO_2), sulfate (SO_4^{2-}), and methanesulfonic acid (MSA). Sulfate and MSA are assumed to be 100% in the particulate phase. The concentrations of short-lived radicals OH, HO_2, and NO_3, and ozone, as well as H_2O_2 photodissociation rates, are prescribed from version 3.2 of the Intermediate Model of Global Evolution of Species (IMAGES) (Müller and Brasseur, 1995). The diurnal cycles of these fields are archived from IMAGES for each month and applied in our model with a time step of 30 minutes, which is also the time step for the physical and chemical processes. Because the concentration of hydrogen peroxide H_2O_2 can be significantly affected upon oxidation of SO_2, especially at high latitude in wintertime, it is also a prognostic variable of the model. Its concentration is computed from prescribed OH and HO_2 concentrations and H_2O_2 photodissociation rates archived from IMAGES. It also undergoes dry and wet scavenging and advective and convective transport.

2.2 Emissions

Emissions of sulfur species are summarized in Table 1. SO_2 is emitted primarily by anthropogenic activities. Here we make use of the emission inventory developed in the framework of the Global Emissions Inventory Activity (GEIA). Our annual emission rate (66.3 Tg S yr^{-1}), representative of the year 1985, is close to the emission rates of Koch et al. (1999) and Barth et al. (2000) but lower than that of Chin et al. (2000a). A small fraction (5%) of SO_2 is emitted directly as sulfate (Benkovitz et al., 1996). We include an anthropogenic source of H_2S of 2.82 Tg S yr^{-1} scaled to the SO_2 source, following the estimate of Watts (2000).

We only consider volcanic sources of SO_2 from continuously erupting volcanoes, which represents an emission rate of 4.8 Tg S yr^{-1} (Andres and Kasgnoc, 1998). Biogenic emissions are dominated by the oceanic emission of DMS, the flux of which is derived off-line from

Table 1: Globally- and annually-averaged emission fluxes of sulfur species (Tg S yr^{-1}).

Sources	SO_2	H_2S	DMS	Total
Volcanoes	4.81			4.81
Biosphere		0.51	0.31	0.82
- Vegetation		0.49	0.29	
- Soils		0.02	0.02	
Biomass burning	2.99			2.99
Ocean			19.10	19.10
Man-made	66.28	2.82		69.10
Total	74.08	3.33	19.41	96.82

5% of the man-made SO_2 is emitted directly as sulfate.

the sea surface DMS concentrations of Kettle et al. (1999) and the sea to air parameterization of Liss and Merlivat (1986). The seasonal cycle in DMS emission is very pronounced, especially at 40-50°S. At 19.4 Tg S yr^{-1}, our total emission rate for DMS is significantly larger than those of Koch et al. (1999), Barth et al. (2000), and Chin et al. (2000a), which are 10.7, 15.5, and 13.3 Tg S yr^{-1}, respectively, and were obtained using different methodologies or DMS concentration fields. It is nevertheless in the middle of the range of 10 to 40 Tg S yr^{-1} usually accepted for DMS emissions. We are currently studying the sensitivity of on-line computation of the DMS emission flux to oceanic DMS concentration and air-sea flux parametrization (Cosme et al., 2002; Boucher et al., 2003). Emissions of DMS and H_2S from the biosphere and emissions of SO_2 from biomass burning are the same as in the IMAGES model (Pham et al., 1995a). They are much smaller compared to the other sources of sulfur compounds (i.e., DMS from the ocean and man-made SO_2, see Table 1).

2.3 Gas-Phase Chemistry

Gas-phase chemistry is based on the scheme introduced in Pham et al. (1995a). The reactions and reaction rates are tabulated in Table 2. DMS is oxidized by OH and NO_3 radicals producing SO_2 and DMSO. No other reaction was considered for DMS, in contrast to Chin et al. (1996) who assumed the presence of an additional oxidant to increase the oxidation rate of DMS by a factor of 2. Following Chatfield and Crutzen (1990), we assume that MSA production proceeds via DMSO through the addition pathway of DMS oxidation. This should be investigated in future studies according to Sciare et al. (1998), who suggested that MSA and DMSO production proceeds through two different channels, namely the abstraction and addition channels respectively. H_2S is oxidized by OH but contributes to a very small fraction of the total production rate of SO_2. The distribution of H_2S and DMSO will not be discussed further because of their small burdens and large uncertainties, but their contributions to the global sulfur budget are included for completeness.

Gas-phase H_2O_2 is formed primarily through the reaction of HO_2 given in Table 2, which includes a bimolecular component, a termolecular component, and an enhancement component due to water vapor. This enhancement is about a factor of 2.6 at 100% relative humidity and 298 K. H_2O_2 is removed from the atmosphere by dry and wet deposition (see Section 2.5), by the gas-phase processes of solar photolysis and reaction with the OH radical, and upon the aqueous-phase oxidation of SO_2 (see below). The diurnal variation in H_2O_2 concentration is therefore simulated consistently with the concentrations of OH and HO_2 and H_2O_2 photodissociation rates.

The gas-phase reactions are evaluated using a 30-min time step with an explicit scheme. This scheme can be used because of the long lifetimes of all of the prognostic chemical species considered here. Moreover it makes easy to compute a mass-balanced sulfur budget (cf. Section 7).

2.4 Aqueous-Phase Chemistry

Aqueous-phase oxidation of SO_2 by O_3 and H_2O_2 is also considered. The concentration of O_3 is prescribed using the results from the IMAGES model, but that of H_2O_2 is computed interactively. The cloud pH is predicted by an electroneutrality equation in which NH_4^+ and H^+ are the only cations and NO_3^- is neglected, as follows:

$$[H^+] = 2\,[SO_4^{2-}] + 2\,[SO_3^{2-}] + [HSO_3^-] + [OH^-] - [NH_4^+] \quad (1)$$

From global sulphate concentrations summarised by Seinfeld and Pandis (1998) and measurements by Covert (1988), a cloudwater $[NH_4^+]/[SO_4^{2-}]$ molar ratio of 1.0 is assumed in remote environments and of 1.5 in polluted environments, where cloudwater sulphate concentrations exceeds 15 μM.

Aqueous S_{IV} species are estimated accounting for ionisation of $SO_2{\cdot}H_20$ using the first and second dissociation constants (Table 2). It is assumed that in-cloud oxidation is not limited by mass transfer (Venkataraman et al., 2001) and would depend only on the gas-phase concentrations of SO_2 and the oxidants. Aqueous S_{IV} species are oxidised by ozone and hydrogen peroxide which partition into aqueous phase following Henry's law (Table 2). Dentener et al. (2002) showed that aqueous-phase oxidation of HSO_3^- by $HOONO_2$ could contribute to sulfate formation. However, this reaction has also been shown to significantly alter H_2O_2 and O_3 concentrations in the boundary layer (Dentener et al., 2002). Since this pathway is still uncertain and O_3 is not simulated by the gas-phase chemistry scheme adopted here, we chose to ignore this reaction in the present study.

The rate expressions and rate constants for the aqueous phase reactions (Table 2) are summarised by Seinfeld and Pandis (1998) based on a best fit to the available kinetic data from various studies (Hoffmann and Calvert, 1985).

Table 2: Reaction rates used in the present study.

Reaction	Rate	Reference
Gaseous-Phase Chemistry		
DMS + OH $\longrightarrow$ SO_2 + ...	$K_1 = 9.6\ 10^{-12}\ e^{-234./T}$	a
DMS + OH $\longrightarrow$ $x$$SO_2$+$(1-x)$DMSO+...	$\begin{cases} K_2 = 3.04\ 10^{-12}\ e^{350./T}\alpha/(1+\alpha) \\ \alpha = 1.15\ 10^{-31}\ e^{7460./T}[M] \quad x = 0.6 \end{cases}$	b
DMS + NO_3 $\longrightarrow$ SO_2 + ...	$K_3 = 1.9\ 10^{-13}\ e^{500./T}$	c
SO_2 + OH $\longrightarrow$ sulfate + ...	$\begin{cases} K_4 = \alpha[M]/(1+\alpha[M])/1.5\ 10^{-12}.0.6^{\beta} \\ \alpha = 3.0\ 10^{-31}\ (300./T)^{3.3} \\ \beta = 1./(1+\log_{10}(\alpha[M]/1.5\ 10^{-12}))^2 \end{cases}$	c
DMSO + OH $\longrightarrow$ $x$$SO_2$+$(1-x)$MSA+...	$K_5 = 5.8\ 10^{-11} \qquad x = 0.6$	b
H_2S + OH $\longrightarrow$ SO_2 + ...	$K_6 = 6.0\ 10^{-12}\ e^{-75./T}$	c
HO_2 + HO_2 $\longrightarrow$ H_2O_2 + ...	$\begin{cases} K_7 = 2.3\ 10^{-13}\ e^{600./T} + 1.7\ 10^{-33}\ [M]\ e^{1000./T} \\ \text{corrected for the effect of water vapour} \end{cases}$	c
H_2O_2 + OH $\longrightarrow$ HO_2 + H_2O	$K_8 = 2.9\ 10^{-12}\ e^{-160./T}$	c
H_2O_2 + hν $\longrightarrow$ 2 OH	Prescribed from IMAGES	
Aqueous-Phase Chemistry		
S(IV) + H_2O_2 $\longrightarrow$ sulfate	$K_{11}^{aq} = 7.5\ 10^{7}\ e^{-4430(1/T-1/298.)}\ [H^+]_{aq}/(1+13[H^+]_{aq})$	d
S(IV) + O_3 $\longrightarrow$ sulfate	$\begin{cases} K_{21}^{aq} = 2.4\ 10^{4} \\ K_{22}^{aq} = 3.7\ 10^{5}\ e^{-5530(1/T-1/298.)} \\ K_{23}^{aq} = 1.5\ 10^{9}\ e^{-5280(1/T-1/298.)} \end{cases}$	d
Solubility Constants		
DMSO	$5.\ 10^{4}$	e
SO_2	$1.4\ e^{2900(1/T-1/298.)}$	f
H_2O_2	$8.3\ 10^{4}\ e^{7400(1/T-1/298.)}$	g
O_3	$1.15\ 10^{-2}\ e^{2560(1/T-1/298.)}$	h
Dissociation Constants		
SO_2 /SO_3^-	$1.3\ 10^{-2}\ e^{1960(1/T-1/298.)}$	d
SO_3^- /SO_3^{2-}	$6.6\ 10^{-8}\ e^{1500(1/T-1/298.)}$	d

Units are cm^3 $molec^{-1}$ s^{-1} for the gas-phase reaction rates (K_i), l mol^{-1} s^{-1} for aqueous-phase reaction rates (K_{ij}^{aq}), mol l atm^{-1} for solubility constants, and mol l^{-1} for dissociation constants.
a Atkinson et al. (1989), b Chatfield and Crutzen (1990), c DeMore et al. (1997), d Seinfeld and Pandis (1998)
e Sander (1999), f Lide and Frederikse (1995), g O'Sullivan et al. (1996), h National Bureau of Standards (1965).

$$\frac{\partial[S_{iv}]_{aq}}{\partial t} = -K_{11}^{aq}\ [H_2O_2]_{aq}\ [HSO_3^-]_{aq} \qquad \frac{\partial[S_{iv}]_{aq}}{\partial t} = -(K_{21}^{aq}\ [SO_2 \cdot H_2O]_{aq} + K_{22}^{aq}\ [HSO_3^-]_{aq} + K_{23}^{aq}\ [SO_3^{2-}]_{aq})\ [O_3]_{aq}$$

Because the reaction rate of aqueous O_3 with SO_2 is pH-dependent (see Table 2), the 30 min time step is split into 15 time steps of 2 min each, for which the oxidation reaction rates and the cloud pH are computed. Aqueous-phase SO_2 oxidation only occurs in the cloudy part of the grid-box; we do not allow mixing of air between clear and cloudy sky during the 30 min time step (i.e., if SO_2 or H_2O_2 are completely consumed in the cloud part of the grid-box, we do not allow SO_2 or H_2O_2 from the clear part to be also consumed). We assume a linear transition between ice and liquid clouds in the temperature range of $-20°$ to $-10°$C. The fraction of condensate that is liquid in the cloud varies from 1 at $-10°$C to 0 at $-20°$. No "aqueous-phase" chemistry takes place in ice clouds. Therefore aqueous-phase chemistry is completely shut off below $-20°$C. No aqueous-phase chemistry is considered in rain or snow.

2.5 Dry and Wet Deposition

Dry deposition is parameterized through deposition velocities, which are prescribed for each chemical species and surface type (Table 3). A more appropriate formulation which depends on vegetation type and atmospheric stability is under development.

Wet deposition (or scavenging) is treated separately for stratiform and convective rain. For in-cloud scavenging, we apply a parameterization similar to that of Giorgi and Chameides (1986). The scavenging rate (s^{-1}) is gi-

ven by

$$W = \beta \; f \; r \tag{2}$$

where f is the cloud volume fraction, r the fraction of the chemical species that is in the aqueous phase, and β is the rate of conversion of cloudwater to rainwater (in unit of kg kg^{-1} s^{-1}). The parameter r is obtained assuming Henry's law equilibrium for gases and is set to 0.7 for sulfate and MSA aerosols. This reflects the fact that a fraction of sulfate aerosols can be interstitial in clouds as shown by a number of measurements (Boucher and Lohmann, 1995). The parameter β at model level k is computed from the three-dimensional precipitation flux (P_r, stratiform or convective, in kg m^{-2} s^{-1}) and a prescribed liquid water content (q_l=0.5 and 1.0 g kg^{-1} for stratiform and convective clouds, respectively):

$$\beta_k = \frac{P_{r,k} - P_{r,k+1}}{\rho_{\mathrm{air},k} \; \Delta z_k \; f_k \; q_l} \tag{3}$$

where ρ_{air} is the air density (kg m^{-3}) and Δz_k is the thickness of layer k. We do not distinguish between liquid and ice precipitation as far as in-cloud scavenging is concerned.

Below-cloud scavenging is considered for aerosols only. By integrating over the population of raindrops the volume of space that is swept by a raindrop during its fallout, the expression for the scavenging rate (s^{-1}) is:

$$K = \frac{3 \; P_r \; \alpha}{4 \; R_r \; \rho_{\mathrm{water}}} \tag{4}$$

where R_r is an average raindrop radius (set to 1 mm here), ρ_{water} the water density (kg m^{-3}), and α is the efficiency with which aerosols are collected by raindrops. For the parameter α, we selected a value of 0.001 and 0.01 for raindrops and snowflakes, respectively, based on measurements compiled by Pruppacher and Klett (1997).

Because the three-dimensional precipitation fluxes are available in the GCM, we do not have to assume an ad-hoc vertical profile of precipitation. and EMEFS, respectively. Model results are also compared to surface of raindrops. The release at a level k is equal to the amount of the given species which was scavenged at higher levels multiplied by the fraction of precipitation which is evaporated. For aerosols, a multiplicative factor of 0.5 is applied to account for the fact that raindrops can shrink without evaporating totally. In the event of a total evaporation of the precipitation flux, the aerosols are released totally as well.

Table 3: Dry deposition velocities (cm s^{-1}).

	DMS	SO_2	H_2S	DMSO[c]
Ocean	0.0	0.7[a]	0.0	1.0
Land	0.0	0.2[b]	0.0	0.0
Ice	0.0	0.2	0.0	0.0
	MSA[d]	Sulfate[d]	H_2O_2	
Ocean	0.05	0.05	1.0	
Land	0.25	0.25	1.5	
Ice	0.25	0.25	0.04	

a Garland (1977)
b Clarke et al. (1997)
c Chatfield and Crutzen (1990)
d Wesely et al. (1985)

2.6 Convective Transport

We use the mass fluxes simulated by the Tiedtke (1989) scheme to parameterize convective transport of gases and aerosols. We account for the vertical transport of trace species in updrafts, downdrafts, and in the environment, and for entrainment and detrainment from and to the environment. The convective transport is performed after the wet scavenging calculation in order to avoid upwards transport of material which is necessarily scavenged by precipitation. In addition, we scavenge a fraction of the soluble tracers released to the environment (Balkanski et al., 1993; Mari et al., 2000; Crutzen and Lawrence, 2000). This fraction is set to 20% and 50% for gases (except DMS) and aerosols, respectively. Note that we apply convective transport in a bulk manner without distinguishing between the interstitial and the dissolved fractions of trace gases and aerosols. This is in contrast with Barth et al. (2000) who treat separately interstitial and dissolved material.

3 Results

Our model is run for 18 months. In the following sections, surface and zonal distributions as well as comparisons with observations are presented for the results of the last 12 months.

There are numerous measurements of DMS, SO_2, sulfates, and MSA from campaigns or continuously monitoring sites. The present version of LMD-ZT represents typical conditions as opposed to specific meteorological situations. In order to assess the performance of this climatologically-driven model, we use data obtained at surface sites for a period of at least one year. These data

Fig. 2: Distribution of DMS mixing ratio (pptv) at the surface in a) January and b) July.

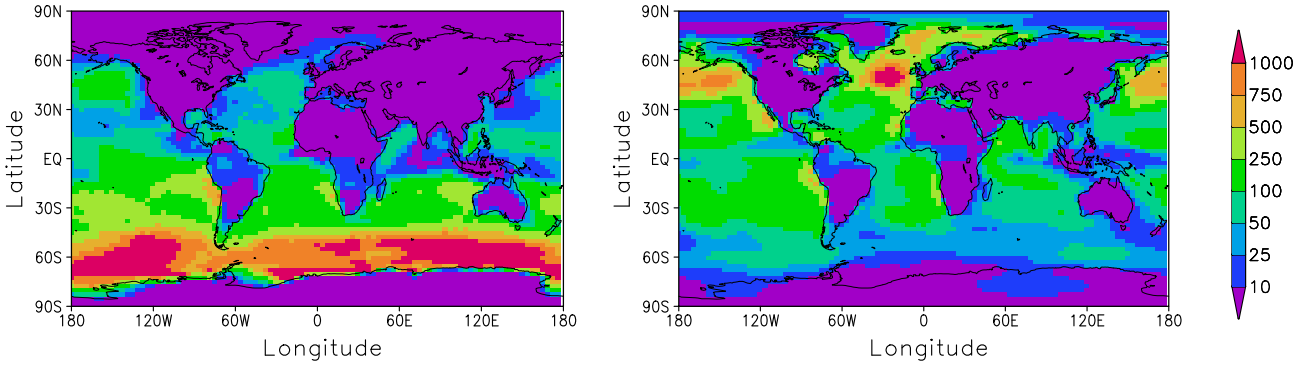

(a) **(b)**

Fig. 3: Distribution of SO_2 mixing ratio (pptv) at the surface in a) January and b) July.

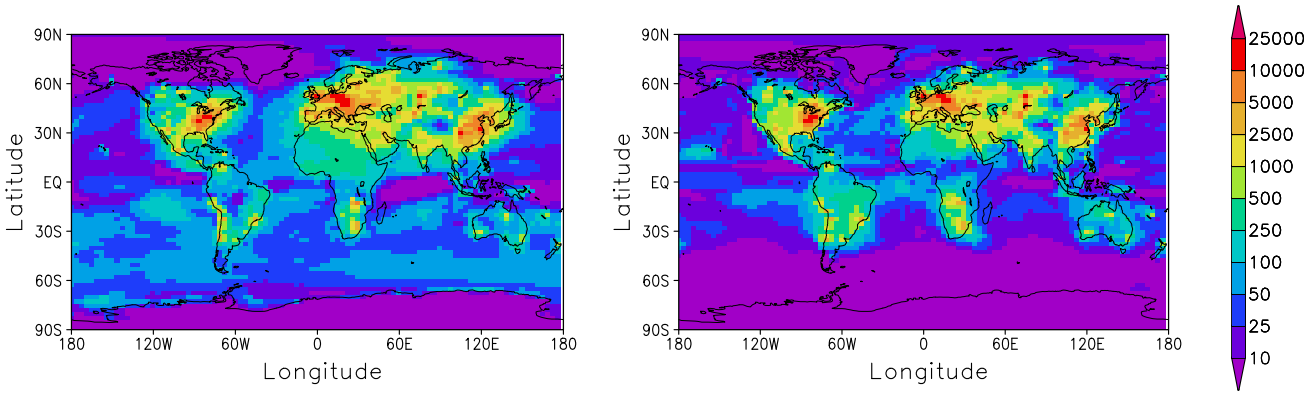

(a) **(b)**

Fig. 4: Distribution of sulfate mixing ratio (pptv) at the surface in a) January and b) July.

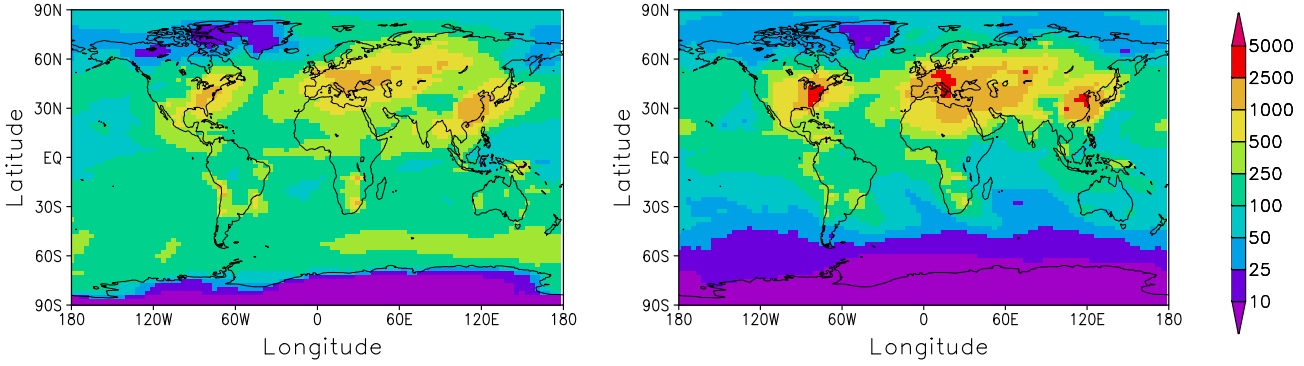

(a) **(b)**

Fig. 5: Zonally-averaged mixing ratio of sulfate (pptv) in a) January and b) July.

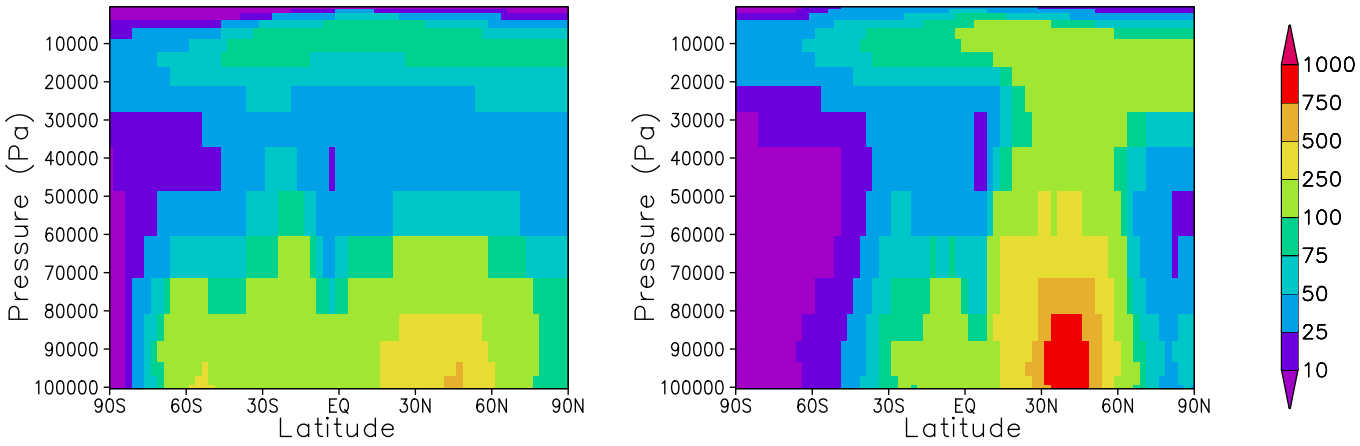

(a) **(b)**

include SO_2 and sulfate measurements from the European Monitoring and Evaluation Programme (EMEP) for Western Europe (see Aas et al., 1999) and the Eulerian Model Evaluation Field Study (EMEFS) for North America (see McNaughton and Vet, 1996). We use data from years 1980–1990 and 1988–1990 for EMEP and EMEFS, respectively. Model results are also compared to surface data from some remote oceanic sites (mostly those of the Sea-Air Exchange program (SEAREX)).

We also compare the model results with data obtained during three aircraft field campaigns which took place in the Pacific Ocean: Pacific Exploratory Mission (PEM)-West A (September–October 1991), PEM-West B (February–March 1994), and PEM-TROPICS-A (August–October 1996). Although these measurements are only representative of a region during the time period of the flights, they enable us to examine the vertical and horizontal distributions of the modelled sulfur species and identify any potential systematic biases.

4 Surface Concentrations of Sulfur Species

The surface distributions of the mixing ratios of DMS, SO_2, and sulfate are presented in Figs. 2–4, respectively. The mixing ratio of DMS at the surface exhibits the same seasonal variation as the emission strength. It is maximum at 50–70°S in January and over the North Pacific and the North Atlantic Oceans in July (Fig. 2). The mixing ratio of SO_2 is largest over the continents and close to the regions of emission (Fig. 3). It shows few differences between January and July, except over the mid-latitudes of the Southern Hemisphere where oxida-

Table 4: Comparison of modelled versus observed annually-averaged concentrations at the surface

Location	Observed[a]	Modelled[a]
DMS		
Cape Grim	65	50
Amsterdam Island	181	118
SO_2		
EMEP sites (<50°N)	3945	4306
EMEP sites (>50°N)	3037	3528
EMEFS sites	3038	5460
Amsterdam Island	18	20
Sulfates		
EMEP sites (<50°N)	1588	1284
EMEP sites (>50°N)	1166	895
EMEFS sites	1252	1449
Oceans (NH)[b]	225	177
Oceans (SH)[c]	80	101
Antarctic[d]	25	33
MSA		
Arctic[e]	6	1
Oceans (NH)[f]	8	5
Oceans (SH)[c]	5	7
Antarctic[g]	9	4

[a] Values are in pptv.
[b] Barbados, Belau, Bermuda, Fanning, Guam, Mace Head, Midway, and Oahu.
[c] American Samoa, Cape Grim, New Caledonia, and Norfolk.
[d] Mawson, Palmer, and the South Pole.
[e] Alert and Heimaey.
[f] Barbados, Bermuda, Fanning, Mace Head, Midway, and Oahu.
[g] Mawson and Palmer.

Fig. 6: Seasonal variations in surface DMS (pptv) at Amsterdam Island and Cape Grim. The open circles and the solid line indicate the monthly-mean observed and modelled mixing ratios, respectively.

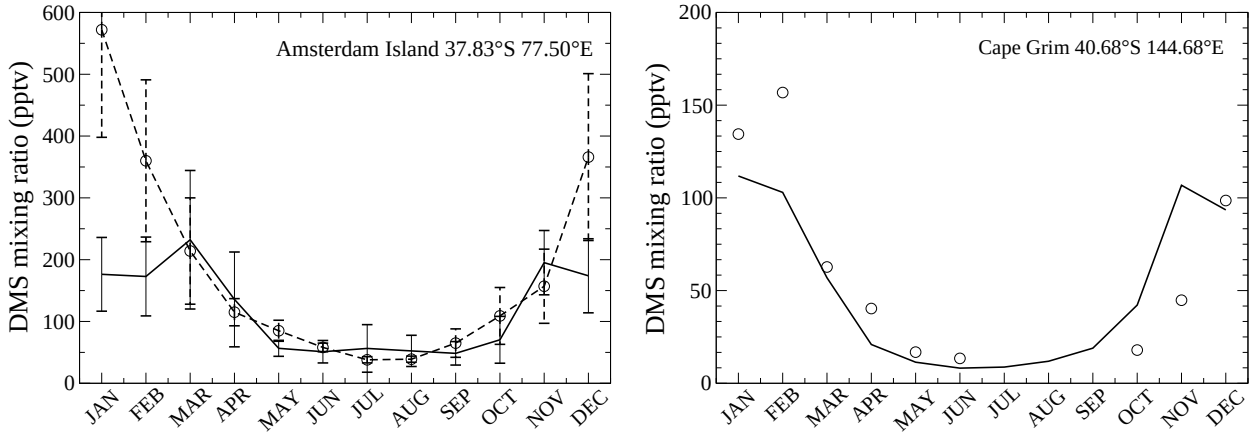

Fig. 7: Seasonal variations in surface SO_2 (pptv) at Amsterdam Island.

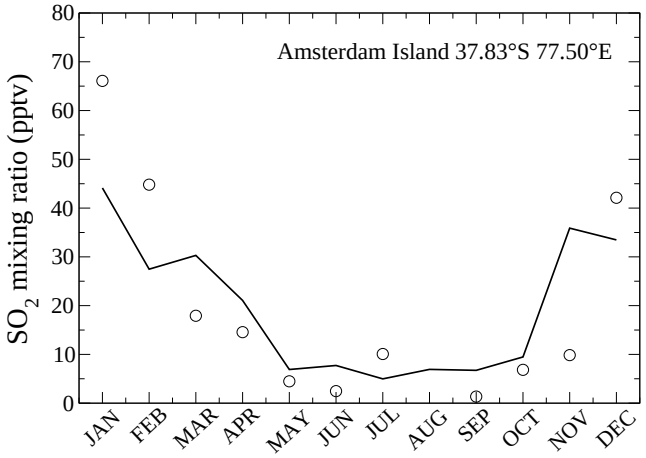

Fig. 8: Seasonal variations in surface sulfate (pptv) at Mawson, Midway, Fanning Island, and Cape Grim.

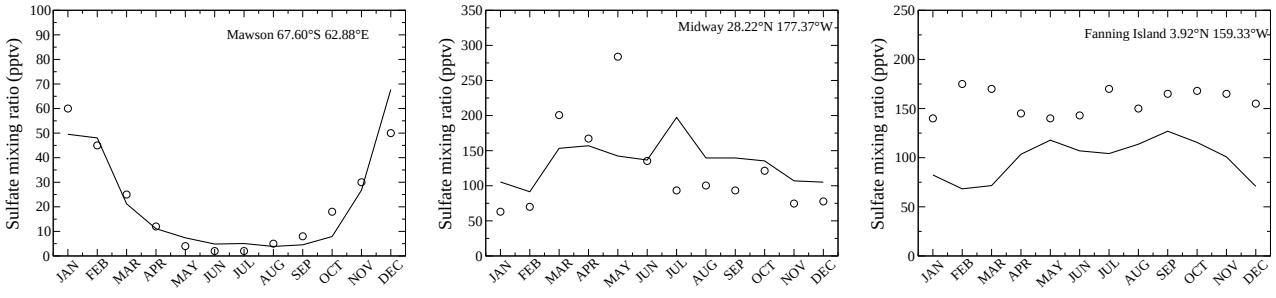

Fig. 9: Seasonal variations in surface MSA (pptv) at Midway, Samoa, and Cape Grim.

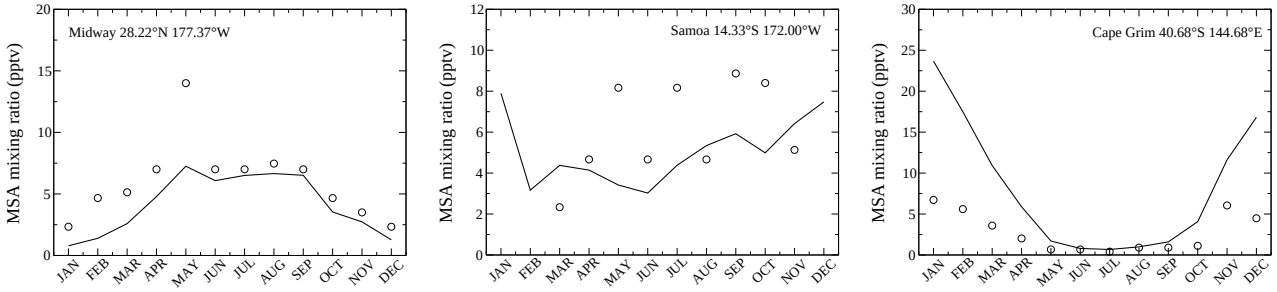

tion of DMS is the main source for SO_2. The spatial distributions of SO_2 and sulfate mixing ratios show some similarities but differ in that sulfate aerosols spread further away from the regions of emissions of industrial SO_2 (Fig. 4), as expected from the longer lifetime of sulfate aerosols compared to SO_2 (see section 7). We could also note from Fig. 5 that sulfate aerosols spread vertically into the free troposphere during summertime.

Table 4 presents a comparison of modelled and observed mixing ratios of DMS, MSA, SO_2, and sulfate; the data are annual-mean mixing ratios averaged over the remote and polluted monitoring stations given in the table caption. Model results are within a factor of 2 of measurements, except for MSA which is underestimated by as much as a factor of 6 in the Arctic and Antarctic sites. This matter should be investigated in the future, by considering direct MSA production from DMS and not from DMSO. In the following subsections, we show the modelled versus observed mixing ratios at some representative sites in order to illustrate and discuss the performance of the model in terms of seasonality.

4.1 Remote oceanic sites

Fig. 6 shows DMS mixing ratios at Amsterdam Island (Sciare et al., 2000) and Cape Grim. Observed mixing ratios at the two sites are characterized by a maximum in summer and a minimum in winter. This cycle is reproduced by the model for DMS, whose variation is intimately related to the variation of DMS emission flux at the two sites. For this compound, the agreement with the observations is good from March to November at Amsterdam Island and March to October at Cape Grim. The model underestimates the summer (January-February) peak in concentration at both sites. A more complete investigation of DMS emission flux and concentration in the southern hemisphere using this model is provided in Cosme et al. (2002). The calculated mixing ratios exhibit a peak which is not observed in the measurements at the two sites. This peak reproduces a similar peak in the DMS emission flux, which may be an artifact due to the very low density of data in the Southern Indian Ocean used in the emission mapping procedure of Kettle et al. (1999).

As showed in Fig. 7, the seasonal cycle of SO_2 at Amsterdam Island is well reproduced if we compare the model results to the data of Putaud et al. (1992). At this site, SO_2 is mainly produced by DMS oxidation. The modelled SO_2 mixing ratio, similarly to DMS, is also overestimated in November but underestimated in January.

Fig. 8 presents comparisons for sulfates at some remote oceanic sites. Two of them (Mawson and Midway) are characterized by large seasonal variations, while Fanning Island does not show any remarkable seasonality. At Cape Grim (not shown), nss-sulfates are overestimated by a factor of more than 5 when compared to measurements by Ayers et al. (1991), while DMS mixing ratios compare well with the observations. Since observations correspond to 'baseline' or clean conditions only, while our results also include anthropogenic sulfates coming from the continent, the discrepancy between model and observation is therefore not meaningful. Note, however, that measurements reported by Andreae et al. (1999), also for baseline conditions, are significantly higher than those of Ayers et al. (1991), reducing the discrepancy. The absence of seasonal variation at Fanning Island is reproduced by the model, though the modelled values are underestimated by a factor of 2, as well as the seasonality of the observed mixing ratios at Mawson. The modelled ratio of the summertime to wintertime values is 12 at Mawson, versus 17 for the observations. The agreement is poorer for the Midway station, where the model does not seem to simulate adequately the transport of Asian pollutants during spring.

As shown on Fig. 9, the model captures well the MSA concentrations at Samoa and Midway, within a factor of 2. At Cape Grim, MSA mixing ratios are largely overestimated in summer, while modelled DMS mixing ratios

Fig. 10: Geographic distribution of the EMEP and EMEFS sites used in this study.

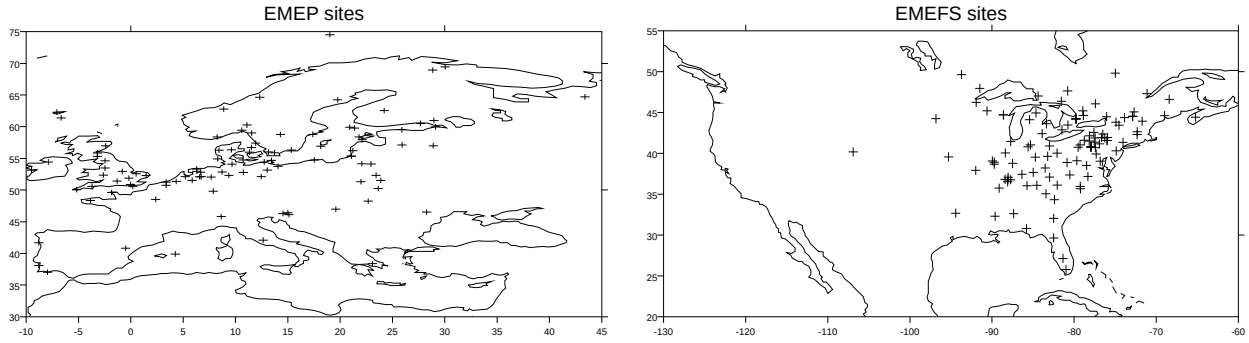

Fig. 11: Scatter plot of measured vs modelled SO_2 mixing ratios (pptv) at EMEP surface sites in January, April, July, and October. The 1:1 line (solid), the 1:2 and 2:1 lines (dashed), and the 1:10 and 10:1 lines (dotted) are shown for reference.

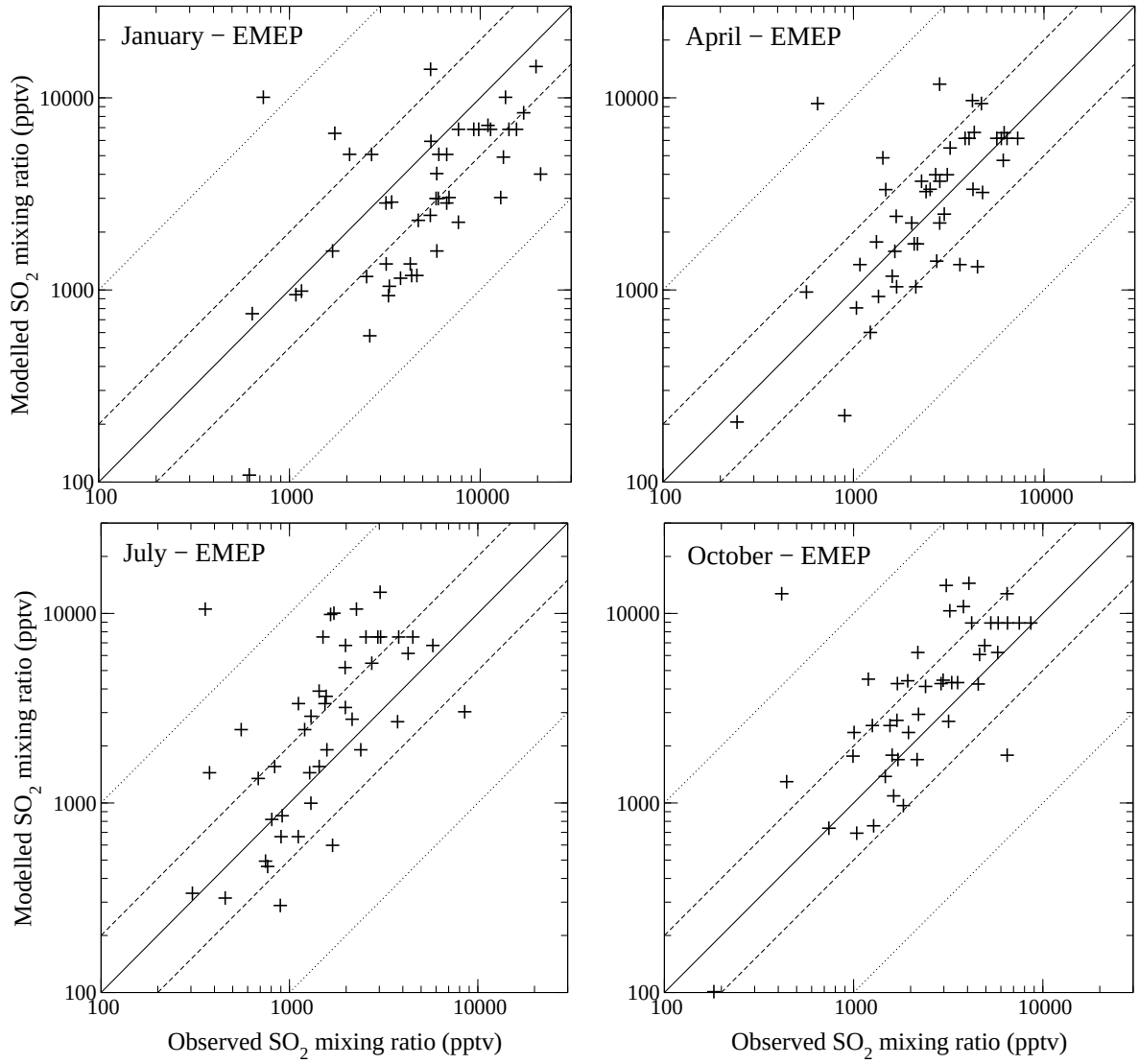

Fig. 12: Same as Fig. 11 but for sulfate.

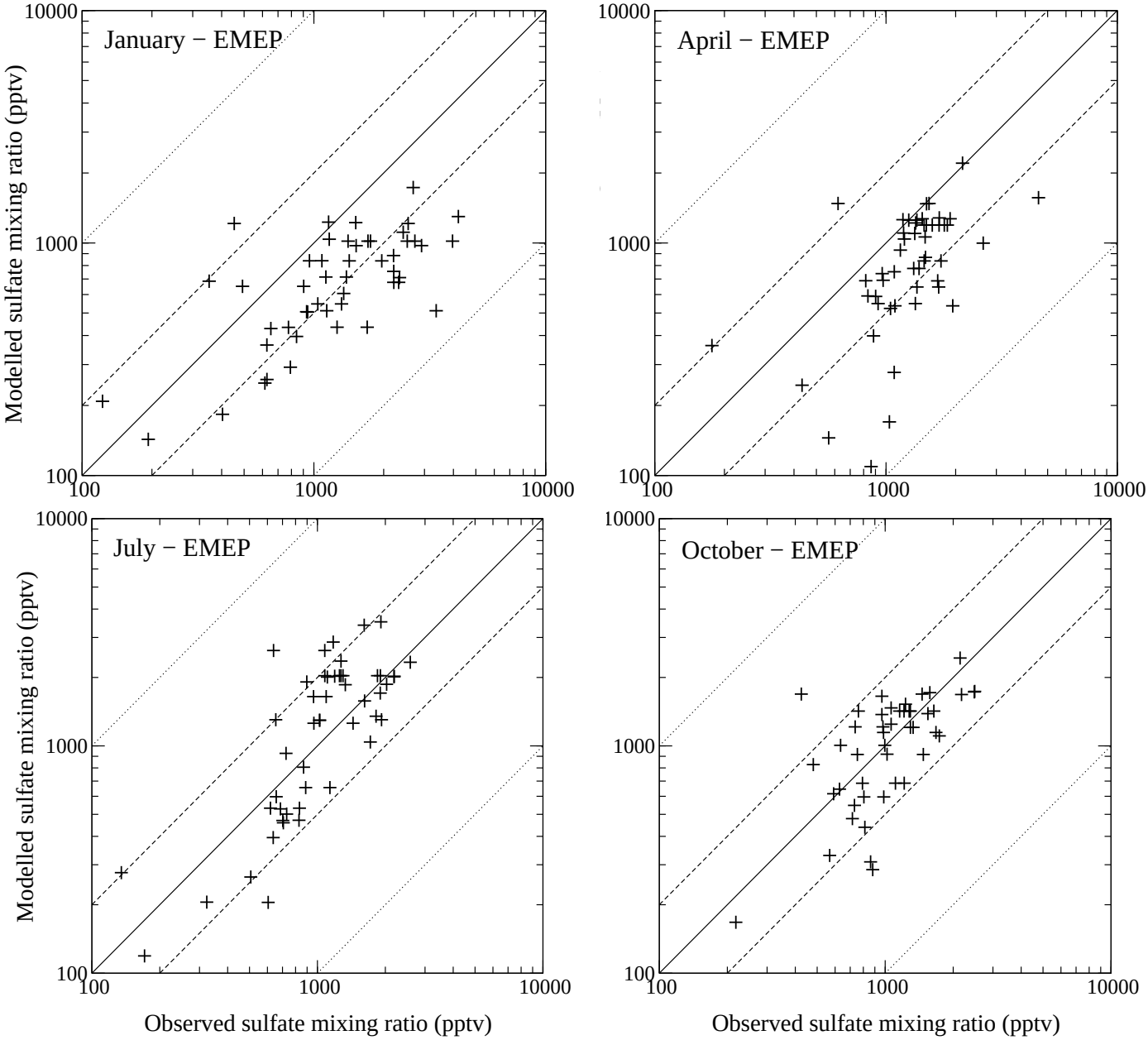

agree rather well with the observations. The agreement is better if we use the data of Andreae et al. (1999), with observed MSA mixing ratios peaking at about 14 pptv in February.

4.2 Continental/Polluted areas

Most of the monitoring stations are located in Europe (EMEP network) and Northern America (EMEFS network) and they report measurements of SO_2 and sulfate concentrations in air, sulfate concentration in rainwater, and precipitation (see Fig. 10). The results for the EMEP and EMEFS stations are summarized as scatter plots in Figs. 11 to 14. For each plot, each point represents the modelled and observed monthly-mean values at one site in January, April, July, and October (a model grid-box can occasionally be compared to several sites if their geographical distance is less than the horizontal resolution of the model).

Modelled and observed SO_2 mixing ratios are evenly dis-

Fig. 13: Same as Fig. 11 but for EMEFS surface sites.

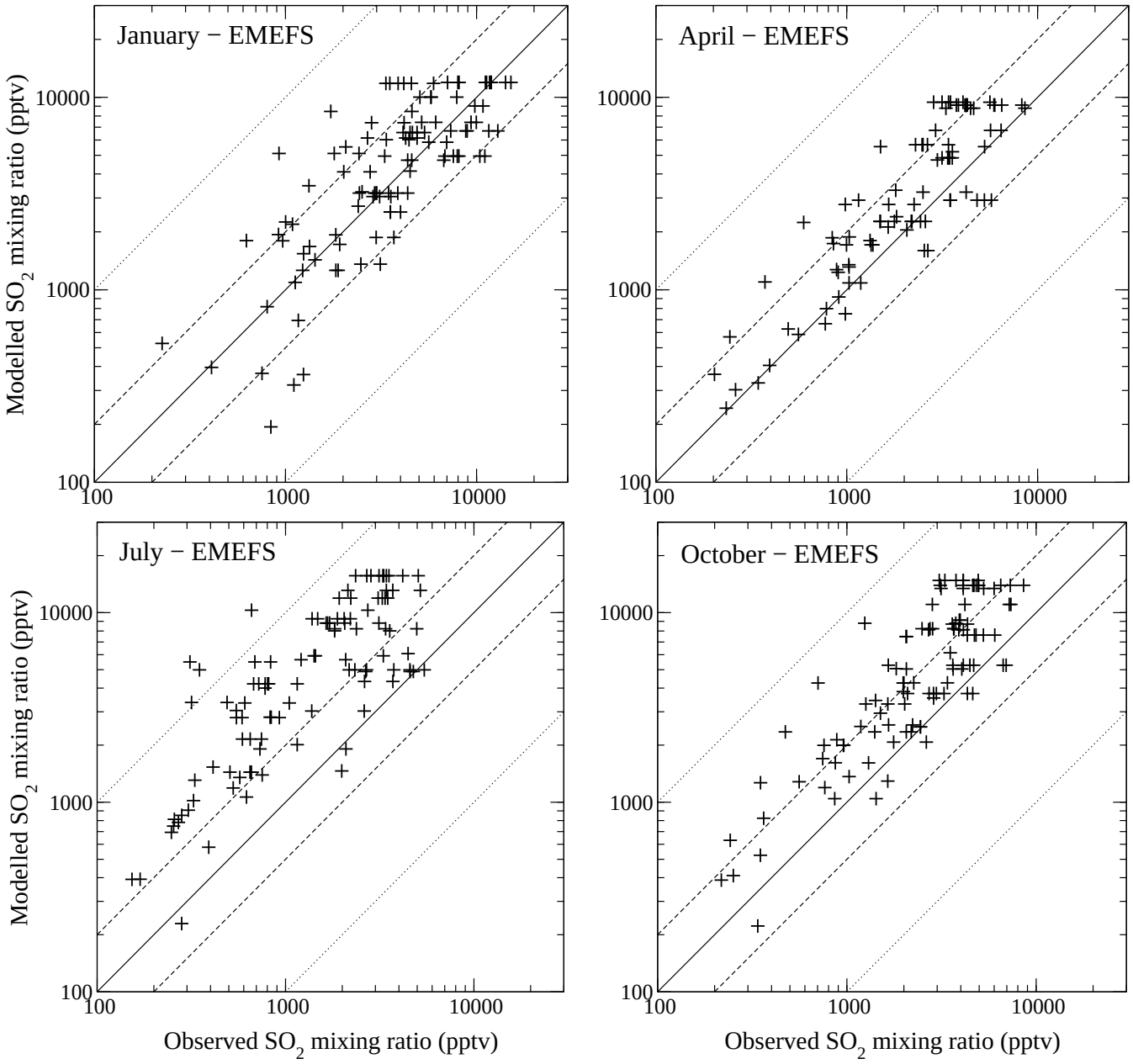

tributed around the 1:1 line in April over Europe and in January over Eastern North America. In both regions SO_2 mixing ratios are overestimated in July and October. They are also underestimated in January over Europe, which is opposite to the recent model results of Koch et al. (1999) and Barth et al. (2000). The overestimates in July and October are probably due to a too weak SO_2 conversion into sulfates since precipitation and cloud cover are underestimated in the model at these periods of the year.

In order to discuss the behavior of the model at different latitude and longitude bands, we also display on Fig. 15 the observed and modelled seasonal cycles at some representative sites in Europe and North America. The underestimate of SO_2 in winter is illustrated on the first row of Fig. 15 with the sites of Cree Lake, Aspvreten, and Krvatn, which are all north to 50°N. At these high latitudes areas, the winter discrepancy might be related to either an insufficient transport of sulfur to the high latitudes, either a too high deposition rate for SO_2, or

Fig. 14: Same as Fig. 12 but for EMEFS surface sites.

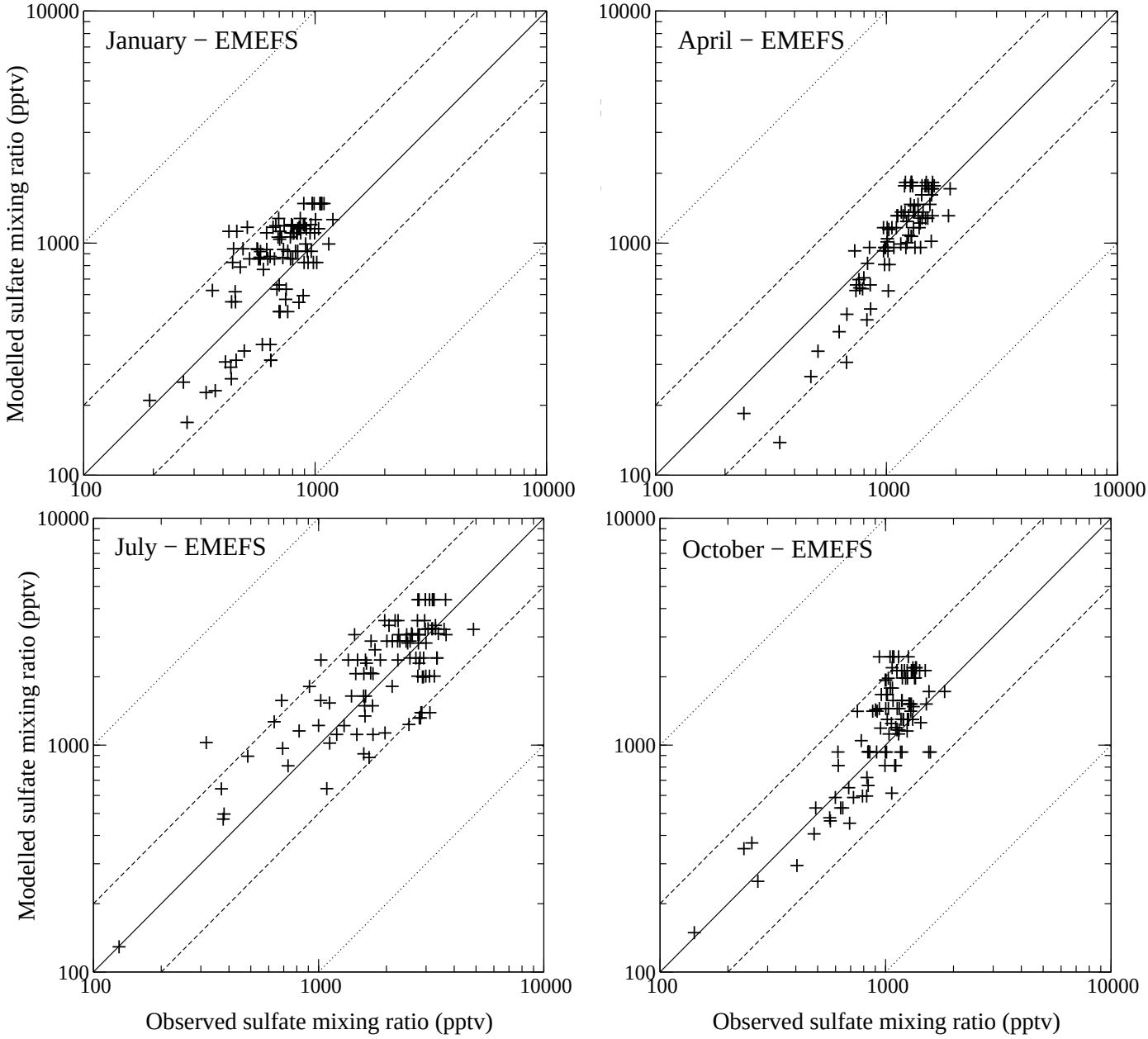

a too strong in-cloud oxidation of SO_2 by O_3. In summer modelled SO_2 mixing ratios compare rather well with observations (less than a factor 2). Going further south, modelled SO_2 is overpredicted from March to December over Europe and North America with slight peaks occurring in August, September, and November (middle row of Fig. 15). The agreement is satisfactory in the latitude band 25–35°N (last row of Fig. 15), where the seasonal variations are respected within a factor of 2 to 3.

The large degree of variability among observed values should be noted. Although distant of less than 2° in latitude and longitude, the observed January maxima at Whiteface and Warwick are less than 3000 pptv and more than 5500 pptv, respectively. Similarly a maximum of 5300 pptv has been observed at Bells (around 35°N, 89°W), while the maximum only reaches 1500 pptv at Caryville (around 30°N, 86°W). The model reproduces satisfactorily these gradients in concentrations.

Fig. 15: Seasonal variations in SO_2 mixing ratio (pptv) at selected sites of the EMEP and EMEFS networks. The open circles and the solid line indicate the monthly-mean observed and modelled mixing ratios, respectively. Note that different plots have different scales on the y-axis.

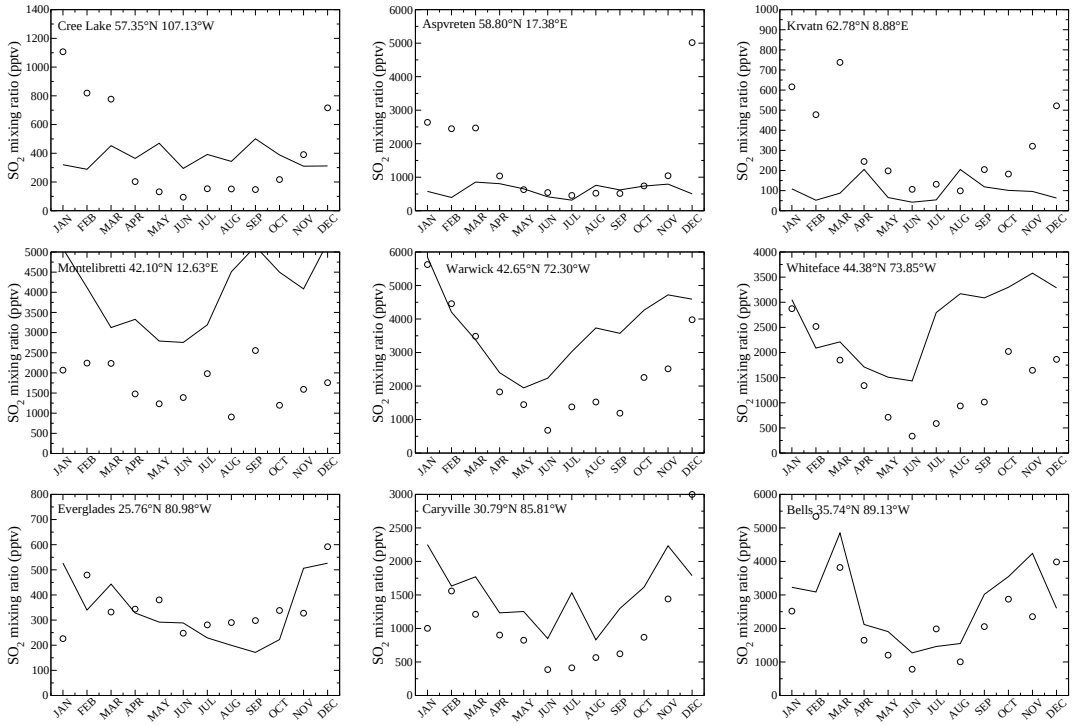

Fig. 16: Seasonal variations in sulfate mixing ratio (pptv) at selected sites of the EMEP and EMEFS networks. The open circles and the solid line indicate the monthly-mean observed and modelled mixing ratios, respectively.

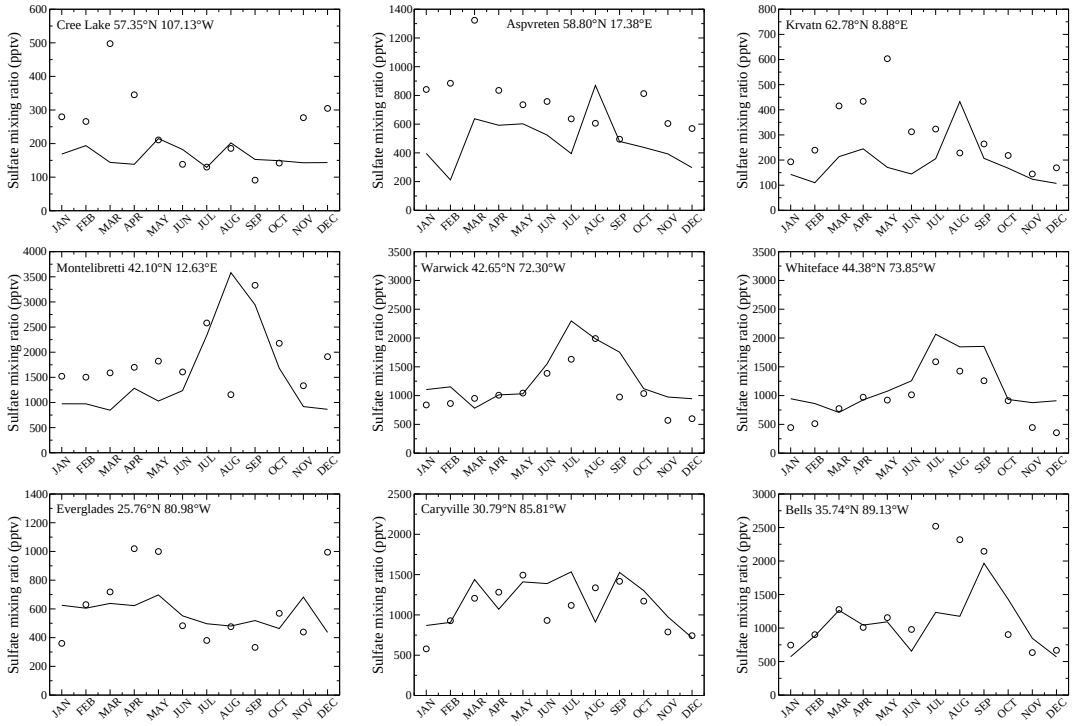

Fig. 17: DMS mixing ratios versus height during a) the PEM-West A, b) PEM-West B, and c) PEM-Tropics A field campaigns. Model results averaged over the region and period of the measurements are indicated by a solid line. The observed mixing ratios averaged in altitude bands of 1 km are also shown with a dashed line.

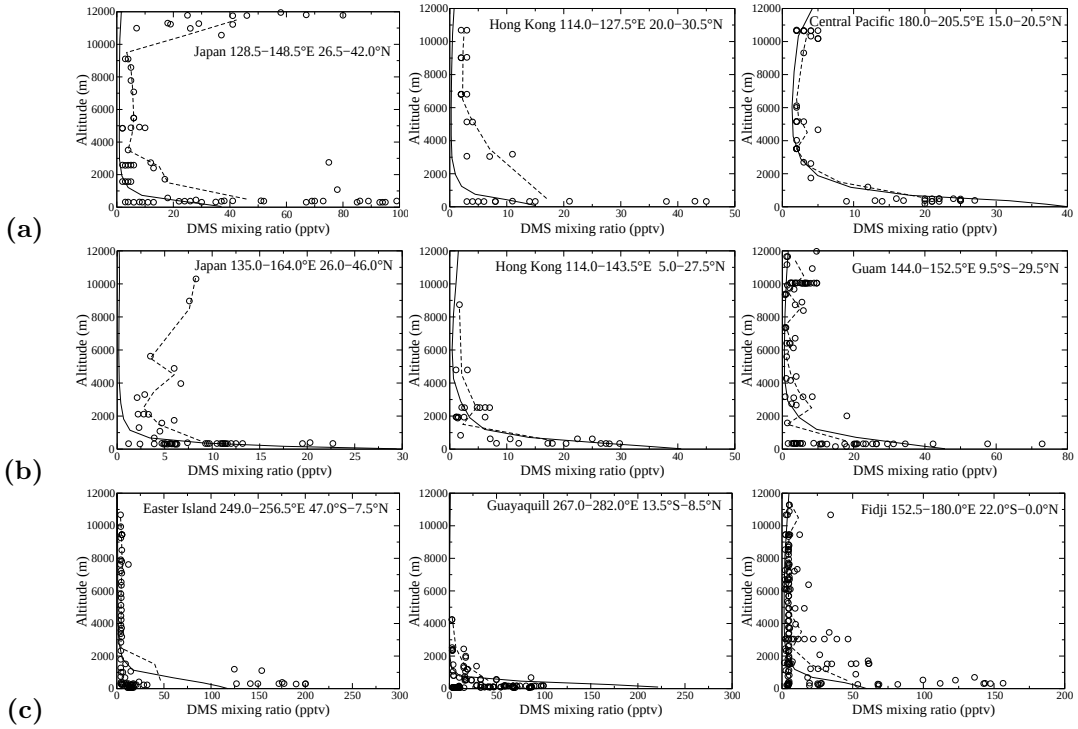

Fig. 18: Same as Fig. 17 but for SO_2.

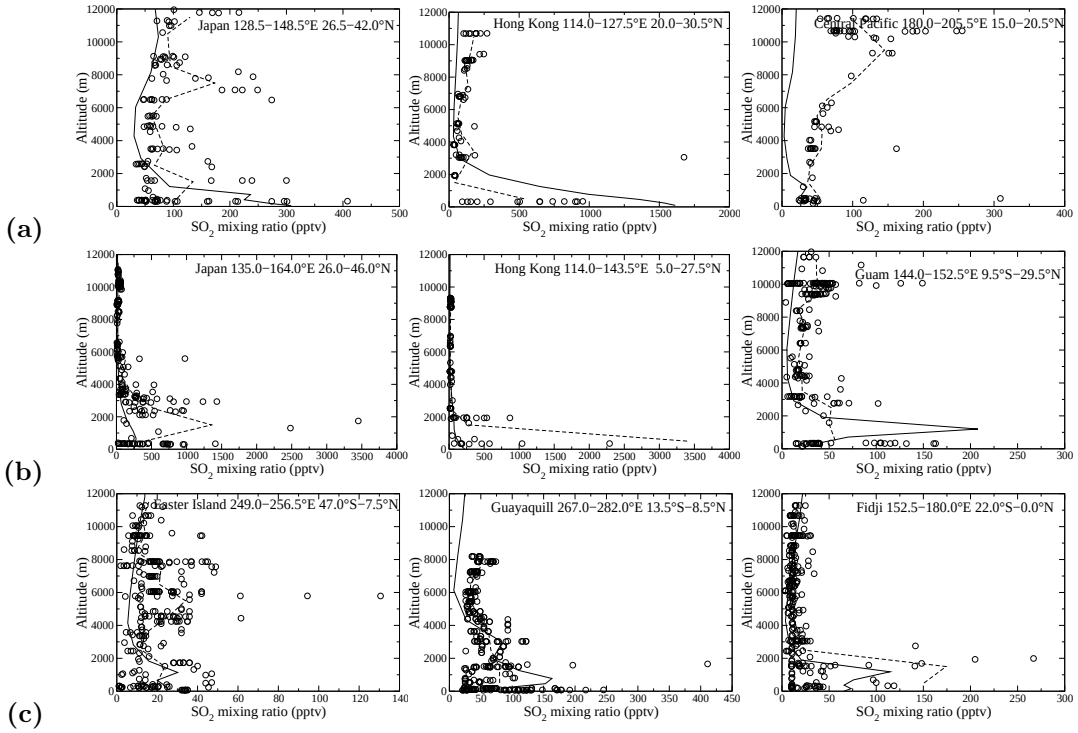

For the continental EMEP and EMEFS stations, most modelled and observed sulfate mixing ratios agree within a factor of 2, except for January and April in Europe (Fig. 12 and Fig. 14). There is a tendency to underestimate the concentrations over Europe in January and April and a slight tendency to overestimate concentrations over America in January and October. As far as EMEFS October data are concerned, this does not necessarily contradict the explanation given above that SO_2 to sulfate conversion rates are too slow. Both SO_2 and sulfate can be overestimated because a too low cloud cover and precipitation rate would result at the same time in too slow a conversion rate of SO_2 and too low a wet scavenging of sulfate. One striking feature of the figures is the large underestimate of sulfates in January and to a lesser extent in April over Europe. This discrepancy is probably due to a too large precipitation rate over Europe in winter maybe associated with a too large transport outside of the boundary layer. It is unlikely to be solely due to an insufficient conversion rate of SO_2 into sulfates, as SO_2 is underestimated in January.

Fig. 16 presents the seasonal behavior of sulfate at the same sites as SO_2. In mid-latitudes over the United States, the sulfate is observed to be highest in July-August. The model tends to give the same behaviour. At Montelibretti, wintertime sulfate mixing ratios are underestimated, due to an insufficient wintertime SO_2 oxidation and/or an excessive sink. North to 50°N, the agreement is within a factor of 2 to 3 although the high mixing ratios of sulfate at springtime are not reproduced by the model at neither three locations.

5 Vertical Profiles of Sulfur Species

This section assesses the model performance in the middle and high troposphere. The data used for the comparison between modelled and observed values have been collected during the PEM campaigns and have been grouped into regions using the same classification as Barth et al. (2000). The data from the different flights have been merged and averaged over nine given regions at each model vertical layer. The model results have been averaged over the selected regions and over the measurement period: February-March for the PEM-West B intensive campaign, September-October for the PEM-West A and PEM-Tropics-A campaigns. Note that the PEM-Tropics-A took place further east in the Pacific Ocean. It should also be noted that the model results represent a climatological situation which does not necessarily correspond to the local meteorological conditions and does not reproduce the variability in the mixing ratios as observed during the time periods of the PEM campaigns.

5.1 DMS

Observed DMS mixing ratios (Fig. 17) vary from around 20–40 pptv at the surface and decrease rapidly with altitude in the PEM-West A and B campaigns. This is well reproduced by the model. Nevertheless, in some cases, modelled mixing ratios are too low in the upper troposphere, where DMS may be pumped up by convective activity with mixing ratios reaching more than 10 pptv (see the Japan area during autumn and early spring, and the Guam area). In the Eastern Pacific (PEM-Tropics A), DMS mixing ratios are higher than in West-A and B (more than 50 pptv at the surface) and decrease rapidly with altitude. The model is in fair agreement with these profiles, except for the surface, where modelled DMS concentrations are overestimated in two cases.

In the Eastern Pacific (PEM-Tropics A), DMS mixing ratios are higher than in West-A and B (more than 50 pptv at the surface) and decrease rapidly with altitude. The model is in fair agreement with these profiles, except for the surface, where modelled DMS concentrations are overestimated in two cases.

5.2 SO_2

SO_2 mixing ratios observed during PEM-West A increase, are constant, or decrease with altitude (Fig. 18). In Japan and Hong-Kong, the model is in good agrement with the observations, but in two cases it tends to overestimate the surface concentrations. Over Central Pacific on the other way, it is below the observed mixing ratios of 100–200 pptv in the high troposphere, which is probably due to long-range transport and convective activity, or return injection of volcanic SO_2 from the stratosphere (Thornton et al., 1996). Peaks of SO_2 are also observed in the boundary layer and free troposphere of the PEM-West B area. The model does not represent properly the transport of pollutants from Asia during spring 1994 at the surface, with too low modelled mixing ratios, except for the Guam area. In the Eastern Pacific (PEM-Tropics A), surface observed mixing ratios are lower than in the western regions, and the observed peaks of SO_2 in the boundary layer are reproduced by the model.

In summary, except for the Central Pacific area, the model reproduces the high mixing ratios in the middle and high troposphere. At the surface, the agrement is within a factor 3.

Fig. 19: Same as Fig. 17 but for sulfates.

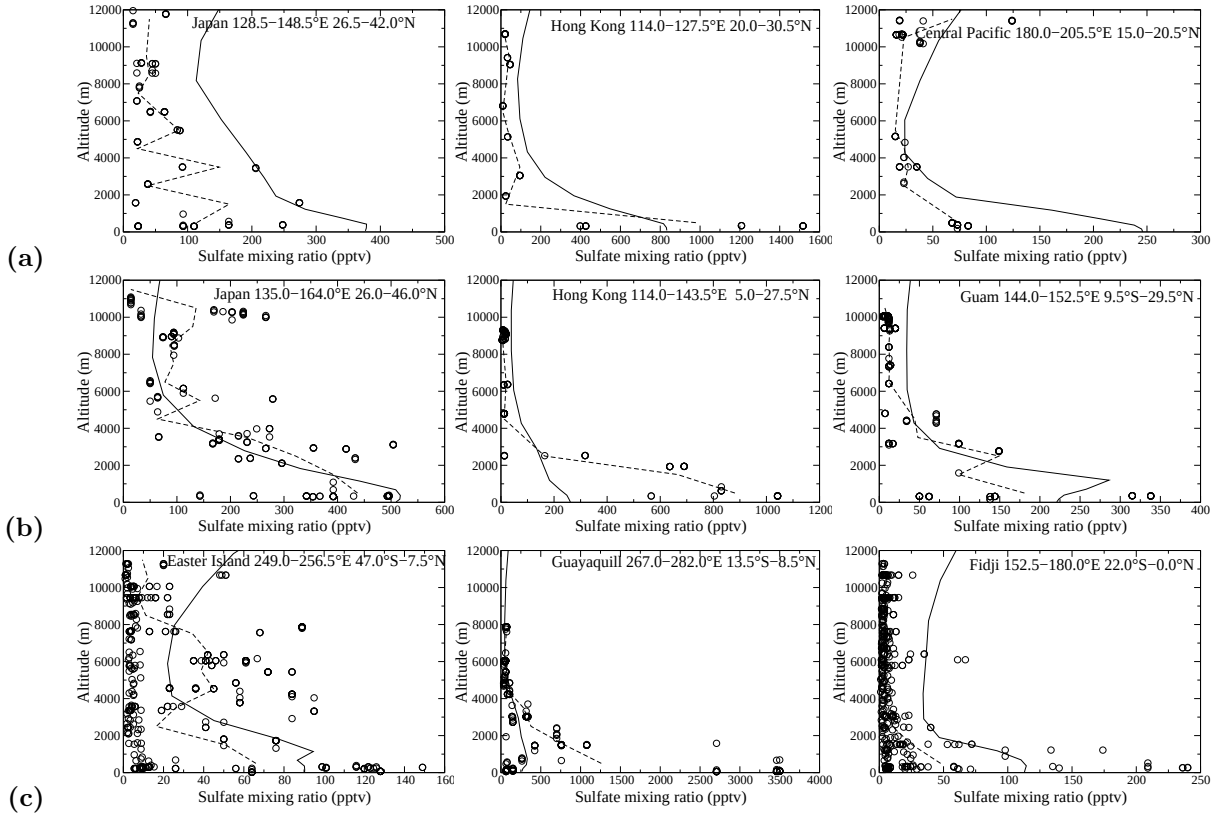

5.3 Sulfates

The agreement between observations and model results of sulfates is variable (Fig. 19). In the boundary layer, the model sometimes underestimates (Hong-Kong area in spring, Guayaquill area in autumn), and sometimes overestimates (Japan and Central Pacific in autumn, Guam in spring) the observed values. In the middle and high troposphere, modelled mixing ratios of sulfates are either too high (Japan in autumn or Fidji) or in agreement (Central Pacific, Japan and Hong-Kong in spring, Easter Island, or Guayaquill).

6 H_2O_2 distribution

The surface (Fig. 21) and zonal (Fig. 22) distribution of the H_2O_2 mixing ratio is in broad agreement with that simulated by other global models (e.g., Barth et al., 2000). There are nevertheless differences between the distribution of H_2O_2 simulated in IMAGES with a full chemical scheme (excluding, however, in-cloud oxidation of SO_2) and that simulated here with a simplified chemical scheme (but including in-cloud oxidation of SO_2). Surface H_2O_2 mixing ratios are larger in IMAGES than in LMD-ZT at high latitudes (north to 45°N and south to 50°S) during January, but are rather similar in July. Over the Northern midlatitudes, the simulated mixing ratios in LMD-ZT are much smaller in wintertime than in summertime, which explains the lower oxidation rate of SO_2 by H_2O_2 in winter. Note also that the largest mixing ratio of H_2O_2 are not found at the surface but at a higher altitude, as observed in field campaigns.

The concentration of H_2O_2 has been measured in several field campaigns (MLOPEX II, PEM, and TRACE) but is not monitored as that of sulfur species. Over continental regions of the Northern Hemisphere, the compilations of Lee et al. (2000) and Grossmann (1999) show that available measurements of H_2O_2 are scarce. In particular, there does not seem to be any measurements of H_2O_2 concentration over Europe in winter.

Table 5 shows a comparison between modelled and measured values of H_2O_2 at long-term (at least one year) monitoring sites as cited by Lee et al. (2000). Except for Cape Grim, where the observed amplitude of the seasonal cycle is more than twice the modelled one, the ratio winter/summer is well represented. The model underestimates the observed concentrations by Boatman

Fig. 20: Same as Fig. 17 but for H_2O_2.

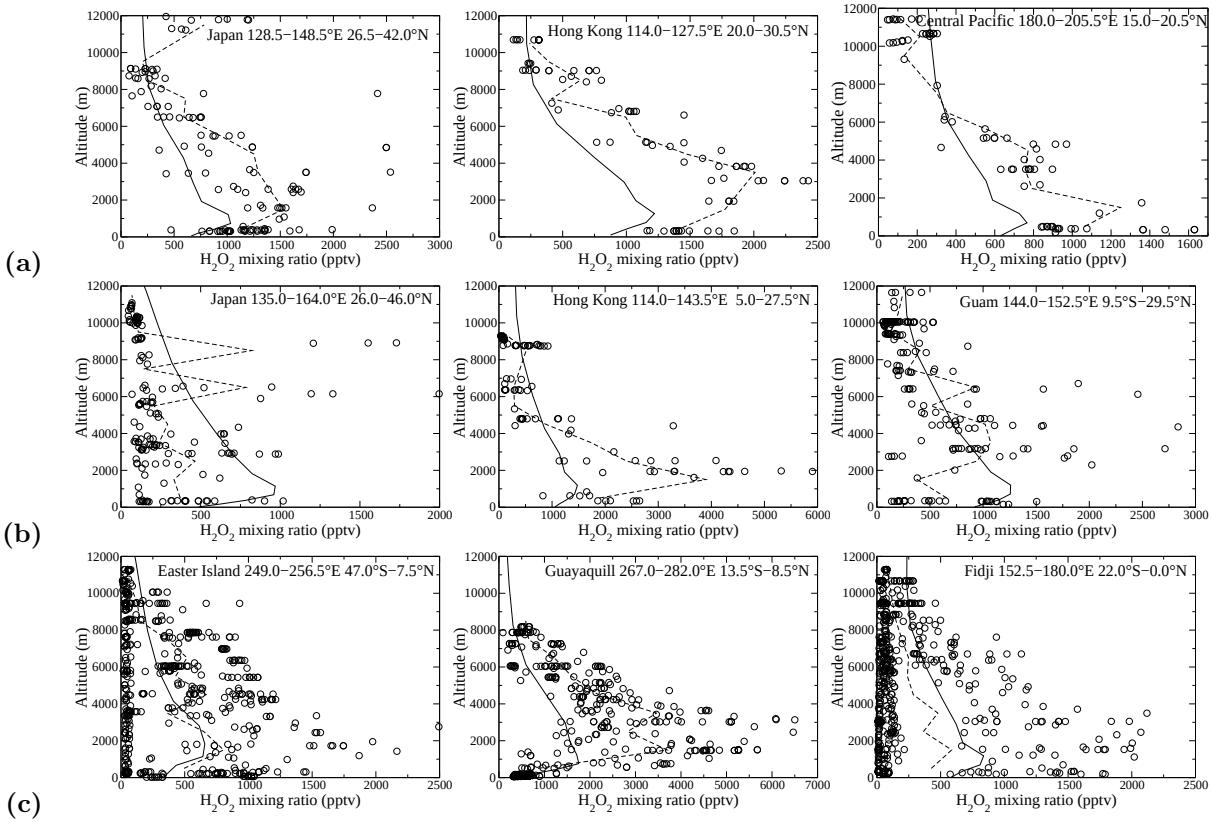

et al. (1989) over Central U.S. but is in the range of the measurements made by Van Valin et al. (1987) during the CURTAIN (Central U.S. RADM Test and Assessment INtensives) campaign which took place in the same area in February 1987. Typical modelled values range from 0.02 to 1.2 ppbv from north (40.5°N) to south (29°N) along the 91.5°W meridian and are within the range of measurements: < 0.01 to 1 ppbv with an increase of 0.04–0.05 ppbv per degree of latitude from North to South.

Over the United States in winter, comparison with measurements by Barth et al. (1989) shows a fair agreement below 3 km, but an overestimate by a factor of about 3 above 3 km. On the other hand, the modelled profile of H_2O_2 is underestimated by a factor of 2 to 4 in October-November over the eastern United States compared to the measurements given by Heikes et al. (1987).

The measured H_2O_2 mixing ratios during the PEM campaigns are in broad agreement with the simulated ones (see Fig. 20). The model reproduces the increase of mixing ratios in the boundary layer as observed during most of the campaigns.

Since H_2O_2 long-term measurements are scarce, it is difficult to draw any definite conclusion about the representation of H_2O_2 in our model. Measurements of H_2O_2 over Europe are also greatly needed to resolve the issue of wintertime underestimation of sulfate concentrations.

Table 5: Comparison of modelled versus observed H_2O_2 mixing ratios (ppbv) at long-term stations.

Location	Observed Winter/ Summer	Modelled Winter/ Summer
Cape Grim	1.4/0.16[a]	0.5/0.13
Los Angeles	0.2/1.0[b]	0.2/0.7
Central U.S. (1.4–1.7 km)	0.3/4.1[c]	0.14/1.6

[a]Ayers et al. (1996)
[b]Sakugawa and Kaplan (1989)
[c]Boatman et al. (1989)

Fig. 21: Distribution of predicted H_2O_2 mixing ratio (pptv) at the surface in a) January and b) July.

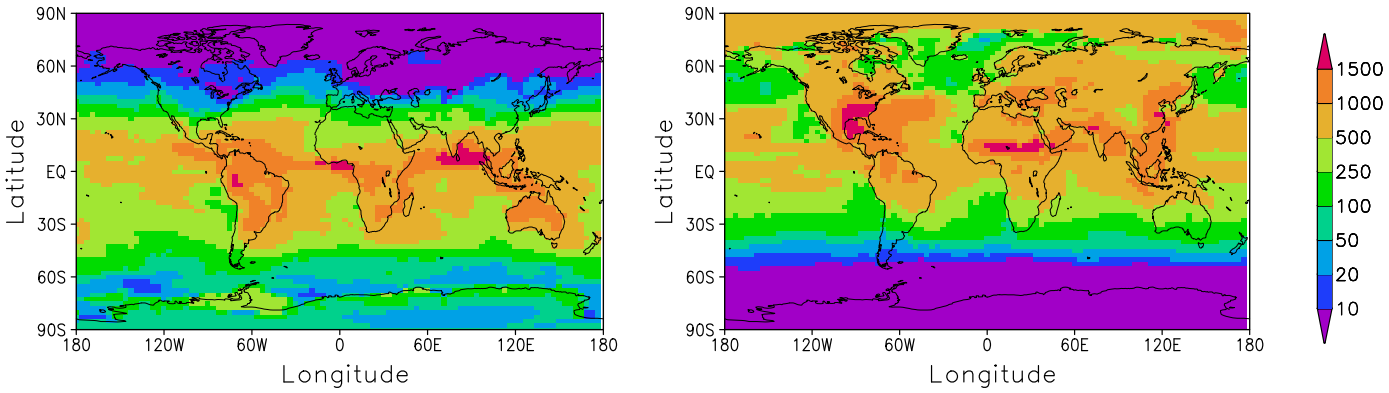

(a) **(b)**

Fig. 22: Zonally-averaged mixing ratio of predicted H_2O_2 (pptv) in a) January and b) July.

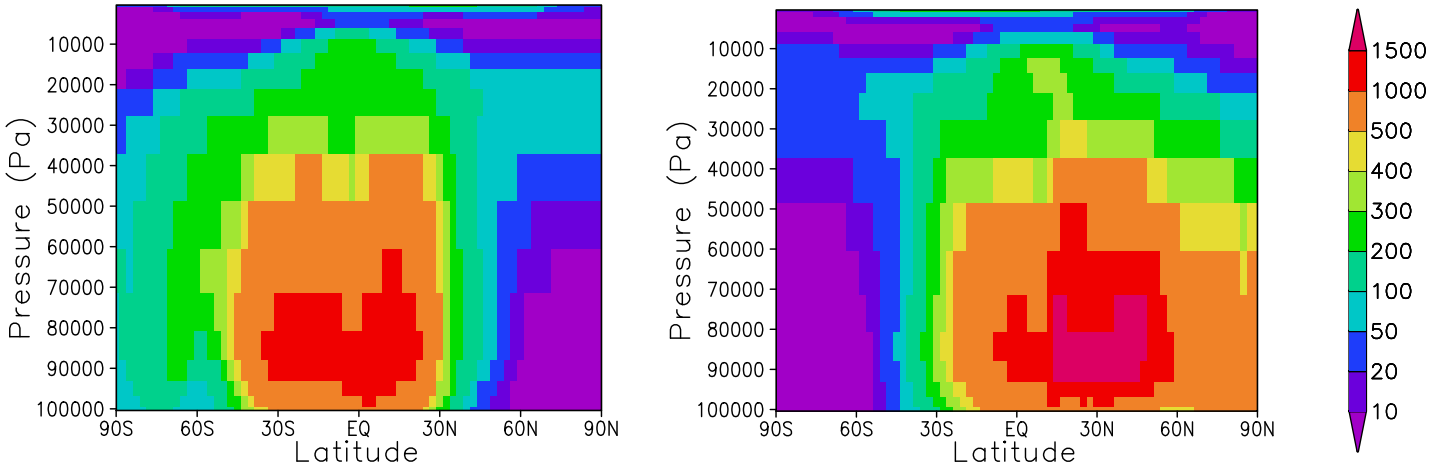

(a) **(b)**

Fig. 23: Globally- and annually-averaged sulfur budget. Burdens are given in Tg S, fluxes in Tg S yr^{-1}, and lifetimes (in italics) in days. Dry and Wet stands for dry and wet depositions, respectively. Wet deposition is due to in-cloud (in) and below-cloud (bc) scavenging from large-scale (lsc) and convective (con) clouds.

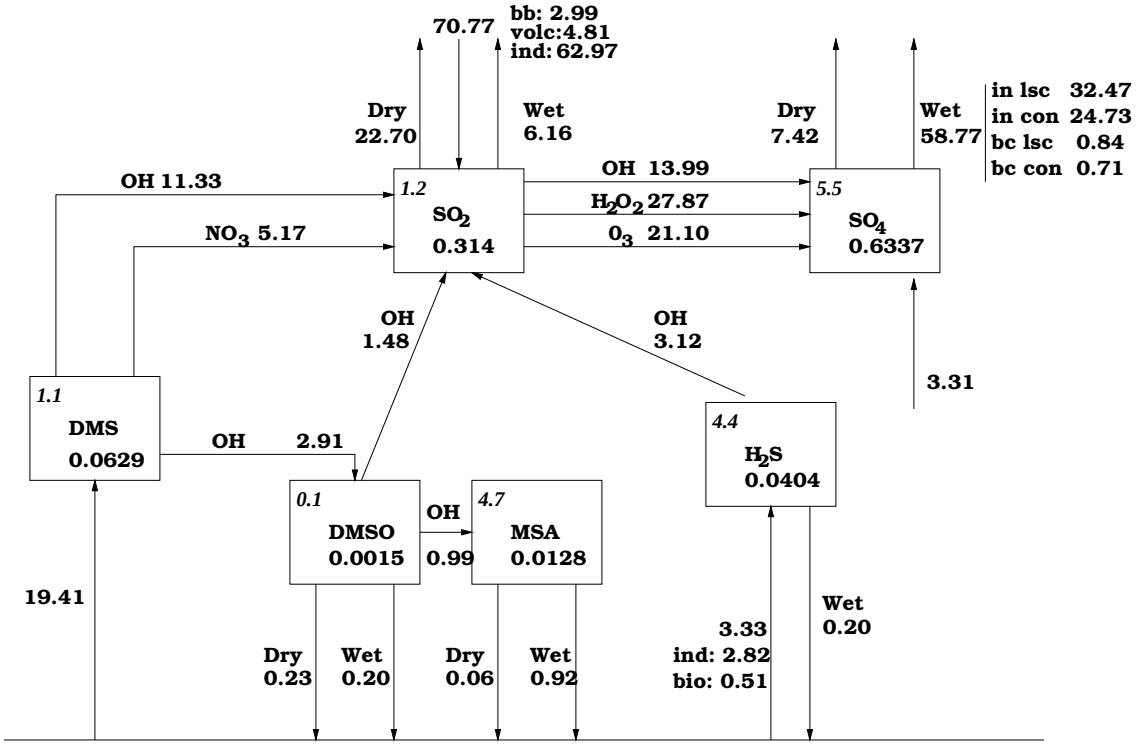

7 Budgets

Fig. 23 shows the budget of sulfur species on a global and annual average. The budget is in balance for all six species. Except for in-cloud sulfate production and sulfate wet scavenging, all the terms of our sulfur budget are in the range of those given by Koch et al. (1999), Barth et al. (2000), and Chin et al. (2000a) (as compiled in Chin et al. (2000a)). Our in-cloud sulfate production and sulfate wet deposition are somewhat larger than those of these authors. In-cloud sulfate production is 49.0 Tg S yr^{-1}, in comparison to a range of 24.5 to 44.4 Tg S yr^{-1} for the three studies cited above. For wet scavenging of sulfate, our model predicts a global- and annual-mean rate of 58.8 Tg S yr^{-1}, in comparison to a range of 34.7 to 51.2 Tg S yr^{-1} for the same three studies.

DMS is oxidized primarily by OH to form SO_2 and DMSO, a smaller fraction being oxidized by NO_3.

SO_2 is depleted by dry deposition (24.7%), wet deposition (6.7%), oxidation in the gas phase (15.2%), and oxidation in the aqueous phase (53.3%). As shown on Fig. 24 which represents the distribution of the vertically- integrated sinks of SO_2 on a common colour scale, dry deposition is important over land, where SO_2 concentrations are large, but also over ocean, where the deposition velocity is larger. Oxidation by OH is more important in summer than in winter, in agreement with the seasonal variations in OH concentrations. Oxidation of SO_2 by O_3 is particularly important in wintertime at midlatitudes, but is supplanted by oxidation by H_2O_2 in summertime.

Sulfate sources include emissions (5.0%) and production by gas- and aqueous-phase oxidation of SO_2 (21.1% and 73.9%, respectively). Its main sink is through wet scavenging (88.8%), with a small contribution from dry deposition (11.2%). In our model, in-cloud oxidation of SO_2 by O_3 plays a much larger role than in the studies of Feichter et al. (1996) and Barth et al. (2000). It amounts to 8.6% and 15.7% of sulfate production in these two studies, but reaches 33.5% in our model. Oxidation of SO_2 by O_3 occurs principally during winter in the polluted regions, for example, over Europe, where the model overestimates cloud cover and precipitation. There is a coupling of the sulphate source from in-cloud oxidation, with the sink from wet scavenging. This would result in a lower net sulphate concentration in-cloud and consequently larger pH, at which the O_3

Fig. 24: Vertically-integrated sinks of SO_2 (mg S m^{-2} yr^{-1}) in January (left) and July (right).

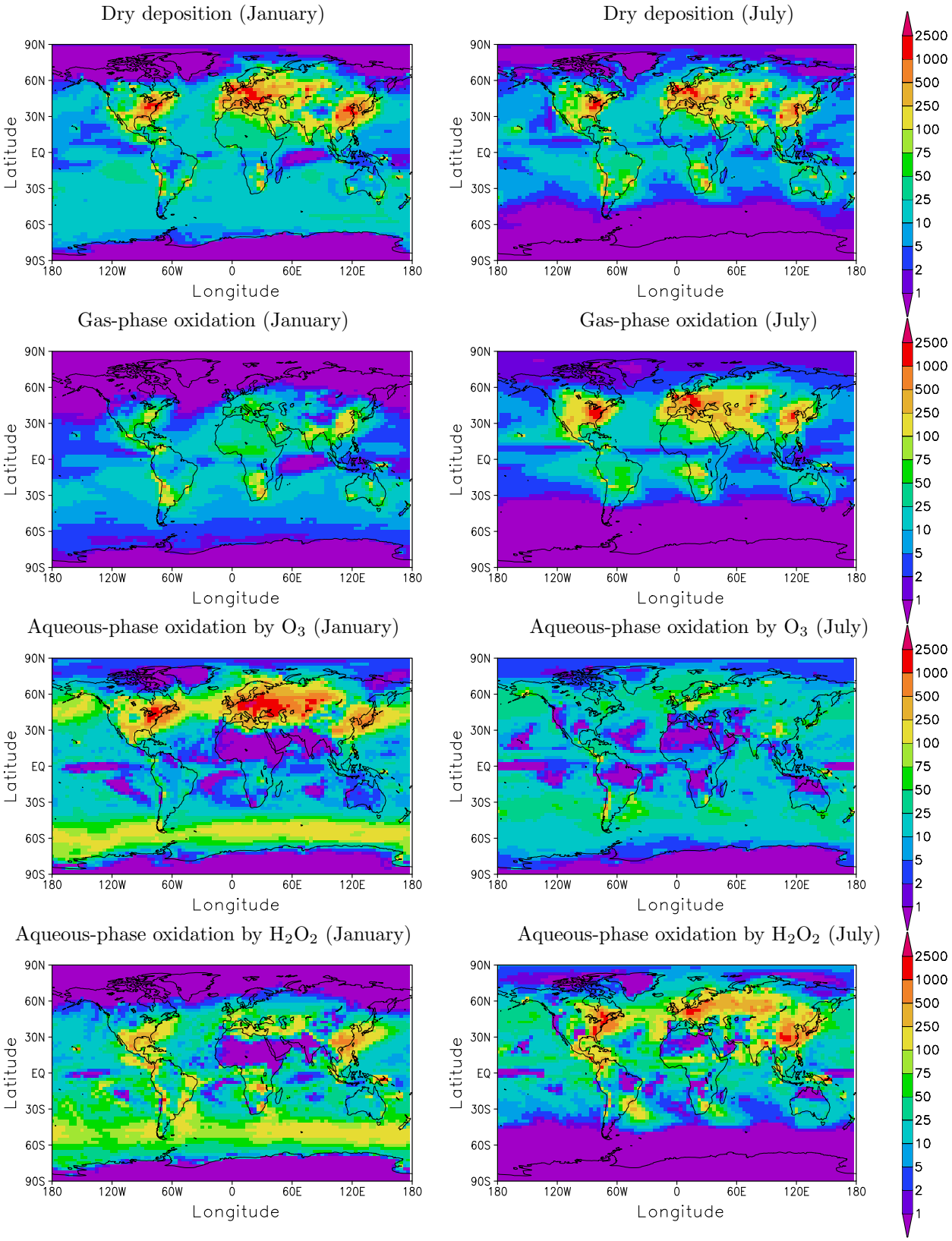

Fig. 25: a) Distribution of predicted H_2O_2 mixing ratio (pptv) at the surface in January in the simulation where H_2O_2 is not depleted upon oxidation of SO_2 (NODEPL). b) Ratio of January H_2O_2 mixing ratios between simulations where H_2O_2 is and is not depleted.

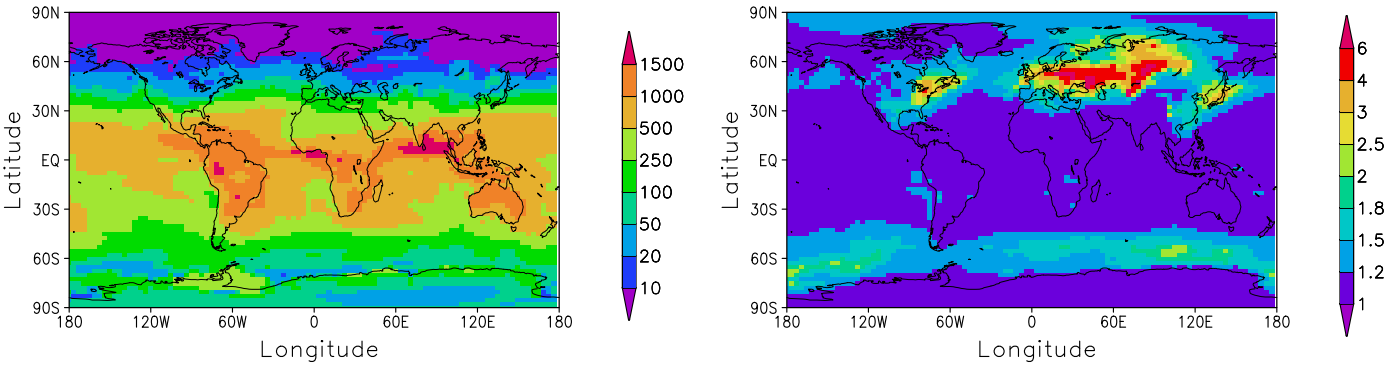

(a) **(b)**

Table 6: Budget of H_2O_2 over the globe and over Europe.

		Global annual		Europe January[a]		Europe July[a]	
Burden (mg H_2O_2 m^{-2})		5.36		1.34		8.23	
Lifetime (days)		1.13		2.51		1.10	
Source (mg H_2O_2 m^{-2} yr^{-1})	HO_2 + HO_2	1735.3	(100.0%)	191.0	(97.9%)	2737.4	(100.0%)
Sinks (mg H_2O_2 m^{-2} yr^{-1})	H_2O_2 + OH	487.2	(28.1%)	19.0	(9.7%)	957.7	(35.0%)
	Photodissociation	534.7	(30.8%)	51.6	(26.5%)	893.7	(32.6%)
	Dry deposition	244.5	(14.1%)	31.8	(16.3%)	342.0	(12.5%)
	Wet deposition	410.8	(23.7%)	37.5	(19.2%)	255.2	(9.3%)
	Oxidation of SO_2	58.1	(3.3%)	55.1	(28.3%)	172.5	(6.3%)
	Total	1735.3	(100.0%)	195.0	(100.0%)	2621.1	(95.8%)

[a]For Europe (defined as the box 20°W–40°E, 30°N–80°N), the budget is not balanced because of a net import or export term.

oxidation rate is enhanced leading to a predominance of this pathway.

The lifetimes for DMS, SO_2, and sulfate are 1.1, 1.2, and 5.5 days, respectively. The lifetimes for DMS and SO_2 are slightly less than in previous studies, while the lifetime for sulfate is slightly greater than in previous studies (Chin et al., 2000a).

8 Sensitivity to Aqueous-Phase Chemistry

In some models, the oxidation of aqueous SO_2 by H_2O_2 is considered either as a titration of SO_2 with H_2O_2 or with a complete module of aqueous chemistry. In several of these models, H_2O_2 is replenished (i.e., it is regenerated to its prescribed value) at the beginning of each time step: every 40 minutes in Feichter et al. (1996), 4 hours in Chin et al. (1996), 3 hours in Chin et al. (2000a, 2000b), or 2 hours in Takemura et al. (2000). It is likely that such parameterizations overestimate the rate of oxidation of SO_2 by H_2O_2 as it can take a much longer time for H_2O_2 to replenish (see below).

In contrast, H_2O_2 is a prognostic species in the GISS GCM (Koch et al., 1999), in the NCAR CCM3 (Barth et al., 2000), and in the present study. The wintertime sulfate concentrations are underestimated in all three models, but to an even greater extent in the NCAR model, although it also considers oxidation of aqueous SO_2 by O_3, while the GISS model does not. As shown in section 4.2, wintertime sulfate concentrations are also underestimated in our model. It is unlikely that this

is due solely to a missing oxidation path for SO_2, as SO_2 concentrations are also underestimated. Instead, this may be due to a too large precipitation rate over Europe in winter. It is, however, difficult to anticipate the extent to which the results would be improved if a more realistic precipitation field was simulated by the GCM. A smaller precipitation rate would increase the sulfate concentration, which would slow down the oxidation of SO_2 by O_3, through a decrease in the cloud droplet pH. It appears that oxidation of SO_2 by O_3 is the major source of sulfates during winter in our model (Fig. 24). It is therefore likely that not only the oxidation rate of aqueous SO_2, but also the scavenging rate of sulfate or the transport outside the boundary layer are at stake. Moreover, it could be that the frequency of occurrence of precipitation is as important as the average precipitation rate to predict accurately the scavenging rate of sulfate (V. Ramaswamy, personal communication). However this parameter is usually not evaluated in GCMs and data are not readily available.

Another source of uncertainty stems from the computation of the pH of cloud droplets in our model. As evident from Eq. 1, one needs to know the concentration in ammonium cation to compute the pH. Our parametrization may not always be appropriate.

We made a sensitivity experiment where H_2O_2 is not depleted when it oxidizes SO_2 in the aqueous phase (NODEPL experiment). Therefore, in this run, H_2O_2 is not interactive with the sulfur cycle, but concentrations of SO_2 and sulfate still depend on H_2O_2 concentrations. Fig. 25a shows the surface mixing ratio of H_2O_2 in January in this sensitivity run. Mixing ratios are larger than in the base run by up to 200% over Europe in January (Fig. 25b). This difference between the two runs is corroborated by analyzing the budget of H_2O_2 in our base run. The concentration of H_2O_2 results from a balance between production from the HO_2+HO_2 reaction and sinks from photodissociation, dry and wet scavenging, and the reaction with OH. Our model does not include neither in-cloud production of H_2O_2 (Mc Elroy, 1986), nor does it include production of HO_x (OH and HO_2) and H_2O_2 from ozonolysis reactions of alkenes (Ariya et al., 2000). Globally- and annually-averaged, oxidation of SO_2 is a rather small sink for H_2O_2, at about 3%. However on the regional scale this reaction can cause a much larger sink for H_2O_2 (see Table 6). This is the case over Europe in wintertime where oxidation of SO_2 represents 28% of the removal rate for H_2O_2. The rather long lifetime of H_2O_2 in wintertime (around 2.5 days) and the importance of oxidation of SO_2 as a sink clearly indicate that the concentration of H_2O_2 cannot be held fixed in global sulfur models, as done in some of the previous studies.

9 Conclusion

We have incorporated the sulfur cycle in the general circulation model LMD-ZT and we have parameterized the processes of convective transport, wet scavenging, and aqueous-phase chemistry as consistently as possible with the model physical parameterizations. The model predicts the atmospheric fate of hydrogen peroxide (H_2O_2) and six sulfur species.

Comparison of surface modelled and observed sulfur distributions at remote monitoring stations shows a fair agreement except for MSA, whose production in the model should be reevaluated. We reiterate the finding previously made that surface concentrations of sulfates are underestimated during wintertime over Europe. We suspect that this is due to biases in the GCM climatology of cloud cover and precipitation, although this may also be due to too low oxidant levels during winter. The budget and concentration of H_2O_2 in Europe and the Northeast United States depend critically on the inclusion of the H_2O_2 sink associated to oxidation of SO_2. We suggest that more effort should be made to measure and monitor the concentrations of hydrogen peroxide over polluted regions, and to assess quantitatively the sources and sinks of this species.

It also appears that, in a few cases, sulfate mixing ratios are overpredicted in the upper troposphere when compared with measurements made during the PEM campaigns. For the other species (DMS, SO_2, and H_2O_2), the modelled vertical profile were generally in agreement, sometimes in disagreement with the PEM measurements, but there is no evidence for any systematic bias in the model.

While some improvements are still needed, we feel that this model is now a useful tool to investigate issues related to heterogeneous chemistry and to the climatic effects of natural DMS emissions and anthropogenic sulfate. In the near future we also plan to run our model in nudged mode and perform further evaluation against observations from field campaigns.

Aknowledgments : we are grateful to D. Hauglustaine, Y. Balkanski, E. Cosme, M. Lawrence, D. L. Roberts and M. C. Barth for helpful discussion, J. Sciare for providing the DMS data at Amsterdam Island, A. Hjellbrekke for providing the EMEP data, and R. Vet and C.-U. Ro for providing the EMEFS data.. The EMEFS

data utilized in this study were collected and prepared under the co-sponsorship of the United States Environmental Protection Agency, the Atmospheric Environment Service, Canada, the Ontario Ministry of Environment, the Electric Power Research Institute, and the Florida Electric Power Coordinating Group. Olivier Boucher would like to thank P. Crutzen, J. Lelieveld, and the Max Planck Institute for Chemistry for their hospitality. Computer time for this study was provided by the Institut du Développement et des Ressources en Informatique Scientifique (IDRIS). This research project is supported by the Programme National de Chimie Atmosphérique (PNCA) of the CNRS and the Indo-French Centre for the Promotion of Advanced Research (IFCPAR).

References

Aas, W., Hjellbrekke, A.-G., Semb, A., Schaug, J. 1999. Data Quality 1997, Quality Assurance, and Field Comparison, EMEP/CCC-Report6/99, 157 pp., Norsk institutt for luftforskning.

Adams, P.J., Seinfeld, J.H., Koch, D.M., 1999. Global concentrations of tropospheric sulfate, nitrate, and ammonium aerosol simulated in a general circulation model. Journal of Geophysical Research 104, 13791–13823.

Andreae, M.O., Elbert, W., Cai, Y., Andreae, T.C., Gras, J., 1999. Non-sea-salt sulfate, methanesulfonate, and nitrate aerosol concentrations and size distributions at Cape Grim, Tasmania. Journal of Geophysical Research 104, 21695–21706.

Andres, R.J., Kasgnoc, A.D., 1998. A time-averaged inventory of subaerial volcanic sulfur emissions. Journal of Geophysical Research 103, 25251–25261.

Ariya, P.A., Sander, R., Crutzen, P.J., 2000. Significance of HO_x and peroxides production due to alkene ozonolysis during fall and winter: A modelling study. Journal of Geophysical Research 105, 17721–17738.

Atkinson, R., Baulch, D.L., Cox, R.A., Hampson, R.F., Kerre Jr., J.A., Troe, J., 1989. Evaluated kinetic and photochemical data for atmospheric chemistry: Supplement III. Journal of Physical and Chemichal Reference Data 18, 881–1097.

Ayers, G.P., Ivey, J.P., Gillett, R.W., 1991. Coherence between seasonal cycles of dimethyl sulphide, methanesulphonate and sulphate in marine air. Nature 349, 404–406.

Ayers, G.P., Penkett, S.A., Gillett, R.W., Bandy, B., Galbally, I.E., Meyer, C.P., Elsworth, C.M., Bentley, S.T., Forgan, B.W., 1996. The annual cycle of peroxides and ozone in marine air at Cape Grim, Tasmania. Journal of Atmospheric Chemistry 23, 221–252.

Balkanski, Y.J., D.J. Jacob, G.M. Gardner, W.C. Graustein, K.K. Turekian, 1993. Transport and residence times of tropospheric aerosols inferred from a global three-dimensional simulation of ^{201}Pb. Journal of Geophysical Research 98, 20573-20586.

Barth, M.C., Hegg, D.A., Hobbs, P.V., 1989. Measurements of atmospheric gas-phase and aqueous-phase hydrogen peroxide concentrations in winter on the east coast of the United States. Tellus 41B, 61–69.

Barth, M.C., Rasch, P.J., Kiehl, J.T., Benkovitz, C.M., Schwartz, S.E., 2000. Sulfur chemistry in the National Center for Atmospheric Research Community Climate Model: Description, evaluation, features, and sensitivity to aqueous chemistry. Journal of Geophysical Research 105, 1387–1415.

Benkovitz, C.M., Berkowitz, C.M., Easter, R.C., Nemesure, S., Wagener, R., Schwartz, S.E., 1994. Sulfate over the North Atlantic and adjacent continental regions: Evaluation for October and November 1986 using a three-dimensional model driven by observation-derived meteorology. Journal of Geophysical Research 99, 20725–20756.

Benkovitz, C.M., Scholtz, M.T., Pacyna, J., Tarrasón, L., Dignon, J., Voldner, E.C., Spiro, P.A., Logan, J.A., Graedel, T.E., 1996. Global gridded inventories of anthropogenic emissions of sulfur and nitrogen. Journal of Geophysical Research 101, 29239–29253.

Boatman, J.F., Wellman, D.L., Van Valin, C.C., Gunter, R.L., Ray, J.D., Sievering, H., Kim, Y., Wilkison, S.W., Luria, M., 1989. Airborne sampling of selected trace chemicals above the central United States. Journal of Geophysical Research 94, 5081–5093.

Boucher, O., Anderson, T.L., 1995. GCM assessment of the sensitivity of direct climate forcing by anthropogenic sulfate aerosols to aerosol size and chemistry. Journal of Geophysical Research 100, 26117–26134.

Boucher, O., Lohmann, U., 1995. The sulfate-CCN-cloud albedo effect: a sensitivity study using two general circulation models. Tellus 47B, 281–300.

Boucher, O., Moulin, C., Belviso, S., Aumont, O., Bopp, L., Cosme, E., von Kuhlmann, R., Lawrence, M.G., Pham, M., Reddy, M. S., Sciare,

J., Venkataraman, C., 2003. DMS atmospheric concentrations and sulphate aerosol indirect radiative forcing: a sensitivity study to the DMS source representation and oxidation. Atmospheric Chemistry and Physics 3, 49–65.

Charlson, R.J., Schwartz, S.E., Hales, J.M., Cess, R.D., Coakley Jr., J.A., Hansen, J.E., Hofmann, D.J., 1992. Climate forcing by anthropogenic aerosols. Science 255, 423–430.

Chatfield, R.B., Crutzen, P.J., 1990. Are there interactions of iodine and sulfur species in marine air photochemistry? Journal of Geophysical Research 95, 22319–22341.

Chin, M., Jacob, D.J., Gardner, G.M., Foreman-Fowler, M.S., Spiro, P.A., 1996. A global three-dimensional model of tropospheric sulfate. Journal of Geophysical Research 101, 18667–18690.

Chin, M., Rood, R.B., Lin, S.-J., Müller, J.-F., Thompson, A.M., 2000a. Atmospheric sulfur cycle simulated in the global model GOCART: model description and global properties. Journal of Geophysical Research 105, 24671–24688.

Chin, M., Savoie, D.L., Huebert, B.J., Bandy, A.R., Thornton, D.C., Bates, T.S., Quinn, P.K., Saltzmann, E.S., De Bruyn, W.J., 2000b. Atmospheric sulfur cycle simulated in the global model GOCART: comparison with field observations and regional budgets. Journal of Geophysical Research 105, 24689–24712.

Chuang, C.C., Penner, J.E., Taylor, K.E., Grossman, A.S., Walton, J.J., 1997. An assessment of the radiative effects of anthropogenic sulfate. Journal of Geophysical Research 102, 3761–3778.

Chuang, C.C., Penner, J.E., Grant, K.E., Prospero, J.M., Rau, G.H., Kawamoto, K., 2002. Cloud susceptibility and the first aerosol indirect forcing: Sensitivity to black carbon and aerosol concentrations, Journal of Geophysical Research, 107(D21), 4564, doi:10.1029/2000JD000215.

Clarke, J.F., Edgerton, E.S., Martin, B.E., 1997. Dry deposition calculations for the clean air status and trends network. Atmospheric Environment 31, 3667-3678.

Cosme, E., Genthon, C., Martinerie, P., Pham, M., Boucher, O., 2002. Sulfur cycle in the high southern latitudes in the LMD-ZT general circulation model. Journal of Geophysical Research, 107(D23), 4690, doi:10.1029/2002JD002149.

Covert, D.S., 1988. North Pacific marine background aerosol: average ammonium to sulfate molar ratio equals 1. Journal of Geophysical Research 93, 8455–8458.

Crutzen, P.J., Lawrence, M.G., 2000. The impact of precipitation scavenging on the transport of trace gases: a 3-dimensional model sensitivity study. Journal of Atmospheric Chemistry 37, 81–112.

Dentener, F.J., Crutzen, P.J., 1993. Reaction of N_2O_5 on tropospheric aerosols: impact on the global distributions of NO_x, O_3 and OH. Journal of Geophysical Research 98, 7149–7163.

Dentener, F., Williams, J., Metzger, S., 2002. Aqueous phase reactions of HNO_4: the impact on tropospheric chemistry. Journal of Atmospheric Chemistry 41, 109–134.

DeMore, W.B., Sander, S.P., Golden, D.M., Hampson, R.F., Kurylo, M.J., Howard, C.J., Ravishankara, A.R., Kolb, C.E., Molina, M.J., 1997. Chemical kinetics and photochemical data for use in stratospheric modeling. Evaluation Number 12, JPL Publication 97-4, Jet Propulsion Lab., Pasadena, CA.

Feichter, J., Kjellström, E., Rodhe, H., Dentener, F., Lelieveld, J., Roelofs, G.-J., 1996. Simulation of the tropospheric sulfur cycle in a global climate model. Atmospheric Environment 30, 1693–1707.

Garland, J.A., 1977. The dry deposition of sulphur dioxide to land and water surfaces. Proceedings of the Royal Society of London A 354, 245-268.

Giorgi, F., Chameides, W.L., 1986. Rainout lifetimes of highly soluble aerosols and gases as inferred from simulations with a general circulation model. Journal of Geophysical Research 91, 14367–14376.

Grossmann, D., 1999. Die Gasphaseozonolyse von Alkenen in Gegenwart von Wasserdampf als Quelle für Wasserstoffperoxid und organische Peroxide in der Atmosphäre. Ph. D. Thesis, University of Mainz.

Heikes, B.G., Kok, G.L., Walega, J.G., Lazrus, A.L., 1987. H_2O_2, O_3 and SO_2 measurements in the lower troposphere over the Eastern United States during fall. Journal of Geophysical Research 92, 915–931.

Hoffmann, M.R., Calvert, J.G., 1985. Chemical transformation modules for Eulerian acid deposition models, Volume 2, The aqueous phase chemistry. EPA/600/3-85/017, US Environmental Protection Agency, Research Triangle Park, North Carolina, USA.

Hourdin, F., Armangaud, A., 1999. The use of finite-volume methods for atmospheric advection of trace species. Part I: Test of various formulations

in a general circulation model. Monthly Weather Review 127, 822–837.

Hourdin, F., Issartel, J.-P., 2000. Sub-surface nuclear tests monitoring through the CTBT xenon network. Geophysical Research Letters 27, 2245–2248.

Kasibhatla, P., Chameides, W.L., John, J.S., 1997. A three-dimensional global model investigation of seasonal variations in the atmospheric burden of anthropogenic sulfate aerosols. Journal of Geophysical Research 102, 3737–3760.

Kettle, A.J., et al., 1999. A global database of sea surface dimethylsulfide (DMS) measurements and a procedure to predict sea surface DMS as a function of latitude, longitude, and month. Global Biogeochemical Cycles 13, 399–444.

Koch, D., Jacob, D., Tegen, I., Rind, D., Chin, M., 1999. Tropospheric sulfur simulation and sulfate direct radiative forcing in the Goddard Institute for Space Studies general circulation model. Journal of Geophysical Research 104, 23799–23822.

Langner, J., Rodhe, H., 1991. A global three-dimensional model of the tropospheric sulfur cycle. Journal of Atmospheric Chemistry 13, 225–263.

Lee, M., Heikes, B.G., O'Sullivan, D.W., 2000. Hydrogen peroxide and organic hydroperoxide in the troposphere: a review. Atmospheric Environment 34, 3475–3494.

Legates, D.R., Willmott, C.J., 1990. Mean seasonal and spatial variability in gauge-corrected, global precipitation, International Journal of Climatology, 10, 111–127.

Lide, D.R., Frederikse, H.P.R., editors, 1995. CRC Hanbook of Chemistry and Physics, 76th edition, CRC Press, Inc., Boca Raton, FL.

Liss, P.S., Merlivat, L., 1986. Air-sea exchange rates: Introduction and synthesis, in The Role of Air-Sea Exchange in Geochemical Cycling, P. Buat-Ménard (Ed.), Norwell, Mass.

Mari, C., Jacob, D.J., Bechtold, P., 2000. Transport and scavenging of soluble gases in a deep convective cloud. Journal of Geophysical Research 105, 22255-22267.

Mc Elroy, W.J., 1986. Sources of hydrogen peroxide in cloudwater. Atmospheric Environment 20, 427–438.

McNaughton, D.J., Vet, R.J., 1996. Eulerian model evaluation field study (EMEFS): A summary of surface network measurements and data quality. Atmospheric Environment 30, 227–238.

Müller, J.-F., Brasseur, G.P., 1995. IMAGES: A three-dimensional chemical transport model of the global troposphere. Journal of Geophysical Research 100, 16455–16490.

National Bureau of Standards, 1965. Selected values of chemical thermodynamic properties, 1. Tech. Note, 270–1, Gaithersburg, MD.

O'Sullivan, D.W., Lee, M., Noone, B.C., Heikes, B.G., 1996. Henry's law constant determinations for hydrogen peroxide, methyl hydroperoxide, hydromethyl hydroperoxide, ethyl hydroperoxide, and peroxyacetic acid. Journal of Physical Chemistry 100, 3241–3247.

Pham, M., Müller, J.-F., Brasseur, G., Granier, C., Mégie, G., 1995a. A three-dimensional study of the tropospheric sulfur cycle. Journal of Geophysical Research 100, 26061–26092.

Pham, M., Müller, J.-F., Brasseur, G., Granier, C., Mégie, G., 1995b. A 3D model study of the global sulphur cycle: Contributions of anthropogenic and biogenic sources. Atmospheric Environment 30, 1815–1822.

Pruppacher, H.R., Klett, J.D., 1997. Microphysics of Clouds and Precipitation, Second Revised and Enlarged Edition with an Introduction to Cloud Chemistry and Cloud Electricity, Kluwer Academic Publishers, Boston, 954 pp.

Putaud, J.-P., Mihalopoulos, N., Nguyen, B.C., Campin, J.M., Belviso, S., 1992. Seasonal variations of atmospheric sulfur dioxide and dimethylsulfide concentrations at Amsterdam Island in the Southern Indian Ocean. Journal of Atmospheric Chemistry 15, 117–131.

Rasch, P.J., Barth, M.C., Kiehl, J.T., Schwartz, S.E., Benkovitz, C.M., 2000. A description of the global sulfur cycle and its controlling processes in the National Center for Atmospheric Research Community Climate Model, Version 3. Journal of Geophysical Research 105, 1367–1385.

Rodhe, H., 1999. Human impact on the atmospheric sulfur balance. Tellus 51AB, 110–122.

Roelofs, G.-J., Lelieveld, J., Ganzeveld, L., 1998. Simulation of global sulfate distribution and the influence on effective cloud drop radii with a coupled photochemistry-sulfur cycle model. Tellus 50B, 224–242.

Sakugawa, H., Kaplan, I.R., 1989. H_2O_2 and O_3 in the atmosphere of Los Angeles and its vicinity: factors controlling their formation and their role as oxidant of SO_2. Journal of Geophysical Research 94, 12957–12973.

Sander, R., 1999. Compilation of Henry's Law Constants for Inorganic and Organic Species of Potential Importance in Environmental Chemistry (Version 3). Available at http://www.mpch-mainz.mpg.de/∼sander/res/henry.html.

Sciare, J., Baboukas, E., Hancy, R., Mihalopoulos, N., Nguyen, B.C., 1998. Seasonal variation of dimethylsulfoxide in rainwater at Amsterdam Island in the Southern Indian Ocean: implications on the biogenic sulfur cycle. Journal of Atmospheric Chemistry 30, 229–240.

Sciare, J., Mihalopoulos, N., Dentener, F.J., 2000. Interannual variability of atmospheric dimethylsulfide in the southern Indian Ocean. Journal of Geophysical Research 105, 26,369–26,378.

Seinfeld, J.H., Pandis, S.N., 1998. Atmospheric Chemistry and Physics, From Air Pollution to Climate Change. John Wiley & Sons, 1326 pp.

Takemura, T., Okamoto, H., Maruyama, Y., Numaguti, A., Higurashi, A., Nakajima, T., 2000. Global three-dimensional simulation of aerosol optical thickness distribution of various origins. Journal of Geophysical Research, 105, 17853-17873.

Thornton, D.C., Bandy, A.R., Blomquist, B.W., Davis, D.D., Talbot, R.W., 1996. Sulfur dioxide as a source of condensation nuclei in the upper troposphere of the Pacific Ocean. Journal of Geophysical Research 101, 1883–1890.

Tiedtke, M., 1989. A comprehensive mass flux scheme for cumulus parameterization in large-scale models. Quaterly Journal of the Royal Meteorological Society 117, 1779–1800.

van Leer, B., 1977. Towards the ultimate conservative difference scheme: IV. A new approach to numerical convection. Journal of Computational Physics 23, 276–299.

Van Valin, C.C., Ray, J.D., Boatman, J.F., Gunter, R.L., 1987. Hydrogen peroxide in air during winter over the South-Central United States. Geophysical Research Letters 14, 1146–1149.

Venkataraman, C., Mehra, A., Mhaskar, P., 2001. Mechanisms of sulphate aerosol production in clouds: effect of cloud characteristics and season in the Indian region. Tellus 53B, 260–272.

Warneck, P., 1999. The relative importance of various pathways for the oxidation of sulfur dioxide and nitrogen dioxide in sunlit continental fair weather clouds. Physical Chemistry and Chemical Physics 1, 5471–5483.

Watts, S.F., 2000. The mass budgets of carbonyl sulfide, dimethyl sulfide, carbon disulfide and hydrogen sulfide. Atmospheric Environment 34, 761-779.

Wesely, M.L., Cook, D.R., Hart, R.L., Speer, R.E., 1985. Measurements and parameterization of particulate sulphur dry deposition over grass. Journal of Geophysical Research 90, 2131-2143.

Chapitre 4

Evolution temporelle du forçage radiatif des aérosols soufrés

Ce chapitre reprend l'article de *Boucher et Pham* [2002] paru au journal *Geophysical Research Letters*.

History of sulfate aerosol radiative forcings

O. Boucher,
Laboratoire d'Optique Atmosphérique,
U.F.R. de Physique, Université des Sciences et Technologies de Lille,
59655 Villeneuve d'Ascq Cedex, France.
(e-mail: boucher@loa.univ-lille1.fr)

M. Pham,
Service d'Aéronomie, Boîte 102,
Université Pierre et Marie Curie,
4 Place Jussieu, 75252 Paris Cedex 05, France.
(e-mail: mai.pham@aero.jussieu.fr)

Abstract. The history of the global sulfur cycle has been simulated using an emission inventory of SO_2 for 1990 and previously published historical trends in emission on a per country basis. The global-mean radiative forcings due to sulfate aerosols increase (in absolute values) from near-zero and -0.17 Wm^{-2} up to -0.4 and -1 Wm^{-2} between 1850 and 1990, for the direct and indirect effects, respectively. The forcing efficiency (defined as the ratio of the radiative forcing to the anthropogenic sulfate burden) is fairly constant for the direct effect at -150 W(g sulfate)$^{-1}$ but decreases significantly for the indirect effect with increasing sulfate burden. The model results are compared with long-term observations for the period 1980 to 1998 in the U.S. and Europe.

1 Introduction

It is important to determine the history of the various radiative forcings (RFs) in the context of the detection of anthropogenic climate change [*IPCC*, 2001]. *Myhre et al.* [2001] compiled the historical evolution of most of the natural and anthropogenic RFs identified so far.

They stressed that the uncertainties are large for the RFs by anthropogenic aerosols because of the uncertainties in emissions and calculations of the RF itself. *Tegen et al.* [2000] computed the trends in aerosol concentrations and direct RF for the period 1950 to 1990. Here we focus on sulfate aerosols because more information on their source are available than for other aerosol species. We present some results on sulfate concentrations, and their direct and indirect effects for the period 1850 to 1990 (1998 over Europe and U.S.).

2 Methodology

2.1 Sulfur Cycle Model

We use the sulfur cycle model implemented in the Laboratoire de Météorologie Dynamique (LMD) general circulation model (GCM). The model is described and evaluated against measurements in *Boucher et al.* [2002]. The model represents many features of the observed concentrations of DMS, SO_2, and sulfate aerosols, although the sulfate concentrations are underestimated over Europe in winter and overestimated over North America in summer and autumn. Model simulations are performed at a horizontal resolution of 96x72 and 19 vertical layers. The RFs are computed as the differences in top-of-atmosphere shortwave radiative flux between two simulations, with and without anthropogenic sulfur emissions. In these simulations sulfate aerosols do not feedback on the radiation and cloud fields (i.e., sulfate radiative effects are purely diagnostic) so that all simulations have the same meteorology. We consider that neither the oxidant fields (except H_2O_2 which is calculated interactively in our model) nor the natural sources of sulfur species (including volcanoes) have changed during the period under study (1850–1998). Therefore the trends simulated in our model only account for changes in the anthropogenic sulfur emissions, which constitutes the focus of this study. All the results presented in this study are annual averages after a 6 month spin up time.

We follow *Boucher and Anderson* [1995] for the parametrization of the sulfate aerosol direct effect, assuming a chemical composition of ammonium sulfate, a log-normal size distribution with a mean geometric volume diameter $D_{gv} = 0.3$ μm and a geometric standard deviation $\sigma_g = 2.0$. The aerosol size distribution and optical properties depend on the relative humidity in the clear-sky fraction of a GCM grid-box, following the laboratory measurements of *Tang and Munkelwitz* [1994].

One usually distinguishes the first aerosol indirect effect (an increase in cloud droplet number concentration at fixed liquid water content) from the second aerosol indirect effect (induced by a reduction in the precipitation efficiency). Here we only consider the first indirect effect and follow the parametrization of *Boucher and Lohmann* [1995]. We use their relationship D to compute the cloud droplet number concentration (CDNC, in droplets per cm^{-3}) from the sulfate mass (m_{SO_4}, in μg SO_4 m^{-3}):

$$\mathrm{CDNC} = 10^{2.21+0.41\ \log(m_{SO_4})} \quad (1)$$

Although empirical, this parametrization predicts RFs of comparable magnitude to those from more elaborate "mechanistic" parametrizations of the aerosol indirect effect [*IPCC*, 2001]. It is appropriate for the purpose of this study since we are interested primarily in the time evolution of the RF.

2.2 Emissions

There are some uncertainties in the emission strengths of all sulfur compounds, including industrial SO_2. Commonly used emission inventories include GEIA for base year 1985 [*Benkovitz et al.*, 1996] –as in *Boucher et al.* [2002]– and EDGAR for base year 1990 [*Olivier et al.*, 1996]. Regional inventories have also been developed in recent years. Because different methodologies and input data have been used, the differences between the 1985 GEIA and 1990 EDGAR inventories do not represent a "real" evolution in the emissions. Instead one should use a same methodology to derive the sulfur emissions for different years. Historical emission inventories have been built by *Örn et al.* [1996] at a 5°x5° resolution for 1860 to 1980 and by *Lefohn et al.* [1999] on a per country basis for 1850 to 1990.

In our CONTROL simulation we use the EDGAR V2.0 database [*Olivier et al.*, 1996] for the year 1990 and scale the emissions country by country using the data by *Lefohn et al.* [1999], in order to build 1°x1° emission inventories for some other years (i.e., 1850, 1900, and 1920 to 1990 with a step of 10 years). The emission strength of SO_2 at a year y is obtained from

$$F(\lambda,\phi,y) = \frac{\sum_c G_c(y)\ \alpha_c(\lambda,\phi)}{\sum_c G_c(1990)\ \alpha_c(\lambda,\phi)} F_{\mathrm{EDGAR}}(\lambda,\phi) \quad (2)$$

where F_{EDGAR} is the EDGAR emission strength, $G_c(y)$ the emission strength for country c and year y according to *Lefohn et al.* [1999], and $\alpha_c(\lambda,\phi)$ the area fraction of country c in the grid-box determined by its latitude λ and longitude ϕ (with a resolution of 1°). There are few countries with missing data. In such cases, the emission strength of a neighbouring country with similar economy was used. When data for the year 1990 were

Fig. 1: Annual-mean emission of anthropogenic SO_2 (Tg S/yr) and anthropogenic sulfate burden simulated by the model (Tg S) for the period 1850 to 1990. The solid and dashed lines are for the CONTROL and EPA–EMEP simulations, respectively.

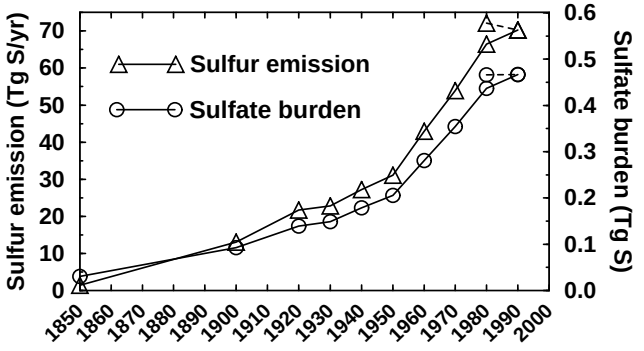

Fig. 2: Time evolution of the global- and annual-mean direct and indirect RFs by sulfate aerosols (Wm^{-2}). The solid and dashed lines are for the CONTROL and EPA–EMEP simulations, respectively.

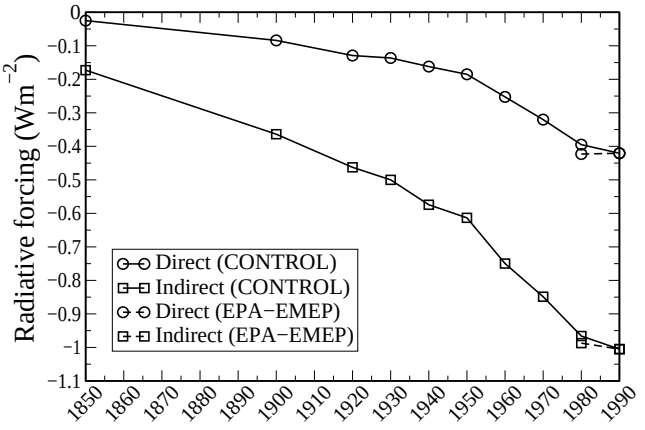

missing, the trend obtained from earlier years was extrapolated to 1990. As there is no information on the time evolution of sulfur emissions from shipping, this source was left out of this study. We consider that a small fraction (5%) of the SO_2 is directly emitted as sulfate and add a small industrial source of H_2S set to 4% of the SO_2 source [*Watts*, 2000; *Boucher et al.*, 2002].

Recent data by the U.S. Environmental Protection Agency [*EPA*, 2000; *Husain et al.*, 1998] and the Cooperative Programme for Monitoring and Evaluation of the Long-Range Transmission of Air Pollutants in Europe (EMEP) [*Mylona*, 1993; *Vestreng and Støren*, 2000] suggest a more rapid decrease in sulfur emissions over U.S. and Europe than in the Lefohn et al. database. In a second set of simulations for years 1980 and 1998 (referred to as EPA–EMEP), the $G_c(y)$ terms of Eq. (2) are prescribed from *EPA* [2000] for the U.S., from *Vestreng*

Fig. 3: Direct (upper panel) and indirect (lower panel) RFs by sulfate aerosols (Wm^{-2}) for the year 1990.

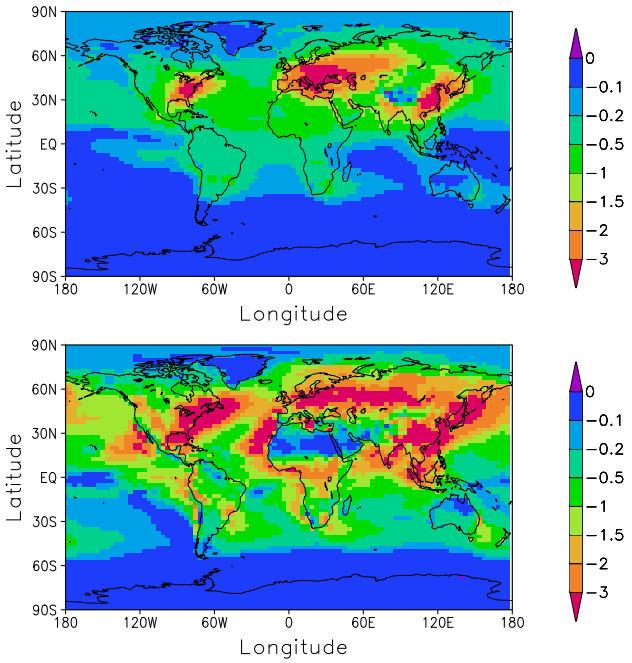

and Støren [2000] for European countries (i.e., Western Europe and former USSR republics west to Russia), and from (or extrapolated in time from) the Lefohn et al. data for the rest of the countries.

3 Discussion

The natural burden of sulfate aerosols is estimated to be 0.19 Tg S. The anthropogenic burden of sulfate aerosols is represented on Fig. 1 along with the emission strength. It increases from 0.03 Tg S in 1850 to 0.47 Tg S in 1990. The NH to SH ratio in burden decreases from 7.2 to 5.8 between 1920 and 1990 (when, in the same time, the NH to SH ratio in emission decreases from 50 to 13). The anthropogenic sulfate burden increases less rapidly than the emission strength, because only a fraction of the sulfur dioxide is oxidized into sulfate (roughly 70% in our model). Note however that the ratio of anthropogenic sulfate burden to the SO_2 emission strength does not change significantly from 1900 to 1990, indicating that the efficiency of SO_2 to sulfate oxidation has not decreased, despite the increasing SO_2 concentrations.

The time evolution of the RFs by sulfate aerosols is represented on Fig. 2. The global- and annual-mean RFs reach -0.42 and -1.0 Wm^{-2} in 1990, for the direct and indirect effects, respectively. In contrast to the direct RF, the indirect RF is not negligible in 1850, reducing

Fig. 4: Sulfate concentrations (μg S m^{-3}) observed and simulated under the two emission scenarii. The values are annual means averaged over the 18 stations of the EMEP network having continuous measurements from 1980 to 1998.

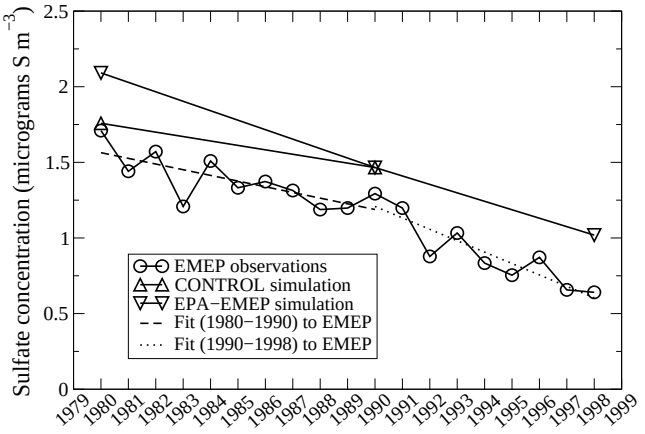

Fig. 5: Wet deposition flux (mg S m^{-2} yr^{-1}) observed and simulated under the two emission scenarii. The values are annual means averaged over the 57 stations of the NADP network having continuous measurements from 1980 to 1998.

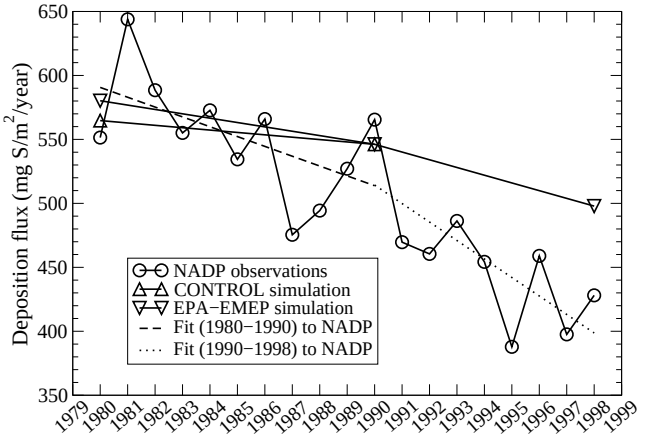

the RF over the period 1850 to 1990 compared to the period from pre-industrial times to 1990. The NH to SH ratios in RFs decrease from maximum values of 9.0 and 6.0 in 1920 to 6.8 and 3.7 in 1990, for the direct and indirect effects, respectively. The spatial distributions of the two effects are quite different as illustrated in Fig. 3 for the year 1990. While the direct effect is concentrated in the midlatitudes of the Northern Hemisphere and above the continents, the indirect effect shows a more widespread distribution with a significant contribution over the oceans.

In contrast to our CONTROL simulation, the EPA–EMEP simulation shows a flattening of both the direct and indirect RFs between 1980 and 1990 (Fig. 2). The direct RF decreases slightly following the decrease in sulfate burden, while the indirect RF increases slightly because of a larger forcing efficiency of the sulfate in the regions of increasing compared to the regions of decreasing concentrations. We follow *Tegen et al.* [2000] and compare the simulated sulfate concentrations over Europe to the EMEP measurements [*Hjellbrekke*, 2001] and the wet deposition flux over the U.S. to the NADP measurements (National Atmospheric Deposition Program, see http://nadp.sws.uiuc.edu). In these comparisons, only sites with continuous measurements over the period 1980 to 1998 have been considered. The model overestimates the mean sulfate concentrations at EMEP sites by 10–25% between 1980 to 1990 (Fig. 4). The observed (negative) slope of the trend is intermediate between those simulated in the CONTROL and EPA–EMEP runs. For the period 1980 to 1998, the simulated slope in the EPA–EMEP run is close to the observed one. There is a good agreement (<10%) for the wet deposition flux of sulfur simulated and observed over the NADP network (Fig. 5). The trend is not as strong in both simulations as in the observations. This discrepancy may be due to a stronger decrease in the emissions than implemented in the model or to changes in the geographical patterns of the emissions or precipitation not accounted for in the model. It is difficult from this limited set of comparisons to select the better of our two scenarios. However, it seems that the observed decrease in sulfate concentrations over Europe and deposition fluxes over U.S. is as large or larger than implied by our EPA–EMEP scenario.

The forcing efficiency is defined as the ratio of the global- and annual-mean RF (in Wm^{-2}) to the anthropogenic sulfate burden (in g m^{-2}), as introduced by *Boucher and Anderson* [1995]. As shown in Fig. 6, the forcing efficiency for the sulfate aerosol direct effect is fairly constant at -150 W(g sulfate)$^{-1}$. It is close to the forcing efficiency of -125 W(g sulfate)$^{-1}$ calculated in *Boucher and Anderson* [1995] for an earlier version of our GCM (with off-line sulfur cycle) and on the low side of the range reported by *Haywood and Boucher* [2000]. Such differences in the forcing efficiency among global models have not been eluded yet, but seem to be due to differences in the treatment of relative humidity and cloud effects, rather than in the radiative transfer itself [*Boucher et al.*, 1998]. In contrast to the direct effect, the forcing efficiency of the sulfate indirect effect shows a large reduction from 1850 to 1990, from -963 to -366 W(g sulfate)$^{-1}$. This illustrates the strong nonlinearities of the aerosol indirect effect induced by the

aerosol-to-CDNC and CDNC-to-cloud albedo relationships.

4 Conclusions

We have computed the RFs due to sulfate aerosols over the period 1850 to 1990. The direct RF increased (in absolute value) from near-zero to -0.42 Wm^{-2}, while the indirect RF increased from -0.17 to -1.0 Wm^{-2} but with a decreasing efficiency. The decrease in SO_2 emissions over U.S. and Europe results in a global-mean RF due to sulfate aerosols which stays fairly constant between 1980 and 1990. There is a shift in the RF patterns from U.S., Europe, Russia, Northern Atlantic Ocean and parts of Africa to South-East Asia and the Indian and Pacific Oceans. This work needs to be extended to other aerosol species, in particular carbonaceous aerosols for which the history of emissions is becoming available.

Acknowledgements. We thank R. Husar for making available his data on the historical trend of sulfur emissions. The EMEP data were downloaded from http://www.nilu.no/projects/ccc. Computer time for this study was provided by the Institut du Développement et des Ressources en Informatique Scientifique (IDRIS) of the CNRS. This research project is supported by the Programme National de Chimie Atmosphérique (PNCA) of the CNRS and the Indo-French Centre for the Promotion of Advanced Research (IFCPAR). Olivier Boucher would like to thank P. Crutzen, J. Lelieveld, and the Max Planck Institute for Chemistry in Mainz for their hospitality.

References

Benkovitz, C. M., M. T. Scholtz, J. Pacyna, L. Tarrasón, J. Dignon, E. C. Voldner, P. A. Spiro, J. A. Logan, and T. E. Graedel, Global gridded inventories of anthropogenic emissions of sulfur and nitrogen, *J. Geophys. Res.*, *101*, 29,239–29,253, 1996.

Boucher, O., and T. L. Anderson, GCM assessment of the sensitivity of direct climate forcing by anthropogenic sulfate aerosols to aerosol size and chemistry, *J. Geophys. Res.*, *100*, 26,117–26,134, 1995.

Boucher, O., and U. Lohmann, The sulfate-CCN-cloud albedo effect: A sensitivity study using two general circulation models, *Tellus*, *47B*, 281–300, 1995.

Boucher, O., et al., Intercomparison of models representing shortwave radiative forcing by sulfate aerosols, *J. Geophys. Res.*, 103, 16,979–16,998, 1998.

Boucher, O., M. Pham, and C. Venkataraman, Simulation of the atmospheric sulfur cycle in the Laboratoire de Météorologie Dynamique General Circulation Model. Model description, model evaluation, and global and European budgets, *Note scientifique de l'IPSL n° 23*, juillet 2002.

EPA, National Air Pollution Emission Trends, 1900–1998, United States Environmental Protection Agency, EPA-454/R-00-002, March 2000. (available from http://www.epa.gov/ttn/chief/trends/trends98)

Haywood, J., and O. Boucher, Estimates of the direct and indirect radiative forcing due to tropospheric aerosols: A review, *Rev. Geophys.*, *38*, 513–543, 2000.

Hjellbrekke, A. G., *Data Report 1999. Acidifying and Eutrophying Compounds. Part 1: Annual summaries, EMEP/CCC Report 2/2001*, 95 pp., 2001. (available from http://www.nilu.no/projects/ccc/reports)

Husain, L., V. A. Dutkiewicz, and M. Das, Evidence for decrease in atmospheric sulfur burden in the Eastern United States caused by reduction in SO_2 emissions, *Geophys. Res. Lett.*, *25*, 967–970, 1998.

IPCC, *Climate Change 2001, The Scientific Basis, Contribution of Working Group I to the Third Assessment Report of the Intergovernmental Panel on Climate Change*, J. T. Houghton et al. (Eds.), Cambridge University Press, Cambridge, U.K., 881 pp., 2001.

Lefohn, A. S., J. D. Husar, and R. B. Husar, Estimating historical anthropogenic global sulfur emission patterns for the period 1850–1990, *Atmos. Env.*, *33*, 3435–3444, 1999.

Mylona, S., Sulphur dioxide emissions in Europe 1880–1991 and their effect on sulphur concentrations and depositions, *Tellus*, *48B*, 662–689, 1996.

Myhre, G., A. Myhre, and F. Stordal, Historical evolution of radiative forcing of climate, *Atmos. Env.*, *35*, 2361–2373, 2001.

Olivier, J. G. J., et al., Description of EDGAR Version 2.0: A set of global emission inventories of greenhouse gases and ozone-depleting substances for all anthropogenic and most natural sources on a per country basis and on 1°x1° grid, *National Institute of Public Health and the Environment (RIVM) report no. 771060 002 / TNO-MEP report no. R96/119*, 1996.

Örn, G., U. Hansson, and H. Rodhe, *Historical Worldwide Emissions of Anthropogenic Sulfur: 1860–1985*, Report CM-91, Department of Meteorology, Stockolm University, 5 pp. + 15 figures, 1996.

Tang, I. N., and H. R. Munkelwitz, Water activities, densities, and refractive indices of aqueous sulfate and

nitrate droplets of atmospheric importance, *J. Geophys. Res.*, *99*, 18,801–18,808, 1994.

Tegen, I., D. Koch, A. L. Lacis, and M. Sato, Trends in tropospheric aerosol loads and corresponding impact on direct radiative forcing between 1950 and 1990: A model study, *J. Geophys. Res.*, *105*, 26,971–26,989, 2000.

Vestreng, V., and E. Støren, *Analysis of UNECE/EMEP Emission Data*, EMEP/MSC-W Note 1/00, 39 pp., March 2000.

Watts, S. F., The mass budgets of carbonyl sulfide, dimethyl sulfide, carbon disulfide and hydrogen sulfide, *Atmos. Env. 34*, 761–779, 2000.

Chapitre 5

Sensibilité du cycle du DMS atmosphérique et de l'effet indirect des aérosols soufrés à la représentation de la source de DMS et de son oxydation

Ce chapitre reprend l'article de *Boucher et al.* [2003] accepté au journal *Atmospheric Chemistry and Physics* (une première version a été publiée au journal électronique *Atmospheric Chemistry and Physics Discussions*).

DMS atmospheric concentrations and sulphate aerosol indirect radiative forcing: a sensitivity study to the DMS source representation and oxidation

O. Boucher[1], C. Moulin[2], S. Belviso[2], O. Aumont[3], L. Bopp[3], E. Cosme[4], R. von Kuhlmann[5], M. G. Lawrence[5], M. Pham[6], M. S. Reddy[1], J. Sciare[2], C. Venkataraman[7]

[1] Laboratoire d'Optique Atmosphérique, CNRS UMR 8518, USTL, Villeneuve d'Ascq, France
[2] Laboratoire des Sciences du Climat et de l'Environnement, CEA / CNRS, Gif sur Yvette, France
[3] Laboratoire d'Océanographie Dynamique et de Climatologie, CNRS / UPMC / IRD, Paris, France
[4] Laboratoire de Glaciologie et Géophysique de l'Environnement, CNRS, Saint-Martin-d'Hères, France
[5] Max Planck Institute for Chemistry, Air Chemistry Department, Mainz, Germany
[6] Service d'Aéronomie, CNRS / UPMC / UVSQ, Paris, France
[7] Centre for Environmental Science and Engineering, Indian Institute of Technology, Bombay, India

Abstract. The global sulphur cycle has been simulated using a general circulation model with a focus on the source and oxidation of atmospheric dimethylsulphide (DMS). The sensitivity of atmospheric DMS to the oceanic DMS climatology, the parameterisation of the sea-air transfer and to the oxidant fields have been studied. The importance of additional oxidation pathways (by O_3 in the gas- and aqueous-phases and by BrO in the gas phase) not incorporated in global models has also been evaluated. While three different climatologies of the oceanic DMS concentration produce rather similar global DMS fluxes to the atmosphere at 24–27 Tg S yr^{-1}, there are large differences in the spatial and seasonal distribution. The relative contributions of

OH and NO_3 radicals to DMS oxidation depends critically on which oxidant fields are prescribed in the model. Oxidation by O_3 appears to be significant at high latitudes in both hemispheres. Oxidation by BrO could be significant even for BrO concentrations at sub-pptv levels in the marine boundary layer. The impact of such refinements on the DMS chemistry onto the indirect radiative forcing by anthropogenic sulphate aerosols is also discussed.

1 Introduction

Although a lot is now understood about the global sulphur cycle, some uncertainties remain, in particular about the emission strength of dimethylsulphide (DMS). The DMS-cloud albedo-climate feedback loop proposed by Shaw (1983) and Charlson et al. (1987) generated many studies, but it is still not clear whether this feedback mechanism involving the biosphere, the ocean, and the atmosphere has played an important role in past climates, and whether it can play a role in future climate change (Bopp et al., 2002, 2003). Several modelling studies attempted to model the global distribution of DMS (e.g., Chin et al., 1998; Sciare et al., 2000b). Recently Jones et al. (2001) showed in a global model study that using the parameterisation of DMS sea-air exchange of Wanninkhof (1992) instead of Liss and Merlivat (1986) results into a doubling of the DMS emission flux and a 25% reduction in the indirect radiative forcing due to anthropogenic sulphate aerosols. This is because the increase in the DMS flux causes an increase in the concentration of sulphate aerosol, thus reducing the cloud susceptibility to anthropogenic aerosols. Nightingale et al. (2000) found that observations of the sea-air exchange rate scatter between the two above-mentioned parameterisations and suggested a revised parameterisation which will be used in the present study.

The estimation of the yield of SO_2 from DMS oxidation is one of the critical points required to evaluate the relative contribution of DMS in the marine sulphate aerosols. Whereas the OH radical is clearly identified as a major DMS oxidant in the atmosphere, strong uncertainties still remain in the estimation of SO_2 yields from the DMS+OH reaction. Another uncertainty in the SO_2 yield from the DMS oxidation concerns the role played by other radicals than OH, and especially nitrate (NO_3) and bromide oxide (BrO) radicals for the most important. Contrary to the reaction DMS+OH which proceeds by two different pathways (the H-abstraction channel leading to SO_2 and the OH-addition channel leading to dimethylsulphoxide (DMSO)), DMS oxidising mechanisms with NO_3 and BrO only proceed through the addition channel leading to DMSO for BrO radicals and the H-abstraction channel leading to SO_2 for NO_3 radicals. Unlike the DMS oxidation by OH, there is no uncertainty in the SO_2 yield from the DMS oxidation by NO_3 and BrO radicals. However, the role of these radicals on the fate of DMS remains elusive since no field experiments were carried out with simultaneous measurements of atmospheric DMS, and BrO and NO_3 radicals. The atmospheric fate of DMSO is also uncertain. If DMSO is preferentially oxidised to methanesulfonic acid (MSA), the production of SO_2 and sulphate aerosols in the clean MBL will be less than presently thought.

The aqueous-phase reaction of DMS and O_3 expected to occur in cloud droplets, has been indicated to be of atmospheric importance (Lee and Zhou, 1994; Gershenzon et al., 2001). This reaction, as well as that in the gas phase, is usually not considered in global models of the sulphur cycle. Campolongo et al. (1999) stressed the importance of multiphase chemistry for determining accurately the latitudinal dependence of the MSA to nss-SO_4^{2-} ratio but did not estimate its importance for DMS oxidation itself. As mentioned above, there are also several indications that reaction with BrO can be a significant loss of DMS in the marine boundary layer (MBL) during daytime. This was first suggested by Toumi (1994) based on box model calculations. Sciare et al. (2000a) found from simultaneous measurements of sea-water and atmospheric DMS, OH radicals, and the boundary layer height that the diurnal variation of gas-phase DMS in the Tropical Atlantic Ocean could not be explained by the oxidation with OH alone. They state that 3 pptv of BrO prescribed during daytime could resolve the discrepancy. Similar problems with too strong measured diurnal variation of DMS compared to model calculations with standard chemistry were also found by Yvon et al. (1996). Box model calculations based on recent kinetic data emphasize the possible strong effects of BrO on DMS and DMSO concentrations (Ingham et al., 1999). Recently, von Glasow et al. (2002) calculated with a 1D model that consideration of BrO increases the DMS oxidation rate by 63% for remote MBL conditions. However, a large uncertainty is associated with the amount and speciation of inorganic bromine, Br_x, in the MBL.

In this paper we use three different distributions of the oceanic DMS concentrations, two parameterisations of the sea-air transfer function, and two distributions of atmospheric oxidants to predict the atmospheric fate of DMS and its impact on the sulphur cycle. We also test the importance of the three additional above-mentioned

Table 1: Characteristics of the experiments performed in this study.

Experiment	Sea-air transfer function	Oxidant fields	Oceanic DMS climatology	Additional DMS oxidation
EXP1	Nightingale et al. (2000)	IMAGES model	Kettle and Andreae (2000)	No
EXP2	Nightingale et al. (2000)	IMAGES model	Belviso et al. (2002)	No
EXP3	Nightingale et al. (2000)	IMAGES model	Aumont et al. (2002)	No
EXP4	Liss and Merlivat (1986)	IMAGES model	Kettle and Andreae (2000)	No
EXP5	Nightingale et al. (2000)	MATCH model	Kettle and Andreae (2000)	No
EXP6	Nightingale et al. (2000)	IMAGES model	Kettle and Andreae (2000)	DMS+O_3 gas / aqueous
EXP7	Nightindale et al. (2000)	IMAGES model	Kettle and Andreae (2000)	DMS + BrO

DMS oxidation pathways.

2 Description of the models and experiments

2.1 Sulphur cycle model

We use here a model of the global sulphur cycle developed in the framework of the general circulation model of the Laboratoire de Météorologie Dynamique, LMD-ZT. This model is fully described and evaluated in Boucher et al. (2002). It has been used in Boucher and Pham (2002) to predict the evolution of the sulphur cycle from 1850 to 1998 and by Cosme et al. (2002) to study the sulphur cycle in the high southern latitudes. Only aspects relevant to DMS sources and sinks and SO_2 oxidation are repeated here.

DMS is emitted using the sea to air parameterisation of Liss and Merlivat (1986) or Nightingale et al. (2000). It is oxidised in the gas phase by OH and NO_3 radicals. While the oxidation of DMS by NO_3 only produces SO_2, the oxidation by OH produces both SO_2 and DMSO through the addition channel and only SO_2 through the abstraction channel. DMSO is oxidised in the gas-phase by OH to produce SO_2 (60%) and MSA (40%) and is also subject to in-cloud and below-cloud scavenging (Boucher et al., 2002). No heterogeneous sink for DMS and DMSO is included. Sulphur dioxide, SO_2, is oxidised in the gas phase by OH and in the aqueous phase by O_3 and H_2O_2. All reaction rates are given in Boucher et al. (2002).

The monthly concentrations of all oxidants except H_2O_2 are prescribed from the IMAGES (Pham et al., 1995) or the MATCH-MPIC (von Kuhlmann, 2001) chemical transport models. The diurnal variations of the oxidant fields are taken from the IMAGES model only and are applied in LMD-ZT with a timestep of 30 minutes. Hydrogen peroxide, H_2O_2, is predicted interactively in the model from prescribed HO_2 concentrations and H_2O_2 photodissociation rates. It also undergoes dry and wet scavenging and is depleted upon SO_2 oxidation, as described in Boucher et al. (2002).

2.2 Experiment design

Our model runs are for 18 months and we present results for the last 12 months. All runs are for the same meteorology so the differences in the runs are only due to differences in the DMS emission or oxidation. The indirect radiative forcing due to sulphate aerosols is estimated as the difference in top-of-atmosphere radiative fluxes obtained in two simulations with and without the anthropogenic emissions of sulphur species, but with the same oxidant fields (except H_2O_2). We follow Boucher and Lohmann (1995) and Boucher and Pham (2002) to estimate the cloud properties from the sulphate mass concentration. This calculation is only diagnostic and therefore only includes the first indirect effect (change in cloud optical properties for a fixed liquid water content). Our estimate is for sulphate aerosols only, but to some extent sulphate aerosols can be used as a proxy for the total anthropogenic aerosol. While improvements on the parameterisation of the aerosol indirect effects are desirable (Lohmann et al., 2000), our parameterisation is still useful to perform the sensitivity experiments of the present study.

Table 1 gives the list and characteristics of the seven experiments performed in this study. EXP1 is our baseline experiment. The sensitivity to the oceanic DMS distribution is evaluated from simulations EXP1, EXP2, and EXP3. The role of the sea-air transfer function is examined by comparing EXP1 and EXP4. EXP1 and EXP5 can be used to estimate the sensitivity of the results to the prescribed oxidant distributions. Finally, the importance of three more pathways for DMS oxidation, not yet incorporated in global models, is investigated in the simulations EXP6 and EXP7.

2.3 Oceanic DMS datasets

We test here three different distributions of the oceanic DMS. The first one is the updated climatology of Kettle and Andreae (2000) which is derived from a compilation of measurements of DMS in the sea water and an interpolation procedure in regions where no data are

Fig. 1: Spatial distribution of the annually-averaged oceanic DMS flux (mg S m^{-2} yr^{-1}) from EXP1, EXP2, EXP3, and EXP4 (from top to bottom).

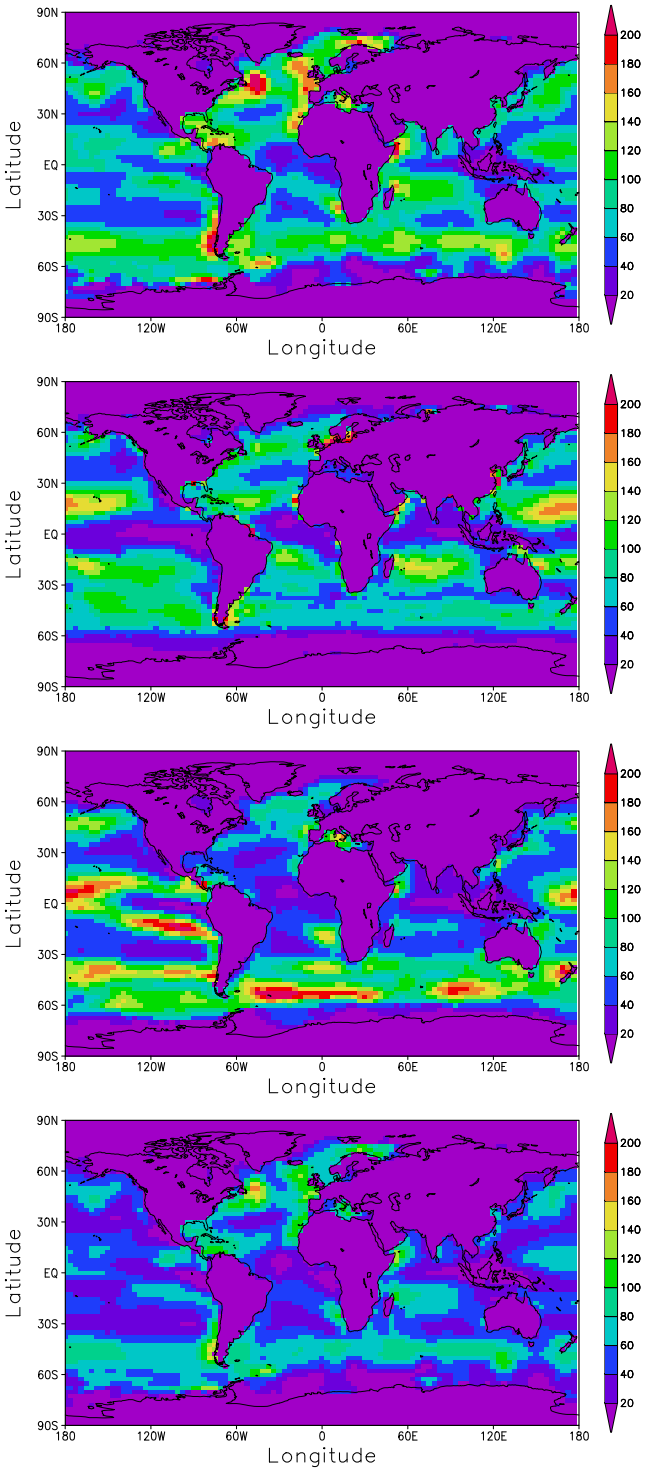

available (Kettle et al., 1999). In this sense the seasonal variability of DMS in the mid and high latitudes of the Southern Hemisphere is better constrained in the spring and summer seasons than in autumn and winter (Curran and Jones, 2000). This climatology is widely used in global models of the sulphur cycle (e.g., Jones et al., 2001; Boucher and Pham, 2002). It is used here in the baseline experiment (EXP1) as well as in EXP4, EXP5, EXP6, and EXP7. The work of Belviso et al. (2002) forms the basis for our second dataset and is used in EXP2. The global distribution of oceanic DMS concentration is estimated from the 1998–2001 SeaWiFS (satellite-based) measurements of the sea-surface chlorophyll *a* (Chl *a*) content and from a phytoplanktonic community structure index which are then empirically linked to the DMS concentration. In EXP2, the phytoplanktonic community structure index is a non-linear function of Chl *a*, so that sea surface DMS concentration was computed solely from the SeaWiFS ocean color measurements. The oceanic DMS concentration is prescribed globally as monthly means based on a four-year climatology with the reservations that (1) a minimum value of 0.2 nmol l^{-1} is assumed in regions where no SeaWiFS data are available in particular at high latitudes in wintertime due to the low insolation and in areas covered of ice, and (2) a maximum value of 50 nmol l^{-1} is also introduced to overcome the few unrealistic values obtained at very large Chl *a* content in coastal waters. Our third DMS climatology, used in EXP3, originates in the modelling work of Aumont et al. (2002). In this study the DMS concentration in sea water is derived from the concentration of Chl *a* and the phytoplanktonic community structure index which are both independently calculated by a global 3-D ocean carbon cycle model. Moreover, the diagnostics of DMS concentrations used by Belviso et al. (2002) and by Aumont et al. (2002) are slightly different.

2.4 Oxidant fields

Oxidant fields from the IMAGES model are used in all experiments except EXP5 in which we use instead the oxidant fields from MATCH-MPIC. The major features of IMAGES are described in Müller and Brasseur (1995) and references herein. The IMAGES model calculates the distribution of about 60 species, including O_3, HO_x, NO_x, sulfur oxides, acetone, methane, non-methane hydrocarbons (NMHC: ethane, ethylene, propylene, isoprene, α-pinene, propane, and *n*-butane as a surrogate for the other higher hydrocarbons) and their degradation products. Heterogeneous reactions of NO_3 and N_2O_5 on prognostic sulfate distributions are taken into account. The model uses emissions described in Müller and Brasseur (1995) except for fossil fuel emis-

Fig. 2: Zonally- and annually-averaged oceanic DMS flux (mg S m^{-2} yr^{-1}).

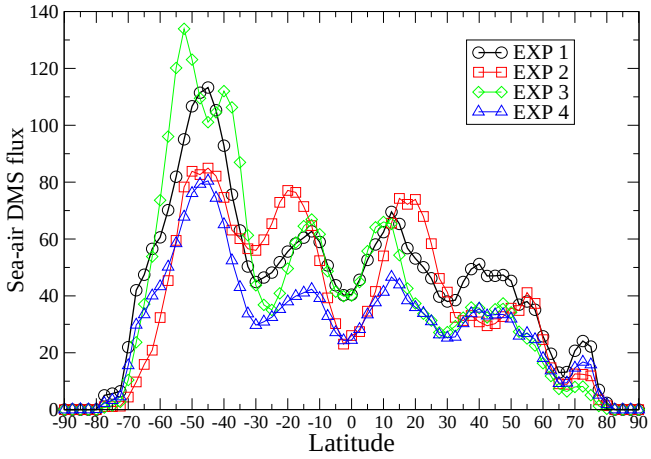

Fig. 3: Seasonal variation of the oceanic DMS flux (Tg S yr^{-1}) averaged over the Northern Hemisphere (top) and the Southern Hemisphere (bottom).

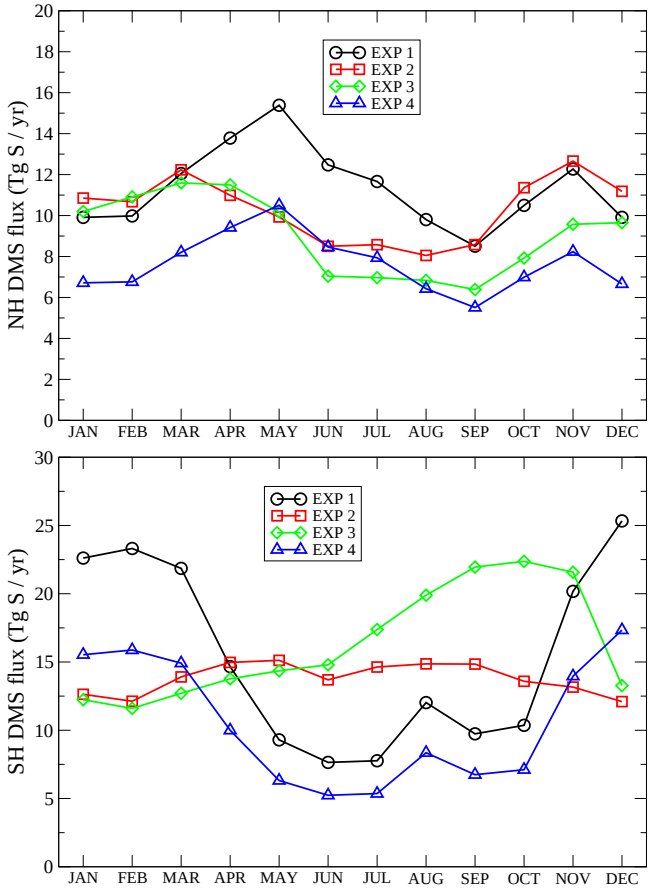

sions of SO_x and NO_x, as well as biogenic continental emissions of NMHC and NO_x, where GEIA inventories have been used, and for biomass burning (Granier et al., 1996) and lightning (Pickering et al., 1998; Price et al., 1997). In this version, no emissions from ocean-going ships have been included.

The model MATCH-MPIC includes up to C5-hydrocarbon chemistry (ethane, propane, ethene, propene, isoprene, higher alkane surrogate) and uses up-to-date emissions mostly from EDGAR or GEIA inventories. Emissions from ocean-going ships represent an additional source of 2.6 Tg N yr^{-1} and follow the distribution of Corbett et al. (1999). Heterogeneous reaction of N_2O_5 on sulphate aerosols is included based on monthly mean fields from Dentener and Crutzen (1993). Further details are described in von Kuhlmann (2001) and Lawrence et al. (1999).

2.5 Additional oxidation pathways

In EXP6, we further consider oxidation of atmospheric DMS by ozone in gas and aqueous phase. While the photochemical sources and sinks of OH and NO_3 radicals are such that the OH reaction occurs during daytime and the NO_3 reaction at night, the aqueous phase ozone reaction would occur during both periods. The reaction was recently investigated as a function of temperature (274–300 K), over a significant range of gas densities from about 10^{15} to 10^{16} cm^{-3} (Gershenzon et al., 2001). The temperature-dependent, second-order aqueous reaction constant was estimated as $5.3\ 10^{12} \exp(-2600/T)$ M^{-1} s^{-1}, and was about six orders of magnitude larger than the corresponding gas-phase rate constant. For this latter rate constant we use the upper limit given by Martinez and Herron (1978) of $5\ 10^{2}$ M^{-1} s^{-1} (or $8.3\ 10^{-19}$ cm^3 $molec^{-1}$ s^{-1}). The concentrations of DMS and O_3 in the cloud phase are computed assuming Henry's law equilibrium. Note finally that the gas-phase reaction with O_3 produces SO_2 only, while the aqueous-phase reaction with O_3 produces DMSO only.

In order to get an indication of the importance of the oxidation of DMS by BrO a simple sensitivity simulation is performed. In the EXP7 experiment we specify a constant mixing ratio for BrO of 1 pptv during daytime in the first four model layers (i.e., up to an altitude of approximately 1.3 km) and zero elsewhere and at night. This value is essentially below the detection limit of current measurement techniques, and has been found to be exceeded in some instances (e.g., Hausmann and Platt, 1994; Hebestreit et al., 1999). Typical mixing ratios of a few pptv have been calculated in other modeling studies (Toumi, 1994; Ingham et al., 1999; von Glasow et al., 2002) and were also supported by the study of Sciare

Fig. 4: Annually-averaged atmospheric DMS mixing ratio (pptv) at the surface from EXP1, EXP2, EXP3, and EXP4 (from top to bottom).

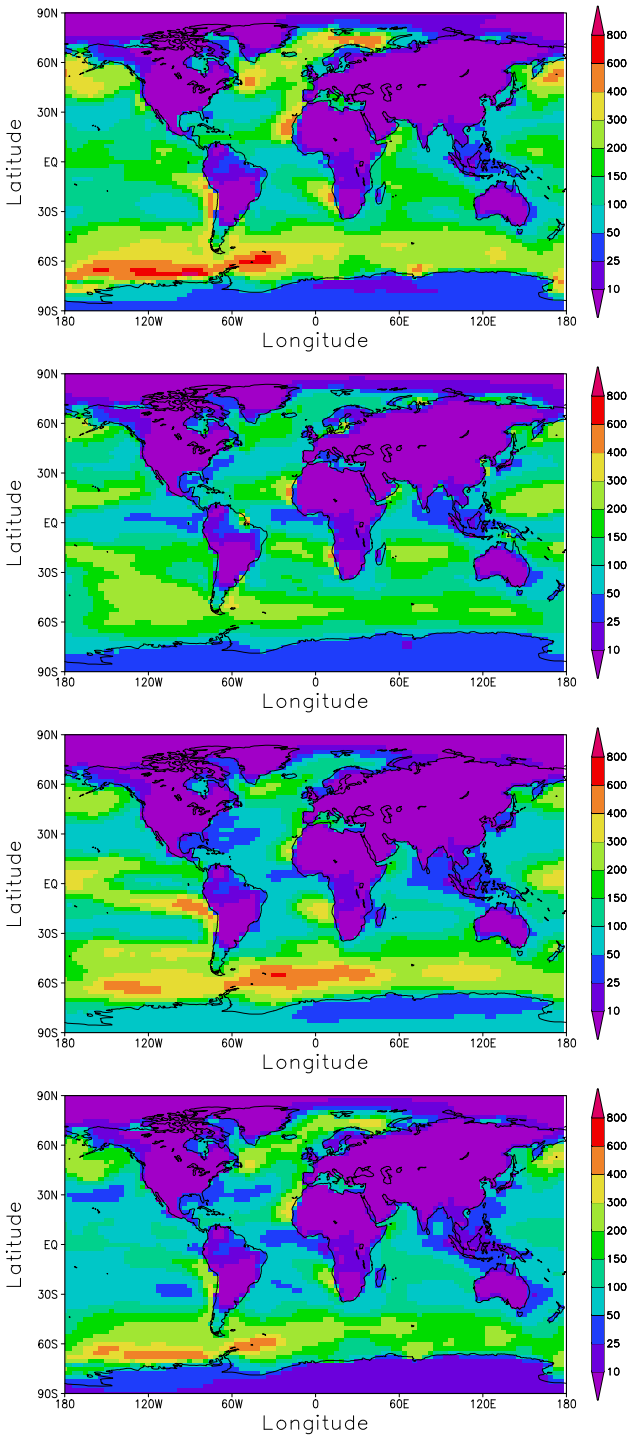

et al. (2000a). The rate constant of $1.3\,10^{-14}\,\exp(1033/T)$ $\mathrm{cm^3\ molec^{-1}\ s^{-1}}$ used here has been determined by Nakano et al. (2001) and is in agreement with the value obtained by Ingham et al. (1999) at 298 K. The temperature dependence is somewhat stronger than the recommendation in DeMore et al. (1997). The oxidation of DMS by BrO produces only DMSO (Ingham et al., 1999).

3 Results and discussion

3.1 DMS flux to the atmosphere

Using the sea-air parameterisation of Nightingale et al. (2000) and the wind fields of the LMD-ZT model the three DMS datasets considered here produce global DMS fluxes of 24–27 Tg S $\mathrm{yr^{-1}}$. Our total emission rates for DMS are significantly larger than those of Koch et al. (1999), Barth et al. (2000), and Chin et al. (2000), which are 10.7, 15.5, and 13.3 Tg S $\mathrm{yr^{-1}}$, respectively, and were obtained using different methodologies or DMS concentration fields. Although significantly larger due to the choice of the Nightingale et al. (2000) parameterization, our emission rates are within the range of 10 to 40 Tg S $\mathrm{yr^{-1}}$ usually accepted for DMS emissions (Penner et al., 2001).

There are however significant disagreements in the spatial (Figs. 1 and 2) and seasonal (Fig. 3) distributions of the DMS flux. There are patches of large DMS flux in the North Atlantic ocean in the EXP1 simulation (Kettle and Andreae, 2000) which do not exist in EXP2 and EXP3. One can also note that the Aumont et al. climatology (EXP3) produces a more inhomogeneous DMS flux. However, the zonal averages of the DMS flux exhibit similar behaviours in the first three experiments, with minima and maxima positioned at about the same latitudes (Fig. 2). Fig. 3 shows the seasonal variations of the hemispherically-averaged DMS fluxes. The differences are particularly large in the Southern Hemisphere. The DMS flux from the Kettle and Andreae database (EXP1) exhibits a large seasonal cycle with low emissions during May to July, whereas the DMS flux predicted using the SeaWiFS data (EXP2) has a rather flat seasonal variation. The DMS flux from Aumont et al. (EXP3) exhibits a maximum in September–October when Kettle and Andreae (2000) predict a secondary minimum. In the Northern Hemisphere, the three climatologies produce more consistent DMS fluxes.

Using the less sophisticated parameterisation of Liss and Merlivat (1986) instead of Nightingale et al. (2000) decreases the global DMS flux from 26.8 to 18.2 TgS $\mathrm{yr^{-1}}$ for the Kettle and Andreae (2000) climatology. The reduction in flux is uniformly distributed throughout the year (Fig. 3). These results are quantitatively consistent with those of Jones et al. (2001).

Fig. 5: Comparison of simulated and measured atmospheric mixing ratios (pptv): a) DMS at Amsterdam Island (37.83° S 77.50° E; data from Sciare et al., 2000b), b) SO_2 at Amsterdam Island (data from Putaud et al., 1992), and c) DMS at Cape Grim (40.68° S 144.68° E; data from Ayers et al., 1991).

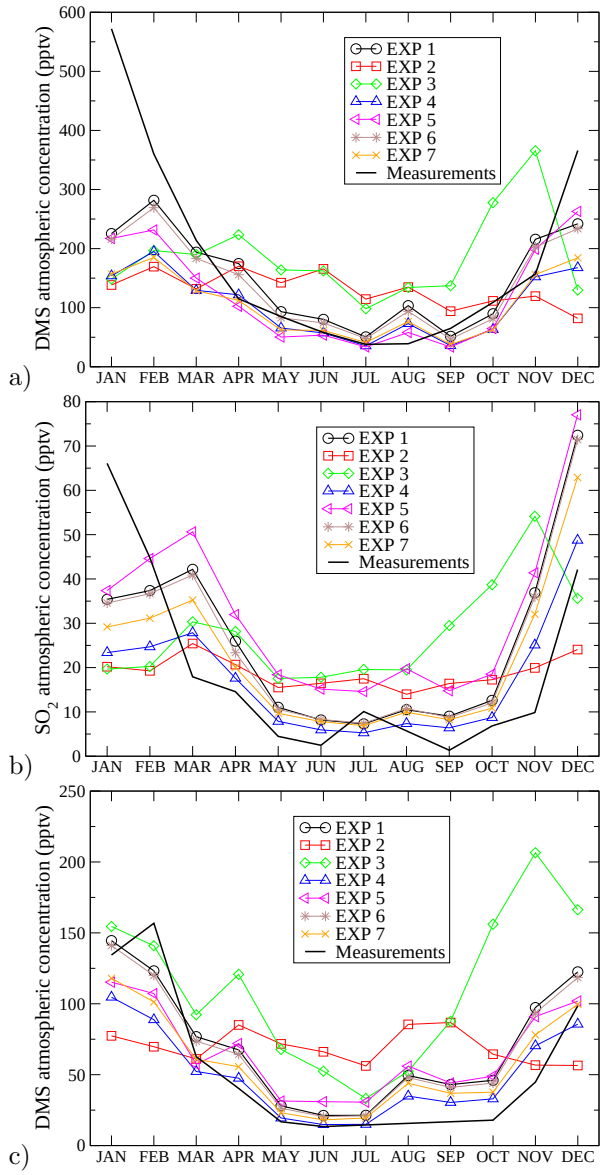

3.2 Atmospheric DMS concentrations

Fig. 4 shows the spatial distribution of DMS mixing ratio at the surface in the EXP1, EXP2, EXP3, and EXP4 experiments. Once again significant differences can be observed. In contrast to EXP2, EXP1 shows among the largest annually-averaged DMS mixing ratios south of 60°S and more specifically in the Pacific sector of the seasonal ice zone (Bellingshausen Sea) where the phytoplanktonic biomass during summer is among the lowest of the Southern Ocean according to SeaWiFS observations. In fact DMS rich waters occupy a small portion of the Bellingshausen Sea (Turner et al., 1995). In EXP1, these large concentrations result from the assimilation methodology of Kettle and Andreae which applies in this region large oceanic DMS levels from other biogeochemical provinces. The relatively low levels of atmospheric oxidants also contribute to enhance the concentrations of atmospheric DMS.

There are few long-term measurements of atmospheric DMS concentrations. We compare here the modelled atmospheric DMS and SO_2 mixing ratios to measurements made at Amsterdam Island in the Southern Ocean (Fig. 5a and b). The EXP1 predicted concentrations and seasonal variations appear to be in reasonable agreement with measured values. However the very large concentrations during the January month is not reproduced by any of the model experiments. EXP2 and EXP3 do not perform well at Amsterdam Island. We already know that Kettle and Andreae (2000) and SeaWiFS DMS datasets are much better constrained in the Northern than in the Southern Hemisphere because most of the in-situ Chl *a* and DMS measurements used to generate the climatology (Kettle and Andreae, 2000) or to estimate the DMS to Chl *a* relationship (Belviso et al., 2002) were performed in northern oceans. In the Indian sector of the Southern Hemisphere, the SeaWiFS DMS dataset is much better constrained by observations in August than in December (Belviso et al., 2002). This is also reflected in Fig. 5a where the agreement between EXP1 and EXP2 (and also EXP3) is better in August than in December. In May, June, July, and September, the marine fields of DMS are poorly constrained by observations. So it is in August when marine data offer the best opportunity to investigate the winter photochemistry of DMS. At Cape Grim EXP1 performs better than EXP2 and EXP3 (Fig. 5c). This does not imply that EXP1 would also perform better at lower or higher latitudes of the Southern Ocean, where the DMS concentrations are less constrained by actual measurements.

We also compare in Fig. 6 the monthly-mean DMS mixing ratios simulated by the model with the mixing ratios measured during the Albatross cruise in the Atlantic Ocean (Sciare et al., 2000a). At most latitudes the observed values lie within the variability simulated by the model, with a noticeable exception in the 30–40°N transect where the observed peak in concentration is not reproduced. This peak is due to the transport of air masses from further south at 20–30°N (Sciare et al.,

Table 2: Characteristics of the global DMS budget and sulphate aerosol indirect radiative forcing (RF) in the seven experiments. Emission fluxes and oxidation rates are given in Tg S yr^{-1}, burdens in Tg S, residence times in days, and RF in Wm^{-2}. In parenthesis are the percentage contributions to the sources and sinks of DMS.

	EXP1	EXP2	EXP3	EXP4	EXP5	EXP6	EXP7
Oceanic DMS emission flux	26.8* (99%)	24.1 (99%)	25.4 (99%)	18.2 (98%)	26.8 (99%)	26.8 (99%)	26.8 (99%)
Oceanic DMS emission flux (NH)	11.4* (42%)	10.3 (42%)	9.1 (35%)	7.6 (41%)	11.4 (42%)	11.4 (42%)	11.4 (42%)
Oceanic DMS emission flux (SH)	15.4* (57%)	13.8 (57%)	16.3 (64%)	10.6 (57%)	15.4 (57%)	15.4 (57%)	15.4 (57%)
Continental DMS emission flux	0.3 (1%)	0.3 (1%)	0.3 (1%)	0.3 (2%)	0.3 (1%)	0.3 (1%)	0.3 (1%)
Oxidation by OH to SO_2	15.5 (57%)	13.1 (53%)	13.8 (53%)	10.5 (57%)	9.0 (33%)	14.1 (52%)	10.6 (39%)
Oxidation by NO_3 to SO_2	7.7 (29%)	8.2 (34%)	8.4 (33%)	5.4 (29%)	15.7 (58%)	7.0 (26%)	6.2 (23%)
Oxidation by OH to DMSO	3.9 (14%)	3.1 (13%)	3.5 (14%)	2.6 (14%)	2.4 (9%)	3.4 (13%)	2.5 (9%)
Oxidation by O_3 (gas phase)	–	–	–	–	–	0.9 (3%)	–
Oxidation by O_3 (aqueous phase)	–	–	–	–	–	1.7 (6%)	–
Oxidation by BrO	–	–	–	–	–	–	7.8 (29%)
DMS burden	0.084	0.075	0.089	0.058	0.060	0.071	0.054
DMS residence time	1.1	1.1	1.2	1.1	0.8	0.9	0.7
Sulphate burden	0.748	0.733	0.731	0.682	0.717	0.742	0.715
Sulphate aerosol indirect RF	−0.99	−1.07	−1.12	−1.15	−0.97	−1.00	−1.04

* The oceanic fluxes of DMS obtained using the earlier version of the climatology (Kettle et al., 1999) are 27.9, 12.8, and 15.1 Tg S yr^{-1} for the globe, the NH, and the SH, respectively.

2000a) and these particular meteorological conditions are not simulated here.

From these comparisons we see that it is difficult to establish which DMS climatology performs best. This clearly points to the need for more numerous continuous long-term measurements of atmospheric DMS in the North Atlantic Ocean and elsewhere.

3.3 Atmospheric DMS budget: OH versus NO_3 oxidation

Table 2 summarises the global annual atmospheric budget of DMS. The different spatial and temporal distributions of DMS emissions result in a different partitioning of DMS oxidation, with a slightly larger role played by NO_3 oxidation in the case of the SeaWiFS and Aumont et al. DMS source (8.24 and 8.42 Tg S yr^{-1} in EXP2 and EXP3, respectively) compared to the Kettle and Andreae (2000) case (7.75 Tg S yr^{-1} in EXP1).

There are significant differences in the DMS oxidation if the oxidant fields are prescribed from the MATCH-MPIC model (EXP5) or from the IMAGES model (EXP1). The relative contributions of DMS+OH and DMS+NO_3 pathways are opposite. This results from similar distributions of OH radical but very different distributions of the NO_3 radical over the oceans between the two chemical models (Fig. 7). These differences remain unresolved at the moment but may be due to different treatments of NMHCs and/or NO_3 heterogeneous sink in the two models. The larger contribution of NO_3 to DMS oxidation in EXP5 is accompanied by a significant decrease in the DMS burden and lifetime (0.060 Tg S and 0.8 day in EXP5 compared to 0.084 Tg S and 1.1 day in EXP1). The decrease in DMS concentration in EXP5 compared to EXP1 occurs throughout the troposphere (Fig. 8a) but it is more pronounced in the 0–30°N latitude band and above 100 hPa.

3.4 Atmospheric DMS budget: importance of new additional oxidation pathways

In EXP6, the gas- and aqueous-phase oxidations of DMS by O_3 account for 3.5 (upper limit) and 6.2% of the total DMS oxidation rate, respectively. The aqueous-phase reaction contributes 15–30% over the regions north to 60°N and in the 50–75°S latitude band over the oceans (Fig. 9a). This reaction plays an important role in regions with significant cloud liquid water content and low concentrations of OH and NO_3 radicals. The gas-phase reaction contributes mostly over Antarctica where no other efficient oxidation pathway is present (Fig. 9b). These additional pathways result in DMS concentrations which are up to 50% smaller at high latitudes and 10–30% smaller at low and middle latitudes (Fig. 8b).

In order to assess the possible limitation on the DMS+O_3 aqueous reaction rate from the aqueous diffusion rate of both species, the characteristic diffusion and reaction times were calculated for an average cloud drop diameter of 50 μm, using the DMS and O_3 concentrations obtained between 50–70°N and 50–70°S, where

Fig. 6: Comparison of simulated and measured monthly-mean atmospheric mixing ratios of DMS (pptv) during the Albatross cruise. The model values are averages for the one-month period corresponding to the cruise, with standard deviations of daily means around monthly means. Observations are from Sciare et al. (2000a).

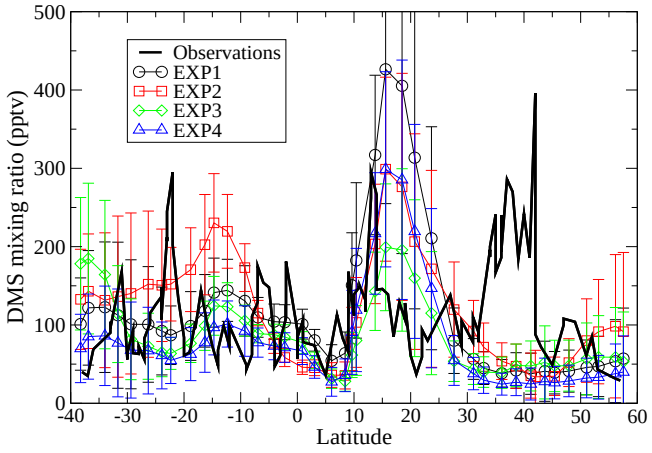

this reaction predominates. Using diffusivities and Henry's constants at 298 K (Gershenzon et al., 2001) for DMS and O_3, the estimated diffusion rates are about 100 times faster than the reaction rate, indicating no diffusion limitation, as also previously reported for the aqueous reactions of SO_2 with O_3 and H_2O_2 (Venkataraman et al., 2001).

Oxidation by BrO is found to be an important sink for DMS in EXP7. Globally it contributes 28.8% to the total DMS oxidation rate, and up to 60% at high latitudes (Fig. 9c) where the concentrations of other oxidants are low. However it should be remembered that this experiment is highly idealised. BrO concentrations are highly variable in space and time, and a uniform mixing ratio of 1 pptv in the MBL is probably an overestimate for some regions or seasons. For instance, the diurnal variations of DMS at Amsterdam Island can be explained with the DMS+OH reaction alone (Sciare et al., 2000c). The EXP7 simulation points to the need for atmospheric measurements of BrO at mixing ratios well below 1 pptv. As pointed out by Ingham et al. (1999) simultaneous measurements of DMS and DMSO can also provide indirect evidence for the importance of BrO. In fact, Nowak et al. (2001) report such measurements and find a DMSO/DMS ratio that is larger than expected if DMSO was only produced from the DMS+OH pathway. However, more data especially at night would be clearly valuable.

Fig. 7: Annually-averaged OH and NO_3 mixing ratios (pptv) at the surface in IMAGES (EXP1) and MATCH-MPIC (EXP5).

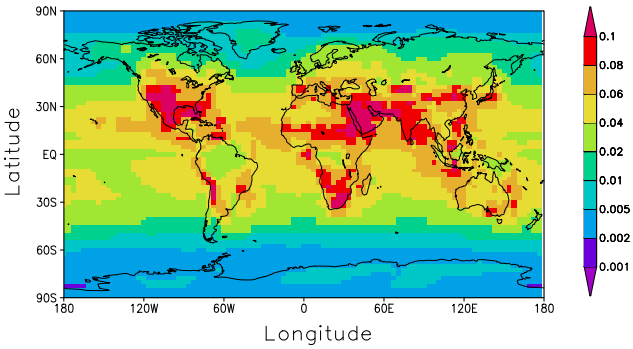

a) IMAGES OH

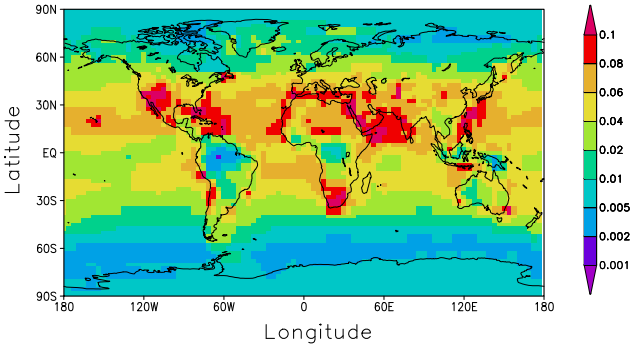

b) MATCH-MPIC OH

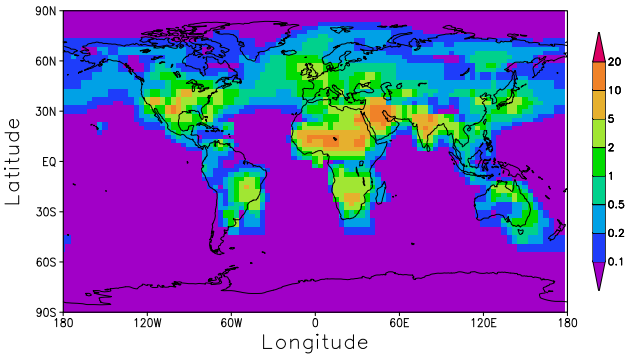

c) IMAGES NO_3

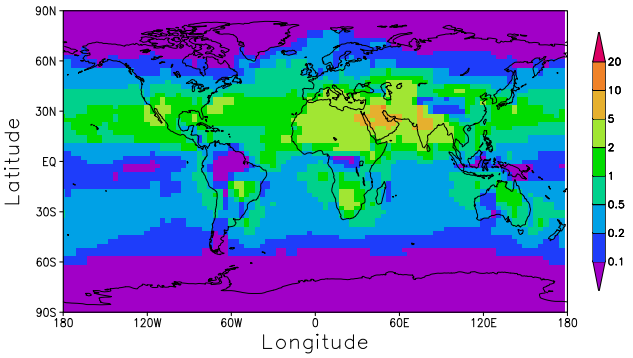

d) MATCH-MPIC NO_3

Fig. 8: Ratio of the zonally- and annually-averaged atmospheric DMS mixing ratio from EXP5, EXP6, and EXP7 to that from EXP1 (from top to bottom).

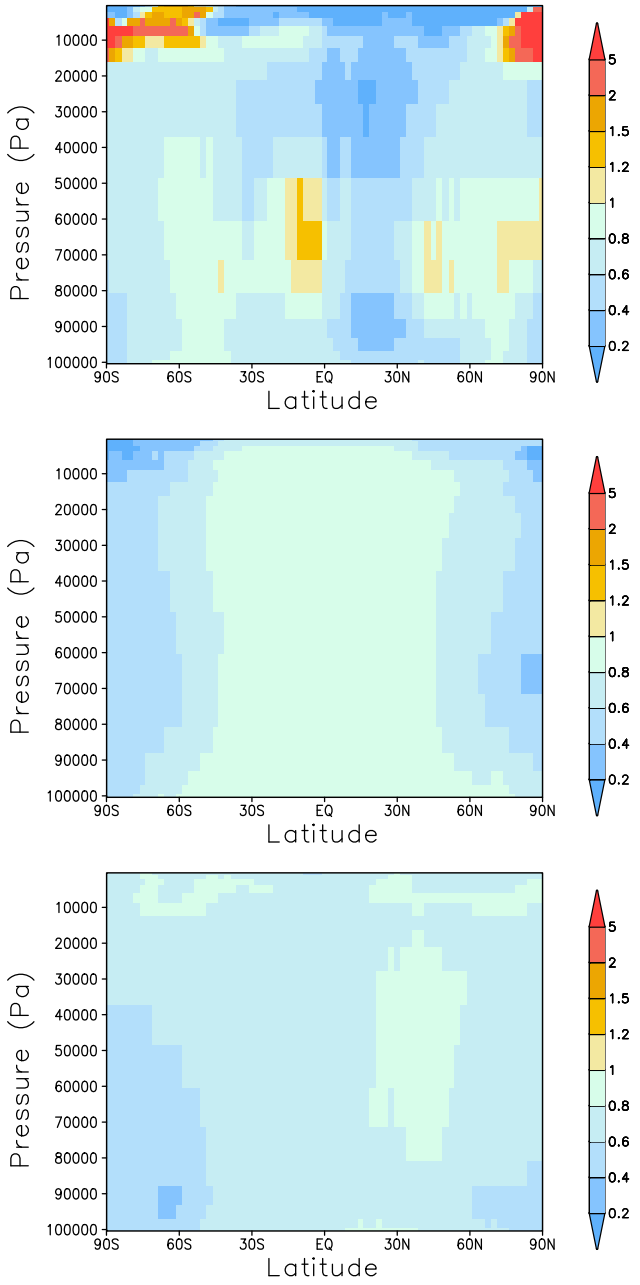

Fig. 9: Relative contribution (%) of the additional oxidation pathways to the vertically-integrated DMS oxidation rate: a) DMS+O_3 in aqueous phase (EXP6), b) DMS+O_3 in gas phase (EXP6), and c) DMS+BrO (EXP7).

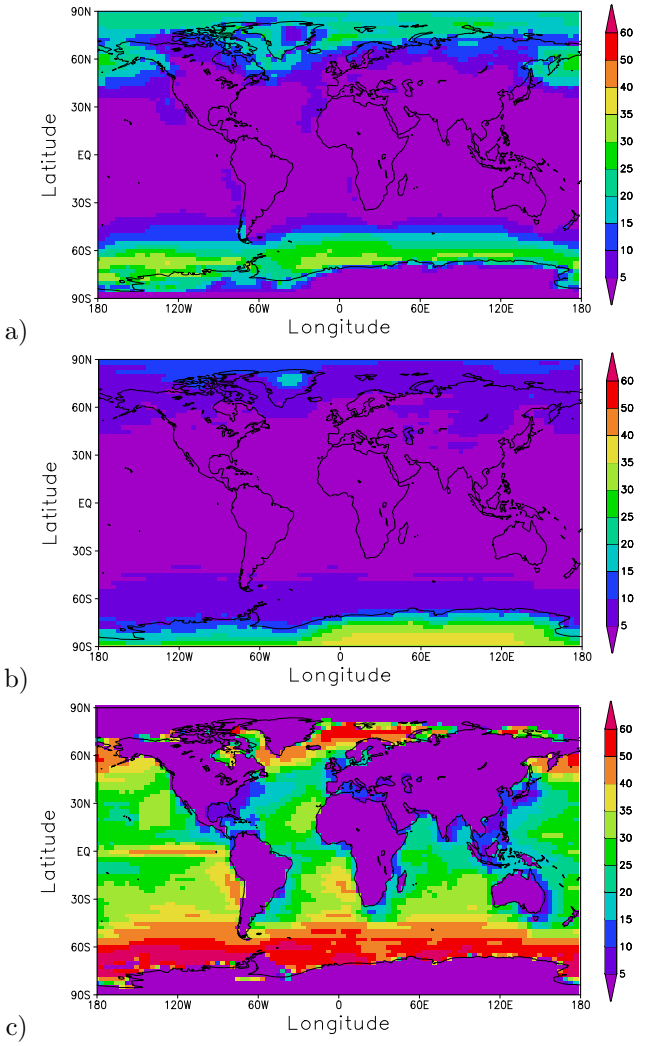

3.5 Production of DMSO

Fig. 10 shows how the DMSO production (as a fraction of the total DMS oxidation) is distributed spatially in EXP1, EXP6, and EXP7 experiments. As expected from the temperature dependences of the DMS+OH reaction rates, a larger fraction of DMS is oxidised in DMSO in the high latitudes (EXP1, Fig. 10a). The asymmetry between the two hemispheres is due to the asymmetry in NO_3 concentrations (Fig. 7c) which oxidise more DMS in SO_2 in the Northern Hemisphere relative to the Southern Hemisphere. Considering the oxidation of DMS by O_3 in the gas- and aqueous-phases (EXP6) leads to enhanced production of DMSO. In this experiment, the fraction of DMS oxidised into DMSO can reach 30 to 40% and 40 to 50% in the high latitudes of the Northern and Southern Hemispheres, respectively (Fig. 10b). The simplified introduction of BrO in our model (EXP7) leads to a very large production of

Fig. 10: Fraction (%) of DMS which is oxidised in DMSO on annual average in EXP1, EXP6, and EXP7 (from top to bottom).

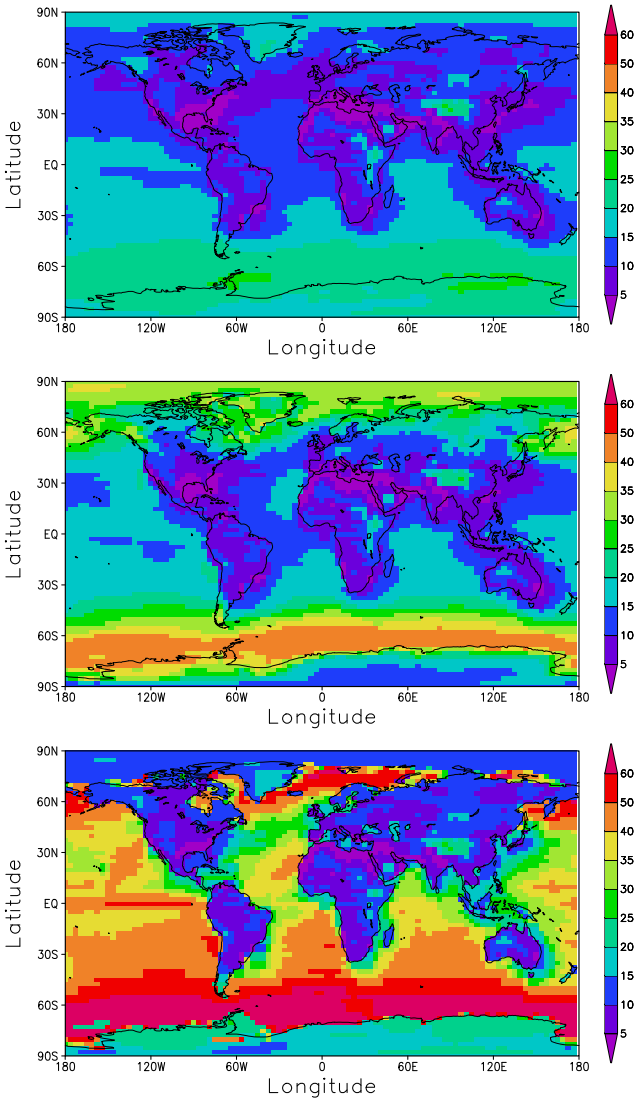

DMSO which can reach more than 60% in the high latitudes of the Southern Hemisphere in agreement with the prescribed temperature dependence of the reaction rate (Fig. 10c). While EXP7 may overestimate the production of DMSO, it is nevertheless important to better understand the atmospheric fate of DMSO and establish whether or not it can contribute significantly to the formation of background sulphate aerosols.

3.6 Indirect radiative forcing of sulphate aerosols

The spatial distribution of the indirect radiative forcing by anthropogenic sulphate aerosols is very similar in all seven experiments. The indirect radiative forcing is

Fig. 11: Spatial distribution of the annually-averaged indirect radiative forcing (Wm^{-2}) by sulphate aerosols for EXP1 (top) and EXP4 (bottom).

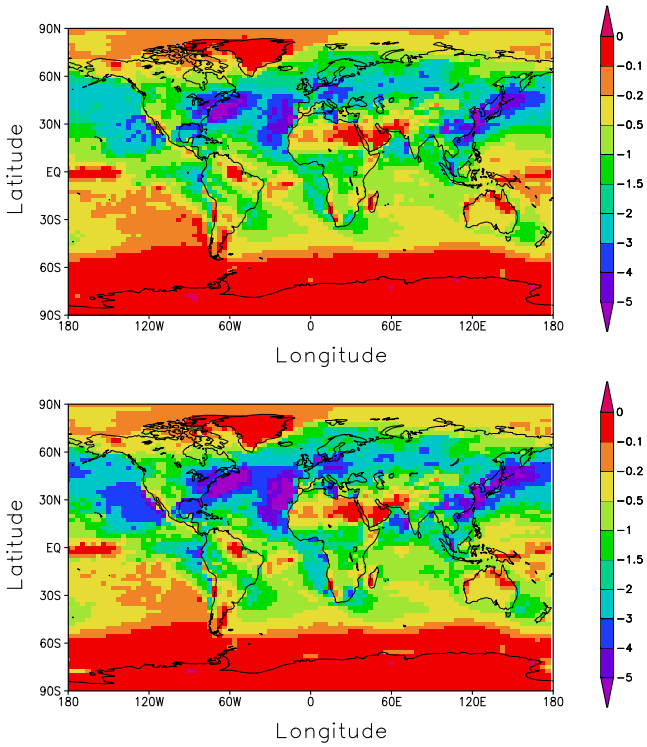

much more sensitive to the assumed relationship between sulphate mass and cloud droplet number concentrations (Boucher and Lohmann, 1995) than the exact distribution of the DMS flux and resulting background sulphate concentration. However, we can estimate the uncertainty in radiative forcing due to uncertainties in the temporal and spatial distributions of the background aerosols (here taken to be sulphate aerosols). The largest difference is between the baseline experiment EXP1 and EXP4 (see Fig. 11). The increase in DMS flux between the EXP4 and EXP1 experiments results in a 14% decrease in radiative forcing. This result is again consistent with that of Jones et al. (2001). It stresses the importance to simulate accurately the concentrations of background accumulation-mode aerosols in the pre-industrial and present-day atmospheres, but also in the future atmosphere when climate change may induce changes in DMS emissions (Bopp et al., 2002, 2003).

4 Conclusions

We tested the sensitivity of the DMS atmospheric budget to the oceanic DMS concentration, the assumed sea-air transfer function, the atmospheric oxidant fields, and additional oxidation paths. The conclusions of the study are the following:

1. Using three different oceanic DMS climatologies results into very similar global DMS fluxes but also into large differences in the spatial and seasonal distribution of the DMS emissions, particularly in the Southern Hemisphere. These differences translate into quite different distributions of atmospheric DMS.

2. Using the more sophisticated parameterisation of DMS sea-air transfer of Nightingale et al. (2000) instead of that of Liss and Merlivat (1986) results in a global DMS flux that is 47% larger and an indirect radiative forcing by sulphate aerosols that is 14% smaller.

3. We found significant differences in the relative contributions of OH and NO_3 to DMS oxidation when using oxidant fields from the IMAGES or MATCH-MPIC chemical transport models. This introduces a significant source of uncertainty in the atmospheric DMS cycle. Measurements of the concentration of NO_3 radical to better constrain the models would be very valuable.

4. Gaseous- and aqueous-phase oxidations of DMS by O_3 are found to contribute 3.5 and 6.2% to the total DMS oxidation, respectively, and up to 30-40% at high latitudes. These reactions should be incorporated in future modelling studies of the sulphur cycle at high latitudes. Note however that we used an upper limit for the reaction rate of DMS by O_3 in gaseous phase, the value of which needs to be refined.

5. Assuming a BrO mixing ratio of 1 pptv in the marine boundary layer at day, oxidation of DMS by BrO proved to be a significant sink for DMS at high latitudes. It is therefore important to measure BrO in the marine boundary layer down to a detection limit of $\sim$0.1 pptv.

6. The oxidation of DMS by O_3 in the aqueous phase and by BrO in the gas phase produces only DMSO. Considering these two reactions results in a very different partitioning of the DMS oxidation between SO_2 and DMSO. It is therefore important to better understand the atmospheric fate of DMSO, the importance of heterogeneous sinks, and whether it can contribute to the production of background sulphate aerosols or not (Sciare et al., 2000c).

7. There are very few long-term measurements of atmospheric DMS to evaluate our model. It is not straightforward to select the most realistic simulations from the limited set of atmospheric DMS measurements. This study points to the need for more numerous continuous multi-year measurements of the DMS concentrations not only in seawater and but also in the atmosphere.

Acknowledgements. We thank E. Chapman for providing her sea-air transfer routine. Computer time for this study was provided by the "Institut du Développement et des Ressources en Informatique Scientifique" (IDRIS) of the CNRS. This research proposal is supported by the "Programme National des PROcessus biogéochimiques dans l'Océan et Flux" (PROOF) and the "Programme National de Chimie atmosphérique" (PNCA) of the CNRS. M. S. Reddy acknowledges support from the Indo-French IFCPAR programme and the EU-funded PHOENICS project EVK2-CT-2001-00098. Olivier Boucher would like to thank the hospitality of P. Crutzen, J. Lelieveld, and the Max Planck Institute for Chemistry in Mainz, where part of this study was performed. The "Institut Polaire Français – Paul-Emile Victor" (IPEV) is acknowledged for its support to long-term measurements at the Amsterdam Island. The Laboratoire d'Optique Atmosphérique is an institute of the "Fédération de Recherche" FR1818 of the CNRS.

References

Aumont, O., Belviso, S., and Monfray, P.: Dimethylsulfoniopropionate (DMSP) and dimethylsulfide (DMS) sea surface distributions simulated from a global three-dimensional ocean carbon cycle model, J. Geophys. Res., 107, 10.1029/1999JC000111, 2002.

Ayers, G. P., Ivey, J. P., and Gillett, R. W.: Coherence between the seasonal cycles of dimethyl sulphide, methanesulphonate, and sulphate in marine air, Nature, 349, 404–406, 1991.

Barth, M. C., Rasch, P. J., Kiehl, J. T., Benkovitz, C. M., and Schwartz, S. E.: Sulfur chemistry in the National Center for Atmospheric Research Community Climate Model: Description, evaluation, features, and sensitivity to aqueous chemistry, J. Geophys. Res., 105, 1387–1415, 2000.

Belviso, S., Moulin, C., Bopp, L., Stefels, J.: Assessment of a global climatology of oceanic dimethylsulfide (DMS) concentrations based on SeaWiFS imagery (1998–2001), Can. J. Fish. Aquat. Sci., submitted, 2002.

Bopp, L., Aumont, O., Belviso, S., and Monfray, P.:Potential impact of climate change on marine DMS (dimethylsulfide) emissions, Tellus, 55B, 11–22, 2003.

Bopp, L., Boucher, O., Aumont, O., Belviso, S., Dufresne, J.-L., Monfray, P., and Pham, M.: Will marine dimethylsulfide emissions amplify or alleviate global warming? – A model study, Can. J. Fish. Aquat. Sci., submitted, 2002.

Boucher, O., and Lohmann, U.: The sulfate-CCN-cloud albedo effect: A sensitivity study with two general circulation models, Tellus, 47B, 281–300, 1995.

Boucher, O., and Pham, M.: History of sulfate aerosol radiative forcings, Geophys. Res. Lett., 29, 10.1029/2001GL014048, 2002.

Boucher, O., Pham, M., and Venkataraman, C.: Simulation of the atmospheric sulfur cycle in the Laboratoire de Météorologie Dynamique General Circulation Model. Model description, model evaluation, and global and European budgets, Note scientifique de l'Institut Pierre Simon Laplace, Paris, France, 2002. http://www.ipsl.jussieu.fr/poles/Modelisation/NotesSciences.htm

Campolongo, F., A. Saltelli, N. R. Jensen, J. Wilson, and J. Hjorth, The role of multiphase chemistry in the oxidation of dimethylsulfide (DMS). A latitude dependent analysis, J. Atmos. Chem., 32, 327–356, 1999.

Charlson, R. J., Lovelock, J. E., Andreae, M. O., and Warren, S. G.: Oceanic phytoplankton, atmospheric sulphur, cloud albedo and climate, Nature, 326, 655–661, 1987.

Chin, M., Rood, R. B., Allen, D. J., Andreae, M. O., Thompson, A. M., Lin, S.-J., Atlas, R. M., and Ardizzone, J. V.: Processes controlling dimethylsulfide over the ocean: Case studies using a 3-D model driven by assimilated meteorological fields, J. Geophys. Res., 103, 8341–8354, 1998.

Chin, M., Rood, R. B., Lin, S.-J., Müller, J.-F., and Thompson, A.M.: Atmospheric sulfur cycle simulated in the global model GOCART: model description and global properties, J. Geophys. Res., 105, 24671–24688, 2000.

Corbett, J. J., Fischbeck, P. S., and Pandis, S. N.: Global nitrogen and sulfur inventories for ocean-going ships, J. Geophys. Res., 104, 3457–3470, 1999.

Cosme, E., Genthon, C., Martinerie, P., Pham, M., and Boucher, O.: Sulfur cycle in the high southern latitudes in the LMD-ZT general circulation model, J. Geophys. Res., 107(D23), 4690, doi:10.1029/2002JD002149, 2002.

Curran, M. A., and Jones, G. B.: Dimethyl sulfide in the Southern Ocean: seasonality and flux, J. Geophys. Res., 105, 20451–20459, 2000.

DeMore, W. B., Sander, S. P., Golden, D. M., Hampson, R. F., Kurylo, M. J., Howard, C. J., Ravishankara, A. R., Kolb, C. E., and Molina, M. J.: Chemical kinetics and photochemical data for use in stratospheric modeling, Evaluation Number 12, JPL Publication 97-4, Jet Propulsion Lab., Pasadena, CA, 1997.

Dentener, F. J., and Crutzen, P. J.: Reaction of N_2O_5 on tropospheric aerosols: Impact on the global distributions of NO_x, O_3, and OH, J. Geophys. Res., 98, 7149–7163, 1993.

Gershenzon, M., Davidovits, P., Jayne, J. T., Kolb, C. E., and Worsnop, D. R.: Simultaneous uptake of DMS and ozone on water, J. Physical Chemistry A, 105, 7031–7036, 2001.

von Glasow, R., Sander, R., Bott A., and Crutzen, P. J.: Modeling halogen chemistry in the marine boundary layer. 2. Interactions with sulfur and the cloud-covered MBL, J. Geophys. Res., 107(D17), 4323, doi:10.1029/2001JD000943, 2002.

Granier, C., Hao, W. M., Brasseur, G., and Müller, J.-F.: Land use practices and biomass burning: Impact on the chemical composition of the atmosphere, in Biomass Burning and Global Change, edited by J. S. Levine, pp. 140–148, MIT Press, Cambridge, Mass., 1996.

Gros, V., Poisson, N., Martin, D., Kanakidou, M., and Bonsang, B: Observations and modeling of the seasonal variation of surface ozone at Amsterdam Island: 1994–1996, J. Geophys. Res., 103, 28103–28109, 1998.

Hausmann, M., and Platt, U.: Spectroscopic measurements of bromine oxide and ozone in the high Arctic during the Polar Sunrise Experiment 1992, J. Geophys. Res., 99, 25399–25413, 1994.

Hebestreit, K., Stutz, J., Rosen, D., Matveiv, V., Peleg, M., Luria, M., and Platt, U.: DOAS measurements of tropospheric bromine oxide in mid-latitudes, Science, 283, 55–57, 1999.

Ingham, T., Bauer, D., Sander, R., Crutzen, P. J., and Crowley, J. N.: Kinetics and products of the reactions BrO + DMS and Br + DMS at 298 K, J. Physical Chemistry A, 103, 7199–7209, 1999.

Jones, A., Roberts, D. L., Woodage, M. J., and Johnson, C. E.: Indirect sulphate aerosol forcing in a climate model with an interactive sulphur cycle, J. Geophys. Res., 106, 20293–20310, 2001.

Kettle, A., et al.: A global database of sea surface dimethylsulfide (DMS) measurements and a procedure to predict sea surface DMS as a function of latitude, longitude, and month, Global Biogeochem. Cycles, 13, 399–444, 1999.

Kettle, A., and Andreae, M. O.: Flux of dimethylsulfide from the oceans: A comparison of updated data sets and flux models, J. Geophys. Res., 105, 26793–26808, 2000.

Koch, D., Jacob, D., Tegen, I., Rind, D., and Chin, M.: Tropospheric sulfur simulation and sulfate direct radiative forcing in the Goddard Institute for Space Studies general circulation model, J. Geophys. Res., 104, 23799–23822, 1999.

von Kuhlmann, R.: Tropospheric photochemistry of O_3, its precursors and the hydroxyl radical: A 3D modeling study considering non-methane hydrocarbons, University of Mainz, Mainz, Germany, PhD Thesis, 2001. (available via http://www.mpch-mainz.mpg.de/∼kuhlmann)

Lawrence, M. G., Crutzen, P. J., Rasch, P. J., Eaton, B. E., and Mahowald, N. M.: A model for studies of tropospheric photochemistry: Description, global distributions, and evaluation, J. Geophys. Res., 104, 26245–26277, 1999.

Lee, Y.-N., and Zhou, X.: Aqueous reaction kinetics of ozone and dimethylsulfide and its atmospheric importance, J. Geophys. Res., 99, 3597–3605, 1994.

Liss, P. S., and Merlivat, L.: Air-sea gas exchange rates: Introduction and synthesis, In: The Role of Air-Sea Exchange in Geochemical Cycling, edited by P. B. Menard and D. Reidel, Norwell, Mass, pp. 113–127, 1986.

Lohmann, U., Feichter, J., Penner, J., and Leaitch, R.: Indirect effect of sulfate and carbonaceous aerosols: A mechanistic treatment, J. Geophys. Res., 105, 12193–12206, 2000.

Martinez, R. I., and Herron, J. T.: Stopped-flow study of the gas-phase reaction of ozone with organic sulfides: Dimethyl sulfide, Int. J. Chem. Kinetics, 10, 433–452, 1978.

Müller, J.-F. and Brasseur, G. P.: IMAGES: A three-dimensional chemical transport model of the global troposphere, J. Geophys. Res., 100, 16445–16490, 1995

Nakano, Y., Goto, M., Hashimoto, S., Kawasaki, M., and Wallington, T. J.: Cavity ring-down spectroscopic study of the reactions of Br atoms and BrO radicals with dimethyl sulfide, J. Physical Chemistry A, 105, 11045–11050, 2001.

Nightingale, P. D., Malin, G., Law, C. S., Watson, A. J., Liss, P. S., Liddicoat, M. I., Boutin, J., and Upstill-Goddard, R. C.: In situ evaluation of air-sea exchange parameterizations using novel conservative and volatile tracers, Global Biogeochem. Cycles, 14, 373–387, 2000.

Nowak, J. B., Davis, D. D., Chen, G., Eisele, F. L., Mauldin, R. L., Tanner, D. J., Cantrell, C., Kosciuch, E., Bandy, A., Thornton, D., and Clarke, A.: Airborne observations of DMSO, DMS, and OH at marine tropical latitudes, Geophys. Res. Lett., 28, 2201–2204, 2001.

Penner, J. E., M. Andrea, H. Annegarn, L. Barrie, J. Feichter, D. Hegg, A. Jayaraman, R. Leaitch, D. Murphy, J. Nganaga, and G. Pitari, Aerosols, their Direct and Indirect Effects, in Climate Change 2001: The scientific basis, pp. 289–348, Cambridge University Press, 2001.

Pham, M., Müller, J.-F., Brasseur, G., Granier, C., and Mégie, G.: A three-dimensional study of the tropospheric sulfur cycle, J. Geophys. Res., 100, 26061–26092, 1995.

Pickering, K. E., Wang, Y., Tao, W.-K., Price, C., and Müller, J.-F.: Vertical distributions of lightning NOx for use in regional and global chemical transport models, J. Geophys. Res., 103, 31 203–31 216, 1998.

Price C., Penner, J., and Prather, M.: NOx from lightning, 1. Global distribution based on lightning physics, J. Geophys. Res., 102, 5929–5941, 1997.

Putaud, J.-P., Mihalopoulos, N., Nguyen, B. C., Campin, J. M., and Belviso, S.: Seasonal variations of atmospheric sulfur dioxide and dimethylsulfide concentrations at Amsterdam Island in the Southern Indian Ocean, J. Atmos. Chem., 15, 117–131, 1992.

Sciare, J., Baboukas, E., Kanakidou, M., Krischke, U., Belviso, S., Bardouki, H., and Mihalopoulos, N.: Spatial and temporal variability of atmospheric sulfur-containing gases and particles during the Albatross campaign, J. Geophys. Res., 105, 14433–14448, 2000a.

Sciare, J., Mihalopoulos, N., and Dentener, F. J.: Interannual variability of atmospheric dimethylsulfide in the southern Indian Ocean, J. Geophys. Res., 105, 26369–26378, 2000b.

Sciare, J., Kanakidou, M., and Mihalopoulos, N.: Diurnal and seasonal variation of atmospheric dimethylsulfoxide at Amsterdam Island in the southern Indian Ocean, J. Geophys. Res., 105, 17257–17265, 2000c.

Sciare, J., Baboukas, E., Mihalopoulos, N.: Short-term variability of atmospheric DMS and its oxidation products at Amsterdam Island during summer time, J. Atmos. Chem., 39, 281–302, 2001.

Shaw, G. E.: Bio-controlled thermostasis involving the sulfur cycle, Clim. Change, 5, 297–303, 1983.

Toumi, R.: BrO as a sink for dimethylsulfide in the marine atmosphere, Geophys. Res. Lett., 21, 117–120, 1994.

Turner, S. M., Nightingale, P. D., Broadgate, W., and Liss, P. S.: The distribution of dimethyl sulfide and dimethylsulphoniopropionate in Antarctic waters and sea ice, Deep-Sea Res., 42, 1059–1080, 1995.

Venkataraman, C., Mehra, A., and Mhaskar, P.: Mechanisms of sulphate aerosol production in clouds: effect of cloud characteristics and season in the Indian region, Tellus, 53B, 260–272, 2001.

Wanninkhof, R.: Relationship between wind speed and gas exchange over the ocean, J. Geophys. Res., 97, 7373–7382, 1992.

Yvon, S. A., Saltzman, E. S., Cooper, D. J., Bates, T. S., and Thompson, A. M.: Atmospheric sulfur cycling in the tropical Pacific marine boundary layer (12°S, 135°W): A comparison of field data and model results, 1. Dimethylsulfide, J. Geophys. Res., 101, 6899–6909, 1996.

Chapitre 6

Les émissions océaniques de DMS peuvent-elles amplifier ou atténuer le réchauffement climatique ?

Ce chapitre reprend l'article de *Bopp et al.* [2002] soumis au *Canadian Journal of Fisheries and Aquatic Sciences.*

Will marine dimethylsulfide emissions amplify or alleviate global warming? – A model study

L. Bopp[1], O. Boucher[2], O. Aumont[3], S. Belviso[1], J.-L. Dufresne[4], P. Monfray[1], M. Pham[5]

[1] Laboratoire des Sciences du Climat et de l'Environnement, CEA / CNRS, Gif sur Yvette, France
[2] Laboratoire d'Optique Atmosphérique, CNRS UMR 8518, USTL, Villeneuve d'Ascq, France
[3] Laboratoire d'Océanographie Dynamique et de Climatologie, CNRS / UPMC / IRD, Paris, France
[4] Laboratoire de Météorologie Dynamique, CNRS / UPMC, Paris, France
[5] Service d'Aéronomie, CNRS / UPMC / UVSQ, Paris, France

Abstract.

Dimethylsulfide (DMS) is a biogenic compound produced in sea-surface water and outgased to the atmosphere. Once in the atmosphere, DMS is a significant source of cloud condensation nuclei (CCN) in the unpolluted marine atmosphere. It has been postulated that climate may be partly modulated by variations in DMS production through a DMS-CCN-cloud albedo feedback. We present here a first modeled estimate of the radiative impact due to changes in DMS air-sea fluxes caused by global warming. A suite of models, including an atmosphere-ocean general circulation model (AOGCM), a marine biogeochemical scheme incorporating a parameterization of DMS emissions to the atmosphere, and an atmospheric model of the global sulfur cycle, are used to simulate the responses of DMS sea-to-air flux and its associated radiative impact to increased greenhouse gas concentration (a 1% increase per year in atmospheric CO_2 until the present-day concentration has doubled). At $2xCO_2$, our model estimates a small increase (3%) in the global DMS flux to the atmosphere but with large spatial heterogeneities (from -15% to 30% in the zonal mean). The radiative perturbation due to the DMS-induced change in cloud albedo is estimated to be -0.05 Wm^{-2}, which represents only a small negative climate feedback on global warming. However there are large regional changes, such as a perturbation of up to -1.5 Wm^{-2} in summer bet-

ween 40°S and 50°S, which can significantly impact the regional climate. In the Southern Ocean, this radiative impact may partly alleviate the radiative forcing due to anthropogenic CO_2 (2.5/3 Wm^{-2} at 2xCO_2 compared to 1xCO_2 conditions).

1 Introduction

Dimethylsulfide (DMS) is the most abundant volatile sulfur-compound at the sea surface and has a strong marine phytoplanktonic origin. Once in the atmosphere, DMS is oxidized and contributes to form sulfate aerosol particles, which may affect the radiative budget as cloud condensation nuclei (CCN). Recently, Jones et al. (2001) and Boucher et al. (2002a) have shown in global model studies that the indirect radiative forcing due to anthropogenic sulfate aerosols was significantly influenced by assumptions made about the marine DMS emission flux. This is because an increase in the DMS flux causes an increase in the concentration of sulfate aerosols, thus increasing background CCN concentrations and reducing the cloud susceptibility to anthropogenic (sulfate) aerosols.

The sea-to-air flux of DMS is controlled by the DMS concentration at the sea surface and by the magnitude of the DMS transfer velocity across the air-sea interface, which both depend on climate variables. Sea-to-air transfer velocity mainly varies with sea-surface temperature and wind velocity (Liss and Merlivat 1986, Wanninkhof 1992). Sea-surface DMS concentration is also regulated by climate variables such as solar irradiance, sea-surface temperature and ocean physics, through their control on the marine biology.

It has been postulated that the Earth's climate is partly regulated by variations in DMS emissions through a DMS-CCN-cloud albedo feedback (Charlson et al. 1987). However, there are large uncertainties both on the sign and on the magnitude of this feedback (Liss et al. 1994) and it is still not clear whether this mechanism can play a role in future climate change.

A first step has been accomplished by Gabric et al. (1998) and Gabric et al. (2001) with the coupling of a general circulation model together with a DMS production model to investigate the response of DMS emissions to climate change. Based on a $10°\times20°$ area in the Subantarctic Southern Ocean, south of Australia, Gabric et al. (2001) estimate an increase in DMS emissions of 5% by 2080 (corresponding to an equivalent CO_2 tripling relative to pre-industrial levels). With this modest increased percentage, they find a small negative radiative impact, which, they conclude, confirms the minor role for DMS-derived aerosols in climate regulation. But this study is essentially a regional one and it is difficult to extend such results to the world ocean. Penner et al. (2001) estimated a small increase in global DMS flux between the years 2000 and 2100, with global DMS fluxes of 26.0 and 27.7 TgS yr^{-1}, respectively. This estimate is for constant marine DMS concentrations and thus includes only the effects of changing wind speed and sea surface temperature which were estimated from the Climate System Model of NCAR. Penner et al. (2001) did not estimate the impact of such changes on the radiation budget.

In a previous paper (Bopp et al. 2003), a model of the global distribution of sea-surface DMS concentrations (Aumont et al. 2002) was coupled to an atmosphere-ocean general circulation model (Barthelet et al. 1998) to predict the evolution of DMS sea-water concentrations and air-sea fluxes in the context of global warming. Here, we propose to extend this previous study. To predict the impact of changes in marine DMS emissions on the atmospheric sulfur cycle and the radiative budget of the Earth, we use a global model of the atmospheric sulfur cycle. The aim of this study is to give a first quantitative assessment of the role of DMS emissions in future climate change.

2 Method

2.1 Marine DMS emissions

Sea-water DMS concentrations for 1xCO_2 and 2xCO_2 conditions are obtained from the work of Bopp et al. (2003). (Note that 1xCO_2 corresponds here to 1990 (350 ppmv) rather than pre-industrial conditions.) In this previous work, the transient climate response to increased atmospheric CO_2 was obtained from simulations with the Institut Pierre-Simon Laplace Coupled Model 1 (IPSL-CM1) ocean-atmosphere general circulation model (OAGCM) (Barthelet et al. 1998). The transient climate run consists of a global warming scenario in which atmospheric pCO_2 was increased from 350 ppmv (1xCO_2) at a rate of 1% per year, reaching 700 ppmv (2xCO_2) after about 70 years. This transient climate was then used to force a marine biogeochemical scheme and to predict the evolution of marine biology (Bopp et al. 2001). The biogeochemical scheme used for this study is a Nutrient Phytoplankton Zooplankton and Detritus (NPZD) type model. Phytoplankton growth depends on the local conditions of light, temperature and turbulence, and considers ${PO_4}^{3-}$ as the only limiting nutrient. Parameterizations of DMS, as non-linear functions of the phytoplankton biomass and the food web structure of the ecosystem, were applied to predict DMS sea-water concentrations (Bopp et al.

Fig. 1: The suite of models used for this study includes an atmosphere-ocean general circulation model, an oceanic biogeochemical scheme incorporating parameterizations of air-sea DMS emissions, and a model of the global atmospheric sulfur cycle.

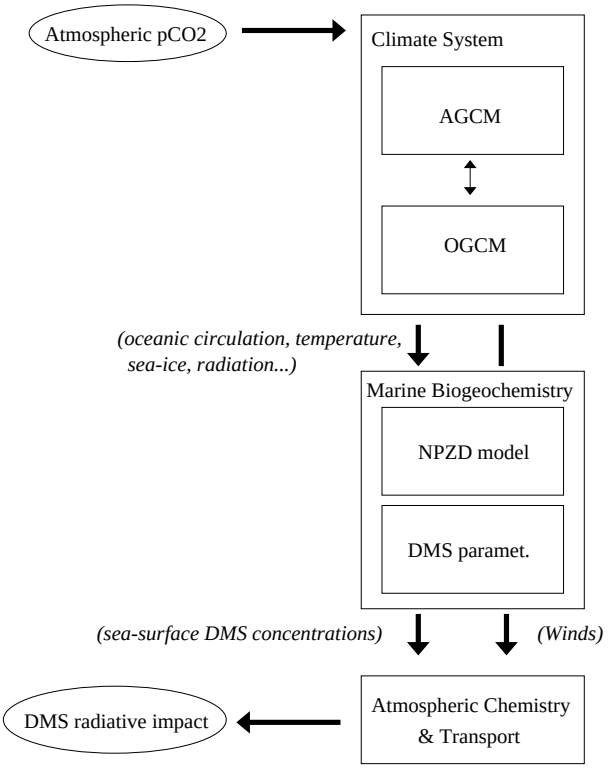

2002). Those relationships (DMS as a function of phytoplankton biomass and the food web structure of the ecosystem) have been established from datasets obtained during several cruises carried out in contrasted areas of the world oceans. The marine biogeochemical scheme and the DMS parameterizations that were used are fully described and evaluated in Aumont et al. (2002).

2.2 Sulfur cycle model and experiment design

A model of the global atmospheric sulfur cycle is used to propagate the DMS fluxes into the atmosphere and to compute the associated radiative impact on clouds. The model used in this study was developed in the framework of the general circulation model of the Laboratoire de Météorologie Dynamique and is fully described in Boucher et al. (2002b). Only aspects relevant to the DMS cycle are recalled here. Once emitted in the atmosphere, DMS is oxidized in the gas phase by OH and NO_3 radicals. Oxidation of DMS by NO_3 produces SO_2 and oxidation of DMS by OH produces either SO_2 or dimethylsulfoxide (DMSO). We also included the oxidation of DMS by O_3 in the gas phase (producing SO_2 only) and aqueous phase (producing DMSO only) as introduced in Boucher et al. (2002b). DMSO is oxidized in the gas phase by OH to produce SO_2 and methanesulfonic acid (MSA). No heterogeneous sink is included for DMS and DMSO. All reaction rates are given in Boucher et al. (2002a) and Boucher et al. (2002b). The monthly concentrations of oxidants are prescribed from the IMAGES model (Pham et al. 1995), except H_2O_2 which is calculated interactively in the model.

Three different experiments were carried out with our global model of the sulfur cycle. All three experiments use the same meteorology (i.e., the radiative impact of changing DMS emissions does not feedback on the meteorology). The three experiments also use the same sources of sulfur compounds other than marine DMS. In particular, the industrial sources of SO_2 are taken from the EDGAR 2.0 database and are representative of year 1990. Thus the three experiments differ only by their marine DMS emissions which are recomputed interactively in the model using the marine DMS concentrations from Bopp et al. (2003) and the parameterization of Nightingale et al. (2000). In the control experiment (CONTROL), marine DMS concentrations are set to their $1xCO_2$ value. In the "global warming" experiment (GW), marine DMS concentrations are set to their $2xCO_2$ value and we correct the air-sea DMS flux by applying a scaling factor on the 10-m wind speed which accounts for the changes in wind speed as simulated in the OAGCM $1xCO_2$ and $2xCO_2$ experiments. This scaling factor is applied as a two-dimensional (latitude-longitude) monthly average and is estimated from the changes in wind stress in the OAGCM experiments. We also perform a third sensitivity experiment (GWdms) similar to GW but without the correction factor on wind speed in order to separate effects of the changes in marine DMS concentrations and wind speed. We do not account in these experiments for changes in the DMS air-sea transfer velocity induced by the change in sea surface temperature and sea-ice, but these have been estimated to be negligible. We do not either consider changes in precipitation which may affect wet scavenging of soluble species. Future research is needed to assess the importance of this. The model was run 18 months for each experiment and we present results for the last 12 months. The spin-up time of 6 months is long enough considering the short lifetime of aerosols.

We follow Boucher and Lohmann (1995) and Boucher and Pham (2002) to estimate the cloud properties from the sulfate mass concentration. This calculation is only diagnostic and therefore only includes the first indirect effect (change in cloud optical properties for a fixed

Fig. 2: Zonally-averaged change (global warming minus control) of (a) sea surface temperature (solid line, °C) and mixed layer depth (dashed line, m, log-scale), (b) surface chlorophyll (solid line, mg m^{-3}) and relative abundance of siliceous phytoplankton species (Si-ratio, dashed line, %), (c) DMS sea-surface concentration (solid line, nM), (d) DMS flux to the atmosphere (solid line, µmol d^{-1} m^{-2}), and (e) associated radiative impact (solid line, Wm^{-2}). For the last two panels (d and e), the solid lines represent both effects of changes in marine DMS and wind speed (GW−CONTROL) while the dashed lines represent the effect of sea-surface DMS concentration changes alone (GWdms−CONTROL).

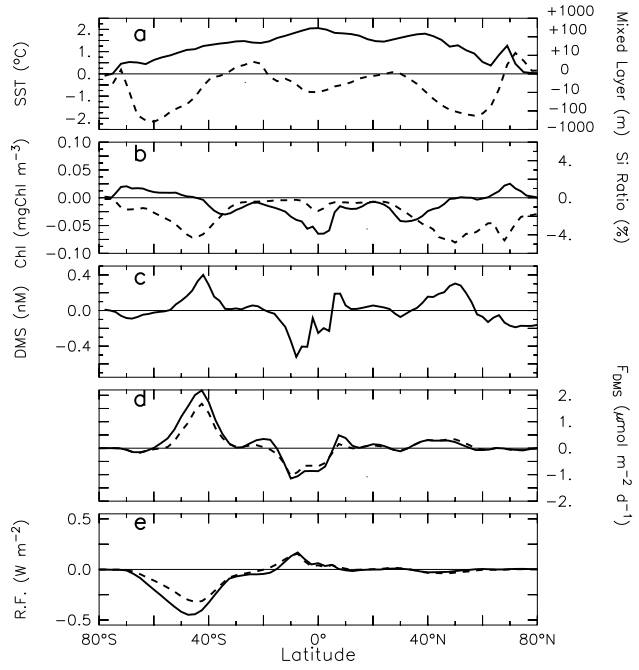

Fig. 3: Change in DMS flux between the CONTROL and GW experiments. Unit is µmol d^{-1} m^{-2}.

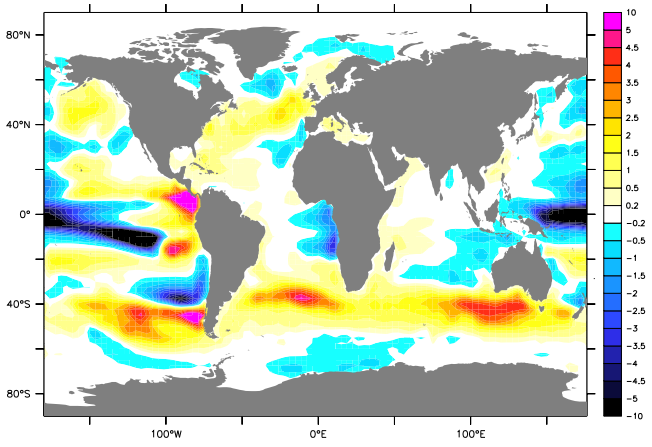

liquid water content). Although very uncertain, the second indirect effect (due to a reduction in precipitation efficiency) may be of similar magnitude than the first indirect effect. The radiative impact on clouds due to changes in DMS emissions is computed as the difference in top-of-atmosphere radiative fluxes between the "global warming" and the control experiments (i.e., with DMS emissions at 2xCO_2 and 1xCO_2, respectively). The results are moderately sensitive to the assumed minimum background cloud droplet number concentration (prescribed here at the rather large value of 50 cm^{-3}). While improvements on the parameterization of the aerosol indirect effects are desirable (Lohmann et al. 2000), our parameterization is still useful to perform the sensitivity experiments of the present study.

3 Results and discussion

3.1 Marine DMS production

At 2xCO_2, the model predicts a 9% global decrease in the mean annual primary production and a small decrease of global sea-surface DMS concentrations ($\sim -1\%$). It also predicts opposing changes between the high and low latitudes (Figure 2b–2c).

In the low latitudes, climate-induced changes (reduced nutrient supply caused by increased stratification of the upper ocean and decreased intensity of tropical upwellings) decrease marine production (-20%) and consequently lead to lower DMS concentrations.

In the high latitudes, climate-induced changes (a longer growing season caused by increased stratification of the upper ocean) increase marine production (30%). In the 40°–60° band (north and south), the model also shows a poleward retreat of siliceous species (considered as low-DMS producers), and their replacement by non-siliceous species (considered as high-DMS producers). This shift in the phytoplankton ecosystem (depicted as the Si-ratio on figure 2b) is responsible for a DMS concentration increase in the mid latitudes at 2xCO_2.

Results, mechanisms, and uncertainties of the response of marine production and DMS concentrations to climate change are described in more details in Bopp et al. (2001, 2003). Here, we investigate how these changes propagate up to sea-to-air DMS emissions, and to the atmospheric sulfur cycle.

3.2 DMS flux to the atmosphere

There is a large spatial heterogeneity in the change in DMS flux (Figure 3). In the tropical Pacific Ocean, the DMS fluxes are reduced by up to 10 µmol m^{-2} d^{-1}

Fig. 4: Annually-averaged radiative impact on clouds (first indirect effect only) due to changes in DMS fluxes associated with a CO_2 doubling (GW minus CONTROL, upper panel). The corresponding radiative forcing due to CO_2 (from $1\times CO_2$ or 350 ppmv to $2\times CO_2$ or 700 pmv) is also shown for comparison (lower panel). Unit is Wm^{-2}).

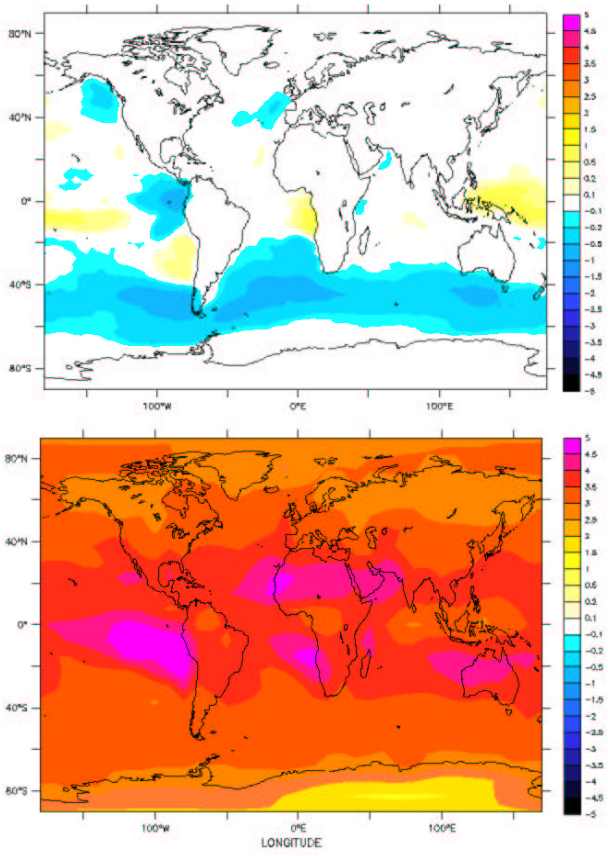

Fig. 5: Latitude-time diagram of the radiative impact (first indirect effect) induced by changes in the DMS flux (GW minus CONTROL, zonal mean, unit is Wm^{-2}).

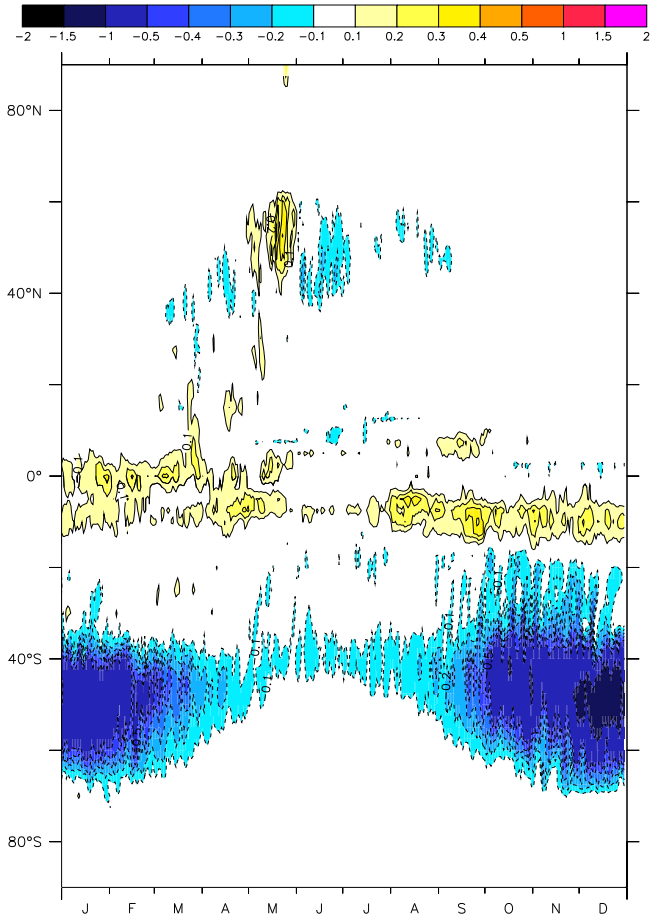

(−50%). Conversely, in the subtropical and subantarctic zones, DMS fluxes are strongly enhanced by up to 6 μmol m^{-2} d^{-1} (or 50%). These regional changes and the latitudinal opposition (Figure 2d) are driven by variations in DMS concentrations. Stronger winds in the Southern Ocean and weaker winds in the equatorial region at $2xCO_2$ amplify the large heterogeneity. On global average, the DMS flux to the atmosphere is increased by about 3%, from 29.1 Tg S yr^{-1} at $1xCO_2$ conditions to 29.9 Tg S yr^{-1} at $2xCO_2$ conditions. The effects of changes in marine DMS and wind speed account for 0.3 and 0.5 Tg S yr^{-1} of this increase, respectively. The effect of wind speed is small on zonal average compared to the effect of marine DMS, but relatively larger on global average because of the cancellation of the marine DMS effect between Tropical and mid-latitude regions.

In the 40°S–50°S band, the model predicts a 20% increase in the annual DMS flux. The effect of wind changes alone accounts for one quarter of the total increase (a 5% increase) whereas the major effect is due to changes in sea-surface DMS concentrations (a 15% increase).

3.3 Atmospheric DMS and sulfate

At $2xCO_2$, the mean atmospheric DMS burden is very similar to its $1xCO_2$ value (0.076 TgS at $1xCO_2$ vs. 0.078 TgS at $2xCO_2$). The DMS lifetime is also unchanged at about 0.9 day. The small increase in the DMS burden is accompanied by a very small decrease in the sulfate burden, probably because of a shift of sulfate production in regions where wet scavenging is more efficient.

However, the differences in the spatial distribution of

Fig. 6: Indirect radiative forcing due to anthropogenic sulfate from present-day relative to pre-industrial conditions, from Boucher and Pham (2002). Unit is W m^{-2}.

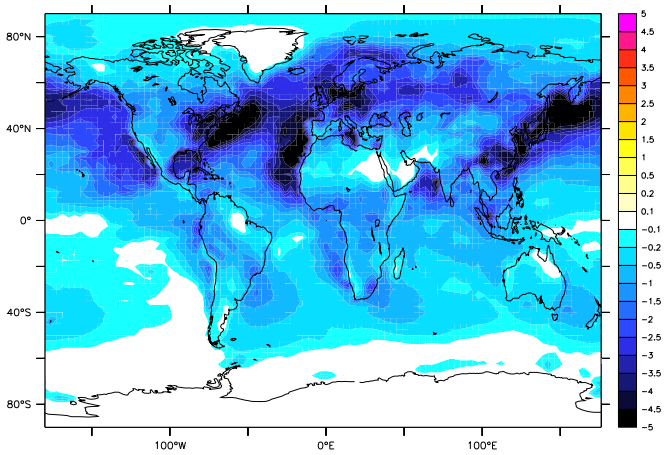

DMS emissions result in large regional differences of atmospheric DMS concentrations. The changes in the distribution of DMS mixing ratios at the surface follow the changes in marine DMS emissions. In the Southern Ocean, DMS mixing ratio is increased by up to 50 pptv (or 25%). It is decreased by up to 40 pptv (or −50%) in the western Equatorial Pacific Ocean.

3.4 Indirect radiative effect

The radiative impact in clear sky (or direct effect) induced by the changes in sulfate aerosol burden is negligible. As mentioned above, we focus here on the radiative impact in cloudy sky and consider only the first indirect radiative effect (changes in cloud optical properties for fixed liquid water content).

The change in radiative flux between the GW and CONTROL experiments (with DMS emissions set to their 2xCO_2 and 1xCO_2 values, respectively) is very small at −0.05 Wm^{-2}. Again, this modest global figure conceals large spatial and temporal heterogeneities. In regions where DMS emissions are increased (decreased) by global warming, sulfate mass and the cloud droplet number concentration increase (decrease). Through the associated changes in cloud optical properties, this increase (decrease) in DMS emission leads to an albedo increase (decrease) and a negative (positive) impact on the radiative budget. The radiative impact of DMS at 2xCO_2 reaches 1 Wm^{-2} in the western Equatorial Pacific Ocean and off the west coasts of Angola and Chile whereas it reaches −1 Wm^{-2} in the South Atlantic Ocean (Figure 4, upper panel).

On figure 4, we compare our estimate of the radiative impact of changes in DMS emissions to the radiative forcing of CO_2 at 2xCO_2, computed with the LMD atmospheric GCM (Laurent Li, personal communication). In the subantarctic Southern Ocean, the radiative impact caused by changes in DMS emissions may partly counteract the CO_2 radiative forcing (−0.5 Wm^{-2} vs 2.5 Wm^{-2} in zonal annual means). Moreover, the DMS radiative impact differs from the CO_2 radiative forcing by its seasonality (Figure 5). Whereas CO_2 radiative forcing is more or less constant over the year, the DMS radiative impact reaches its maximum in summer, with values up to −1.5 Wm^{-2} in the 40°S–60°S band (Figure 5).

There are several reasons why the symmetry in marine DMS change between the northern (NH) and southern (SH) hemispheres (Figure 2c) does not translate into a similar symmetry in the radiative impact (Figure 2e). In the first place, the surface covered by the ocean is less in the SH than in NH. In the second place, the amplification of the change in DMS flux due to changes in wind speed occurs only in the SH (Figure 2d). Finally, the radiative impact is expected to be negligible in polluted regions where the cloud droplet number concentration and the indirect aerosol forcing are already large (Figure 6). The radiative impact induced by changes in DMS was estimated assuming constant anthropogenic emissions of SO_2 over the period of doubling CO_2 concentrations. These emissions and those of other aerosol types are expected to change in the future. There are observed negative trends in sulfate aerosol emissions and concentrations over Europe and North America (Boucher and Pham, 2002), while emissions are expected to continue to grow over Asia and some other regions of the world. If this trend continue, it would result in a positive radiative impact in the mid-latitudes of the NH thus strengthening the hemispheric contrast observed in Figure 4 (upper panel).

4 Conclusion

Future climate changes are likely to affect the ocean circulation, the marine biological productivity, and in turn the marine and atmospheric sulfur cycle. Here, using (1) a coupled ocean-atmosphere model forced by increasing atmospheric CO_2, (2) a marine biogeochemical scheme, (3) data-based parameterizations of sea-surface DMS, and (4) an atmospheric model of the global sulfur cycle, we could estimate the impact of future climate change on DMS fluxes to the atmosphere and the associated radiative impact through changes in cloud albedo. At 2xCO_2, the DMS flux is similar to its 1xCO_2 value (at about 29 Tg S yr^{-1}), however we found large regional contrasts. Main results are a reduction (−15%) of the

DMS flux in the tropical band and an increase (30%) in the mid latitudes of the Southern hemisphere. Those regional changes are mainly driven by a chlorophyll decrease at low latitudes and by a shift of phytoplankton species (from diatoms to other species more efficient to produce DMS) at mid latitudes.

Those changes propagate to the DMS atmospheric cycle and significantly impact the regional radiative budget, up to -1.5 Wm^{-2} in summer between 40°S and 50°S. In the Southern Ocean, this radiative impact may partly cancel out the radiative forcing of anthropogenic CO_2 (2.5/3 Wm^{-2} at $2xCO_2$). The strength of the DMS-CCN-cloud albedo feedback is nevertheless small at the global scale.

Our results strongly depends on the skill of our models to simulate marine productivity, on the relationships we use to predict DMS from biological variables, and on the parameterization of the aerosol indirect effect used in the atmospheric model of the sulfur cycle. Improvements in all aspects will be necessary to develop greater confidence in such future predictions. In particular, the role of sea-salt particles as CCN and the potential change in sea-salt induced by changes in wind speed should also be considered. Whereas such a study must be viewed as a sensitivity study more than a prediction, it represents a first step toward the assessment of the DMS-cloud albedo climate feedback loop.

Acknowledgments: This work was supported by the Environment and Climate Programme of the European Community (IRONAGE contract EVK2-1999-00227 and PHOENICS contract EVK2-CT-2001-00098) and the French national programmes PROOF and PNCA of CNRS/INSUE. Computing time was provided by CNRS/IDRIS under projects 020040 and 021167. The Laboratoire d'Optique Atmosphérique is an institute of the "Fédération de Recherche" FR1818 of the CNRS.

References

Aumont, O., Belviso, S., and Monfray, P., 2002, Dimethylsulfoniopropionate (DMSP) and dimethylsulfide (DMS) sea surface distributions simulated from a global 3-D ocean carbon cycle model. *J. Geophys. Res.*, **107**, 10.1029/1999JC000111.

Barthelet, P., Bony, S., Braconnot, P., Braun, A., Cariolle, D., Cohen-Solal, E., Dufresne, J.-L., Delecluse, P., Déqué, M., Fairhead, L., Filiberti, M.-A., Forichon, M., Grandpeix, J.-Y., Guilyardi, E., Houssais, M.-N., Imbard, M., Le Treut, H., Lévy, C., Li, Z., Madec, G., Marquet, P., Marti, O., Planton, S., Terray, L., Thual, O., and Valcke, S., 1998, Simulations couplées globales des changements climatiques associés à une augmentation de la teneur atmosphérique en CO_2. *C. R. Acad. Sci. Paris*, **326**:677–684.

Bates, T. S., and P. K. Quinn, Dimethylsulfide (DMS) in the equatorial Pacific Ocean (1982 to 1996): Evidence of a climate fedback?, *Geophys. Res. Lett.*, **24**, 861–864, 1997.

Bopp, L., Monfray, P., Aumont, O., Dufresne, J.-L., Le Treut, H., Madec, G., Terray, L., and Orr, J., 2001, Potential impact of climate change on marine export production. *Global Biogeochem. Cycles*, **15**:81–99.

Bopp, L., Aumont, O., Belviso, S., and Monfray, P., 2003, Potential impact of climate change on marine DMS (dimethylsulfide) emissions. *Tellus*, **55B**:11–22.

Boucher, O. and Lohmann, U., 1995, The sulfate-CCN-cloud-albedo effect: A sensitivity study with two general circulation models. *Tellus*, **47B**:281–300.

Boucher, O., Moulin, C., Belviso, S., Aumont, O., Bopp, L., Cosme, E., von Kuhlmann, R., Lawrence, M., Pham, M., Reddy, M., Sciare, J., and Venkataraman, C., 2002a, Sensitivity study of dimethylsulfide (DMS) atmospheric concentrations and sulphate aerosol indirect radiative forcing to the DMS source representation and oxidation. *Atmos. Chem. Phys. (Discuss.)*, **2**:1181–1216.

Boucher, O., Pham, M., and Venkataraman, C., 2002b, Simulation of the atmospheric sulfur cycle in the Laboratoire de Météorologie Dynamique General Circulation Model. Model description, model evaluation, and global and European budgets. Notes scientifiques du pôle de modélisation, IPSL, Paris, France, (http://www.ipsl.jussieu.fr/poles/Modelisation/NotesSciences.htm).

Boucher, O. and Pham, M., 2002, History of sulfate aerosol radiative forcings. *Geophys. Res. Lett.*, **29**, 10.1029/2001GL014048.

Charlson, R. J., Lovelock, J. E., Andreae, M. O., and Warren, S. G., 1987, Oceanic phytoplankton, atmospheric sulphur, cloud albedo and climate. *Nature*, **326**:655–661.

Gabric, A. J., Whetton, P. H., Boers, R., and Ayers, G. P., 1998, The impact of simulated climate change on the air-sea flux of dimethylsulphide in the subantarctic Southern Ocean. *Tellus*, **50B**:388–399.

Gabric, A. J., Whetton, P. H., and Cropp, R., 2001, Dimethylsulphide production in the subantarctic Southern Ocean under enhanced greenhouse conditions. *Tellus*, **53B**:273–287.

Jones, A., Roberts, D., Woodage, M., and Johnson, C., 2001, Indirect sulphate aerosols forcing in a climate mo-

del with an interactive sulphur cycle. *J. Geophys. Res.*, **106**:20293–20310.

Liss, P. and Merlivat, L., 1986, Air-sea gas exchange: Introduction and synthesis. In *The Role of Air-Sea Exchange in Geochemical Cycling* (Ed. P. Buat-Ménard), D. Reidel.

Liss, P., Malin, G., Turner, S. M. and Holligan, P. M., 1994, Dimethylsulphide and *Phaeocystis*: a review. *J. Mar. Sys*, **5**:41–53.

Lohmann, U., Feichter, J., Penner, J., and Leaitch, R., 2000, Indirect effect of sulfate and carbonaceous aerosols: A mechanistic treatment, *J. Geophys. Res.*, **105**:12193–12206.

Nightingale, P. D., Malin, G., Law, C. S., Watson, A. J., Liss, P. S., Liddicoat, M. I., Boutin, J., and Upstill-Goddard, R. C., 2000, In-situ evaluation of air-sea exchange parameterizations using novel conservative and volatile tracers. *Global Biogeochem. Cycles*, **14**:373–387.

Penner, J., Andreae, M., Annegarn, H., Barrie, L., Feichter, J., Hegg, D., Jayaraman, A., Leaitch, R., Murphy, D., Nganga, J., and Pitari, G., 2001, Aerosols, their direct and indirect effects, In *Climate Change 2001, The Scientific Basis, Contribution of Working Group I to the Third Assessment Report of the Intergovernmental Panel on Climate Change*, pp. 289–348, Cambridge University Press, New York.

Pham, M., Müller, J. F., Brasseur, G. P., Granier, C., and Mégie, G., 1995, A three-dimensional study of the tropospheric sulfur cycle. *J. Geophys. Res.*, **100**:26061–26092.

Wanninkhof, R., 1992, Relationship between wind speed and gas exchange over the ocean. *J. Geophys. Res.*, **97**:7373–7382.

Chapitre 7

Calcul de la perturbation radiative en ciel clair due aux aérosols à partir des observations POLDER

Ce chapitre reprend l'article de *Boucher et Tanré* [2000] paru dans le journal *Geophysical Research Letters*.

Estimation of the aerosol perturbation to the Earth's radiative budget over oceans using POLDER satellite aerosol retrievals

O. Boucher and D. Tanré,
Laboratoire d'Optique Atmosphérique,
Bât. P5, Université des Sciences et Technologies de Lille,
59655 Villeneuve d'Ascq Cedex, France.
(e-mail: boucher@loa.univ-lille1.fr, tanre@loa.univ-lille1.fr)

Abstract. POLDER satellite retrievals of aerosol properties over oceans are used to estimate a global-mean clear-sky aerosol shortwave flux perturbation of order -5 to -6 Wm^{-2}. Uncertainties due to aerosol absorption and POLDER cloud screening algorithm are quantified. In order to bound the radiative forcing by anthropogenic aerosols, we attempt to remove the contribution of background aerosols from these estimates and present all-sky aerosol radiative effects for three regions and two methods. The results are sensitive to the thresholds used to define the background conditions.

1 Introduction

Aerosols influence the radiative balance of the Earth through scattering of radiation (the direct effect) and by modifying the microphysical and optical properties of clouds (the indirect effect). Estimates of the aerosol direct effect and aerosol direct radiative forcing (defined as the anthropogenic fraction of the aerosol direct effect) are largely based on models. Aircraft observations [*Hignett et al.*, 1999] confirm that aerosols cause a significant modification in the clear-sky radiative budget. *Haywood et al.* [1999] have shown that model-based aerosol distributions could explain a large part of the discrepancies between ERBE satellite-observed and model-simulated clear-sky albedos. *Bergstrom and Russell* [1999] estimated the direct aerosol effect over the mid-latitude North Atlantic Ocean by combining AVHRR measurements of aerosol optical depth to in-situ measurements of aerosol physical properties obtained during the TARFOX campaign. Improved algorithms applied to AVHRR [*Nakajima and Higurashi*, 1998] or POLDER (Polarization and Directiona-

lity of the Earth's Reflectances, *Deuzé et al.* [1999]) radiometers now make it possible to retrieve the aerosol Ångström coefficient. In this paper, we use the POLDER retrieved aerosol properties to estimate the global-scale aerosol impact on the Earth's radiative budget.

2 Aerosol radiative perturbation

2.1 Description of POLDER aerosol products

We limit our analysis to oceanic regions. The aerosol products consist of the aerosol optical thickness (at 865 nm), aerosol Ångström coefficient (computed between the 670 and 865 nm channels) [*Deuzé et al.*, 1999]. The spatial resolution for the level-2 data is about 20 km x 20 km. The aerosol retrieval is based on a look-up table (LUT) approach including 12 different aerosol models using 3 different representative refractive indices (Table 1). The aerosol optical depth and Ångström coefficient are adjusted in order to obtain the best fit to the observed radiances at 670 and 865 nm. For Ångström coefficient below −0.2, which are usually associated to low aerosol optical depths, aerosol model #5 in Table 1 is used. Note finally that the cloud screening is quite stringent in its present version.

Table 1: Description of aerosol models used in this study. Columns 2–4 correspond to the aerosol models used in the POLDER retrieval and in our calculation of aerosol-induced flux change. Columns 5–7 correspond to the modified models used for sensitivity tests (see text). For computing the Mie scattering properties, log-normal size distributions are used with geometric standard deviation, σ_g=2.37. The aerosol refractive index is assumed constant over the solar spectrum.

Aerosol Model	Aerosol Modal Radius (μm)	Refractive Index	α	Modified Refractive Index	Modified Aerosol Radius (μm)	SSA at 550 nm
1	0.2710	1.33−0.0i	0.0	1.33−0.01i	0.2119	.832
2	0.1445	1.33−0.0i	0.3	1.33−0.01i	0.1308	.874
3	0.0713	1.33−0.0i	0.8	1.33−0.01i	0.0678	.907
4	0.0335	1.33−0.0i	1.4	1.33−0.01i	0.0324	.916
5	0.2239	1.40−0.0i	0.0	1.40−0.01i	0.1805	.846
6	0.1216	1.40−0.0i	0.3	1.40−0.01i	0.1116	.886
7	0.0602	1.40−0.0i	0.8	1.40−0.01i	0.0584	.916
8	0.0293	1.40−0.0i	1.4	1.40−0.01i	0.0285	.926
9	0.1815	1.50−0.0i	0.0	1.50−0.01i	0.1485	.859
10	0.1000	1.50−0.0i	0.3	1.50−0.01i	0.0921	.896
11	0.05096	1.50−0.0i	0.8	1.50−0.01i	0.0489	.924
12	0.02520	1.50−0.0i	1.4	1.50−0.01i	0.0246	.935

2.2 Computation of aerosol flux perturbation

We first construct a look-up table of the aerosol-induced top-of-atmosphere flux change for each of the 12 aerosol models of Table 1 and for 10 values of the solar zenith angle. Since it was shown in *Boucher et al.* [1998] that the aerosol forcing was to a good approximation proportional to $(1 - e^{-\tau})$, we only compute the aerosol radiative perturbation for an aerosol optical depth τ_0=0.1 at 865 nm. We use the Streamer radiative code [*Key*, 1994] which compares well with more elaborated codes [*Boucher et al.*, 1998]. For all seasons, we use a mid-latitude summer profile. Use of different profiles makes very small (at most 5%) differences. We also assume that the aerosol layer is located below 2 km. The surface reflectance is that of the open ocean and includes variation with solar zenith angle, although it is assumed to be Lambertian. For the calculations of the surface reflectance due to the presence of foam and the effect of waves on the Fresnel reflection, the 10-m wind speed is taken constant at 10 ms^{-1}.

Fig. 1 shows the aerosol perturbation to the radiative budget as a function of the solar zenith angle for a constant aerosol optical depth of 0.1 at 865 nm. We recognize on Fig. 1 the conventional maximum in aerosol radiative effect for scattering angles of about 60° [*Boucher et al.*, 1998]. This maximum is somewhat reduced because of the increase in surface reflectance with solar zenith angle [*Russell et al.*, 1997].

For computing the aerosol perturbation pixel-by-pixel, the values of aerosol-induced flux change of the LUT are interpolated in solar zenith angle and aerosol Ångström coefficient, but not in aerosol refractive index, which only takes the 3 values of Table 1. For each pixel i, the daily-averaged aerosol perturbation at the top-of-atmosphere is then approximated as:

$$\Delta F_i = \int_{\text{day}} \Delta F(\tau_0, \alpha_i, m_i, \mu_i(t)) \frac{1 - e^{-\tau_i}}{1 - e^{-\tau_0}} dt \; / \int_{\text{day}} dt \qquad (1)$$

Fig. 1: Change in solar radiative flux at the top-of-atmosphere due to aerosols as function of the cosine of the solar zenith angle. The data are for an aerosol optical depth of 0.1 at 865 nm and for the 12 aerosol models from Table 1. The aerosol models for the dashed curves are hardly used by the algorithm.

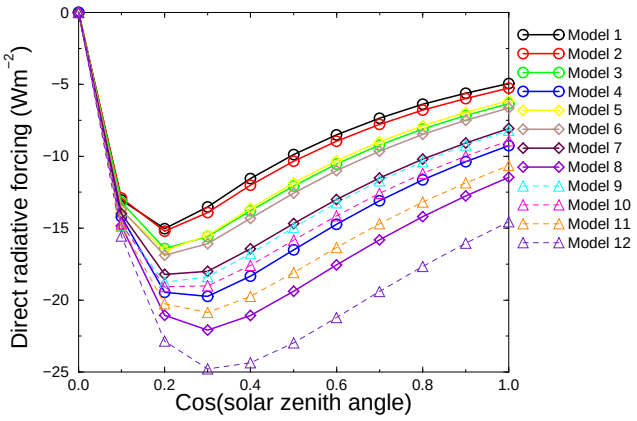

Fig. 2: Clear-sky shortwave aerosol radiative perturbation (Wm^{-2}) computed from the POLDER aerosol retrievals for a) December 1996 and b) June 1997.

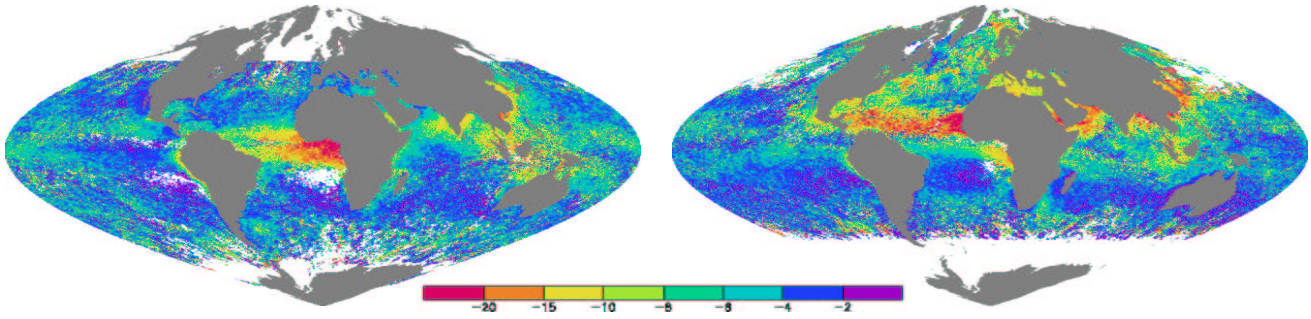

where $\mu_i(t)$ is the cosine of the solar zenith angle at time of the day t; τ_i, α_i, and m_i are the measured aerosol optical depth, Ångström coefficient, and refractive index at pixel i. It is implicit in Equation (1) that the one-time daily observation of POLDER (10.30 local time at the Equator) is representative of daytime values.

2.3 Results

Fig. 2 shows the change in clear-sky top-of-atmosphere solar radiative flux for the aerosol distribution retrieved by POLDER for December 1996 and June 1997. These maps resemble maps of the monthly-mean aerosol optical depth showed in *Deuzé et al.* [1999], except for that the aerosol radiative effect is enhanced in regions of high Ångström coefficient. It should be made clear that the POLDER clear-sky conditions are different –and may not be representative– of the actual clear-sky conditions, especially in regions of fractional cloudiness. This may result in an underprediction of the radiative impact of secondary aerosols which are partly produced through in-cloud processes. We displayed the global and hemispheric means of the aerosol direct effect in Fig. 3. The global mean is relatively constant at -5 to -6 Wm^{-2}. The mean is larger in the northern hemisphere than in the southern hemisphere by 1 to 3 Wm^{-2}, depending on the season. These numbers fall in the range of the model-based estimates of the clear-sky aerosol effect given by *Haywood et al.* [1999] assuming low and high sea-salt burdens.

3 Discussion of uncertainties

There are various sources of uncertainties in our estimates. These can be due to uncertainties in the retrieved aerosol properties, or in the aerosol vertical profile, spectral refractive index, and sea surface albedo used for the flux calculations. The uncertainties that are most easily quantifiable are discussed below.

3.1 Influence of aerosol absorption

The aerosol models used in the POLDER algorithm (Table 1, columns 1–4) are non-absorbing in the solar spectrum. We have introduced some absorption by setting the imaginary index to $-0.01i$ throughout the solar spectrum. The aerosol models are modified in such a way that the Ångström coefficients for scattering remain the same (Table 1, columns 5–7). This results in aerosol single scattering albedo at 550 nm ranging from 0.83 to 0.94 depending on the model. The aerosol flux perturbation is then computed for the new aerosol radiative properties in the same way as before, except that the measured aerosol optical depth is increased by a factor equal to one over the aerosol single scattering albedo at 865 nm, ω. This accounts for the fact that, at first order, the aerosol contribution to the observed radiance is proportional to the product $\omega\ \tau$. For a constant $\omega\ \tau$, the flux change induced by absorbing aerosols is smaller than induced by non-absorbing aerosols by 10 to 20% and 20 to 70% for large and small solar zenith angles, respectively. The reason for this decrease is in enhanced absorption due to multiple scattering effects within the aerosol layer and between the sea surface and the aerosol layer. Globally averaged, the aerosol flux perturbation is decreased by 32% upon inclusion of aerosol absorption. We think that this represents an upper limit for the effect of aerosol absorption.

3.2 Influence of POLDER cloud screening

By eliminating aerosol optical depth larger than about 0.8, the present cloud screening tends to bias the retrieval towards smaller values of aerosol optical depth. The aerosol retrieval in June 1997 was reprocessed with a less stringent cloud screening. This results in a 34% increase in the aerosol-induced flux change for June 1997. The bulk of the increase comes from the Atlantic Ocean where optical depths for dust aerosol are significantly

Fig. 3: Global and hemispheric means in clear-sky aerosol radiative perturbation (Wm^{-2}).

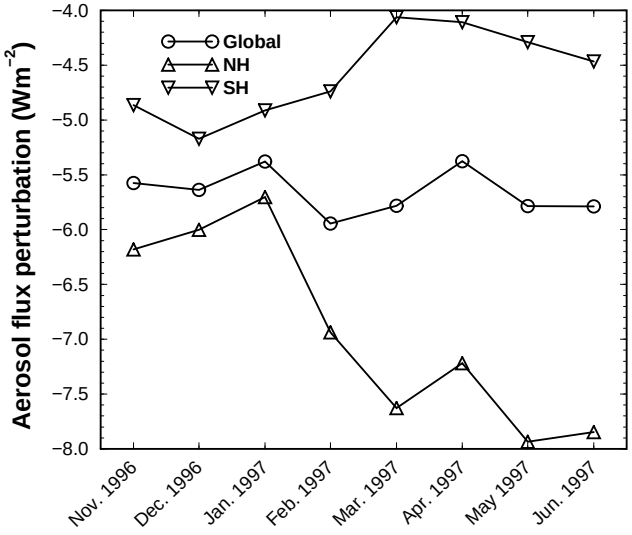

increased. This 34% increase in flux change should nevertheless be seen as an upper bound since it may also incorporate pixels contaminated by clouds.

3.3 Influence of aerosol Ångström coefficient

Goloub et al. [1999] showed that the POLDER aerosol optical depth was in good agreement with surface-based sun-photometer measurements ($\pm 0.05 \pm 0.05\ \tau$, with no bias observed). However the aerosol Ångström coefficient was underpredicted for aerosol optical depths larger than 0.1. Globally-averaged, a 10% underestimation in the Ångström coefficient results into a 1% underestimation of the aerosol-induced flux change.

3.4 Influence of geometric standard deviation

The geometric standard deviation, σ_g, is fixed at 2.37 in the aerosol retrieval scheme. We conducted a sensitivity test where σ_g is taken equal to 2.0 and 2.7 in the flux calculations. As for the test on absorption, the aerosol modal radii are modified as to keep the Ångström coefficient to the same reference values. Such modifications have a negligible influence on our results.

However, the use of bimodal aerosol models, in contrast to the monomodal aerosol models of the present retrieval scheme, could lead to differences in the retrieved aerosol properties. It is not yet possible to quantify the subsequent uncertainty in aerosol flux change.

4 Towards estimating aerosol forcing

4.1 Method

The perturbation to the Earth's radiative budget computed in the previous subsection includes the effects of both natural and anthropogenic aerosols, the relative contributions of which are difficult to determine in the context of present satellite (and in-situ) measurements. In order to place an upper bound on the aerosol radiative forcing, we attempt to define a "background" (or natural) aerosol level and substract its radiative effect from the total aerosol radiative effect. For this, we compute a clear-sky aerosol radiative perturbation as

$$\Delta RF_{\mathrm{clear}} = \sum\nolimits_{i \notin \mathrm{bg}} (\Delta F_i - \overline{\Delta F_{\mathrm{bg}}})/N \qquad (2)$$

where N is the number of equal-area pixels in the region under consideration, $\overline{\Delta F_{\mathrm{bg}}}$ is the average radiative perturbation over the background pixels, while i runs over the remaining pixels.

The all-sky radiative effect is computed as the product of the clear-sky effect by the fraction of clear sky as given by the cloud processing line of the POLDER algorithm [*Buriez et al.*, 1997]. By so doing, we assume (i) that the fraction of clear sky where the aerosol retrieval is performed is representative of the total clear sky, and (ii) that the cloudy-sky part of the direct aerosol effect is negligible, which is still under debate.

In method A the background encompasses all the pixels where the aerosol optical depth is smaller than a threshold, so that $\overline{\Delta F_{\mathrm{bg}}} = \overline{\Delta F_{\tau<\tau_{\mathrm{min}}}}$. In method B, the background is defined as in method A but the summation in Eq. 2 is restricted to pixels for which both τ and α are larger than the thresholds τ_{min} and α_{min}. While method A assumes that anthropogenic effects can be bounded by considering only the largest aerosol optical depths, method B also implies that only small particles are of anthropogenic origin. Since some large aerosols, such as Saharan dust, may be of anthropogenic origin, the actual aerosol radiative forcing may lie somewhere between the estimates given by methods A and B.

4.2 Results

The all-sky radiative effects are considerably reduced compared to their clear-sky counterparts. For illustration, we plot in Fig. 4 the seasonal (i.e., 8 month) variation in aerosol all-sky radiative effect for three regions. As expected, aerosol radiative effects estimated from method B are smaller than from method A. Their temporal variation may also be different, which indicates a seasonal evolution in the aerosol properties.

Fig. 4: Seasonal variation in all-sky aerosol radiative effect (Wm^{-2}) over the North Atlantic, off the west African coast, and over the North Pacific for methods A (upper panels) and B (τ_{min}=0.10, lower panels).

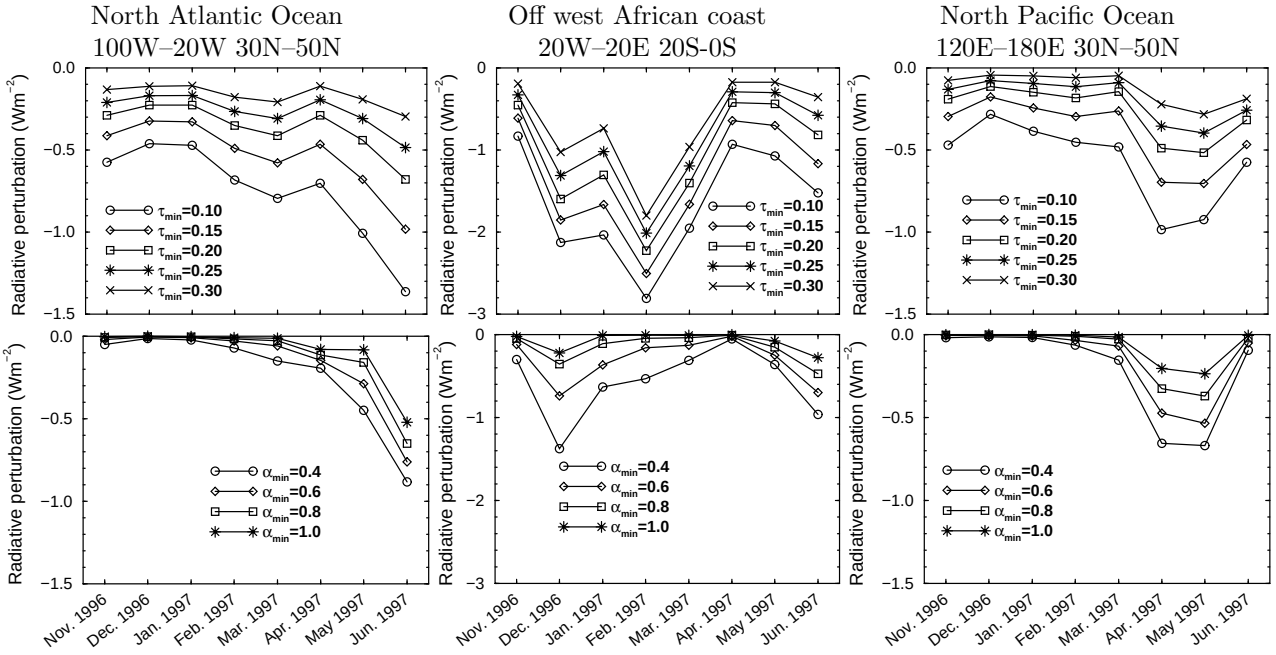

Over the North Atlantic Ocean (30N-50N), the aerosol effect as computed by method A includes an important contribution by mineral dust particles through November to April. The anthropogenic origin of this dust is however not established. In May and June, the effect is rather due to small aerosol particles coming from the United States, as evidenced by the larger effect predicted by method B. Off west African coast (20S-0S), large radiative effects are found in December 1996 and June 1997 according to method B, which are probably due to biomass burning. It is intriguing that the large peak observed in February in method A is absent in method B. It may be due to dust transported from arid regions or aged particles coming from biomass burning and transported over long distances. Over the North Pacific Ocean (30N–50N), the effect is maximum in April–May 1997, when aerosols with high Ångström coefficients are observed.

The choice of the threshold aerosol optical depth and Ångström coefficient remains open. The background maritime conditions corresponds to POLDER aerosol optical depth of the order of 0.1 and Ångström coefficient close to 0. Ångström coefficients larger than 0.4 are only found close to the continents, which could indicate an anthropogenic origin. Sunphotometer measurements suggest, however, larger Ångström coefficients for industrial aerosols. This and the large sensitivity of the aerosol effect to the threshold Ångström coefficient prevent us from a definitive conclusion.

5 Conclusions

We estimated the shortwave radiative flux change due to aerosols from the POLDER satellite retrievals. Our results show that the clear-sky shortwave radiative perturbation amounts to about -5.5 Wm^{-2}, globally-averaged, with significant uncertainties due to aerosol absorption and choice of the POLDER cloud screening method. We further attempted to remove the contribution of background aerosols from the estimates given above in order to bound the radiative forcing by anthropogenic aerosols. This was done by applying thresholds on the aerosol optical depth and Ångström coefficient. It turned out that the estimated radiative effects vary considerably depending on the choice of these thresholds. A research effort is needed to identify aerosol types and the anthropogenic fraction of the aerosol burden from remote and in-situ measurements.

Acknowledgements. Aurélia Marchand is acknowledged for her help in processing the POLDER data. POLDER is a joint CNES/NASDA effort. Information on the POLDER products can be found at http://smsc.cnes.fr/POLDER/index.htm. We thank two reviewers for their constructive comments.

References

Bergstrom, R. W., and P. B. Russell, Estimation of aerosol direct radiative effects over the midlatitude North Atlantic from satellite and in situ measurements, *Geophys. Res. Lett.*, *26*, 1731–1734, 1999.

Boucher, O., et al., Intercomparison of models representing shortwave radiative forcing by sulfate aerosols, *J. Geophys. Res.*, *103*, 16,979–16,998, 1998.

Buriez, J.-C, C. Vanbauce, F. Parol, P. Goloub, M. Herman, B. Bonnel, Y. Fouquart, P. Couvert, and G. Sèze, Cloud detection and derivation of cloud properties from POLDER, *Int. J. Remote Sensing*, *18*, 2785–2813, 1997.

Deuzé, J.-L., M. Herman, P. Goloub, and D. Tanré, Characterization of aerosols over ocean from POLDER/ADEOS-1, *Geophys. Res. Lett.*, *26*, 1421–1424, 1999.

Goloub, P., D. Tanré, J.-L. Deuzé, M. Herman, A. Marchand, and F.-M. Bréon, Validation of the first algorithm applied for deriving the aerosol properties over the ocean using the POLDER/ADEOS measurements, *IEEE Trans. Geosc. Rem. Sens.*, *37*, 1586–1596, 1999.

Haywood, J. M., V. Ramaswamy, and B. J. Soden, Tropospheric aerosol climate forcing in clear-sky satellite observations over the oceans, *Science*, *283*, 1299–1303, 1999.

Hignett, P., J. P. Taylor, P. N. Francis, and M. D. Glew, Comparison of observed and modeled direct aerosol forcing during TARFOX, *J. Geophys. Res.*, *104*, 2279–2287, 1999.

Key, J., *Streamer user's guide*, Coop. Inst. Res. Environ. Sci., University of Colorado, 71 pp., 1994.

Nakajima, T., and A. Higurashi, A use of two-channel radiances for an aerosol characterization from space, *Geophys. Res. Lett.*, *25*, 3815–3818, 1998.

Russell, P. B., S. A. Kinne, and R. W. Bergstrom, Aerosol climate effects: Local radiative forcing and column closure experiments, *J. Geophys. Res.*, *102*, 9397–9407, 1997.

Estimation de la perturbation radiative des aérosols à la surface et au sommet de l'atmosphère à partir d'une combinaison de mesures POLDER et photomètres

Cette étude est une extension de l'article précédent visant à améliorer l'estimation de la perturbation radiative des aérosols, non seulement au sommet de l'atmosphère mais aussi à la surface. Dans l'étude précédente, nous avons montré que l'absorption par les aérosols entraînait une diminution de l'impact radiatif des aérosols au sommet de l'atmosphère au-dessus des océans : l'augmentation de l'épaisseur optique mesurée à réflectance égale était en effet plus que compensée par une diminution de l'impact radiatif due à l'absorption elle-même. Cependant, il ne s'agissait là que d'une expérience de sensibilité car nous ne disposions pas d'information quantitative sur l'absorption par les aérosols à l'échelle régionale. Ce manque a été en partie comblé par l'étude de Dubovik et al (2002) qui a estimé la variation spectrale de l'albédo de diffusion simple des aérosols pour différentes régions (Figure 1). On remarque par exemple que l'absorption par les poussières désertiques (en haut à droite de la Figure 1) est limitée aux longueurs d'onde inférieures à 500–600 nm. L'albédo de diffusion simple vaut 0.98 à 670 nm pour le modèle "Cap Verde". L'aérosol rencontré aux Maldives pendant l'expérience INDOEX (en haut à gauche de la Figure 1) est en revanche très absorbant, avec un albédo de diffusion simple de 0.90 à 670 nm et une dépendance spectrale inverse de celle des poussières désertiques. Nous avons modifié les modèles d'aérosols de POLDER (indice imaginaire de réfraction et rayon modal de la distribution en taille) de manière à reproduire ces deux dépendances spectrales de l'absorption tout en conservant les 4 valeurs du coefficient d'Angström de l'algorithme POLDER. Nous avons ensuite utilisé ces modèles pour estimer, de la même manière que précédemment, la perturbation radiative des aérosols au sommet de l'atmosphère. Compte-tenu de l'importance de l'absorption par les aérosols et de l'effet semi-direct, nous avons complété ce calcul par une estimation de la perturbation radiative des aérosols à la surface.

La Figure 2 montre les résultats pour l'aérosol désertique au-dessus de l'Océan Atlantique Nord. Le rapport entre les perturbations radiatives à la surface et au sommet de l'atmosphère est d'environ 1,3 à 1,4. Il y a donc relativement peu d'absorption due aux aérosols dans la colonne d'atmosphère. La situation est tout autre en ce qui concerne les aérosols représentatif d'INDOEX. La perturbation radiative au sommet de l'atmosphère est relativement faible compte-tenu des épaisseurs optiques en aérosols. Le rapport entre les perturbations radiatives à la surface et au sommet de l'atmosphère vaut cette fois environ 4, ce qui implique un fort réchauffement de l'atmosphère par les aérosols qui pourrait être à l'origine de l'effet semi-direct proposé par Ackerman et al. (2000).

Fig. 1 : Variation spectrale de l'albédo de diffusion simple de différents types d'aérosols obtenus à partir du réseau AERONET. D'après Dubovik et al. (2002), Figure 1.

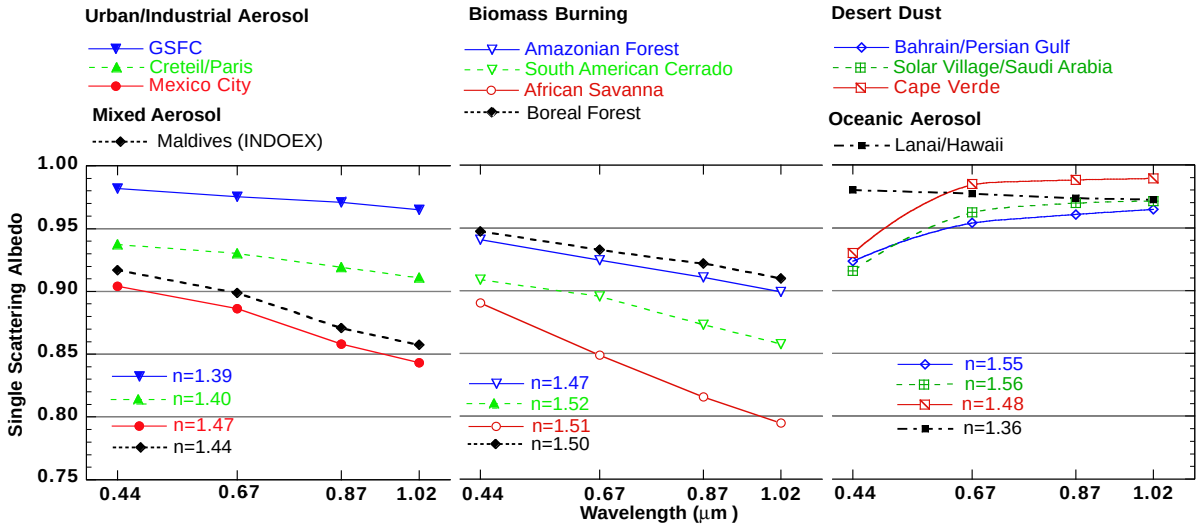

Fig. 2 : Perturbation radiative au sommet de l'atmosphère (à gauche) et à la surface (à droite) due aux aérosols désertiques en moyenne sur le mois de mai 1997.

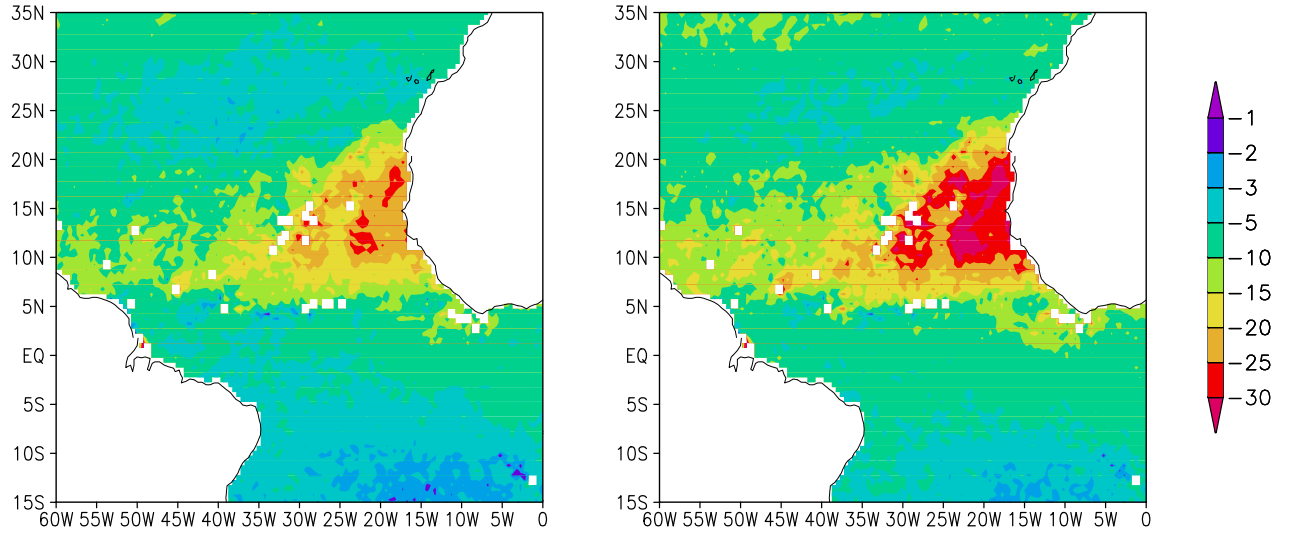

Fig. 3 : Perturbation radiative au sommet de l'atmosphère (à gauche) et à la surface (à droite) due aux aérosols de pollution typiques d'INDOEX en moyenne sur le mois de mars 1997.

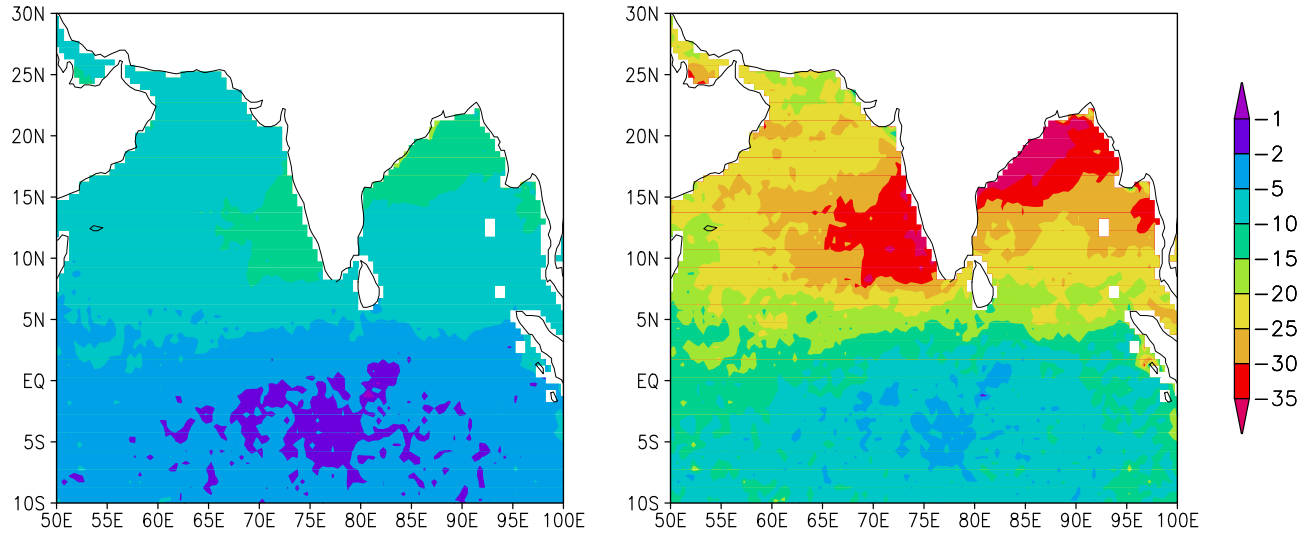

Chapitre 8

Etude de l'effet indirect des aérosols à partir des observations POLDER

Ce chapitre reprend une étude qui n'a pas été publiée.

Is there a discernible aerosol indirect effect on the cloud albedo in the POLDER satellite retrievals?

O. Boucher, J.-C. Buriez, M. Doutriaux-Boucher, I. Chiapello
Laboratoire d'Optique Atmosphérique
U.F.R. de Physique, Bâtiment P5
Université des Sciences et Technologies de Lille
59655 Villeneuve d'Ascq Cedex, France

G. Sèze
Laboratoire de Météorologie Dynamique
Université Pierre et Marie Curie
4 place Jussieu
75252 Paris Cedex 05, France

Abstract. POLDER satellite retrievals of aerosol and cloud properties over ocean are used to detect and quantify the aerosol indirect effect on clouds over the Atlantic Ocean. We find that cloud optical depth covaries with aerosol optical depth and aerosol index off the eastern coast of the United States and off the western coast of Africa in June 1997. We investigate the robustness of this relationship to various assumptions and input parameters of our analysis. The interpretation of the simultaneous increases in aerosol and cloud optical depths is hindered by the fact that other cloud properties (such as the average cloud fraction at the super-pixel size or the Rayleigh cloud-top pressure) also vary with changes in aerosol concentrations and properties. It is not possible to infer whether these concurrent changes in cloud properties are a consequence of aerosol effects or a sampling effect in our analysis. It should also be noted that a significant fraction of the cloud cover (cloud edges near

clear sky and cloud cores far from any clear sky) cannot be linked to aerosol properties in our analysis; this fraction may be of importance for the aerosol indirect effects.

1 Introduction

Anthropogenic aerosols serve as cloud condensation nuclei (CCN), the concentration of which is one of the parameters that determines the cloud droplet number concentration, and hence the cloud microphysical and optical properties. An increase in CCN, for a constant liquid water content, leads to a larger concentration of cloud droplets of smaller radii, thus increasing cloud reflectivity [*Twomey*, 1977]. Many pieces of evidence suggest the potential of such an effect from the smaller scales (shiptracks, aircraft observations of clouds, models of cloud microphysics) to the larger scales (satellite observations of cloud droplet size, general circulation model studies). One can refer to the review study by *Haywood and Boucher* [2000] for more details. Recently, the Aerosol Characterization Experiment (ACE-2) provided evidences for significant differences in the microphysical and radiative properties of stratocumulus clouds which formed in marine versus continental air masses [*Brenguier et al.*, 2000].

Wetzel and Stowe [1999] analyzed aerosol and cloud products from AVHRR data. Their results indicate an inverse relationship between zonal and seasonal averages of aerosol optical depth and droplet size of stratus clouds over ocean. *Bréon et al.* [2002] came to a similar conclusion using the POLDER (Polarization and Directionality of the Earth's Reflectances) data over land and oceans. They showed that regions of large aerosol index coincide with regions of low cloud droplet size. In contrast to *Wetzel and Stowe* [1999] who considered monthly mean parameters at collocated pixels, *Bréon et al.* [2002] related cloud-sky pixels to the clear-sky pixels encountered on a backtrajectory. This should avoid inconsistencies due to different temporal samplings of aerosol and cloud properties made in clear and cloudy sky, respectively. The technique of *Bréon et al.* is limited to homogeneous low clouds, as discussed in *Bréon and Goloub* [1998]. *Schwartz et al.* [2002] combined modelled sulfate aerosol concentrations with satellite-observed cloud properties over the North Atlantic Ocean to show that, within a week time, an increase in sulfate concentrations in the model was accompanied by a decrease in the cloud droplet effective radius. However they could not relate the changes in sulfate concentration and droplet size to a change in cloud optical depth or albedo. So it is clear from the above observational studies that there is a measurable effect of aerosols on the cloud microphysics. However, a clear link relating aerosols to cloud albedo (and eventually aerosol indirect radiative forcing) at the regional (or global) scale is still missing.

In this paper, we investigate the relationships between aerosol optical depth, aerosol index, cloud optical depth, cloud fraction, and cloud-top pressure retrieved by the POLDER instrument over ocean. In contrast to previous studies (with the exception of *Bréon et al.* [2002]), we do not average these parameters over large regions and long timescales; rather we seek relationships between parameters derived from collocated (within a few degree resolution) and simultaneous measurements. While this approach is appropriate to detect a direct link between aerosol and cloud properties, it allows to assess the aerosol effects on a regional scale only.

POLDER is a spaceborne radiometer which worked on board the Japanese ADEOS platform from November 1996 to June 1997. Cloud and aerosol products were retrieved within two distinct processing lines. The cloud processing line includes retrieval of the cloud fraction, cloud optical depth, cloud thermodynamic phase, cloud "Rayleigh" pressure, cloud O_2 pressure, and shortwave albedo [*Buriez et al.*, 1997; *Parol et al.*, 1999]. The O_2 pressure may be less appropriate than the Rayleigh pressure to detect the cloud top because of the photon penetration effect [*Vanbauce et al.*, 1998]. Therefore we use the cloud Rayleigh pressure although it requires specific viewing geometries. The aerosol products over ocean consist of the aerosol optical thickness (at 865 nm) and aerosol Ångström coefficient [*Goloub et al.*, 1999]. The spatial resolution for the level-2 data is about 60 km x 60 km and 20 km x 20 km for the cloud and aerosol products, respectively (see Fig. 1). The cloud screening algorithm for the aerosol retrieval is based on a threshold on the standard deviation of the reflectances at 865 nm in the neighbouring pixels (presently set to $8x10^{-3}$) and a threshold on the reflectance itself (set to 0.2). A minimum of 5 clear-sky level-1 pixels (out of 9) are required to produce the aerosol product at the level 2. This algorithm is quite efficient to avoid cloud contamination in the aerosol retrieval. Some pixels can be declared as clear sky by the cloud processing line, without nevertheless fulfilling the criteria for aerosol retrieval (Fig. 1).

We focus on the month of June 1997 and two different oceanic regions, which are depicted in Fig. 2, namely the West African coast (WAC, 20–0°S, 20°W–20°E) and the North Atlantic Ocean (NAO, 30–50°N, 100–20°W). These two regions were selected because i) there are large concentrations of small aerosols coming from anthropogenic pollution or biomass burning sources

Fig. 1: Schematic of the grid-boxes. Each x° by x° grid-box includes a number of super-pixels (from the POLDER cloud processing line) and a number of pixels (from the POLDER aerosol processing line).

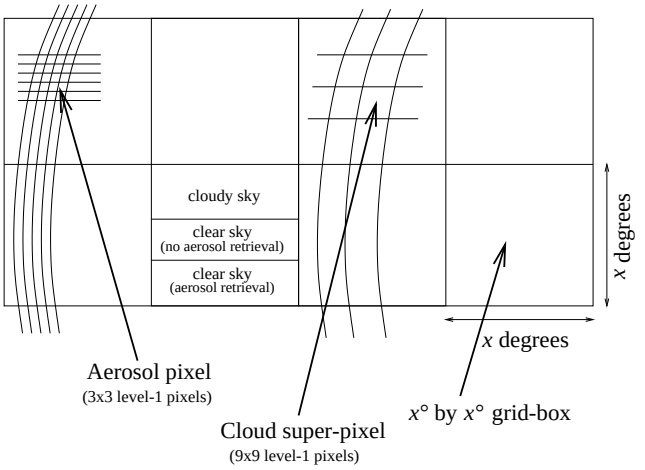

Fig. 2: The two regions examined in this study.

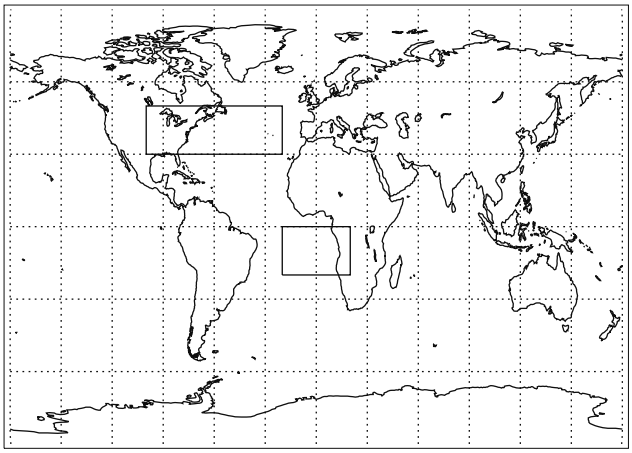

ii) aerosol plumes get mixed in some oceanic cloud fields, and iii) the cloud cover is not too large so aerosols can be retrieved often enough. Examination of the POLDER and TOMS aerosol retrievals [*Herman et al.*, 1997; *Chiapello et al.*, 1999] suggests that these regions are free from desert dust particles. The POLDER aerosol retrieval for June 1997 shows significant aerosol burdens associated with high Ångström coefficients, which indicates the presence of industrial and biomass burning aerosols [*Deuzé et al.*, 1999].

2 Methodology

We adopt a similar approach to *Kaufman and Fraser* [1997]. The different regions are divided into grid-boxes of x degrees by x degrees, where x takes values of 1, 2, 5, and 10 (Fig. 1). The POLDER level-2 data are used to derive, over each grid-box, the average aerosol optical depth at 865 nm in clear-sky pixels, the average cloud optical depth at 670 nm, the average cloud fraction at the super-pixel size, and the average Rayleigh cloud-top pressure in cloudy-sky pixels. Only clouds classified as liquid (according to the cloud phase product) are retained. Because the Rayleigh pressure is not defined under all viewing geometries, its grid-box average is computed over a fraction of the cloudy pixels used to compute the average cloud optical depth and cloud fraction. As we have less confidence in the POLDER cloud products in case of fractional cloudiness, we introduce a threshold cloud fraction $\mathrm{CN_{min}}$ at the super-pixel size. Only super-pixels with a cloud fraction greater than $\mathrm{CN_{min}}$ are considered for computing the average cloud properties described above. This threshold cloud fraction is set to 0.2, 0.5 and 1 in our different estimations.

3 Results

Fig. 3 shows the average cloud optical depth, $\overline{\tau_c}$, in each class of aerosol optical depth for the region off the West African coast. Also shown as whiskers are the average departures in each aerosol class, $\sum_i |\tau_c(i) - \overline{\tau_c}|/N$, computed over grid-boxes with cloud optical depths larger and smaller than $\overline{\tau_c}$, respectively. One observes that the cloud optical depth generally increases with aerosol optical depth. The large scatter, as inferred from the whiskers in Fig. 3, is due to the fact that aerosol optical depth is only one of the many parameters which we expect to control cloud albedo. The average cloud optical depth varies in different ranges of values for different resolutions. It is larger at 10°x10° with $\overline{\tau_c}$ at about 6 than at 1°x1° with $\overline{\tau_c}$ at about 3. Since our analysis requires the presence of both clear and cloudy skies, the larger resolution includes more clouds with a large horizontal extension than the smaller resolution. Horizontally larger clouds are also deeper clouds. The slope of the relationship between cloud and aerosol optical depths also depends on the chosen resolution. However, we could not find any obvious explanation for that. More intriguing is the fact that the increase in cloud optical depth with aerosol optical depth is accompanied by an increase in the average cloud fraction (taken at the super-pixel size) and a decrease in cloud Rayleigh pressure. If we think of the average cloud fraction as an independent parameter, its increase can also explain the increase in cloud optical depth as these two parameters have been shown to be positively correlated in the POLDER data.

Fig. 3: Averaged cloud optical depth as a function of averaged aerosol optical depth for the oceanic region off the West African coast (WAC) for different resolution (10°x10°, 5°x5°, 2°x2°, and 1°x1° from top to bottom). The rectangles represent the average cloud optical depth weighted by the cloud fraction in each class of aerosol optical depth. The whiskers are the average departures computed over grid-boxes with cloud optical depths larger and smaller than the average, respectively. The distributions of the cloud optical depth are given for different thresholds on the cloud fraction at the super-pixel size (CN_{min}=0.2, 0.5, and 1). The distributions of the averaged cloud fraction (CN) and cloud Rayleigh pressure (P_c) are also given for the case CN_{min}=0.5. The red curves indicate the number of grid-boxes entering the average in each class of aerosol optical depth. Averaged cloud optical depths are not plotted when this number is smaller than 200, 200, 50, and 20 at the 1°x1°, 2°x2°, 5°x5°, and 10°x10° resolutions, respectively.

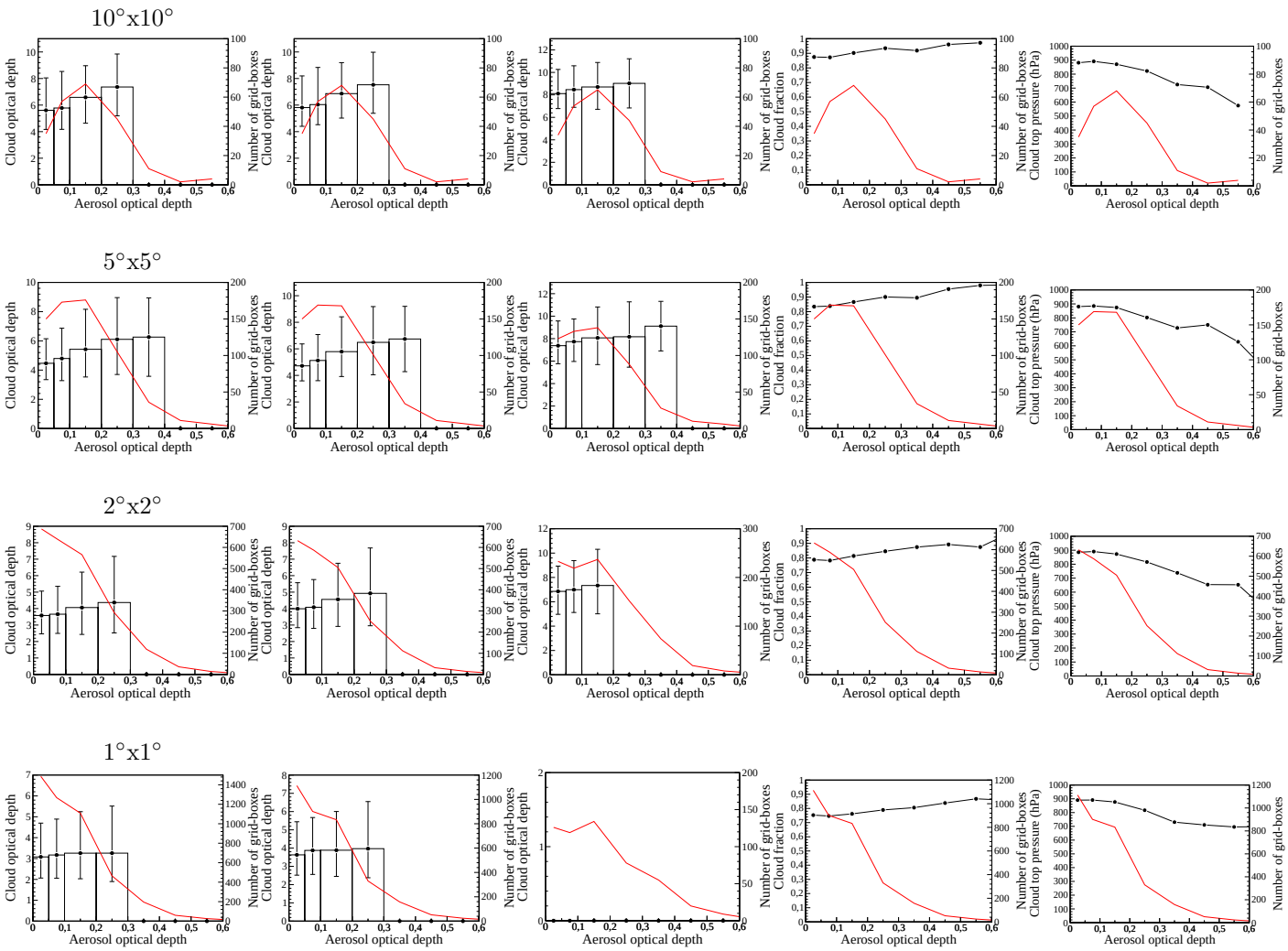

It is noteworthy that the slope of the cloud to aerosol optical depth relationship decreases when only completely cloudy super-pixels are considered (CN$_{min}$=1), which supports the hypothesis that changes in cloud optical depth are related to some extent to changes in the average cloud size. Similarly the decrease in cloud Rayleigh pressure (or say differently the increase in cloud top height) with aerosol optical depth can also explain

Fig. 4: Same as Figure 3 but as a function of the POLDER aerosol index.

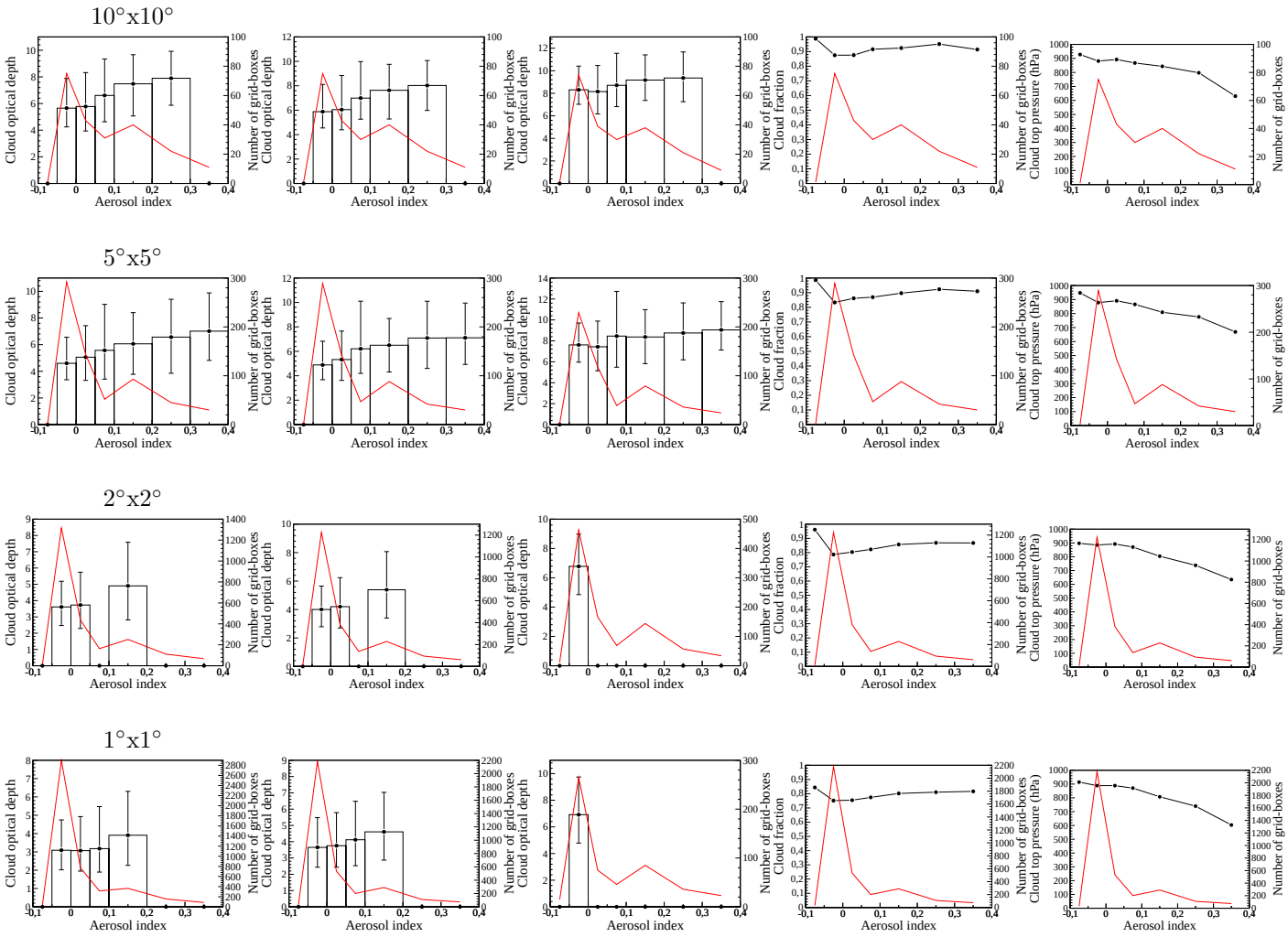

some of the variations in cloud optical depth, although the relationship between these two parameters is more complex. It is not yet possible to prioritize these two potential explanations:

A/ Aerosols influence clouds through the second indirect effect, changing not only their microphysical but also their macroscopic properties, such as their average horizontal and vertical extension. In this case the observed increase in cloud optical depth with aerosol optical depth can be entirely attributed to aerosol effects.

B/ The increase in average cloud fraction and the decrease in cloud Rayleigh pressure are an artifact of our sampling method. For some reason, related for instance to the synoptic-scale meteorology, clouds have different macroscopic properties when meteorological conditions allow the transport of aerosol plumes from the African continent. It is also conceivable that the aerosol plumes are above (i.e., decoupled from) the cloud layers. In this case the observed increase in cloud optical depth with aerosol optical depth is not the signature of an aerosol microphysical effect.

The same analysis repeated as a function of the POLDER aerosol index instead of the aerosol optical depth shows the same features: an increase in cloud optical depth with aerosol index, which is more pronounced at larger resolution and low threshold cloud fraction. We also perform the same analysis off the coast of Eastern

Fig. 5: Same as Figure 3 but for the oceanic region off the Eastern United States over the North Atlantic Ocean.

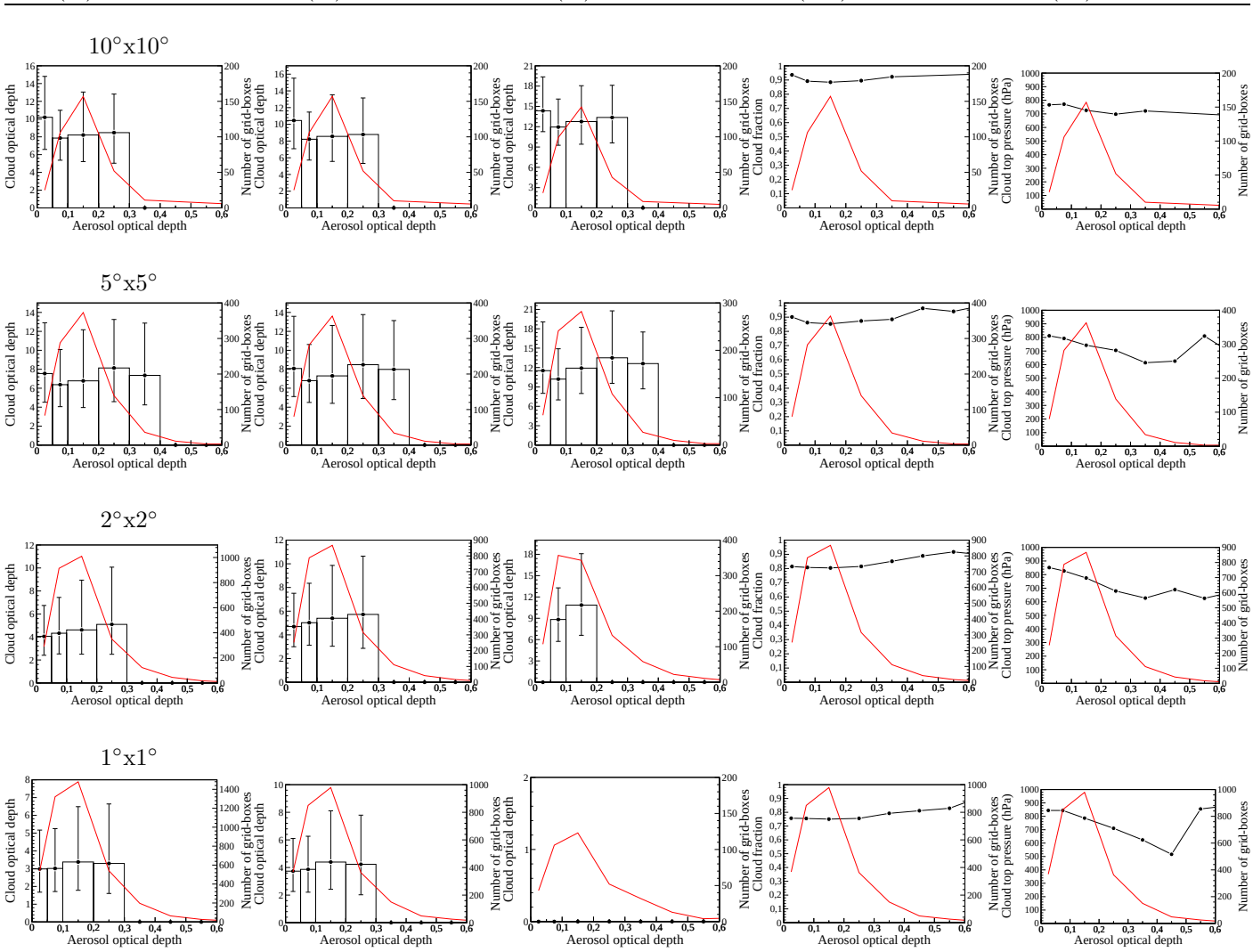

United-States over the North Atlantic Ocean (Figs. 5 and 6). For this region the cloud to aerosol relationships are less clear. Cloud optical depth increases with aerosol optical depth and aerosol index at some resolutions but a decrease or no clear tendency is observed at some other resolutions. In most cases the changes in average cloud optical depth follow the changes in average cloud fraction. This suggests that the average cloud fraction has more predictive skills than the aerosol optical depth and aerosol index, as also shown by multiple linear regressions performed over the full set of sampled grid-boxes.

4 Conclusions

We have shown an increase in cloud optical depth with aerosol optical depth over the Atlantic Ocean off the coast of West Africa and to some extent off the coast of Eastern United States. Although we expect such a relationship to occur it is not clear whether it can really be attributed to an aerosol effect. We have seen that concurrent changes in the average cloud fraction at the super-pixel size (taken as an indicator of the spatial extent of clouds) can also explain the increase in cloud optical depth.

A significant fraction of the cloud cover (either cloud edges near clear sky regions or cloud cores far from any

Fig. 6: Same as Figure 5 but as a function of the POLDER aerosol index.

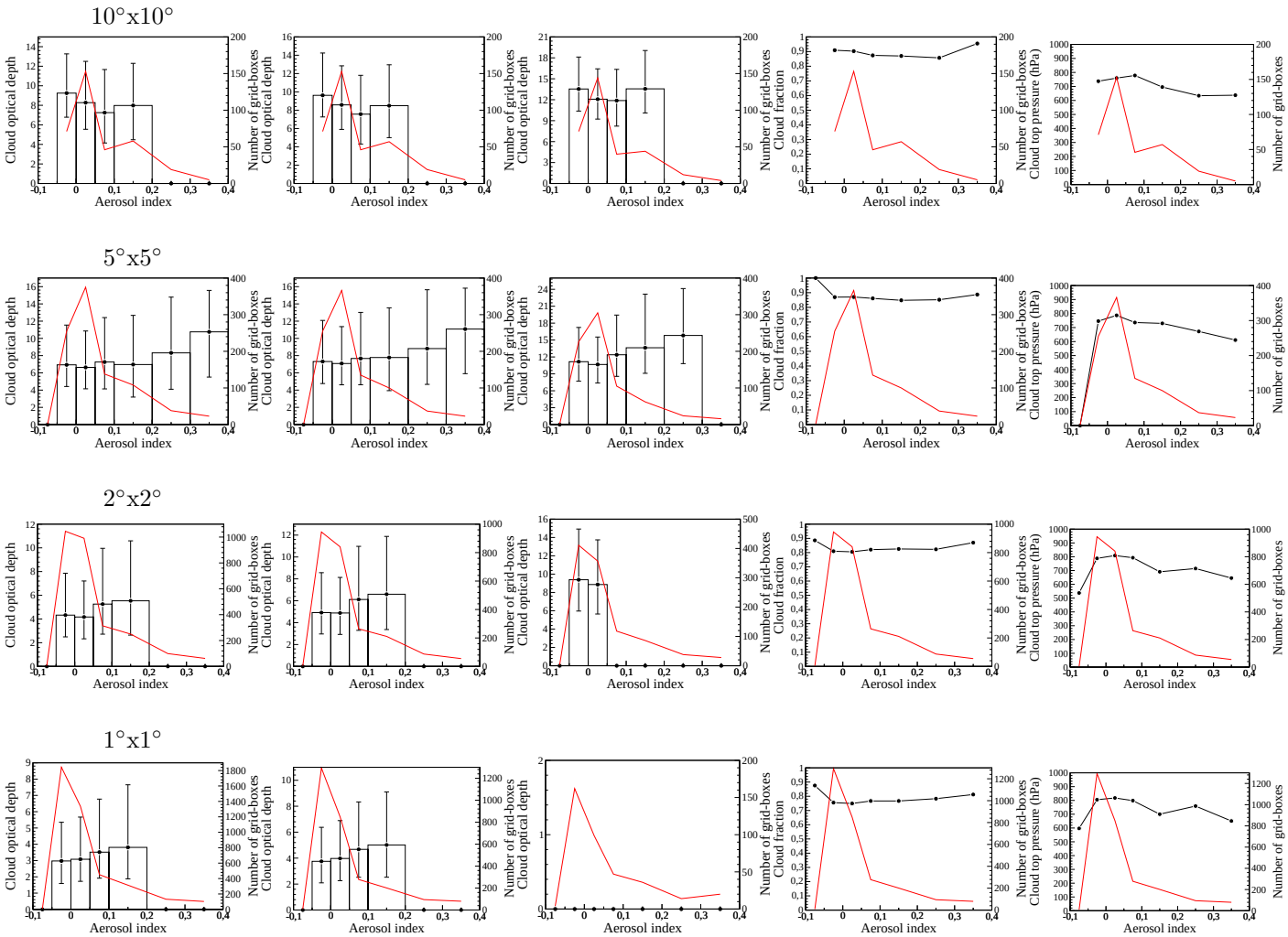

clear sky region) cannot be linked to aerosol properties in our analysis; this fraction may be of importance for the aerosol indirect effects. It should also be noted that we have less confidence in the retrieved cloud properties in the case of fractional cloudiness at the super-pixel size. However this class of fractional clouds may play an important role in the issue of aerosol indirect effects. This study also points out to the fact that satellite measurements should be examined very carefully when it comes to determining the aerosol indirect effect. A correlation between cloud and aerosol optical depth (and likewise between cloud droplet size and aerosol optical depth) may simply arise because the two quantites both vary with a third parameter, such as the relative humidity or the cloud macroscopic properties. Also, it may not be appropriate to scale up results obtained under very specific conditions or for a particular cloud type.

This study raises more questions than provides answers. More detailed studies are needed whereby the analysis of satellite data should be strengthened by model results. For instance the origin of the cloudy air masses sampled in our analysis by POLDER should be determined from meteorological analysis to see whether there are other plausible explanations than aerosols for the observed changes in cloud properties. The forthcoming AQUA-train mission composed of the AQUA, PARASOL, CloudSat and CALIPSO satellites will even-

tually provide a more comprehensive set of measurements which should allow deeper analysis of aerosol-cloud interactions.

Acknowledgements. We acknowledge Aurélia Marchand and Françoise Hennequart for their help in processing the POLDER data. POLDER is a joint CNES/NASDA effort. Information on the POLDER products can be found at http://smsc.cnes.fr/POLDER/index.htm. Olivier Boucher would like to thank the Max Planck Institute for chemistry for hospitality. Jim Haywood and Jean-Louis Brenguier are acknowledged for their constructive comments on earlier versions of this draft.

References

Boucher, O., and D. Tanré, Estimation of the aerosol perturbation to the Earth's radiative budget over oceans using POLDER satellite aerosol retrievals, *Geophys. Res. Lett.*, *27*, 1103–1106, 2000.

Brenguier, J.-L., P. Y. Chuang, Y. Fouquart, D. W. Johnson, F. Parol, H. Pawlowska, J. Pelon, L. Schüller, F. Schröder, and J. Snider, An overview of the ACE-2 CLOUDYCOLUMN closure experiment, *Tellus*, *52B*, 815–827, 2000.

Bréon, F.-M., and P. Goloub, Cloud droplet effective radius from spaceborne polarization measurements, *Geophys. Res. Lett.*, *25*, 1879–1882, 1998.

Bréon, F.-M., D. Tanré, and S. Generoso, Aerosol effect on cloud droplet size monitored from satellite, *Science*, *295*, 834–838, 2002.

Buriez, J.-C, C. Vanbauce, F. Parol, P. Goloub, M. Herman, B. Bonnel, Y. Fouquart, P. Couvert, and G. Sèze, Cloud detection and derivation of cloud properties from POLDER, *Int. J. Remote Sensing*, *18*, 2785–2813, 1997.

Chiapello, I., J. M. Prospero, J. R. Herman, and N. C. Hsu, Detection of mineral dust over the North Atlantic Ocean and Africa with the Nimbus 7 TOMS, *J. Geophys. Res.*, *104*, 9277–9291, 1999.

Deuzé, J.-L., M. Herman, P. Goloub, and D. Tanré, Characterization of aerosols over ocean from POLDER/ADEOS-1, *Geophys. Res. Lett.*, *26*, 1421–1424, 1999.

Goloub, P., D. Tanré, J.-L. Deuzé, M. Herman, A. Marchand, and F.-M. Bréon, Validation of the first algorithm applied for deriving the aerosol properties over the ocean using the POLDER/ADEOS measurements, *IEEE Trans. Geosc. Rem. Sens.*, *37*, 1586–1596, 1999.

Haywood, J., and O. Boucher, Estimates of the direct and indirect radiative forcing due to tropospheric aerosols: A review, *Rev. Geophys.*, 38, 513–543, 2000.

Herman, J. R., P. K. Barthia, O. Torres, C. Hsu, C. Seftor, and E. Celarier, Global distribution of UV-absorbing aerosols from NIMBUS-7/TOMS data, *J. Geophys. Res.*, *102*, 16911–16922, 1997.

Kaufman, Y. J., and R. S. Fraser, The effect of smoke particles on clouds and climate forcing, *Science*, *277*, 1636–1639, 1997.

Nakajima, T., A. Higurashi, K. Kawamoto, and J. Penner, A possible correlation between satellite-derived cloud and aerosol microphysical parameters, *Geophys. Res. Lett.*, *28*, 1171–1174, 2001.

Parol, F., J.-C. Buriez, C. Vanbauce, P. Couvert, G. Sèze, P. Goloub, and S. Cheinet, First results of the POLDER "Earth Radiation Budget and Clouds" operational algorithm, *IEEE Trans. Geosc. Rem. Sens.*, *37*, 1597–1612, 1999.

Schwartz, S., Harshvardhan, and C. M. Benkovitz, Influence of anthropogenic aerosol on cloud optical depth and albedo shown by satellite measurements and chemical transport modeling, *Proc. Natl. Acad. Sci. USA*, *99*, 1784–1789, 2002.

Suttles, J. T., et al., Angular radiation models for Earth-Atmosphere system, Volume I – Shortwave radiation, *NASA Ref. Publ. 1184*, 147 pp., 1988.

Twomey, S., The influence of pollution on the shortwave albedo of clouds, *J. Atmos. Sci.*, *34*, 1149–1152, 1977.

Vanbauce, C., J.-C. Buriez, F. Parol, B. Bonnel, G. Sèze, and P. Couvert, Apparent pressure derived from ADEOS-POLDER observations in the oxygen A-band over ocean, *Geophys. Res. Lett.*, *25*, 3159–3162, 1998.

Wetzel, M. A., and L. L. Stowe, Satellite-observed patterns in stratus microphysics, aerosol optical depth and shortwave radiative forcing, *J. Geophys. Res.*, *104*, 31286–31299, 1999.

Chapitre 9

Prospective : comment réduire les incertitudes des forçages radiatifs des aérosols

Ce chapitre reprend ma contribution à l'atelier de prospective de l'International Global Atmospheric Chemsitry (IGAC planning meeting) qui s'est tenu à Stockholm en janvier 2002. Cette contribution a été publiée dans la revue IGACtivities (Boucher, 2002).

Aerosol radiative forcing and related feedbacks: How do we reduce uncertainties?

Contributed by **O. Boucher** (boucher@loa.univ-lille1.fr), *Laboratoire d'Optique Atmosphérique, CNRS / USTL, Villeneuve d'Ascq, France.*

1. Introduction

There are now well established definitions for the climatic effects of aerosols which are split into the direct, semi-direct, first and second indirect aerosol effects. The direct effect refers to the extinction of sunlight by aerosols (as well as aerosol extinction and emission of longwave radiation), which acts primarily in clear sky. The semi-direct effect encompasses the impacts of aerosol absorption in clear (and cloudy) sky on the temperature and humidity profiles, which can feedback on cloud formation and cloud cover. The first indirect effect relates to the increase in cloud optical depth and cloud albedo due to an increase in the number and a decrease in the size of cloud droplets (for a fixed liquid water content). Finally, the second indirect effect refers to an increase in the cloud liquid water content, cloud height, or cloud lifetime due to a reduced precipitation efficiency because of the decrease in the cloud droplet size. While the first and second indirect effects can be easily separated in a model framework, it may not be possible to observe them independently from each other.

The climatic effects are one among many reasons to study aerosols. It is clear from the Third Assessment Report of the Intergovernmental Panel on Climate Change that the current uncertainty on aerosol radiative forcing prevents us from a straightforward interpretation of the temperature record [Boucher and Haywood, 2001; Knutti *et al*., 2002]. Figure 1 shows that, accounting for the uncertainties given by Ramaswamy *et al*. [2001] for the individual radiative forcings, the total aerosol radiative forcing has a much broader distribution than the total non-aerosol radiative forcing. Anthropogenic aerosols are known as an important climate agent not only affecting the Earth's temperature but also the water cycle (see contribution by U. Lohmann). Natural aerosols are part of the climate system and may be involved in climate feedbacks in a changing climate. The source of mineral dust may change following changes in the soil moisture, land use, or wind fields. The source of dimethylsulfide (a precursor of sulfate aerosols in maritime environment) may change because of a different wind field or if the oceanic food-web is changed in a warmer climate. Finally the source of sea salt aerosol may also change if the wind field is changing. Acidic aerosols are responsible for acid deposition ("acid rain") which can be very harmful to the ecosystems. Aerosols participate to air pollution – they are usually measured as PM2.5 or PM10 – and may be responsible for problems on human health. Regional to intercontinental transport of aerosols needs to be understood before designing regional policies of aerosol pollution monitoring and emission abatements. Fertilization of the world oceans occurs through deposition of aerosols; there is here a potential link between the carbon and aerosol biogeochemical cycles. Improving medium-range weather forecasts now requires to better consider the day-to-day variability of the aerosol radiative effects and make better atmospheric corrections on satellite-retrieved variables which are assimilated in numerical weather prediction models. The impacts of heterogeneous chemistry in urban to global air chemistry are still not well quantified and would also deserve more studies.

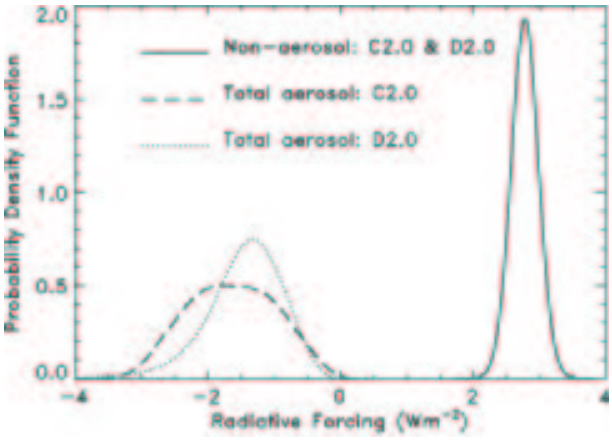

Figure 1. Probability function of the aerosol and non-aerosol radiative forcings (Wm-2). The total aerosol radiative forcing has a much broader distribution than the total non-aerosol radiative forcing. This conclusion is fairly independent from the assumptions made on the exact shape of the distribution functions of the individual forcings. From Boucher and Haywood [2001].

In this paper, we are more particularly concerned by the direct and semi-direct effects of aerosols, the indirect effects being covered in the contributions of C. Facchini and U. Lohmann in this issue of IGAC*tivities*. Our focus here is on *modeling* and *observing* aerosols at the *global scale*.

2. Evolution of global aerosol modeling

Global models have been used extensively to predict the global aerosol distribution and their radiative forcings. Although they include many simplifying assumptions, they remain essential tools to investigate the climatic role

of aerosols. There has been considerable progress on aerosol modeling over the last 10 years (Figure 2), from the pioneering work of Langner and Rodhe [1991] to the most recent global simulations of the multi-component aerosols including sulfate, black and organic carbon aerosols from fossil fuel and biomass burning, mineral dust, and sea salt [e.g., Chin *et al*., 2002]. Exploratory studies also simulate the contribution of ammonium and nitrate to the burden of inorganic aerosol [Adams *et al*., 2001]. Fly ash from industrial activities may also contribute significantly to the aerosol mass in some regions [Reddy and Venkataraman, 2002; Satheesh and Ramanathan, 2000]. Aerosols were first modeled as an external mixture [e.g., Tegen *et al*., 1997; Chin *et al*., 2002] but progress is now made to simulate the growth of mixed aerosol populations [Wilson *et al*., 2001].

The direct radiative effects of aerosols depend on parameters which can be classified in 3 categories: biogeochemical parameters (such as the emission strength of the primary or secondary aerosols and the aerosol lifetime), atmospheric parameters (such as the clear-sky relative humidity, cloud cover, or surface albedo), and microphysical parameters (such as the aerosol size distribution, hygroscopicity, optical properties, and state of mixture). These 3 classes of parameters were initially dealt separately, and in-situ measurements were used to prescribe the microphysical parameters not predicted by the global models. Global aerosol models are becoming able to predict the aerosol microphysical parameters, in a way that is more coherent with the rest of the physical and chemical processes [e.g., Wilson *et al*., 2001]. This evolution in aerosol modeling has some consequences on the observational strategies needed to address the radiative effects of aerosols.

There is a large range in the simulated direct radiative forcings due to different aerosol species. The discrepancies in direct radiative forcing calculations seem to originate from the treatment of the hygroscopic and optical properties of the aerosols (as well as from the role of cloudiness in the direct aerosol effect) rather than from the aerosol burdens alone [Haywood and Boucher, 2000]. Despite the attempts of Charlson *et al*. [1992] and Penner *et al*. [2001] there does not exist a thorough budget of uncertainties of the aerosol radiative forcings. This is because the uncertainties in the individual parameters entering the calculation of the direct aerosol radiative forcing themselves are not well known. One can for instance raise the question whether the uncertainty on the cloud cover, which is mostly due to very thin cirrus clouds, is critical or not –the direct effect by aerosols may still be significant in the presence of a very thin cirrus cloud cover. Moreover, correlations among the different parameters are not well known (e.g., diurnal cycle in relative humidity, cloud cover, aerosol chemical composition, and size distribution). However, some aspects can clearly be identified as causing significant uncertainties. These include the hygroscopic properties of the mixed aerosol and the sub-grid scale distribution of relative humidity and clouds in models, the aerosol absorption (through the *spectrally-resolved* aerosol single scattering albedo), the emission strength of carbonaceous aerosols, especially in Africa and Asia, or the vertical distribution of mineral dust.

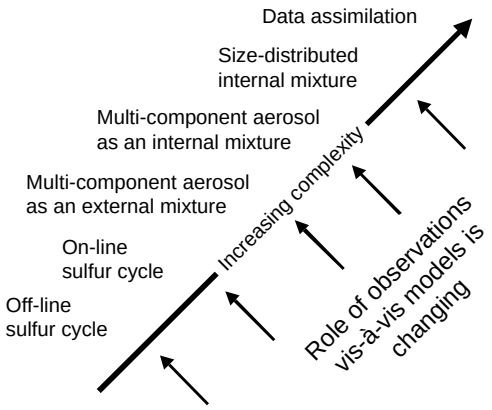

Figure 2. Schematic diagram showing the evolution of global aerosol models.

The ranges in radiative forcings given by IPCC for the aerosol direct effect are to a great extent based on the existing literature. It is hardly possible at the moment to rate the performances of the different models objectively and/or to interpret the model-to-model differences in terms of their parameterizations [Lohmann *et al*., 2001]. There is a risk that the current spread in model results does not narrow down as the models get more complex. One suggestion to get out of this dilemma would be to pin down and understand the model-to-model discrepancies in terms of what is causing the largest differences in aerosol radiative forcing. These aspects of the models should then be confronted to observations so that eventually one can decide which model results are most reliable.

There have been so far few links between the urban, regional, and global scales. Different models and measurement networks are involved. Yet, mega-cities emerge as an important research topic in atmospheric chemistry, the concerns about air pollution are raising to the regional or even hemispheric scales, and the resolution of global models is improving rapidly over time. As a consequence, it would be valuable to establish bridges between the urban and the global scales, for instance by rationalizing routine measurements. One can imagine that air pollution networks become interested in aerosol optical depth (a measurement typically made for monitoring the aerosol radiative effects) and global modelers find

some interest in measurements of PM2.5 concentrations averaged over large cities.

3. Role of observations

Clearly the role of observations vis-à-vis global-scale modeling is changing. Observations can serve many different functions.

Evaluating Models: Aerosol models should be evaluated with a full range of observations, including chemical, physical, and optical measurements of aerosols. Long-term continuous measurements are particularly useful to evaluate the seasonal variations in aerosol concentrations and properties in models. Particularly interesting in this context is the AERONET/AEROCAN/PHOTONS network of sunphotometers which provides measurements of aerosol optical depth as well as information on the aerosol size distribution [Holben *et al*., 2001]. Dubovik *et al*. [2002] also analyzed these data to infer the wavelength dependence of the aerosol single scattering albedo at different locations worldwide. We are also learning a lot as well from networks set up for monitoring aerosol concentration and deposition at the regional or continental scale (such as EMEP or EMEFS) . For aerosol properties more difficult to measure and for which no monitoring is possible, compilations of existing data from field campaigns can also be very valuable. One can mention here the compilation of aerosol size distribution in the marine environment made by Heintzenberg *et al*. [2000].

Testing Parameterizations: Not only model results should be evaluated but also parameterizations. The most critical parameterizations in global-scale models are those of wet scavenging (in-cloud, below-cloud, or through entrainment in convective updrafts), convective transport, sub-grid scale distribution of relative humidity and cloud cover. Evaluation of these parameterizations may require dedicated measurements and a hierarchy of models.

Bridging Aerosol Knowledge Gaps: There are still many gaps in aerosol knowledge that only innovative research can tackle. Among those gaps, one can mention i) the hygroscopic properties of the mixed aerosol (containing in particular carbonaceous species), ii) the absorption properties of the mixed aerosol (with a focus on aerosols containing black and organic carbon and dust), and iii) the formation of secondary organic aerosols. (See the contribution of C. Facchini in this issue).

Developing Data Assimilation Schemes: Data assimilation in global models requires data of good and uniform quality. Satellite observations with their regional or global coverage are obviously well suited for that and will be playing an increasing role in the future [Collins *et al*., 2001]. Ground-based networks are also very interested in this respect. There is also the need for standardized continuous measurements that can easily fit in global models. T. L. Anderson suggested for instance that the accumulation to coarse mode ratio in aerosol optical depth or aerosol mass could be one such parameter.

Satellite observations of aerosols are playing an increasing role. However, aerosol remote sensing only recently left its infancy. There is a large variety of instruments and algorithms used for aerosol remote sensing. Aerosol products from TOMS (over land and ocean) and METEOSAT (over ocean only) turned out to be useful because of their long temporal series. New instruments, more specifically designed for aerosol retrievals, such as POLDER, MISR or MODIS, now provide more accurate measurements of aerosol optical depth. Some information is also available on the aerosol size distribution through the Angström coefficient or the relative weight of the accumulation and coarse modes. Aerosol retrieval over land surfaces is more difficult than over the ocean but progress has also been made. Using measurements of polarized light, POLDER can retrieve an aerosol index over land surfaces that may be interpreted as the optical depth of the aerosol accumulation mode [Deuzé *et al*., 2001]. MODIS can retrieve the aerosol optical depth over land surfaces which are not too bright. Although these satellite aerosol products have been compared with ground-based measurements from sunphotometers, it is not clear how these measurements should be compared with each other and with model outputs. It will be particularly important to understand the exact nature of the satellite aerosol measurements made by the various instruments and reconcile the observed differences. Quite some attention should be given to potential biases that could arise from the satellite sampling and the cloud screening algorithm. Figure 3 shows the spatial and temporal scales involved in global-scale models, geostationary and sun-synchronous satellites. Comparisons between satellite observations and models (and *a fortiori* data assimilation) should consider the differences in scales, which can impact for instance the definition of clear sky. The scientific community (and the funding agencies) should progressively move from aerosol observation to aerosol monitoring.

4. The future

What should be the foci of future aerosol research to reduce the uncertainties of aerosol radiative forcings and climate feedbacks in which aerosols may be involved? It is, of course, not possible to give a complete answer. But, some research directions appear clearly. These include:

Improving present and future emission inventories

This implies designing the emission inventories for anthropogenic aerosols in a way that makes it easy to update them. Future emissions of aerosols (on which the

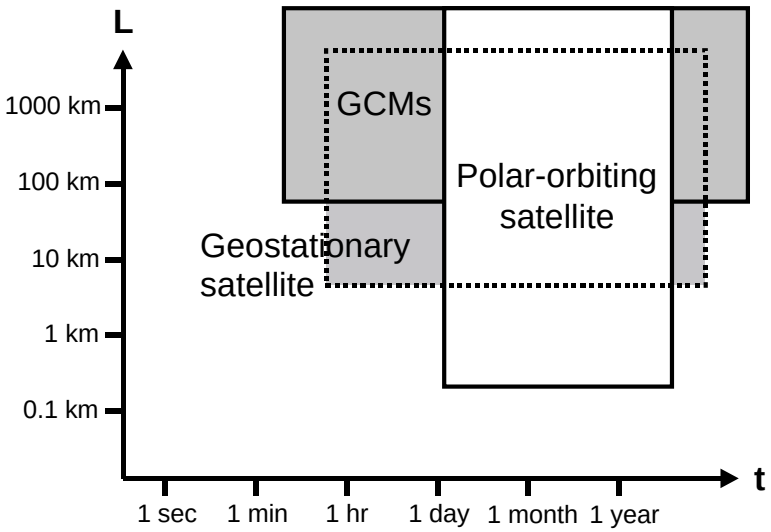

Figure 3. Spatial (L) and temporal(t) scales resolved explicitly in general circulation models (GCMs), geostationary and polar-orbiting satellites.

future climate depends to some extent) are driven by the magnitude of the impacts on human health and ecosystems people will tolerate more than by considerations on the climate! Therefore future emission inventories should incorporate social aspects in addition to economical ones. There is also a need to derive robust, physically-based parameterizations for natural aerosol sources.

Focusing on the aerosol vertical profile

Surface and spaceborne passive instruments miss the vertical dimension of the aerosol distribution. However aerosol scavenging and transport and the direct effect in the longwave –which is important for mineral dust – depend critically on the vertical profile of aerosol properties. There is a large potential to improve models in this respect with the help of surface lidar networks (such as EARLINET) and the forthcoming spaceborne lidar missions (GLAS, CALIPSO, and EarthCare).

Integrating scales using a hierarchy of models

There is a variety of spatial and temporal scales involved in aerosol measurements and modeling [Charlson, 2001]. Developing simple routine measurements worldwide and introducing data assimilation in global aerosol models can help to get a global aerosol picture.

Observing and modeling the state of mixture of multi-component aerosols

We should determine simple ways to describe and predict the hygroscopic and optical properties of the mixed aerosol from a limited number of parameters. Special attention should be given to the aerosol single scattering albedo, which is a critical parameter in aerosol radiative forcing.

Distinguishing natural and anthropogenic contributions to the observed aerosol

It is not easy to separate the natural and anthropogenic components of the aerosol. Natural and anthropogenic material can even be mixed in a single particle. We should try however to see whether there are means to separate the natural and anthropogenic contributions to the aerosol using a combination of in-situ and remote observations.

Studying the transition between clear and cloudy sky

Remote sensing tends to separate artificially clear-sky from cloudy-sky scenes and disregard partially cloudy scenes. For instance the POLDER algorithm considers 20% of the pixels being non-cloudy but not clear enough to perform an aerosol retrieval (this percentage depends critically on the spatial resolution, 6 km in the case of POLDER). In reality, we know that there can be a continuum between clear and cloudy skies, with situations of haze composed of aerosol droplets not activated but of micronic size [Charlson *et al.*, 2001].

Developing a synergy between models and different satellite datasets

As mentioned above, this requires first an understanding of the effects of sampling and cloud screening in satellite data. Models and satellite data can be married through inversion and assimilation techniques. Model improvements should continue and satellite data should be used in more innovative ways. They can be useful to diagnose and monitor the regions of aerosol emissions. We should develop more original aerosol products, e.g. by deriving the aerosol radiative perturbation directly from the measurements of aerosol radiances or by combining aerosol retrievals from radiometers and radiation budget instruments (such as ERBE and CERES). Different satellite aerosol datasets can be merged together to develop level-4 aerosol products which combine the strengths of each dataset.

5. References

Adams, P. J., J. H. Seinfeld, D. Koch, L. Mickley, and D. Jacob, General circulation model assessment of the direct radiative forcing by the sulfate-nitrate-ammonium-water inorganic aerosol system, *J. Geophys. Res.*, **106**, 1097-1111, 2001.

Boucher, O., and J. Haywood, On summing the components of radiative forcing of climate change, *Clim. Dyn.*, **18**, 297-302, 2001.

Charlson, R. J., S. E. Schwartz, J. M. Hales, R. D. Cess, J. A. Coakley, J. E. Hansen, and D. J. Hofmann, Climate forcing by anthropogenic aerosols. *Science*, **255**, 423-430, 1992.

Charlson, R. J., J. H. Seinfeld, A. Nenes, M. Kulmala, A. Laaksonen, and C. M. Facchini, Reshaping the theory of cloud formation, *Science*, **292**, 2025-2026, 2001.

Charlson, R. J., Extending atmospheric aerosol measurements to the global scale, IGAC*tivities*, **25**, 11-14, December 2001.

Chin, M., P. Ginoux, S. Kinne, O. Torres, B. N. Holben, B. N. Duncan, R. V. Martin, J. A. Logan, A. Higurashi, and T. Nakajima, Tropospheric aerosol optical thickness from the GOCART model and comparisons with satellite and sun photometer measurements, *J. Atmos. Sci.*, **59**, 461-483, 2002.

Collins, W. D., P. J. Rasch, B. E. Eaton, B. V. Khattatov, J.-F. Lamarque, and C. S. Zender, Simulating aerosols using a chemical transport model with assimilation of satellite aerosol retrievals: Methodology for INDOEX, *J. Geophys. Res.*, **106**, 7313-7336, 2001.

Deuzé, J.-L., F.-M. Bréon, C. Devaux, P. Goloub, M. Herman, B. Lafrance, F. Maignan, A. Marchand, F. Nadal, G. Perry, and D. Tanré, Remote sensing of aerosols over land surfaces from POLDER-ADEOS-1 polarized measurements, *J. Geophys. Res.*, **106**, 4913-4926, 2001.

Dubovik, O., B. Holben, T. F. Eck, A. Smirnov, Y. J. Kaufman, M. D. King, D. Tanré, and I. Slutsker, Variability of absorption and optical properties of key aerosol types observed in worldwide locations, *J. Atmos. Sci.*, **59**, 590-608, 2002.

Haywood, J. M., and O. Boucher, Estimates of the direct and indirect radiative forcing due to tropospheric aerosols: A review, *Rev. Geophys.*, **38**, 513-543, 2000.

Heintzenberg, J., D. C. Covert, and R. van Dingenen, Size distribution and chemical composition of marine aerosols: A compilation and review, *Tellus*, **52B**, 1104-1122, 2000.

Holben, B. N., *et al.*, An emerging ground-based aerosol climatology: Aerosol optical depth from AERONET, *J. Geophys. Res.*, **106**, 12067-12097, 2001.

Knutti, R., T. F. Stocker, F. Joos, and G.-K. Plattner, Constraints on radiative forcing and future climate change inferred from a combination of observed warming and climate models, *Nature*, in press, 2002.

Langner, J., and H. Rodhe, A global three-dimensional model of the tropospheric sulfur cycle, *J. Atmos. Chem.*, **13**, 225-263, 1991.

Lohmann, U., *et al.*, Vertical distributions of sulfur species simulated by large-scale atmospheric models in COSAM: Comparison with observations, *Tellus*, **53B**, 646-672, 2001.

Penner, J., *et al.*, Aerosols, their direct and indirect effects, In: *Climate Change 2001: The Scientific Basis, Chapter 5, Contribution of Working Group I to Third Assessment Report of the Intergovernmental Panel on Climate Change,* Cambridge University Press, Cambridge, UK, pp. 289-348, 2001.

Ramaswamy, V., *et al.*, Radiative forcing of climate change, In: *Climate Change 2001: The Scientific Basis, chapter 6, Contribution of Working Group I to Third Assessment Report of the Intergovernmental Panel on Climate Change,* Cambridge University Press, Cambridge, UK, pp. 349-416, 2001.

Reddy, M. S., and C. Venkataraman, Inventory of aerosol and sulphur dioxide emissions from India: Part I –Fossil fuel combustion, *Atmos. Env.*, **36**, 677-697, 2002.

Satheesh, S. K., and V. Ramanathan, Large differences in tropical aerosol forcing at the top of the atmosphere and Earth's surface, *Nature*, **405**, 60-63, 2000.

Tegen, I., P. Hollrig, M. Chin, I. Fung, D. Jacob, and J. Penner, Contribution of different aerosol species to the global aerosol extinction optical thickness, *J. Geophys. Res.*, **102**, 23895-23915, 1997.

Wilson, J., C. Cuvelier, and F. Raes, A modeling study of global mixed aerosol fields, J. *Geophys. Res.*, **106**, 34081-34108, 2001.

Appendix

Acronyms reffered to in this article:

AERONET = Aerosol Robotic Network

CALIPSO = Cloud-Aerosol Lidar and Infrared Pathfinder Satellite Observations

CERES = Clouds and the Earth's Radiant Energy System

EARLINET = European AeRosol LIdar NETwork

EarthCare = Earth Cloud, Aerosol and Radiation Explore

EMEFS = Eulerian Model Evaluation Field Study

EMEP = Co-operative programme for monitoring and evaluation of the long-range transmissions of air pollutants in Europe

ERBE = Earth Radiation Budget Experiment

GLAS = Geoscience Laser Altimetry System

MISR = Multiangle Imaging SpectroRadiometer

MODIS=MODerate resolution Imaging Spectroradiometer

PHOTONS = PHOtométrie pour le Traitement Opérationnel de Normalisation Satellitaire

POLDER = Polarization and Directionality of the Earth's Reflectances

TOMS = Total Ozone Mapping Spectrometer

Chapitre 10

Conclusion

Il est intéressant de constater que l'incertitude du forage radiatif des aérosols ne s'est pas réduite pendant les cinq années qui séparent les deuxième et troisième rapports d'évaluation du Groupe Intergouvernemental d'Experts sur l'Evolution du Climat (GIEC ou IPCC en anglais) – elle a en fait augmentée compte-tenu de la multiplication du nombre de forçages radiatifs liés aux aérosols –. Il est toutefois réaliste de penser que les estimations des effets directs des aérosols verront leurs incertitudes diminuer au cours des prochaines années et que l'on n'est plus très loin d'une estimation fiable (voir la partie prospective "Aerosol radiative forcing: How to reduce uncertainties?"). De larges progrès restent néanmoins à accomplir pour quantifier l'absorption de rayonnement solaire par les aérosols et son rôle dans le changement climatique. Bien qu'encore controversée, la possibilité que les émissions de carbone-suie soit à l'origine d'un impact climatique important a déjà envahi la sphère publique, certains y voyant un argument pour relativiser (minimiser) l'impact des gaz à effet de serre. Il faut donc maintenant aborder plus sérieusement le problème de l'absorption par les aérosols. Enfin, le rôle des aérosols naturels en tant que partie intégrante du système climatique devient de plus en plus évident. Il convient donc d'étudier plus en avant les rétroactions climatiques impliquant les sels marins, les poussières désertiques tout comme nous avons commencé à le faire pour les aérosols soufrés naturels. De même, il convient de mesurer les effets secondaires que pourraient avoir certaines mesures de "protection du climat" comme une fertilisation à grande échelle des océans. Une telle solution est déjà proposée par certaines entreprises privées pour piéger du dioxyde de carbone au fond des océans (Falkowski, 2002). Nous montrons sur la Figure 1 quelle serait l'augmentation de la colonne d'aérosols soufrés si la biologie marine n'était pas limitée par les apports en fer (ce qui équivaut au cas extrême d'une fertilisation totale de l'océan par le fer). Les résultats parlent d'eux-mêmes... mais restent très préliminaires. A ce titre, il est important de mentionner ici le développement du modèle couplé océan-atmosphère-biosphère à l'Institut Pierre Simon Laplace auquel nous sommes associés. Ce "modèle du système Terre" permettra d'appréhender ces questions dans toute leur complexité mais à la condition d'en avoir une utilisation maîtrisée.

Si on aperçoit maintenant le bout du tunnel pour l'effet direct des aérosols, tel n'est pas le cas pour les effets indirects des aérosols dont on commence seulement à mesurer toute la complexité. La représentation de ces effets dans les modèles de climat, point de passage obligé pour une estimation globale, reste rudimentaire et de nombreux progrès sont encore à faire, en particulier en ce qui concerne la phase glace (Lohmann, 2002). On a vu également dans le chapitre 8 les limites d'une approche basée sur l'analyse des données d'un seul instrument satellitaire. On trouve là la justification des nouvelles missions spatiales et en particulier celle de l'AQUA-train composé des satellites AQUA (équivalent de TERRA sur une orbite héliosynchrone de l'après-midi incluant le radiomètre MODIS et l'instrument de bilan radiatif CERES), CALIPSO (lidar et radiomètre infrarouge), PARASOL (instrument POLDER sur micro-satellite), et CloudSat (radar). La combinaison des observations provenant de ces trois satellites devrait permettre d'en apprendre plus sur l'impact des aérosols sur les nuages et sur le bilan radiatif. En particulier, nous pourrons prendre en compte la composante verticale du problème qui est cruciale en ce qui concerne l'effet indirect : non seulement la morphologie des nuages semble jouer un rôle important mais n'oublions pas également que les aérosols et les nuages doivent être dans les mêmes couches atmosphériques pour interagir (Figure 2) !

Figure 1 : Augmentation de la colonne d'aérosols soufrés dans le cas extrême d'une fertilisation totale de l'océan par le fer. Les quatre cas correspondent à quatre formulations différentes de la production de DMS par le phytoplancton.

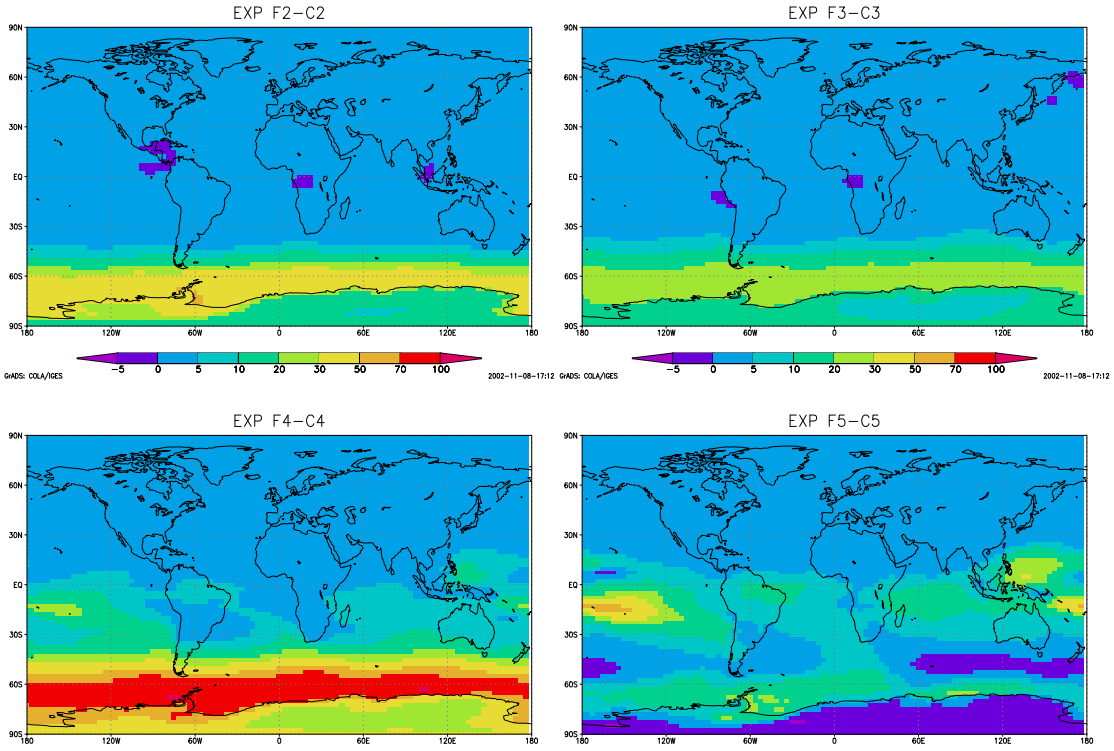

Figure 2 : Vue d'artiste de l'AQUA-train.

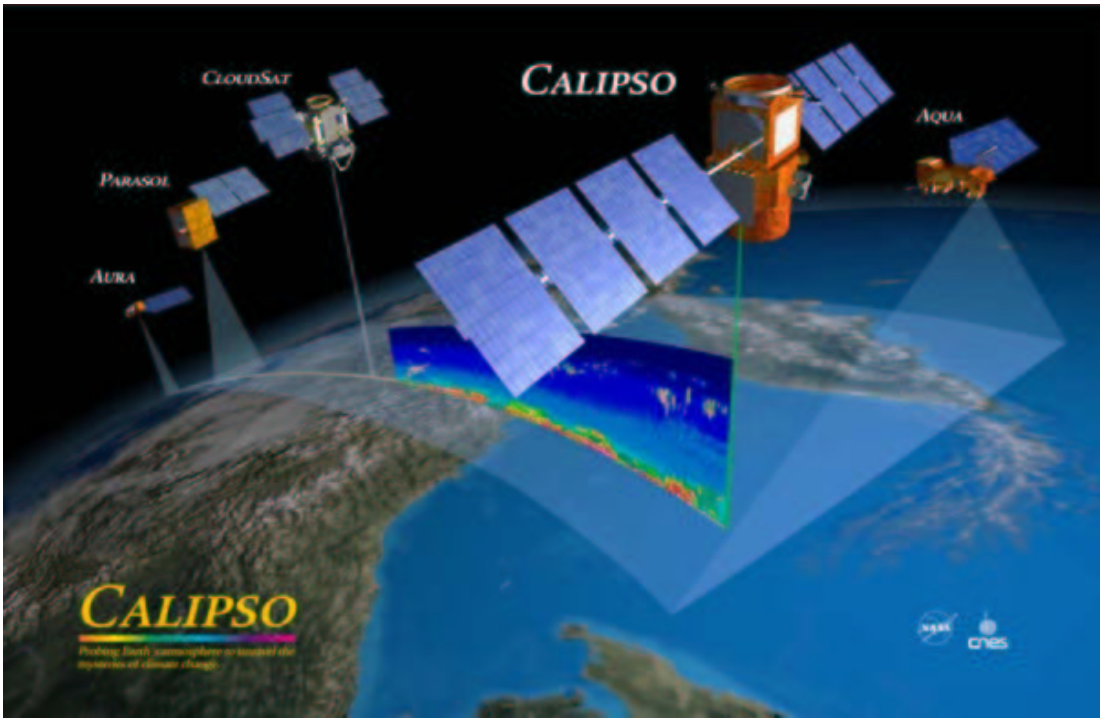

Nous avons donc vu que la problématique des effets climatiques directs et indirects des aérosols a suscité une nouvelle impulsion et un renouveau des recherches sur les aérosols atmosphériques. S'il n'est certainement pas approprié de justifier toutes les recherches sur les aérosols atmosphériques par cette seule problématique, il convient néanmoins d'exploiter les synergies pouvant résulter des intérts multiples suscités par les aérosols. Cela concerne plus particlièrement l'étude de la pollution atmosphérique aux échelles urbaine, régionale et continentale, des effets des aérosols sur la végétation (modification de la radiation photosynthétique ou PAR, pluies acides, dépôt d'aérosols et des polluants qui y sont associés sur les feuilles), des effets des aérosols sur les écosystèmes marins (dépôts d'aérosols désertiques contenant du fer), du rôle des aérosols sur les corrections atmosphériques ou la prévision numérique du temps (taux de chauffage atmosphérique, prise en compte des corrections atmosphériques dans l'assimilation de variables atmosphériques ou océaniques).

Le chemin parcouru est grand entre les premiers modèles "hors-ligne" relativement grossiers des aérosols soufrés à l'échelle globale et les modèles "en-ligne" actuels impliquant les différentes composantes chimiques de l'aérosol. La télédétection des aérosols a également énormément progressé après le premier débroussaillage réalisé à partir des instruments opérationnels tels que METEOSAT ou AVHRR jusqu'à l'apparition d'instruments satellitaires dédiés à l'étude des aérosols tels que POLDER ou MODIS. C'est donc de manière naturelle que l'idée de marier modèles et observations des aérosols est arrivée, tirant profit des avancées considérables des techniques d'assimilation variationnelle développées à l'origine dans le cadre de la prévision numérique du temps. C'est à ce titre que le projet GEMS-aérosol est né au Centre Européen des Prévisions Météorologiques à Moyen Terme (CEPMMT). GEMS-aérosol vise à fournir dans le cadre de GMES (Global Monitoring of the Environment and Security) un système opérationnel de prévision et d'analyse des propriétés des aérosols atmosphériques à une échelle spatiale d'environ 100 km. Il s'agit donc de mettre à profit les progrès réalisés en modélisation globale, en télédétection des aérosols, et en assimilation variationnelle pour satisfaire un grand nombre d'applications telles que la prévision de la visibilité atmosphérique, la fourniture de conditions initiales et aux limites pour les modèles à plus petite échelle de pollution régionale ou urbaine, la correction atmosphérique des aérosols troposphériques et stratosphériques permettant d'observer les surfaces continentales et océaniques ou la composition chimique de l'atmosphère (gaz réactifs et gaz à effet de serre). Nous sommes maintenant prêts à relever les aspects scientifiques de ce défi !

Chapitre 11

Références

Ackerman, A.S., O. B. Toon, D. E. Stevens, A. J. Heymsfield, V. Ramanathan, E. J. Welton, Reduction of tropical cloudiness by soot, Science, 288, 1042–1047, 2000.

Bergstrom, R. W., and P. B. Russell, Estimation of aerosol direct radiative effects over the midlatitude North Atlantic from satellite and in situ measurements, Geophysical Research Letters, 26, 1731–1734, 1999.

Bessemoulin, P., et O. Boucher, Les besoins en observations pour la climatologie, La Météorologie, n° 39, pp. 36-42, novembre 2002.

Bopp, L., O. Boucher, O. Aumont, S. Belviso, J.-L. Dufresne, P. Monfray, and M. Pham, Will marine dimethylsulfide emissions amplify or alleviate global warming? – A model study, Canadian Journal of Fisheries and Aquatic Sciences, soumis, 2002.

Boucher, O., Etude de quelques interactions aérosol-nuage-rayonnement : modélisation et simulations avec un modèle de circulation générale, Thèse de Doctorat de l'Université Paris 6, 228 pages, décembre 1995.

Boucher, O., GCM Estimate of the indirect aerosol forcing using satellite-retrieved cloud effective droplet radii, Journal of Climate, 8, 1403–1409, 1995.

Boucher, O., Aerosol radiative forcing and related feedbacks: How do we reduce the uncertainties?, IGAC planning meeting, 27-30 Jan. 2002, IGACtivities, n° 36, pp. 8-12, May 2002.

Boucher, O. and T. L. Anderson, GCM assessment of the sensitivity of direct climate forcing by anthropogenic sulfate aerosols to aerosol size and chemistry, Journal of Geophysical Research, 100, 26117–26134, 1995.

Boucher, O., and J. M. Haywood, On summing the components of radiative forcing of climate change, Climate Dynamics, 18, 297–302, 2001.

Boucher, O. and U. Lohmann, The sulfate-CCN-cloud albedo effect: A sensitivity study using two general circulation models, Tellus, 47B, 281–300, 1995.

Boucher, O., C. Moulin, S. Belviso, O. Aumont, L. Bopp, E. Cosme, R. von Kuhlmann, M. G. Lawrence, M. Pham, M. S. Reddy, J. Sciare, and C. Venkataraman, Sensitivity study of dimethylsulphide (DMS) atmospheric concentrations and sulphate aerosol indirect radiative forcing to the DMS source representation and oxidation, Atmospheric Chemistry and Physics Discussions, 2, 1181–1216, 2002b.

Boucher, O., C. Moulin, S. Belviso, O. Aumont, L. Bopp, E. Cosme, R. von Kuhlmann, M. G. Lawrence, M. Pham, M. S. Reddy, J. Sciare, and C. Venkataraman, DMS atmospheric concentrations and sulphate aerosol indirect radiative forcing: a sensitivity study to the DMS source representation and oxidation, Atmospheric Chemistry and Physics, 3, 49–65, 2003.

Boucher, O. and M. Pham, History of sulfate aerosol radiative forcings, Geophysical Research Letters, 29, 1308, 10.1029/2001GL014048, 2002.

Boucher, O., M. Pham, and C. Venkataraman, Simulation of the atmospheric sulfur cycle in the Laboratoire de Météorologie Dynamique General Circulation Model. Model description, model evaluation and global and European budgets, *Note scientifique de l'IPSL n° 23*, juillet 2002a.

Boucher, O., S. E. Schwartz, T. P. Ackerman, T. L. Anderson, B. Bergstrom, B. Bonnel, P. Chylek, A. Dahlback, Y. Fouquart, Q. Fu, R. N. Halthore, J. Haywood,

T. Iversen, S. Kato, S. Kinne, A. Kirkevg, E. Knapp, A. Lacis, I. Laszlo, M. I. Mishchenko, S. Nemesure, V. Ramaswamy, D. Roberts, P. Russell, M. Schlesinger, G. L. Stephens, R. Wagener, M. Wang, J. Wong, and F. Yang, Intercomparison of models representing shortwave radiative forcing by sulfate aerosols, Journal of Geophysical Research, 103, 16979–16998, 1998.

Boucher, O., and D. Tanré, Estimation of the aerosol perturbation to the Earth's radiative budget over oceans using POLDER satellite aerosol retrievals, Geophysical Research Letters, 27, 1103–1106, 2000.

Bréon, F.-M., D. Tanré, and S. Generoso, Aerosol effect on cloud droplet size monitored from satellite, Science, 295, 834–838, 2002.

Charlson, R. J., S. E. Schwartz, J. M. Hales, R. D. Cess, J. A. Coakley, J. E. Hansen, and D. J. Hofmann, Climate forcing of anthropogenic aerosols, Science, 255, 423–430, 1992.

Claquin, T., M. Schulz, Y. Balkanski and O. Boucher, Uncertainties in assessing radiative forcing by mineral dust, Tellus, 50B, 491–505, 1998.

Collins, W. D., P. J. Rasch, B. E. Eaton, B. V. Khattatov, J.-F. Lamarque, and C. S. Zender, Simulating aerosols using a chemical transport model with assimilation of satellite aerosol retrievals: Methodology for INDOEX, Journal of Geophysical Research, 106, 7313–7336, 2001.

Cosme, E., C. Genthon, P. Martinerie, M. Pham, and O. Boucher, Sulfur cycle in the high Southern latitudes in the LMD-ZT general circulation model, Journal of Geophysical Research, 107(D23), 4690, doi:10.1029/2002JD002149, 2002.

Deschamps, P.-Y., F.-M. Bréon, M. Leroy, A. Podaire, A. Bricaud, J.-C. Buriez, and G. Sèze, The POLDER mission: Instrument characteristics and scientific objectives, IEEE Transactions on Geosciences and Remote Sensing, 32, 598–615, 1994.

Deuzé, J.-L., M. Herman, P. Goloub, D. Tanré, and A. Marchand, Characterization of aerosols over ocean from POLDER/ADEOS-1, Geophysical Research Letters, 26, 1421–1424, 1999.

Deuzé, J.-L., P. Goloub, M. Herman, A. Marchand, G. Perry, S. Susana, and D. Tanré, Estimate of the aerosol properties over the ocean with POLDER, Journal of Geophysical Research, 105, 15329–15346, 2000.

Deuzé, J.-L., F.-M. Bréon, C. Devaux, P. Goloub, M. Herman, B. Lafrance, F. Maignan, A. Marchand, F. Nadal, G. Perry, and D. Tanré, Remote sensing of aerosol over land surfaces from POLDER-ADEOS-I polarized measurements, Journal of Geophysical Research, 106, 4913–4926, 2001.

Dubovik, O., B. N. Holben, T. F. Eck, A. Smirnov, Y. J. Kaufman, M. D. King, D. Tanré, and I. Slutsker, Variability of absorption and optical properties of key aerosol types observed in worldwide locations, Journal of Atmospheric Sciences, 59, 590–608, 2002.

Falkowski, P., Une forêt sous la mer, Pour la Science, 301, 28–34, novembre 2002.

Formenti, P., T. Reiner, D. Sprung, M. O. Andreae, M. Wendisch, H. Wex, D. Kinkred, K. Dewey, J. Kent, M. Tzourtziou, A. Vasaras, and C. Zerefos, The STAAARTE-MED 1998 airborne measurements over the Aegean Sea: I. Aerosol particles and trace gases, Journal of Geophysical Research, 107, 4450, doi:10.1029/2001JD001337, 2002a.

Formenti, P., O. Boucher, T. Reiner, D. Sprung, M. O. Andreae, M. Wendisch, H. Wex, D. Kinkred, M. Tzourtziou, A. Vasaras, and C. Zerefos, The STAAARTE-MED 1998 airborne measurements over the Aegean Sea: II. Aerosol scattering and absorption, and radiative calculations, a case study, Journal of Geophysical Research, 107, 4451, doi:10.1029/2001JD001536, 2002b.

Goloub, P., D. Tanré, J.-L. Deuzé, M. Herman, A. Marchand, and F. M. Bréon, Validation of the first algorithm applied for deriving the aerosol properties over the ocean using the POLDER/ADEOS measurements, IEEE Transactions on Geosciences and Remote Sensing, 37, 1586–1596, 1999.

Guyon, P., O. Boucher, B. Graham, J. Beck, O. L. Mayol-Bracero, P. Artaxo, W. Maenhaut, and M. O. Andreae, Refractive index of aerosol particles over the Amazon Tropical forest during LBA-EUSTACH 1999, Journal of Aerosol Science, soumis, 2002.

Guyon, P., B. Graham, J. Beck, O. Boucher, E. Gerasopoulos, O. L. Mayol-Bracero, G. C. Roberts, P. Artaxo, and M. O. Andreae, Physical properties and concentration of aerosol particles over the Amazon tropical forest during background and biomass burning conditions, Atmospheric Chemistry and Physics, soumis, 2003.

Hansen, J.E., M. Sato, A. Lacis, R. Ruedy, I. Tegen, E. Matthews, Climate forcings in the Industrial era, Proceedings of the National Academy of Sciences of USA, 95, 12753–12758, 1998.

Haywood, J. M., and O. Boucher, Estimates of the direct and indirect radiative forcing due to tropospheric aerosols: A review, Reviews of Geophysics, 38, 513–543, 2000.

Heintzenberg, J., R. J. Charlson, A. D. Clarke, C. Liousse, V. Ramaswamy, K. P. Shine, M. Wendisch, and G. Helas, Measurements and modeling of aerosol single scattering albedo: progress, problems and prospects, Contribution to Atmospheric Physics, 70, 249–263, 1997.

Herman, M., J.-L. Deuzé, C. Devaux, P. Goloub, F.-M. Bréon, and D. Tanré, Remote sensing of aerosols over land surfaces including polarization measurements and application to POLDER measurements, Journal of Geophysical Research, 102, 17039–17049, 1997.

Holben, B. N., et al., An emerging ground based aerosol climatology: Aerosol optical depth from AERONET, Journal of Geophysical Research, 106, 12067–12097, 2001.

IPCC, Climate Change 1995, The Science of Climate Change, Contribution of Working Group I to the Second Assessment Report of the Intergovernmental Panel on Climate Change, J. T. Houghton et al. (Eds.), Cambridge University Press, Cambridge, 572 pp., 1996.

IPCC, Climate Change 2001, The Scientific Basis, Contribution of Working Group I to the Third Assessment Report of the Intergovernmental Panel on Climate Change, J. T. Houghton et al. (Eds.), Cambridge University Press, Cambridge, 881 pp., 2001.

Kaufman, Y. J., D. Tanré, O. Dubovik, A. Karnieli, and L. A. Remer, Absorption of sunlight by dust as inferred from satellite and ground-based remote sensing, Geophysical Research Letters, 28, 1479–1482, 2001.

Kaufman, Y.J., D. Tanré, and O. Boucher, A satellite view of aerosols in the climate system, Nature, 419, 215–223, 2002.

Knutti, R., T. F. Stocker, F. Joos, and G.-K. Plattner, Constraints on radiative forcing and future climate change from observations and climate model ensembles, Nature, 416, 719–723, 2002.

Le Treut, H., M. Forichon, O. Boucher, and Z.-X. Li, Sulfate aerosol indirect effect and CO2 greenhouse forcing: equilibrium response of the LMD GCM and associated cloud feedbacks, Journal of Climate, 11, 1673–1684, 1998.

Lohmann, U., Interactions between anthropogenic aerosols and the hydrologic cycle, IGAC planning meeting, 27-30 Jan. 2002, IGACtivities, n° 36, pp. 3–7, May 2002.

Menon, S., J.-L. Brenguier, O. Boucher, P. Davison, A. D. Del Genio, J. Feichter, S. Ghan, S. Guibert, X. Liu, U. Lohmann, H. Pawlowska, J. E. Penner, J. Quaas, D. L. Roberts, L. Schller, and J. Snider, Evaluating cloud-aerosol process parameterizations with single column models and ACE-2 Cloudy Column observations, Journal of Geophysical Research, soumis, 2002.

Myhre, G., O. Boucher, and A. Myhre, Direct human influence of irrigation on atmospheric water vapor and climate, Science, soumis, 2002.

Ramanathan, V., et al., The Indian Ocean Experiment: An integrated assessment of the climate forcing and effects of the great Indo-Asian haze, Journal of Geophysical Research, 106, 28371–28398, 2001.

Ramaswamy, V., O. Boucher, J. Haigh, D. Hauglustaine, J. Haywood, G. Myhre, T. Nakajima, G.-Y. Shi, and S. Solomon, Radiative forcing of climate change, chapter 6, IPCC Third Assessment Report, J. T. Houghton et al. (Eds), Cambridge University Press, Cambridge, UK, pp. 349–416, 2001.

Rasch, P. J., W. D. Collins, and B. E. Eaton, Understanding the Indian Ocean Experiment (INDOEX) aerosol distributions with an aerosol assimilation, Journal of Geophysical research, 106, 733–7355, 2001.

Reddy, M. S., and C. Venkataraman, Inventory of Aerosol and Sulphur Dioxide Emissions from India: I Fossil Fuel Combustion, Atmospheric Environment, 36, 677–697, 2002a.

Reddy, M. S., and C. Venkataraman, Inventory of Aerosol and Sulphur Dioxide Emissions from India: II Biomass Combustion, Atmospheric Environment, 36, 699–712, 2002b.

Rotstayn, L. D., and J. E. Penner, Indirect aerosol forcing, quasi-forcing, and climate response, Journal of Climate, 14, 1960–2975, 2001.

Satheesh, S. K., and V. Ramanathan, Large differences in tropical aerosol forcing at the top of the atmosphere and Earth's surface, Nature, 405, 60–63, 2000.

Tegen, I., P. Hollrig, M. Chin, I. Fung, D. Jacob, and J. Penner, Contribution of different aerosol species to the global aerosol extinction optical thickness: Estimates from model results, Journal of Geophysical Research, 102, 23895–23915, 1997.

Trentmann, J., B. Früh, O. Boucher, T. Trautmann, and M. O. Andreae, Three-dimensional solar radiation effects on the actinic flux field in a biomass burning plume, Journal of Geophysical Research, soumis, 2002.

Annexe A

Revue sur le forçage radiatif par les aérosols

Nous reproduisons ici l'article de Haywood et Boucher publié en 2000 dans la revue *Reviews of Geophysics*.

ESTIMATES OF THE DIRECT AND INDIRECT RADIATIVE FORCING DUE TO TROPOSPHERIC AEROSOLS: A REVIEW

James Haywood
Meteorological Research Flight
U.K. Meteorological Office
Farnborough, England

Olivier Boucher[1]
Laboratoire d'Optique Atmosphérique
Université des Sciences et Technologies de Lille
Villeneuve d'Ascq, France

Abstract. This paper reviews the many developments in estimates of the direct and indirect global annual mean radiative forcing due to present-day concentrations of anthropogenic tropospheric aerosols since *Intergovernmental Panel on Climate Change* [1996]. The range of estimates of the global mean direct radiative forcing due to six distinct aerosol types is presented. Additionally, the indirect effect is split into two components corresponding to the radiative forcing due to modification of the radiative properties of clouds (cloud albedo effect) and the effects of anthropogenic aerosols upon the lifetime of clouds (cloud lifetime effect). The radiative forcing for anthropogenic sulphate aerosol ranges from -0.26 to -0.82 W m^{-2}. For fossil fuel black carbon the radiative forcing ranges from $+0.16$ W m^{-2} for an external mixture to $+0.42$ W m^{-2} for where the black carbon is modeled as internally mixed with sulphate aerosol. For fossil fuel organic carbon the two estimates of the likely weakest limit of the direct radiative forcing are -0.02 and -0.04 W m^{-2}. For biomass-burning sources of black carbon and organic carbon the combined radiative forcing ranges from -0.14 to -0.74 W m^{-2}. Estimates of the radiative forcing due to mineral dust vary widely from $+0.09$ to -0.46 W m^{-2}; even the sign of the radiative forcing is not well established due to the competing effects of solar and terrestrial radiative forcings. A single study provides a very tentative estimate of the radiative forcing of nitrates to be -0.03 W m^{-2}. Estimates of the cloud albedo indirect radiative forcing range from -0.3 to approximately -1.8 W m^{-2}. Although the cloud lifetime effect is identified as a potentially important climate forcing mechanism, it is difficult to quantify in the context of the present definition of radiative forcing of climate change and current model simulations. This is because its estimation by general circulation models necessarily includes some level of cloud and water vapor feedbacks, which affect the hydrological cycle and the dynamics of the atmosphere. Available models predict that the radiative flux perturbation associated with the cloud lifetime effect is of a magnitude similar to that of the cloud albedo effect.

1. INTRODUCTION

There has been much recent interest in the radiative effects of aerosols, particularly because anthropogenic activity is thought to have increased atmospheric concentrations. Atmospheric aerosols come from a wide variety of natural and anthropogenic sources and have typical radii ranging from 0.001 to 10 μm. Primary aerosols are emitted directly at the source, whereas secondary aerosols are generally formed from gaseous precursors by various gas and aqueous phase oxidation pathways. Primary aerosols include, for example, fly ash from industrial activities, sea-salt particles emitted at the ocean surface, or mineral dust aerosol that is emitted by the effects of wind erosion on arid land. An example of a secondary aerosol is sulphate aerosol that is formed from dimethyl sulphide (DMS) emissions by marine phytoplankton and from sulphur emissions from fossil fuel burning. Aerosols may undergo complex chemical reactions in the atmosphere and mix with each other either externally (where each particle contains a chemically distinct aerosol species) or internally (where each particle contains a combination of different aerosol species). Atmospheric aerosols are removed from the atmosphere either by impacting with the surface of the Earth (dry deposition) or by raining out in precipitating clouds (wet deposition). Typically, the lifetimes of aerosols in the troposphere range from a few minutes to several weeks. The geographically localized sources and sinks and relatively short atmospheric lifetimes give aerosols an extreme spatial and temporal inhomogeneity in the atmosphere. Tropospheric aerosols that are thought to have a substantial anthropogenic component include sulphate, black carbon, organic carbon, mineral dust, and nitrate aerosol. Anthropogenic aerosols influence the radiative budget of the Earth-atmosphere system in two different ways. The first is the direct effect, whereby aerosols scatter and absorb solar and thermal infrared

[1]On sabbatical leave at Abteilung Chemie der Atmosphäre, Max-Planck-Institut für Chemie, Mainz, Germany.

Reviews of Geophysics, 38, 4 / *November 2000*
pages 513–543
8755-1209/00/1999RG000078*$15.00*
Paper number 1999RG000078

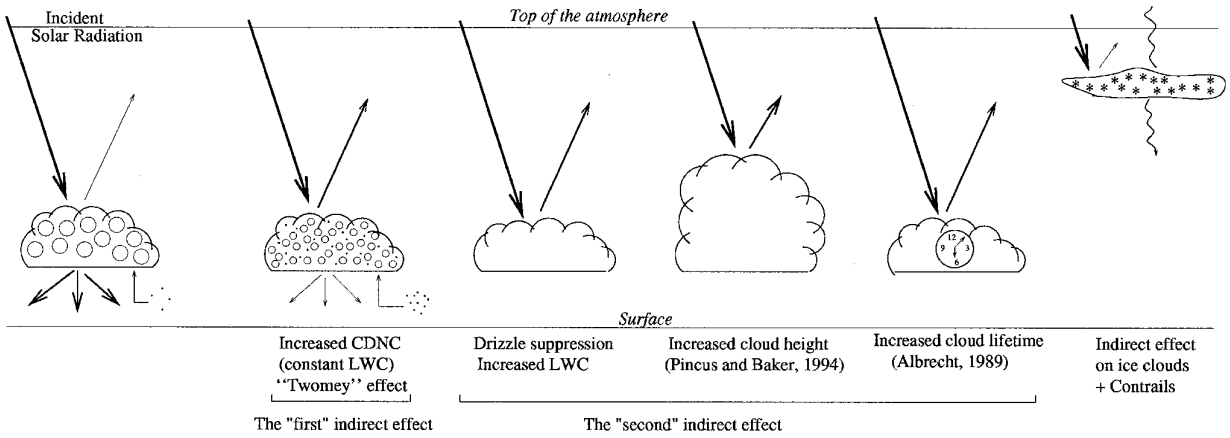

Figure 1. Schematic of the aerosol indirect effects. CDNC means cloud droplet number concentration, and LWC means liquid water content.

radiation, thereby altering the radiative balance of the Earth-atmosphere system or, equivalently, the planetary albedo. The second is the indirect effect, whereby aerosols modify the microphysical and hence the radiative properties and lifetime of clouds.

Radiative forcing is defined as the change in net irradiance at the tropopause due to an applied perturbation holding all atmospheric variables fixed, once stratospheric temperatures have been allowed to adjust to equilibrium. The concept of radiative forcing was first developed for one-dimensional (1-D) radiative convective models [e.g., *Manabe and Wetherald*, 1967; *Ramanathan and Coakley*, 1978; *Hansen et al*., 1981], which investigated the change in the global mean surface air temperature at equilibrium, $dT_{\text{global mean}}$, due to the global mean radiative forcing $dF_{\text{adj global mean}}$ for radiatively active species. The relationship

$$dT_{\text{global mean}} = \lambda dF_{\text{adj global mean}},$$

where λ is the model-dependent climate sensitivity parameter, was found to be approximately independent of the forcing mechanism causing the radiative perturbation. Subsequent equilibrium model studies have extended the concept to 3-D models [e.g., *Cox et al*., 1995; *Ramaswamy and Chen*, 1997; *Le Treut et al*., 1998] and find that the relationship between $dT_{\text{global mean}}$ and $dF_{\text{adj global mean}}$ continues to hold to within an accuracy of ~20%. Stratospheric adjustment is important for atmospheric perturbations that change the temperature of the stratosphere and is particularly important for mechanisms such as stratospheric ozone depletion. For the majority of tropospheric aerosols the effects of stratospheric adjustment are likely to be insignificant, and stratospheric adjustment is often not accounted for. As the spatial and temporal variability of tropospheric aerosols is large, many studies report the global annual mean radiative forcing, which is a useful concept in determining the relative importance of perturbations of atmospheric species due to anthropogenic activity. This statement will be qualified when it comes to the aerosol indirect effect.

Intergovernmental Panel on Climate Change (*IPCC*) [1996] considered the direct radiative forcing from three different anthropogenic aerosol species: sulphate, fossil fuel black carbon (or soot), and biomass-burning aerosols. *IPCC* [1996] suggested a range of −0.2 to −0.8 W m^{-2} ("best guess" of −0.4 W m^{-2}) for sulphate aerosols, +0.03 to +0.3 W m^{-2} (best guess of +0.1 W m^{-2}) for fossil fuel black carbon aerosols, and −0.07 to −0.6 W m^{-2} (best guess of −0.2 W m^{-2}) for biomass-burning aerosols. The subjective confidence level of *IPCC* [1996] was "low" for sulphate aerosol and "very low" for fossil fuel black carbon and biomass-burning aerosol. Although best guess and confidence levels are presented by *IPCC* [1996], here we concentrate upon specific estimates available in the literature and present compilations of the ranges of estimates. This approach is taken because the validity of simply summing best guess estimates for the radiative forcing of each anthropogenic species to obtain an overall "best estimate" is very questionable. This is because different levels of uncertainty are associated with different aerosol species, because the ranges associated with each species make such a summation difficult, and because internal mixing complications lead to nonlinear absorption effects.

As is depicted in Figure 1, the aerosol indirect effect is usually split into two effects: the first indirect effect, whereby an increase in aerosols causes an increase in droplet concentration and a decrease in droplet size for fixed liquid water content [*Twomey*, 1974], and the second indirect effect, whereby the reduction in cloud droplet size affects the precipitation efficiency, tending to increase the liquid water content, the cloud lifetime [*Albrecht*, 1989], and the cloud thickness [*Pincus and Baker*, 1994]. The first and second indirect effects are also termed the "cloud albedo" and "cloud lifetime"

effects, respectively. Until recently, the first indirect effect has received much more attention than the second indirect effect. *IPCC* [1994] and *IPCC* [1996] only considered the cloud albedo effect. *Shine et al*. [1996] in the work of *IPCC* [1996] suggested a range of 0 to -1.5 W m^{-2} and no best guess value for the indirect radiative forcing. However, a value of -0.8 W m^{-2} was used for the year 1990 in the IS92a scenario by *Kattenberg et al*. [1996] in the work of *IPCC* [1996] and also *IPCC* [1999]. The confidence level for the indirect effect was classified as very low by *IPCC* [1996].

2. DIRECT RADIATIVE FORCING

Since *IPCC* [1996], there have been advances in both modeling and observational studies of the direct effect of tropospheric aerosols (see also the review by *Shine and Forster* [1999]). Global chemical transport modeling studies encompass a greater number of aerosol species and continue to improve the representation of the aerosol physical and chemical processes. The global models are more numerous and include more accurate radiative transfer codes, more sophisticated treatments of the effects of relative humidity for hygroscopic aerosols, better treatment of clouds, and better spatial and temporal resolution than some earlier studies. Additionally, dedicated field campaigns have been performed, and satellite retrieval methods for detecting the direct radiative effect of aerosols have been developed. The present-day direct radiative forcing due to aircraft emissions of sulphate and black carbon aerosol has been calculated to be insignificant [*IPCC*, 1999]. Section 2.1 provides an introduction to the methods used in determining the direct effect, and sections 2.2 and 2.3 consider sulphate and black and organic carbon aerosols. Section 2.4 investigates the radiative forcing due to anthropogenic mineral dust aerosol, and nitrates are briefly discussed in section 2.5. The complexities of treating internally mixed aerosols are discussed in section 2.6. Section 2.7 discusses field campaigns, and section 2.8 discusses developments in satellite retrievals. Section 2.9 discusses the uncertainties related to calculating the direct radiative forcing for aerosols.

2.1. Determining the Direct Radiative Forcing

Global mean calculations of the direct radiative forcing are made up of a series of local column calculations carried out either within a general circulation model (GCM) framework or off-line; thus it is useful to consider what factors determine the local radiative forcing at a particular geographic location. The optical properties of anthropogenic aerosols are described by three parameters: the extinction coefficient k_e, which determines the degree of interaction of radiation and the aerosol particles; the single scattering albedo ω_0, which determines the degree of absorption; and the scattering phase function, which determines the angular distribution of scattered radiation [e.g., *Kiehl and Briegleb*, 1993]. The scattering phase function may be integrated to provide parameters such as the asymmetry factor g, which is used in two-stream radiative transfer calculations, or the backscattered fraction β, which is used in more simple radiative transfer models [e.g., *Charlson et al*., 1992]. These parameters are most frequently determined as a function of wavelength by assuming spherical particles and applying Mie scattering theory to a size distribution of aerosols with a specified refractive index. The local radiative forcing will depend upon the local atmospheric column burden of a particular anthropogenic aerosol species in the atmosphere, the underlying surface reflectance and the relative vertical position of the aerosol and cloud, the relative humidity if the aerosol is hygroscopic, and the insolation.

Figure 2 shows that partially absorbing aerosols (i.e., $\omega_0 \neq 1$) may exert a local negative forcing over regions with low surface reflectance and a positive forcing over regions of high surface reflectance [e.g., *Haywood and Shine*, 1995; *Chýlek and Wong*, 1995]. The boundary between local negative and positive solar forcing regimes is shown as a function of the single scattering albedo and surface reflectance for aerosols with differing backscattered fractions when clouds are excluded from the calculations. Similar results are found if partially absorbing aerosol resides above clouds that have a high albedo [e.g., *Haywood and Shine*, 1997]. It is not only the sign, but also the magnitude of the local radiative forcing, that is a function of the surface reflectance. Figure 3 shows idealized column calculations of the clear-sky radiative local forcing as a function of the solar zenith angle for scattering aerosol (Figure 3a) and absorbing aerosol (Figure 3b) [*Haywood and Shine*, 1997]. The clear-sky local radiative forcing due to scattering aerosol is a function of the solar zenith angle, showing a maximum radiative forcing at solar zenith angles of between 60° and 80° due to the nature of the scattering phase function of the aerosol [e.g., *Pilinis et al*., 1995; *Nemesure et al*., 1995; *Boucher et al*., 1998]. The radiative forcing is also a function of the surface reflectance, showing the strongest radiative forcing when the surface reflectance is low. For the absorbing aerosol the strongest radiative forcing occurs when the surface reflectance is high.

The global annual mean radiative forcing of a particular anthropogenic aerosol is determined by its temporal and spatial distribution in the atmosphere together with its optical properties. The atmospheric burden is determined by emission processes, chemical reactions, and deposition and transport processes, each of which must be accurately modeled by global chemical transport models [e.g., *Langner and Rodhe*, 1991; *Pham et al*., 1995; *Penner et al*., 1998]. The optical properties of aerosols may depend upon the three-dimensional geographic distribution of the aerosols. For example, in conditions of high relative humidity, hygroscopic aerosols take up water, leading to changes in chemical composition and size of the aerosol particles and hence

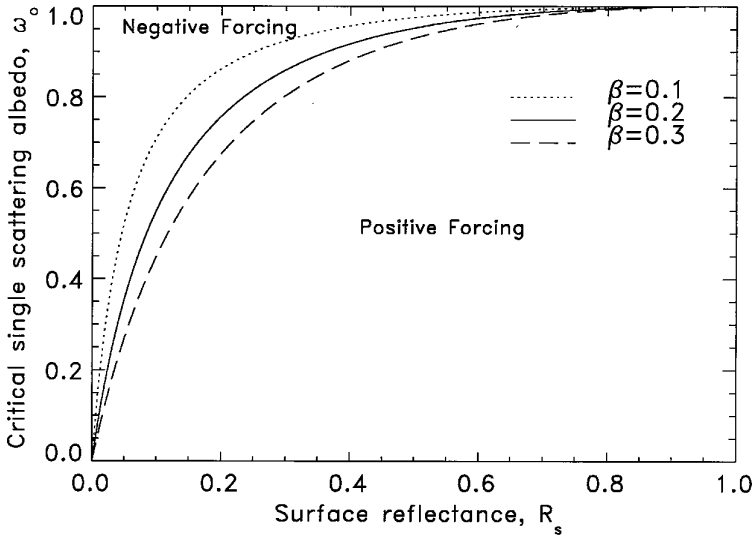

Figure 2. The critical single scattering albedo ω_0, at which the clear-sky radiative forcing changes sign as a function of surface reflectance R_s, for different backscattered fractions β (adapted from *Haywood and Shine* [1995]).

variations in the optical parameters. The global annual mean radiative forcing is also dependent upon the three-dimensional distribution in the atmosphere because the radiative forcing depends upon spatially dependent fields such as insolation, cloud amount, and underlying surface reflectance. In 3-D modeling studies of the direct effect discussed here, it is important to realize that the radiative forcing is calculated in a purely diagnostic way. Radiative calculations are performed excluding and including the aerosol perturbation, and the difference in the net radiation at the tropopause yields the radiative forcing. In GCM calculations the effect of the aerosols upon the atmospheric heating rates is not included in the dynamical evolution of the atmosphere, and thus no feedback mechanisms are included. We now concentrate upon estimates of the global annual mean radiative forcing estimates for specific species.

2.2. Sulphate Aerosol

The main source of anthropogenic sulphate aerosol is via sulphur dioxide emissions from fossil fuel burning, with a relatively small contribution from biomass burning. The main natural sources of sulphate aerosol are from DMS emissions and volcanoes. Estimates of the

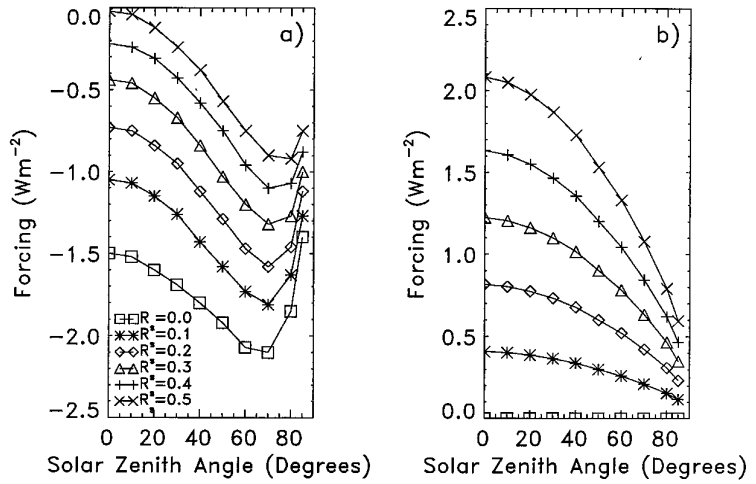

Figure 3. Examples of column calculations of the clear-sky radiative forcing for (a) scattering aerosol (sulphate) and (b) absorbing aerosol (black carbon) as a function of solar zenith angle for different Lambertian surface reflectances, R_s (adapted from *Haywood and Shine* [1997]). Reprinted with permission from The Royal Meteorological Society.

global emissions of sulphate aerosol from anthropogenic and natural sources are given in Table 1. Estimates of the current magnitude and geographic distribution of emissions of sulphur from fossil fuels are fairly well known because inventories of fossil fuel burning are available [e.g., *Benkovitz et al*., 1996]. Global mean emissions used in recent chemical transport modeling of the sulphur cycle range from 66.8 to 92.4 Tg S yr^{-1} for anthropogenic emissions and from 91.7 to 125.5 Tg S yr^{-1} for total emissions. The main oxidation pathways that transform sulphur dioxide into sulphate aerosols are via gaseous phase reactions with the hydroxyl radical and aqueous phase reactions within cloud droplets [e.g., *Pham et al*., 1995]. These reactions are parameterized in chemical transport models (CTMs) together with dry and wet deposition processes. While these parameterizations are physically based wherever possible, uncertainties in the input parameters lead to differences in the atmospheric burdens of sulphate aerosol; the burdens of total and anthropogenic sulphate from different models are shown in Table 1.

Having briefly discussed the results from CTMs, we now focus on estimates of the direct radiative forcing. Early 1-D box-model estimates of the radiative forcing [e.g., *Charlson et al*., 1992] using simplified expressions for radiative forcing have been superseded by global calculations using prescribed aerosol concentrations from CTMs. These studies use either 3-D observed fields of, for example, clouds, relative humidity, and surface reflectance [e.g., *Kiehl and Briegleb*, 1993; *Myhre et al*., 1998], or GCM-generated fields [e.g., *Boucher and Anderson*, 1995; *Haywood et al*., 1997a] together with the prescribed aerosol distributions from CTMs and detailed radiative transfer codes in calculating the radiative forcing. A growing number of studies perform both the chemical transportation of aerosols and the radiative forcing calculations, which have the advantage of correlating predicted aerosol distributions precisely with fields determining aerosol production and deposition such as clouds [e.g., *Penner et al*., 1998]. Table 2 summarizes estimates of the radiative forcing due to sulphate from global modeling studies.

The global mean radiative forcing ranges from −0.26 to −0.82 W m^{-2}, although most lie in the range −0.26 to −0.4 W m^{-2}. The spatial distribution of the forcings is similar in all of the studies, an example of which is shown in Plate 1a [*Haywood et al*., 1997a]. The radiative forcing is negative everywhere and is strongest over industrial regions of the Northern Hemisphere, although the ratio of the annual mean Northern Hemisphere/Southern Hemisphere radiative forcing varies from 2.0 [*Graf et al*., 1997] to 8.7 [*Koch et al*., 1999]. The ratio of the annual mean radiative forcing over land to that over ocean also varies considerably, ranging from 1.3 [*Kiehl et al*., 2000] to 3.4 [*Boucher and Anderson*, 1995]. The seasonal cycle is strongest in the Northern Hemisphere summer when the insolation is the highest, although different seasonal cycles of the sulphate burden from the chemical trans-

TABLE 1. Estimates of the Global Present-Day Emissions of Various Different Types of Aerosol From Various Sources

Emission	*Source*	*Langner and Rodhe [1991]*	*Pham et al. [1995]*	*Chin and Jacob [1996]*	*Chuang et al. [1997]*	*Feichter et al. [1997]*	*van Dorland et al. [1997]*	*Graf et al. [1997]*	*Restad et al. [1998]*	*Koch et al. [1999]*	*Lohmann et al. [1999b]*
SO_2, Tg S yr^{-1}	anthropogenic	70.0	92.4	67.4	75.7	66.8	74	78	65	66.6	66.8
	biomass burning	2.5	3.0	NA	2.2	2.5	2	2	2	2.3	2.5
	volcanic	8.5	9.2	6.7	3.4	8.0	6	14	8.7	3.5	8.0
	oceanic	16.0	19.7	22.6	23.7	18.1	16	25	16	10.7	17.5
	other	1.0	1.2	0	1.0	0.9	NA	NA	NA	0.1	0.9
	total	98.0	125.5	96.7	106.0	96.3	98	119	91.7	83.2	95.7
Atmospheric burden, Tg SO_4	total	2.31 (1.56s)[a]	2.4	1.59	1.65	2.04	NA	2.34	1.51	2.19	3.09
	anthropogenic	1.18 (0.90s)	1.65	0.60	1.07	1.14	1.08	0.87	0.97	1.68	NA

Emission	*Source*	*Ghan and Penner [1992]*	*Cooke and Wilson [1996]*	*Liousse et al. [1996]*	*Cooke et al. [1999]*	*Penner et al. [1993]*
Black carbon, Tg C yr^{-1}	fossil fuel	5.8	8.0	6.6	6.4	6.6
	biomass burning	NA	6.0	12.3	NA	17.2
Organic carbon, Tg C yr^{-1}	fossil fuel	NA	NA	20.4	10.1	NA
	biomass burning	NA	NA	31.9	NA	NA

NA means not accounted for or not available.
[a]In Tables 1 and 2, appended "s" indicates the slow oxidation case rather than the standard oxidation case.

TABLE 2. The Global-Mean Annual-Average Direct Radiative Forcing Due to Sulphate Aerosols From Different Global Studies

Study	ω_0 (0.55 μm)	k_e, $m^2\ g^{-1}\ SO_4$ (0.55 μm)	g (0.55 μm)	Direct Radiative Forcing, $W\ m^{-2}$	Anthropogenic Column Burden, $mg\ m^{-2}$	Normalized Radiative Forcing, $W\ g^{-1}$	Cloud Scheme	Direct Radiative Forcing		Source of Sulphate Data
								NH/SH	Land/Ocean	
Boucher and Anderson [1995]	1.0	3.12	0.60	−0.29	2.32	−125	frac	4.3	3.4	*Langner and Rodhe* [1991]
Graf et al. [1997]	NA	NA	NA	−0.26	1.70	−153	frac	2.0	NA	*Graf et al.* [1997]
Feichter et al. [1997]	<1.0	5.0	NA	−0.35	2.23	−157	frac	4.2	1.4	*Feichter et al.* [1997]
Kiehl and Briegleb [1993]	1.0	5.0	0.69	−0.28	1.76	−159	frac	3.3	NA	*Langner and Rodhe* [1991]s
Myhre et al. [1998]	1.0	5.0	0.64	−0.32	1.90	−169	frac	6.9	NA	*Restad et al.* [1998]
van Dorland et al. [1997]	<1.0	4.0	NA	−0.36	2.11	−171	frac	5.0	NA	*van Dorland et al.* [1997]
Koch et al. [1999]	1.0	5.0	NA	−0.68	3.3	−200	frac	8.7	NA	*Koch et al.* [1999]
Kiehl and Rodhe [1995]	1.0	5.0	0.69	−0.66	3.23	−204	frac	NA	NA	*Pham et al.* [1995]
				−0.29	1.76	−165	frac	NA	NA	*Langner and Rodhe* [1991]s
Chuang et al. [1997]	1.0	5.0	0.64	−0.43	2.10	−205	on/off[a]	4.7	2.4	*Chuang et al.* [1997]
Haywood et al. [1997a]	1.0	5.0	0.64	−0.38	1.76	−215	frac	4.0	NA	*Langner and Rodhe* [1991]s
Hansen et al. [1998]	1.0	NA	NA	−0.28	1.14	−246	frac	NA	NA	*Chin and Jacob* [1996]
Kiehl et al. [2000]	1.0	5.0	0.66	−0.56	2.23	−251	frac	2.7	1.3	*Barth et al.* [2000]
Haywood and Ramaswamy [1998]	1.0	5.0	0.64	−0.63	1.76	−358	on/off	3.6	2.6	*Langner and Rodhe* [1991]s
				−0.82	1.76	−460	on/off	5.8	2.7	*Kasibhatla et al.* [1997]
Penner et al. [1998] and *Grant et al.* [1999]	1.0	5.07	0.65	−0.81	1.82	−445	on/off	4.5	2.3	*Penner et al.* [1998]

The optical parameters for sulphate aerosol at 0% relative humidity at a wavelength of 0.55 μm are shown. The anthropogenic column burden of sulphate and the source of the sulphate data are shown together with the normalized radiative forcing. "Frac" indicates a cloud scheme with fractional grid box cloud amount, and "on/off" indicates that a grid box becomes totally cloudy once a certain relative humidity threshold is reached. The ratio of the Northern Hemisphere direct radiative forcing to the Southern Hemisphere direct radiative forcing and the ratio of the mean radiative forcing over land to the mean radiative forcing over oceans are also shown. NA means that data are not available. LR91s indicates that the slow oxidation case was used in the calculations.

[a]The maximum hygroscopic growth of the aerosols was restricted to a relative humidity of 90%.

port models result in maximum global mean radiative forcings ranging from May to August [e.g., *Haywood and Ramaswamy*, 1998]. The ratio of the June-July-August/December-January-February (JJA/DJF) radiative forcing is estimated to lie in the range from less than 2 [*van Dorland et al*., 1997] to more than 5 [*Grant et al*., 1999]. The range in the normalized radiative forcing (i.e., the radiative forcing per unit mass of sulphate aerosol as defined by *Nemesure et al*. [1995] or *Pilinis et al*. [1995]) accounts for different anthropogenic loadings from the chemical transport models and is similar to the uncertainty in the total radiative forcing. This indicates that differences in the radiative forcing are not due solely to different mass loadings from the CTMs. The optical parameters for sulphate aerosol in each of the studies may vary. Although the single scattering albedo of pure sulphate is close to unity, some of the studies [e.g., *van Dorland et al*., 1997; *Feichter et al*., 1997] include some absorption. *Charlson et al*. [1999] shows considerable variation in the specific extinction coefficient used in different studies, particularly when accounting for relative humidity effects. The treatment of the effects of relative humidity and cloud appear to be particularly important in determining the radiative forcing. The studies of *Haywood and Ramaswamy* [1998], *Penner et al*. [1998], and *Grant et al*. [1999] produce normalized radiative forcings a factor of 2–3 higher than the other studies. Both *Haywood and Ramaswamy* [1998] and *Penner et al*. [1998] acknowledge that their use of on/off cloud schemes where cloud fills an entire grid box once a threshold relative humidity is exceeded may lead to strong radiative forcings due to strong nonlinear relative humidity effects. *Chuang et al*. [1997] use an on/off cloud scheme and report a radiative forcing lower than these two studies, but the hygroscopic growth is suppressed above a relative humidity of 90%. The use of monthly-mean relative humidity fields in some of the calculations [e.g., *Kiehl and Briegleb*, 1993; *Myhre et al*., 1998] leads to lower radiative forcings, as temporal variations in relative humidity and associated nonlinear effects are not accounted for. *Kiehl et al*. [2000] improve the treatment of relative humidity compared with *Kiehl and Briegleb* [1993] and *Kiehl and Rodhe* [1995] by improving the relative humidity dependence of the aerosol optical properties and by using on-line GCM relative humidities rather than monthly mean analyses, resulting in a larger normalized radiative forcing. *Haywood and Ramaswamy*'s [1998] GCM study indicates a stronger radiative forcing when sulphate resides near the surface because the relative humidity is higher. GCM sensitivity studies [*Boucher and Anderson*, 1995] and column calculations [*Nemesure et al*., 1995] show that the radiative forcing is a strong function of relative humidity but relatively insensitive to chemical composition. The contribution to the global forcing from cloudy regions is predicted to be 4% [*Haywood et al*., 1997a], 11% [*Haywood and Ramaswamy*, 1998], 22% [*Boucher and Anderson*, 1995], and 27% [*Myhre et al*., 1998] and hence remains uncertain. Studies that impose clear skies [e.g., *Schult et al*., 1997; *Kirkevåg et al*., 1999] obtain radiative forcings much stronger than those using observed or modeled cloud distributions. The global mean longwave radiative forcing has been estimated to be less than $+0.01$ W m^{-2} and is insignificant [*Haywood et al*., 1997a].

Boucher and Anderson [1995] investigate the effects of different size distributions, finding a 20–30% variation in the radiative forcing for reasonable accumulation-mode size distributions. *Nemesure et al*. [1995] and *Boucher et al*. [1998] find a much larger sensitivity to the assumed size distribution, as sulphate is modeled by much narrower size distributions. Column radiative forcing calculations by 15 radiative transfer codes of varying complexity [*Boucher et al*., 1998] show that for well-constrained input data, differences in the computed radiative forcing when clouds are excluded are relatively modest at approximately $\pm 20\%$ (Figure 4). This indicates that uncertainties in the input parameters and in the implementation of the radiative transfer codes and the inclusion of clouds lead to the large spread in estimates, as suggested by *Penner et al*. [1994].

Additional column calculations show a weakened radiative forcing when the cloud optical depth is much greater than the aerosol optical depth [*Haywood and Shine*, 1997; *Liao and Seinfeld*, 1998] and that the forcing is insensitive to the relative vertical position of the cloud and aerosol. *Haywood et al*. [1997b, 1998] used a cloud-resolving model and investigated effects of subgrid-scale variations in relative humidity and cloud. For their case study the optical depth and radiative forcing in a GCM-sized grid box were underestimated by 60%. *Ghan and Easter* [1998] came to similar conclusions. Effects of subgrid-scale variations in relative humidity and cloud on a global scale have not been rigorously investigated.

2.3. Black Carbon and Organic Carbon

Measurements show that atmospheric black carbon (BC) and organic carbon (OC) aerosol particles frequently contribute significantly to the total aerosol mass [e.g., *Novakov et al*., 1997]. BC is emitted as primary particles from incomplete combustion processes, such as fossil fuel and biomass burning, and therefore much atmospheric BC is of anthropogenic origin. Naturally occurring biomass fires do occur, but the quantity of BC emitted from these nonanthropogenic sources is very difficult to quantify. OC is emitted as both primary particles and by secondary production from gaseous compounds via condensation or gas phase oxidation of hydrocarbons. Primary organic aerosols come from both anthropogenic sources (fossil fuel and biomass burning) and from natural sources (such as debris, pollen, spores, and algae). Detailed emission inventories for both BC and OC have recently been developed [e.g., *Penner et al*., 1993; *Cooke and Wilson*, 1996; *Liousse et al*., 1996; *Cooke et al*., 1999] that consider both fossil fuel and biomass components (see Table 1). The inventories of biomass-

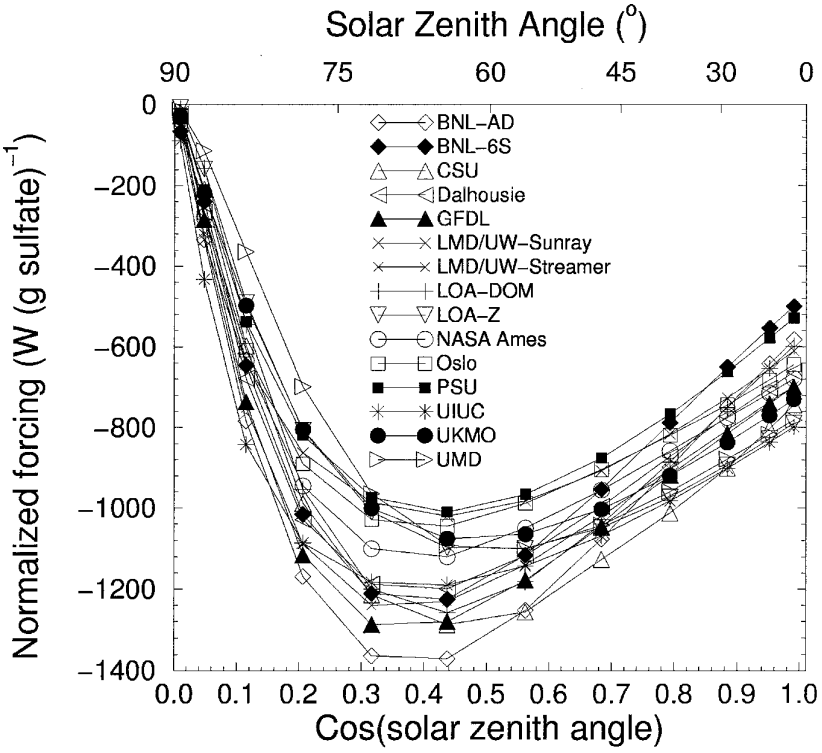

Figure 4. The normalized clear-sky radiative forcing for sulphate aerosol from the intercomparison study of *Boucher et al.* [1998]. A lognormal distribution with a geometric mean diameter of 0.170 μm and a geometric standard deviation of 1.105, together with an aerosol optical depth of 0.20 at 0.55 μm and a Lambertian surface reflectance of 0.15, were assumed. For details of the radiation codes used in the calculations, see *Boucher et al.* [1998].

burning BC and OC particles are more difficult to constrain than fossil fuel emissions, owing to the paucity of data. OC emissions are particularly difficult to constrain because measurements of OC are particularly difficult to make and often include a substantial natural component and because of secondary production. Currently, the complex reactions that form secondary organic aerosol are not included explicitly in model estimates of the OC burden and the subsequent radiative forcing [e.g., *Cooke et al.*, 1999; *Penner et al.*, 1998]. *Cooke et al.* [1999] attempt to account for these important processes by multiplying the burden of primary OC by a factor of 2, while *Penner et al.* [1998] account for the formation of secondary OC particles in the construction of the emission inventories [*Liousse et al.*, 1996].

Since *IPCC* [1996], there have been a number of more refined 3-D global model estimates of the radiative forcing due to BC aerosol from fossil fuel burning that have superseded calculations using simple expressions for the radiative forcing [e.g., *Haywood and Shine*, 1995; *Chýlek and Wong*, 1995] where the contribution from cloudy regions was not included. These estimates now include the contribution to the total radiative forcing from areas where BC exists either above or within clouds, although the treatment of BC within clouds remains crude. There are two main sources of black carbon aerosol: fossil fuel and biomass burning. The radiative forcing due to fossil fuel BC is considered in section 2.3.1, and the radiative forcing due to fossil fuel OC is considered in section 2.3.2. Section 2.3.3 considers the radiative forcing due to OC and BC from biomass emissions, and section 2.3.4 considers other studies that have examined OC and/or BC. Table 3 summarizes recent global annual-mean estimates of the radiative forcing due to BC and OC aerosol from recent studies.

2.3.1. Fossil fuel BC. The radiative forcing of fossil fuel BC has received considerable attention. *Haywood et al.* [1997a] and *Myhre et al.* [1998] assumed that fossil fuel BC was directly proportional to the mass of sulphate from *Langner and Rodhe* [1991] and *Restad et al.* [1998], respectively, by applying a 7.5% mass scaling (equivalent to a global mean burden of approximately 0.13 to 0.14 mg m^{-2}). Global annual-mean radiative forcings of +0.20 and +0.16 W m^{-2} are calculated for external mixtures from the respective studies. If BC were modeled as an internal mixture with sulphate aerosol, *Haywood et al.* [1997a] and *Myhre et al.* [1998] suggest that the degree of absorption may be considerably enhanced and the radiative forcing strengthens to +0.36 and +0.44 W m^{-2}, respectively. These estimates were performed

TABLE 3. The Global-Mean Annual-Average Direct Radiative Forcing Due to Black Carbon and Organic Carbon Aerosols From Different Studies

Aerosol	*Author*	*Mixing or Optical Parameters*	ω_o	k_e, $m^2\ g^{-1}$	*Direct Radiative Forcing, W m^{-2}*	*Column Burden, mg m^{-2}*	*Normalized Radiative Forcing, W g^{-1}*	*Remarks*
Fossil fuel BC	*Haywood et al.* [1997a]	external	0.21	9.3	+0.20	0.13	1525	GCM study; 7.5% mass scaling of BC to SO_4 assumed; SO_4 from *Langner and Rodhe* [1991] (slow oxidation case); λ = 0.55 μm, RH = inv
		internal with sulphate	0.91	11.1	+0.36	0.13	2770	internal mixing approximated by volume weighting the refractive indices of BC and SO_4; λ = 0.55 μm, RH = 80%
	Myhre et al. [1998]	external	0.21	9.3	+0.16	0.14	1123	three-dimensional study using global climatologies for cloud, surface reflectance, etc.; 7.5% mass scaling of BC to SO_4 assumed; SO_4 from *Restad et al.* [1998]; λ = 0.55 μm, RH = inv
		internal with sulphate	0.77	5.5	+0.42	0.14	3000	internal mixing approximated by volume weighting the refractive indices of BC and SO_4; λ = 0.55 μm, RH = 0%
	Penner et al. [1998] and *Grant et al.* [1999]	internal	NA	NA	+0.20	0.16	1287	BC modeled using chemical transport model and GCM; BC and OC fractions vary geographically
	Cooke et al. [1999]	external	0.23	11.0	+0.17	0.14	1210	BC modeled using chemical transport model and GCM; λ = 0.50 μm, RH = inv
	Haywood and Ramaswamy [1998]	external mixture	0.21	9.3	+0.2	0.13	1500	three-dimensional GCM study using *Cooke and Wilson* [1996] BC data scaled to *Liousse et al.* [1996] total BC mass; 50% of the BC mass assumed to be from fossil fuels; λ = 0.55 μm, RH = inv
Fossil fuel OC	*Penner et al.* [1998]	internal with fossil fuel BC	1.0	5.3	−0.04	~0.7	−60	OC modeled using chemical transport model and GCM; may be more negative due to mixing and effects of RH; 0.5–0.69 μm, RH = 0%
	Cooke et al. [1999]	external mixture	0.98	3.6	−0.02	0.34	−70	OC modeled using chemical transport model and GCM; may be more negative due to effects of RH and assumption of partial absorption of OC; λ = 0.5 μm, RH = inv
Biomass burning (BC + OC)	*Hobbs et al.* [1997]	optical parameters of biomass smoke	0.88	4.3	−0.3	3.7	−80	uses simplified expression from *Chylek and Wong* [1995]; neglects radiative forcing from cloudy areas; other parameters including estimated column burden from *Penner et al.* [1992]; λ = 0.55 μm, RH = 80%
	Iacobellis et al. [1999]	optical parameters of biomass smoke	0.97	9.06	−0.74	3.5	−210	three-dimensional chemical transport model and GCM; simplified expressions also examined; λ = 0.25–0.68 μm, RH = 0%
	Penner et al. [1998] and *Grant et al.* [1999]	internal mixture of OC and BC	0.98	2.4	−0.14 to −0.21	1.76	−80 to −120	three-dimensional chemical transport model and GCM using biomass optical parameters modeled from two observational studies; λ = 0.5–0.69 μm, RH = 0%
Fossil fuel and biomass-burning BC	*Haywood and Ramaswamy* [1998]	external mixture	0.21	9.3	+0.4	0.27	1500	three-dimensional GCM study using *Cooke and Wilson* [1996] BC data scaled to *Liousse et al.* [1996] total BC mass; λ = 0.55 μm, RH = inv
Fossil fuel and biomass-burning BC	*Hansen et al.* [1998]	observed ω_0	NA	NA	+0.27	NA	NA	adjustment of modeled single scattering albedo from 1.0 to 0.92–0.95 to account for the absorption properties of BC
Fossil fuel and biomass-burning OC	*Hansen et al.* [1998]	external mixture	1.0	NA	−0.41	NA	NA	three-dimensional GCM study using *Liousse et al.* [1996] OC data; OC modeled as scattering aerosols; λ = 0.55, RH = inv

The type of mixing or source of optical parameters is shown. The single scattering albedo ω_0 and the specific extinction coefficient k_e are shown together with the wavelength λ and the relative humidity (RH). "Inv" indicates that the optical parameters are invariant with relative humidity. The anthropogenic column burdens of black carbon (BC) and organic carbon (OC) are shown together with the normalized direct radiative forcing. GCM means general circulation model.

before global modeling studies for BC were generally available. *Haywood and Ramaswamy* [1998] rescaled the global column burden of BC from *Cooke and Wilson* [1996] to that of *Liousse et al*. [1996], which is thought to be more representative of optically active BC, and estimated the radiative forcing due to fossil fuel and biomass burning to be approximately $+0.4$ W m^{-2}. Approximately half of the radiative forcing due to BC was attributed to fossil fuel burning sources, leading to a fossil fuel BC radiative forcing of $+0.2$ W m^{-2}. *Penner et al*. [1998] and *Grant et al*. [1999] used a chemical transport model in conjunction with a GCM to estimate a global column burden of BC from fossil fuel emissions of 0.16 mg m^{-2} and a radiative forcing of $+0.20$ W m^{-2}. *Cooke et al*. [1999] estimated the global burden of optically active BC aerosol from fossil fuel burning from a $1° \times 1°$ inventory of emissions to be 0.14 mg m^{-2} and a subsequent radiative forcing of $+0.18$ W m^{-2}. The good agreement of the assumed column burdens of *Haywood et al*. [1997a] and *Myhre et al*. [1998] should be noted. *Grant et al*. [1999] suggest that the global mean radiative forcing due to fossil fuel BC is strongest in JJA owing to the larger insolation coupled with higher atmospheric concentrations in the Northern Hemisphere. The normalized radiative forcing due to an external mixture of BC appears reasonably consistent throughout the studies, ranging from $+1123$ to $+1525$ W g^{-1}. However, all these studies used the same size distribution and exclude effects of relative humidity, and thus the modeled specific extinction is independent of the relative humidity at approximately 10 m^2 g^{-1} at 0.55 μm. Observational studies show a wide range of specific extinction coefficients [e.g., *Liousse et al*., 1993; *Horvath*, 1993; *Martins et al*., 1998] of approximately 5–20 m^2 g^{-1} at 0.55 μm, and thus the uncertainty in the associated radiative forcing is likely to be higher than the global model results suggest. Additionally, if BC were modeled as an internal mixture, *Haywood et al*. [1997a] and *Myhre et al*. [1998] suggest the degree of absorption may be considerably enhanced, the radiative forcing being estimated as $+0.36$ and $+0.44$ W m^{-2}, respectively. Both of these studies use relatively simple effective medium mixing rules for determining the composite refractive index of internally mixed BC with sulphate and water. Detailed scattering studies including a randomly positioned black carbon sphere in a scattering droplet show that the absorption is relatively well represented by effective medium approximations [*Chýlek et al*., 1996b]. Column studies by *Haywood and Shine* [1997] and *Liao and Seinfeld* [1998] and the global studies by *Haywood and Ramaswamy* [1998] and *Penner et al*. [1998] suggest that the radiative forcing due to BC will be enhanced if BC exists above the cloud but will be reduced if the BC is below the cloud; thus the vertical profile of BC aerosol must be modeled accurately.

2.3.2. Fossil fuel OC. The radiative forcing due to fossil fuel OC has been investigated by *Penner et al*. [1998] and *Grant et al*. [1999]. They modeled the radiative forcing due to an internal mixture of fossil fuel BC and OC and found that the radiative forcing weakened from $+0.20$ W m^{-2} for BC alone to $+0.16$ W m^{-2} (or by -0.04 W m^{-2}) for a global mean OC burden of approximately 0.7 mg m^{-2}. However, if OC were modeled as an external mixture with BC and/or if the effects of relative humidity are included, the radiative forcing due to OC from fossil fuels is likely to be more negative, and thus -0.04 W m^{-2} represents an approximate lower limit for the strength of the forcing due to fossil fuel OC. *Cooke et al*. [1999] perform calculations for an external mixture assuming OC is partially absorbing with a modeled ω_0 of approximately 0.97 at a wavelength of 0.55 μm and find a radiative forcing of -0.02 W m^{-2} from a global mean burden of 0.34 mg m^{-2}. If OC were modeled as purely scattering or if the effects of relative humidity were considered, the radiative forcing may be significantly stronger. Thus these modeling estimates suggest an approximate lower limit for the normalized radiative forcing for OC of approximately -60 W g^{-1}, which is significantly smaller in magnitude than that due to BC or sulphate aerosol. This may be due to the modeling studies using different size distributions based on observations, which yield lower extinction efficiencies than for sulphate aerosols, and to smaller hygroscopic effects [*Penner et al*., 1998].

2.3.3. Biomass-burning BC and OC. The annual mean radiative forcing due to biomass-burning aerosol where BC and OC are combined has been studied by *Hobbs et al*. [1997], *Iacobellis et al*. [1999], *Penner et al*. [1998], and *Grant et al*. [1999]. *Hobbs et al*. [1997] performed aircraft measurements of smoke from biomass burning during the Smoke, Clouds, and Radiation–Brazil (SCAR–B) experiment and used the model of *Penner et al*. [1992] to estimate a global mean radiative forcing of -0.3 W m^{-2} as an approximate upper limit for OC and BC combined. *Penner et al*. [1998] and *Grant et al*. [1999] perform 3-D GCM modeling studies of the radiative forcing of OC and BC combined as an internal mixture and determine a radiative forcing of between -0.14 and -0.21 W m^{-2} depending upon the assumed optical parameters. *Iacobellis et al*. [1999] calculate the radiative forcing due to biomass-burning BC and OC combined to be -0.7 W m^{-2} but use an emission factor that *Liousse et al*. [1996] suggest may be a factor of 3 too high, leading to a possible overestimate of the atmospheric burden. Additionally, the specific extinction coefficient used by *Iacobellis et al*. [1999] is significantly larger than those of *Penner et al*. [1998], who base their model calculations upon observed extinction coefficients; thus *Iacobellis et al*. [1999] calculate a larger normalized radiative forcing (see Table 3).

2.3.4. Other studies. The radiative forcing for BC from both fossil fuels and biomass burning has been studied by *Haywood and Ramaswamy* [1998] and *Hansen et al*. [1998]. *Haywood and Ramaswamy* [1998] determine a radiative forcing due to combined biomass and fossil fuel sources of $+0.4$ W m^{-2}; approximately half of this radiative forcing is attributed to fossil fuel and half is

attributed to biomass burning. *Hansen et al*. [1998] used a different approach and adjusted the single scattering albedo of purely scattering sulphate and organic aerosols from unity to 0.92–0.95 to account for the absorption characteristics of BC. *Hansen et al*. [1998] used the geographical distribution of OC derived from the chemical transport model of *Liousse et al*. [1996] to estimate the radiative forcing due to purely scattering fossil fuel and biomass OC to be -0.41 W m^{-2}.

The geographic distribution of the radiative forcing of fossil fuel BC and OC combined from the study of *Penner et al*. [1998] is shown in Plate 1b. Because the contribution to the global mean radiative forcing due to fossil fuel OC is relatively small (see Table 3), the radiative forcing tends to be positive almost everywhere due to the strong absorption characteristics of BC (see section 2.1 and Figures 2 and 3). The geographic distribution of the radiative forcing of biomass-burning BC and OC combined from the study of *Penner et al*. [1998] is shown in Plate 1c. The radiative forcing is calculated to be negative over the majority of the globe, but some limited areas of positive forcing exist over areas with a high surface reflectance, due to the dependence of the radiative forcing upon the underlying surface albedo (see section 2.1 and Figures 2 and 3) and the partially absorbing nature of combined OC and BC.

2.4. Mineral Dust Aerosol

Mineral dust is created by wind erosion of arid areas of the Earth. Dust production is typically parameterized in transport models as a function of the vegetation fraction and surface wind speed and includes a soil moisture–dependent threshold velocity below which no dust is produced. Recent studies have suggested that between 20% and 50% of the total mineral dust in the atmosphere originates from anthropogenic activities [*Sokolik and Toon*, 1996; *Tegen and Fung*, 1995]. Determination of the anthropogenic fraction of mineral dust in the atmosphere is exceedingly difficult for many reasons. There is no physically based inventory of emissions except from models. Additionally, the influence of anthropogenic activity upon land-use change is difficult to determine because it is likely that some changes occur due to natural climate variability or as a feedback in response to changing atmospheric conditions [e.g., *Myhre and Stordal*, 2000]. Here only the radiative forcing from this anthropogenic component is considered, as there is no evidence that the naturally occurring component has changed since 1750. However, over longer timescales, ice core measurements suggest that atmospheric concentrations of dust have varied substantially, with significantly more mineral dust deposited in the Antarctic and Greenland ice sheets during the Last Glacial Maximum [e.g., *Reader et al*., 1999, and references therein]. Because mineral dust particles are of a large size and because they become lofted to high altitudes in the troposphere, in addition to the solar radiative forcing, dust may exert a significant thermal infrared radiative forcing. The global mean radiative forcing will be negative in the solar part of the spectrum, due to the predominantly scattering nature of mineral dust aerosol at these wavelengths, and positive in the thermal infrared.

Sokolik and Toon [1996] estimated the anthropogenic contribution to the dust loading due to changes in land use associated with anthropogenic activity to be 20% of the total dust burden and neglected forcing in cloudy regions to estimate a solar radiative forcing of -0.25 W m^{-2} over ocean and -0.6 W m^{-2} over land, leading to a global forcing of approximately -0.46 W m^{-2}. They point out that this is offset to some extent by a positive thermal infrared forcing. *Tegen and Fung* [1995] modeled dust aerosol and estimated that approximately 30–50% of the total dust burden is due to changes in land use associated with anthropogenic activity. The radiative forcing using these data was estimated by *Tegen et al*. [1996] to be -0.25 W m^{-2} in the solar spectrum and $+0.35$ W m^{-2} in the thermal infrared, resulting in a net radiative forcing of $+0.09$ W m^{-2}. Updated calculations of the net radiative forcing based on the work of *Miller and Tegen* [1998] estimate the radiative forcing to be -0.22 W m^{-2} in the solar spectrum and $+0.16$ W m^{-2} in the thermal infrared, resulting in a net radiative forcing of -0.06 W m^{-2}. *Hansen et al*. [1998] perform similar calculations and calculate a net radiative forcing of -0.12 W m^{-2} by assuming a different vertical distribution and different optical parameters and using a different global model. These global studies have considered mineral dust as a homogeneous mixture of minerals; that is, they have used a constant refractive index that is independent of the mineral composition of the aerosols. More recent studies have started to incorporate the mineral composition as a function of the dust sources [e.g., *Claquin et al*., 1999; *Sokolik and Toon*, 1999] and have examined the effect of the optical parameters. *Myhre and Stordal* [2000] perform a sensitivity study of the effects of mineral dust using a global model and two different 3-D data sets for mineral dust. They investigate the effects of altitude, size distribution, and refractive index and find a large sensitivity in the radiative forcing to each, but particularly to the assumed refractive index, which is dependent upon the mineral composition. The effects of nonsphericity of the mineral dust are not accounted for in any of these calculations. *Mishchenko et al*. [1997] model dust particles as spheroids and suggest that differences in the optical parameters between model spheroids and spheres do not exceed 10–15%, although changes of this magnitude may have a large effect on the radiative forcing [*Miller and Tegen*, 1998]. An example of the geographical distribution of the radiative forcing is shown in Plate 1d [*Tegen et al*., 1996]. This shows regions of positive and negative forcing. Positive forcing tends to exist over regions of high surface reflectance, and negative radiative forcings tend to exist over areas of low surface reflectance due to the dependence of the forcing on surface reflectance, as

described in section 2.1, and the additional effects of the longwave radiative forcing.

One problem that needs to be solved is uncertainty in representative refractive indices [*Claquin et al*., 1998]. The modeling study of *Hansen et al*. [1998] calculates that the net radiative forcing changes from -0.12 to -0.53 W m^{-2} when dust is treated as conservatively scattering. *Sokolik et al*. [1993] present a summary of solar imaginary refractive indices from many geographical locations showing a range of $-0.003i$ to $-0.009i$ at 0.55 μm. Differences in refractive index in the thermal infrared from different geographical sources are also reported by *Sokolik et al*. [1998]. *von Hoyningen-Huene et al*. [1999] determine the imaginary part of the refractive index from surface-based absorption and scattering measurements and find that a refractive index of $-0.005i$ best fits the observations. The radiative forcing is particularly sensitive to the single scattering albedo [*Miller and Tegen*, 1999]. Additional uncertainties lie in modeling the size distributions [*Tegen and Lacis*, 1996; *Claquin et al*., 1998] that together with the refractive indices, determine the optical parameters. Although there have been a growing number of estimates of the local, clear-sky radiative effect and optical depths of Saharan dust from satellite instruments [e.g., *Ackerman and Chung*, 1992; *Swap et al*., 1996; *Goloub et al*., 1999], relating instantaneous observational measurements that do not account for the effects of clouds, diurnal averaging of the radiation, the seasonal signal associated with emissions, and the fraction of mineral dust that is anthropogenic to the global mean radiative forcing is very difficult. Note also that the effects of stratospheric adjustment have not been considered in any study to date: This is likely to be more important for tropospheric aerosols that are lofted to high altitudes in the troposphere, such as mineral dust. Because the resultant global mean net radiative forcing is a residual obtained by summing the solar and the thermal infrared radiative forcings that are of roughly comparable magnitudes, the uncertainty in the radiative forcing is large, and even the sign is in doubt due to the competing nature of the solar and thermal infrared effects.

2.5. Nitrate Aerosol

Although *IPCC* [1994] identified nitrate aerosol as a significant anthropogenic source of aerosol, there have been few studies of the direct radiative effect. *Adams et al*. [1999] perform a global chemical modeling study of sulfate, nitrate, and ammonium aerosol and estimate a global mean burden of approximately 0.13 Tg NO_3 (0.25 mg m^{-2}). Also, *van Dorland et al*. [1997] have produced a radiative forcing estimate of approximately -0.03 W m^{-2} for ammonium nitrate, but as acknowledged by the authors, many of the assumptions implicit within the calculations make this a first-order estimate only. Recent measurement studies by *Veefkind et al*. [1996] and *ten Brink et al*. [1997] in the Netherlands have shown that nitrate aerosol in the form of ammonium nitrate is a locally important aerosol species in terms of aerosol mass in the optically active submicron size range and hence in the associated local radiative forcing. They also emphasize the problems in measuring the concentrations and size distributions of nitrate, which is a semivolatile substance. The paucity of global studies of this aerosol species means that an assessment of the radiative forcing due to anthropogenic nitrate aerosol is not possible at the present time.

2.6. Mixed Aerosols

Most of the global modeling studies performed to date consider tropospheric aerosol to be externally mixed (i.e., each aerosol chemical species exists independently of the others), which makes modeling the sources, atmospheric transport, and radiative properties simpler [e.g., *Tegen et al*., 1997; *Haywood et al*., 1999]. However, single particle analysis of particles containing mineral dust [e.g., *Levin et al*., 1996] and sea salt [e.g., *Murphy et al*., 1998] have often shown them to be internally mixed with sulphate and other aerosols of anthropogenic origin. This means that submicron particles such as anthropogenic sulphate may be removed from the optically active region through heterogeneous processes and become internally mixed with larger supermicron species [e.g., *Dentener et al*., 1996], an effect that has not yet been accounted for in global modeling studies. Global studies that examine the radiative forcing of absorbing and scattering particles such as BC and sulphate [e.g., *Haywood et al*., 1997a; *Myhre et al*., 1998; *Chýlek et al*., 1995] suggest that an internal mixture may be more absorbing than a corresponding external mixture. Also, *West et al*. [1998] suggest that for internally mixed aerosol particles containing sulphate, the radiative forcing may not increase monotonically with sulphate loading due to chemical interactions between sulphate and other chemical components such as ammonium, nitrate, and water. Additionally, *McInnes et al*. [1998] suggest that OC may act to suppress the hygroscopic nature of sea salt and sulphate; thus the effect of OC emissions may, under certain circumstances, result in a net positive forcing. Thus it is very unlikely that the radiative forcing from different species will add linearly. Further modeling work where all aerosol types, including natural species, are included in chemical transport models is necessary if the effects of internal mixing upon the overall radiative forcing are to be assessed on a global scale.

2.7. Field Campaigns

Field campaigns such as the Tropospheric Aerosol Radiative Forcing Observational Experiment (TARFOX) and the Aerosol Characterization Experiment (ACE 1 and 2), the Indian Ocean Experiment (INDOEX) and SCAR–B (Smoke, Clouds, and Radiation–Brazil), and long-term monitoring networks such as Aerosol Robotic Network (AERONET) provide essential information on the chemical, physical, and optical properties of aerosol particles, without which it would be impossible to vali-

date assumptions used in modeling studies [e.g., *Novakov et al*., 1997; *Hegg et al*., 1997; *Murphy et al*., 1998; *Hobbs et al*., 1997; *Ross et al*., 1998; *Holben et al*., 1998]. TARFOX has helped validate current treatment of radiative transfer by comparing in situ radiances and irradiances with those predicted by radiation codes using in situ observations of aerosol chemical composition and morphology and atmospheric concentrations. *Hignett et al*. [1999] modeled TARFOX aerosol as an internal mixture of sulphate, OC, and BC and used in situ aircraft observations to show the importance of the BC component in obtaining good agreement between modeled and observed broadband irradiances. Similar calculations were performed by *Russell et al*. [1999], who also showed good agreement between modeled and measured irradiances and that the strongest forcing occurred not at midday but when the solar zenith angle was approximately 60°–70°, in agreement with theoretical calculations (see Figure 4). *Francis et al*. [1999] made similar modeling assumptions and found reasonable agreement between the modeled and measured radiances, indicating that the scattering phase function was in reasonable agreement with theory. The hygroscopic growth factor of the aerosol was investigated in detail by *Kotchenruther et al*. [1999], who found different growth factors for different large-scale flow regimes and that, on average, the direct radiative forcing at 80% relative humidity was approximately double that of the dry aerosol. The results from TARFOX suggest that under certain circumstances, the use of an internal mixture may be more appropriate for modeling the physical and radiative properties of aerosols (see section 2.6) rather than the assumption of external mixtures that have been widely used in modeling studies. INDOEX provided information on the chemical, physical, and optical properties of aerosols in the Indian Ocean, chemical analysis revealing that aerosol can be transported for thousands of kilometers from the source regions [*Podgorny et al*., 2000; *Satheesh et al*., 1999]. A significant degree of absorption due to the large quantities of atmospheric BC aerosol was noted, as evidenced by the fact that the change in irradiance at the surface was 2–3 times that observed at the top of the atmosphere [*Podgorny et al*., 2000]. This means that there is a vertical redistribution of energy throughout the atmosphere that does not occur with purely scattering aerosols. Modeling studies suggest that for absorbing aerosols, the climate sensitivity parameter λ may differ significantly due to diabatic heating in the aerosol layer modifying the temperature structure of the atmosphere, which may affect the formation of clouds [*Hansen et al*., 1997b]. SCAR–B studied biomass-burning aerosol over Brazil and provided important information on the refractive indices [e.g., *Yamasoe et al*., 1998], size parameters [e.g., *Remer et al*., 1998], optical parameters [e.g., *Dubovik et al*., 1998], relative humidity growth factors [e.g., *Ross et al*., 1998], and radiative effects [e.g., *Eck et al*., 1998; *Ross et al*., 1998] of biomass-burning aerosol. *Hobbs et al*. [1997] highlight the significant absorption of biomass-burning aerosols and the fact that biomass-burning aerosol is not as hygroscopic as industrial aerosol measured off the coast of the continental United States (see also *Kotchenruther et al*. [1999] and *Ross et al*. [1998]). ACE 2 provided much information on the physical characteristics of aerosol over the eastern Atlantic. *Russell and Heintzenberg* [2000] summarize a variety of column closure experiments for Saharan dust and for marine boundary-layer aerosol performed during the campaign and highlight differences between observed and calculated aerosol optical depths due to particle shapes, complex refractive indices, and single scattering albedos. *Schmid et al*. [2000] perform local closure experiments for aerosol size distributions and aerosol optical depths using in situ measurements of the size distributions and Sun-photometer data and find excellent agreement despite the fact that the desert dust aerosols are assumed to be spherical. *Haywood et al*. [2000] use aircraft measurements of the scattered radiance at 0.55 μm in a Saharan dust layer and find good agreement with modeling calculations that assume spherical particles. These studies suggest that for reasonable accuracy in radiative calculations, dust particles may be modeled as spheres (see section 2.4). Field campaigns have helped verify our understanding of radiative transfer and aerosol physical properties and thus are extremely valuable in verifying assumptions for input parameters in global modeling studies. However, note that the limited-area nature of measurement campaigns and the difficulties in distinguishing between aerosols from anthropogenic and natural sources mean that global models remain necessary in estimating the global radiative forcing.

2.8. Satellite Measurements

Remote sensing of aerosols has made considerable progress in the past few years [*King et al*., 1999]. Spaceborne instruments, such as the advanced very high resolution radar (AVHRR) [*Husar et al*., 1997; *Nakajima and Higurashi*, 1998; *Higurashi and Nakajima*, 1999] and Meteosat [e.g., *Jankowiak and Tanré*, 1992; *Moulin et al*., 1997], have proven useful in retrieving aerosol optical depth. More recently dedicated instruments, such as Polarization and Directionality of the Earth's Reflectance (POLDER) [*Goloub et al*., 1999; *Deuzé et al*., 1999], Moderate-Resolution Imaging Spectroradiometer (MODIS) [*King et al*., 1992; *Kaufman et al*., 1997; *Tanré et al*., 1997], Ocean Color Temperature Scanner (OCTS) [*Nakajima et al*., 1999], or Along Track Scanning Radiometer (ATSR) [*Veefkind et al*., 1999], have been designed to monitor aerosol properties, and accurate retrieval of the aerosol optical depth over the ocean in clear-sky conditions has proved to be feasible [*Goloub et al*., 1999; *Tanré et al*., 1999; *Veefkind et al*., 1999].

Cusack et al. [1998] report better agreement between GCM clear-sky top and bottom of atmosphere irradiances over oceans and observations from Earth Radiation Budget Experiment (ERBE) and Scanner for Ra-

diation Budget (ScaRab) when a simple aerosol climatology is included. *Haywood et al*. [1999] find that inclusion of chemical transport model based aerosol climatologies and radiative effects can explain much of the magnitude and the spatial distribution of differences between GCM modeled and observed ERBE irradiances over oceans. Plate 2 shows an example of the radiative effect of tropospheric aerosols as computed from the POLDER aerosol retrievals [*Boucher and Tanré*, 2000]. The radiative signatures of biomass-burning aerosols and the Saharan dust plume off the coast of west Africa and that of industrial aerosols off the east coast of the United States and over the Mediterranean Sea are clearly visible. There is also a clear seasonal variation in the aerosol radiative effects.

Aerosol retrievals over land are also developing rapidly but are complicated by the spectral and angular dependence of the surface reflectivity [e.g., *Leroy et al*., 1997; *Wanner et al*., 1997]. *Soufflet et al*. [1997] developed an aerosol retrieval algorithm over dark land surfaces using AVHRR. *Kaufman et al*. [1997] undertake a similar approach with the MODIS instrument. *M. Herman et al*. [1997] suggest that the surface contribution could be more easily corrected for the polarized radiances than for the total radiances, which would allow the retrieval of the aerosol optical depth over land. *Flowerdew and Haigh* [1996] and *Veefkind et al*. [1998] used the dual-look capability of the ATSR 2 instrument in order to retrieve the aerosol optical depth over land by assuming that the ratio of the surface reflectances in the two viewing directions is independent of the wavelength. *Li and Kou* [1998] determine the radiative effect of smoke over visible wavelengths using GOES data over boreal forests in western Canada, where the surface reflectance is also relatively invariant. The infrared radiances from Meteosat (and other sensors) can also be used to detect desert dust events over bright surfaces [*Legrand et al*., 1989; *Ackerman*, 1997] and diagnose their radiative impact. The Total Ozone Mapping Spectrometer (TOMS) instrument [*J. Herman et al*., 1997] has the capability to detect partially absorbing aerosols over land and ocean, but the measured signal is a function of the vertical distribution of aerosols and therefore remains semi-quantitative.

In addition to aerosol optical depth, the Angström coefficient can also be retrieved with reasonable agreement when compared with ground-based Sun-photometer data [*Goloub et al*., 1999; *Nakajima and Higurashi*, 1998; *Higurashi and Nakajima*, 1999]. The Angström coefficient gives an indication of the vertically averaged size distribution of the aerosol particles. The retrieval of the single scattering albedo, which is important in predicting the sign of the direct radiative forcing, is still an unresolved issue despite exploratory studies [*Kaufman*, 1987]. Although satellite measurements of aerosols will undoubtedly help in estimating the aerosol direct radiative forcing and validating model predictions of the global aerosol cycles in the future, there are few studies on this topic to date. Moreover, the problem of separating the natural from the anthropogenic components of the atmospheric aerosols remains, although the Angström coefficient can discriminate between primary and secondary aerosols [*Boucher and Tanré*, 2000]. In particular, the fraction of emitted dust that originates from changes in land use remains very uncertain. Finally, aerosol retrieval is usually associated with a stringent cloud-screening algorithm, which raises the issue of the representativeness of sampled (cloud-free) pixels. In particular, aerosol retrievals over and close to cloudy regions are not possible. In this perspective, future satellite lidar measurements are very promising. Despite these potential problems, it is very likely that more and more global modeling efforts will use satellite retrievals of the clear-sky radiative effect or the optical depth to help better constrain the radiative effects of aerosols, particularly when the models incorporate all of the natural and anthropogenic aerosol components discussed here.

2.9. Discussion of Uncertainties of Direct Effect

While the radiative forcing due to greenhouse gases may be determined to a reasonably high degree of accuracy [*IPCC*, 1996], the range of estimates due to aerosol direct radiative forcings remains large, and estimations of the aerosol forcing rely to a large extent on global modeling studies that are difficult to verify at the present time. The range of estimates presented in this section represents the structural uncertainties (i.e., differences in the model structures and assumptions) rather than the parametric uncertainties (i.e., the uncertainties in the key parameters such as optical parameters, burden, and so on [see *Pan et al*., 1997]). Three major areas of uncertainty exist: uncertainties in the atmospheric burden, uncertainties in the optical parameters, and uncertainties in implementation of the optical parameters and burden to give a radiative forcing. The atmospheric burden of an anthropogenic aerosol species is determined by factors such as combustion, emission, aging, convective transport, and scavenging processes, each of which has an associated uncertainty. The optical parameters have associated uncertainties in size distribution, chemical composition, state of mixing, method of mixing, and asphericity. Uncertainties in calculating the radiative forcing from specified burdens and optical parameters arise from uncertainties in the parameterization of relative humidity effects; the horizontal and vertical distributions of the aerosol; the uncertainties and subgrid-scale effects in other model fields such as clouds, humidity, temperature, and surface reflectance; the representation of the diurnal cycle; and the accuracy of the radiation code used in the calculations. Accurate satellite retrievals of aerosol radiative effects show promise for helping to constrain estimates of the model input parameters such as size distribution as well as to constrain the radiative effects on a close to global scale. While the general spatial distribution of the radiative

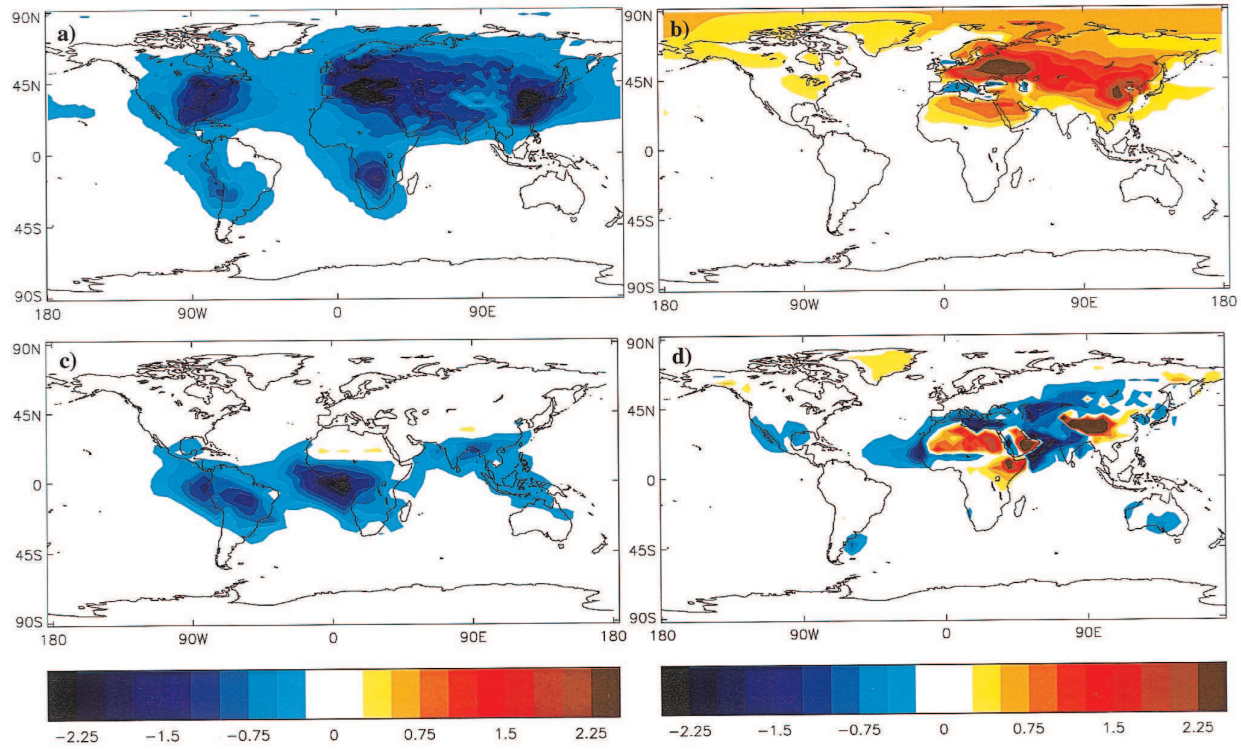

Plate 1. Examples of the radiative forcing (W m^{-2}) due to (a) the direct effect of sulphate aerosol [*Haywood et al*., 1997a], (b) the direct effect of organic carbon and black carbon from fossil fuel burning [*Penner et al*., 1998; *Grant et al*., 1999], (c) the direct effect of organic carbon and black carbon from biomass burning [*Penner et al*., 1998; *Grant et al*., 1999], and (d) the direct effect of anthropogenic emissions of mineral dust [*Tegen et al*., 1996]. Different modeling studies may show substantially different spatial patterns, as described in the text.

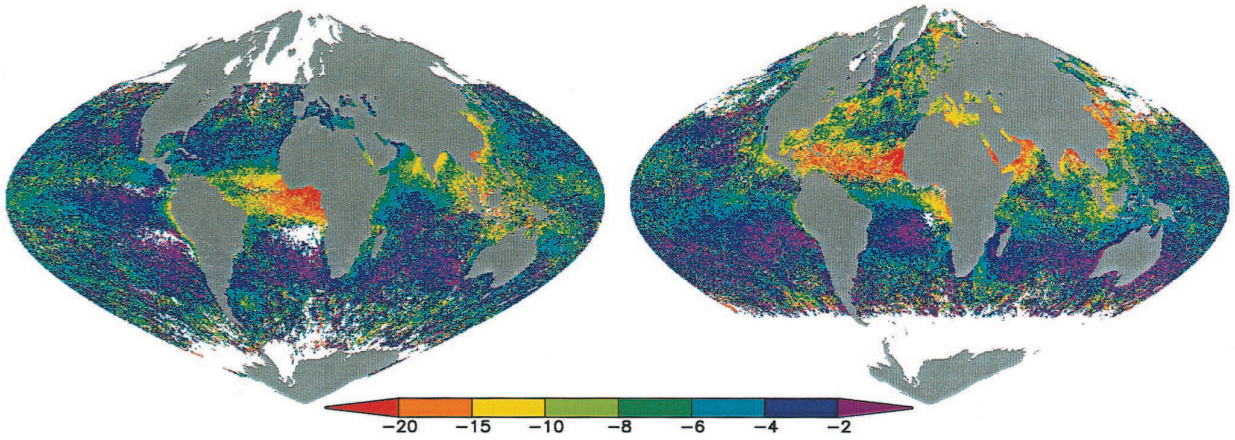

Plate 2. Clear-sky shortwave radiative perturbation (W m^{-2}) computed from POLDER aerosol retrieval for (left) December 1996 and (right) June 1997 [from *Boucher and Tanré*, 2000].

forcing for sulphate aerosol from different studies appears to be similar, some important features such as the seasonal cycle in the radiative forcing remain highly uncertain, which may have important consequences in terms of the detection and attribution of climate change. Additionally, we have concentrated specifically upon the radiative forcing of anthropogenic aerosol species; a further uncertainty highlighted by *Hansen et al*. [1997b] is that for absorbing aerosols, the climate sensitivity parameter λ may differ significantly due predominantly to the feedback effect of clouds.

3. INDIRECT RADIATIVE FORCING

Aerosols serve as cloud condensation and ice nuclei. An increase in aerosol concentration and/or properties can therefore modify the microphysical and radiative properties of clouds, as well as the precipitation efficiency and hence the cloud lifetime. A review of theoretical and observational evidence for the aerosol indirect effects is given by *Schwartz and Slingo* [1995]. The observational evidence includes measurements of an anthropogenic influence on cloud condensation nuclei (CCN) concentrations [e.g., *Hegg et al*., 1993], correlative measurements of sulphate or aerosol concentrations and cloud droplet number concentration [e.g., *Leaitch et al*., 1992; *Martin et al*., 1994; *Novakov et al*., 1994], and studies of the so-called "ship track" phenomenon [e.g., *Coakley et al*., 1987; *Radke et al*., 1989]. Recently, the ACE 2 CloudyColumn experiment focused on the contribution of stratocumulus clouds to the indirect effect in June–July between Portugal and the Canary Islands [*Brenguier et al*., 2000a]. Significantly larger cloud droplet number concentrations and smaller cloud droplet size were reported for clouds formed in air masses of continental origin compared with air masses of marine origin [*Brenguier et al*., 2000b]. A clear comparison of the cloud visible reflectance or cloud optical depth between polluted and nonpolluted clouds is complicated by the fact that these clouds have different geometrical thicknesses. When the effect of geometrical thickness is accounted for, a correlation is found between the cloud optical depth and the cloud droplet number concentration, albeit with considerable scatter [*Brenguier et al*., 2000b, Figure 6b]. It should be noted that there are, to date, no convincing observations showing the entire chain of processes of the aerosol indirect effect from enhanced aerosol concentrations to enhanced cloud albedo on a scale large enough to influence significantly the Earth's radiation budget. This is due, in particular, to the large variability in the cloud albedo parameter due to the large natural variability in cloud types and cloud liquid water path.

Below, we review and discuss the various estimates of the globally averaged aerosol indirect radiative forcing by anthropogenic aerosols. Because of the inherent complexity of the aerosol indirect effect, GCM studies dealing with its quantification necessarily include a significant degree of simplification. While this is a legitimate approach, it should be clear that GCM estimates of the aerosol indirect effect are very uncertain. Section 3.1 investigates the indirect radiative forcing due to sulphate aerosols, on which most efforts have concentrated, while other aerosol types are treated in section 3.2. Section 3.3 is devoted to alternative approaches, while section 3.4 investigates the aerosol indirect effects on ice clouds.

3.1. Sulphate Aerosols

3.1.1. Estimates of the cloud albedo effect. The indirect radiative forcing by sulphate aerosols has received a lot of attention since *IPCC* [1996]. Table 4 reports the studies available in the literature. These studies use different GCMs and different methods for computing the droplet number concentration. While some authors [e.g., *Boucher and Lohmann*, 1995] used empirical relationships between the sulphate mass and the cloud droplet number concentration, other studies [e.g., *Jones et al*., 1994] rely on empirical relationships between the sulphate aerosol number concentration and the cloud droplet number concentration. In the latter case one has to assume a size distribution for sulphate aerosols to convert the sulphate mass concentration predicted by the CTM or GCM into an aerosol number concentration. Among the most recent studies, *Chuang et al*. [1997], *Lohmann et al*. [2000], and *Ghan et al.* [2000a] developed parameterizations of the cloud nucleation process. This approach (sometimes referred to as a "mechanistic" approach) accounts for other preexisting aerosol types and variations in the cloud vertical updraft and avoids the problem of prescribing a unique relationship between aerosol mass and cloud droplet concentration. While this represents a more comprehensive approach, it also adds to models one degree of complexity by introducing a process not yet fully understood. Some of the relationships are plotted in Figure 5. A comparison between diagnostic and prognostic relationships is not straightforward. For *Jones et al*. [1999], over the ocean the relationship also depends on the sea-salt concentration. The best fit between sulphate mass and cloud droplet number concentration obtained with the *Lohmann et al*. [2000] parameterization is also due to other aerosol types, which are correlated to sulphate aerosols and also serve as cloud condensation nuclei. Figure 5 nevertheless suggests that the empirical relationships used by the first investigators show the same qualitative behavior as the new "mechanistic" parameterizations, although, of course, they cannot be considered as universally valid.

One can see from Table 4 that the radiative forcing estimates for the cloud albedo effect range from -0.3 to -1.8 W m^{-2}, which is close to the range of 0 to -1.5 W m^{-2} given by *IPCC* [1996] when only a few estimates were available. There does not seem to be an obvious relationship between the level of model complexity and

TABLE 4. The Global-Mean Annual-Average Indirect Radiative Forcing Due to Aerosols From Different Global Studies

Reference	Aerosol Type	Forcing Estimate, $W\,m^{-2}$			Remarks
		Cloud Albedo	*Cloud Lifetime*	*Both Effects*	
Boucher and Rodhe [1994][a]	SO_4			−0.65 to −1.35	(P) use three relationships between SO_4 mass and CCN/CDN concentrations
Chuang et al. [1994]	SO_4	−0.47			(C) include a parameterization of cloud nucleation processes
Jones et al. [1994]	SO_4	−1.3			(P) use a relationship between aerosol and droplet number concentrations
Boucher and Lohmann [1995]	SO_4	−0.5 to −1.4 −0.45 to −1.5			(P) LMD, GCM } use four different relationships between SO_4 mass (P) ECHAM } and CCN/CDN concentrations (A, B, C, and D)
Jones and Slingo [1996]	SO_4	−0.3 to −1.5			(P) use two different SO_4 distributions; follow *Jones et al.* [1994] and *Boucher and Lohmann* [1995] "D"
Kogan et al. [1996, 1997]	SO_4	−1.1			use a cloud climatology rather than GCM-simulated clouds
Chuang et al. [1997]	SO_4	−0.4 to −1.6			(C) include a parameterization of cloud nucleation processes; use a mixture of preexisting aerosols
Feichter et al. [1997]	SO_4	−0.76			(C) use *Boucher and Lohmann* [1995] "A" relationship
Jones and Slingo [1997]	SO_4	−0.55 to −1.50			(P) use two different versions of the Hadley Centre model
Lohmann and Feichter [1997][a]	SO_4	−1		−1.4 to −4.8	(C) use *Boucher and Lohmann* [1995] "A" relationship
Rotstayn [1999][a]	SO_4	−1.1 to −1.7	−0.4 to −1.0	−1.6 to −3.2	(P) include a (small) LW radiative forcing
Jones et al. [1999][a,b]	SO_4	−0.91	b.e. −0.66	−1.18	(C) include a (small) LW radiative forcing; the two effects add nonlinearly
Kiehl et al. [2000]	SO_4	−0.40 to −1.78			(C)
Lohmann et al. [2000][a]	SO_4			0 to −0.4	(C)
	carb			−0.9 to −1.3	(C) include a parameterization of cloud nucleation
	both	~40%	~60%	−1.1 to −1.5	(C)
Ghan et al. [2000a][a]	SO_4	~50%	~50%	−1.6 to −3.2 (b.e. −1.7)	(C) include a parameterization of cloud nucleation; predicted aerosol size distribution

Letters P (prescribed) and C (computed) refer to off-line and on-line SO_4 aerosol calculations, respectively; CCN and CDN stand for cloud condensation nuclei and cloud droplet number, respectively; "b.e." stands for best estimate; "carb" stands for carbonaceous aerosols.

[a]The estimate in flux change due to the indirect effect of aerosols was computed as the difference in top-of-atmosphere fluxes between two distinct simulations and therefore does not represent a forcing in the strict sense.

[b]Predicts SO_4 concentrations which are too small on average.

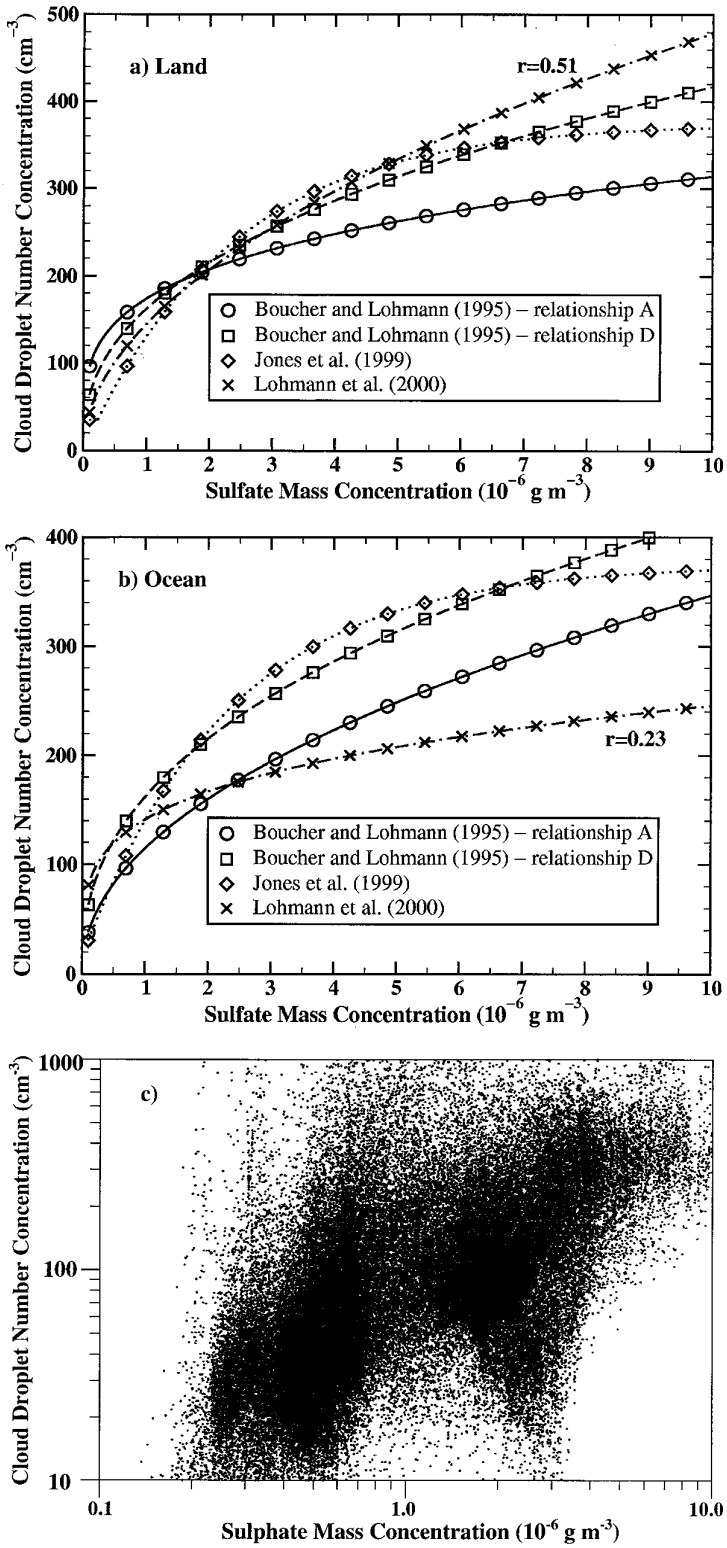

Figure 5. Cloud droplet number concentration as a function of sulphate mass concentration over (a) land and (b) ocean. The empirical relationships of *Boucher and Lohmann* [1995] and *Jones et al.* [1999] are shown, along with a best fit obtained with the mechanistic parameterization of *Lohmann et al.* [2000]. The correlation coefficient is indicated for the *Lohmann et al.* [2000] fit to the data. The relationship obtained by *Ghan et al.* [2000a] is displayed as a separate scatterplot in Figure 5c. See text for more details.

the magnitude of the forcing, as each of the approaches discussed above leads to a rather large range of forcings. There is a tendency for more and more studies to use interactive (on-line) rather than prescribed (monthly- or annual-mean) sulphate concentrations. *Feichter et al*. [1997] pointed out that the first indirect effect calculated from monthly-mean sulphate concentrations is 20% larger than that calculated from interactive sulphate concentrations. *Jones et al*. [1999] found that the total indirect effect was overestimated by about 60% if they used seasonal- or annual-mean sulphate concentrations.

The various GCM studies show some disagreement on the spatial distribution of the forcing, an example of which is shown in Plate 3. The Northern to Southern Hemisphere (NH:SH) ratio varies from 1.4 to 4 depending on the models. It is generally smaller than the NH:SH ratio of anthropogenic sulphate aerosol concentrations because of the higher susceptibility of the clouds in the SH [*Platnick and Twomey*, 1994; *Taylor and McHaffie*, 1994]. The ocean to land ratio depends very much on the type of sulphate mass to cloud droplet number concentration used and on the natural background aerosol concentrations. It was generally found to be smaller than unity [*Boucher and Lohmann*, 1995; *Jones and Slingo*, 1997; *Kiehl et al*., 2000]. Larger ratios, such as 1.6 [*Chuang et al*., 1997] and 5 [*Jones and Slingo*, 1997], are reported in some of the GCM sensitivity experiments. Using a detailed inventory of ship sulphur emissions and a simple calculation of the aerosol indirect effect, *Capaldo et al*. [1999] suggested that a significant fraction of the effect over the oceans (-0.11 W m^{-2}, averaged globally) could be due to ship-emitted particulate matter (sulphate plus organic material in this case). So far, this source of aerosols has not been included in the GCM studies.

Kogan et al. [1996, 1997] used the *Warren et al*. [1988] cloud climatology over the oceans rather than a GCM to predict the indirect effect by sulphate aerosols on cloud albedo. The cloud albedo susceptibility was evaluated from a large eddy simulation model applied to stratocumulus clouds. They found an indirect shortwave forcing of -1.1 W m^{-2} over the oceans, with a small hemispheric difference of 0.4 W m^{-2} (i.e., a NH:SH ratio of about 1.4). In their study the forcing had a strong seasonal cycle, with the SH forcing prevailing in some seasons.

3.1.2. Estimates of the cloud lifetime effect and the combined effects. Whereas the first indirect effect can be computed diagnostically, assessment of the second indirect effect implies that two independent (i.e., with the same fixed sea surface temperatures but with different meteorologies) GCM simulations be made, the first with preindustrial aerosols and the second with present-day aerosols. The difference in top-of-atmosphere fluxes or cloud radiative forcings between two such simulations is used by some authors as a proxy of the forcing due to the second aerosol indirect effect. The simulations need to be sufficiently long (usually 5 years) so that the effects of natural variability can be expected to average out. However, as a consequence, the estimates of the aerosol indirect effect may include some undesirable feedbacks, involving, for instance, changes in the temperature and water vapor fields. There are no studies yet to confirm unambiguously that the radiative impacts associated with the second indirect effect and computed in such a way can be interpreted in the strict sense of a radiative forcing. While some authors call their estimate of the cloud lifetime effect a radiative forcing [e.g., *Rotstayn*, 1999], some others [e.g., *Jones et al*., 1999] label it as just a radiative effect.

Jones et al. [1999] and *Rotstayn* [1999] provide estimates for the cloud lifetime effect alone with ranges of -0.53 to -2.29 and -0.4 to -1.0 W m^{-2}, respectively. For the combined effect (first and second effects estimated together), *Jones et al*. [1999] and *Rotstayn* [1999] give best estimates of -1.18 and -2.1 W m^{-2}. Larger forcings are found by *Rotstayn* [1999], who uses the parameterization for droplet concentration proposed by *Roelofs et al*. [1998] and *Lohmann and Feichter* [1997], who test two alternative cloud schemes, giving values of -3.2 and -4.8 W m^{-2}, respectively. In contrast, *Lohmann et al*. [2000] predict a much smaller combined effect, with radiative impacts of 0.0 and -0.4 W m^{-2}, assuming externally and internally mixed sulphate aerosols, respectively. The authors attribute this rather small radiative impact to the small increase in anthropogenic sulphate aerosol number concentrations. *Ghan et al.* [2000a] estimate a combined effect of -1.7 W m^{-2} using a mechanistic approach similar to that of *Lohmann et al*. [2000] but with aerosol size distribution predicted rather than prescribed. The larger forcing is due to a variety of differences in the models that remain to be investigated. The studies by *Rotstayn* [1999] and *Jones et al*. [1999] both indicate that the longwave (positive) radiative effect associated with the indirect aerosol effect is small (between 0.0 and 0.1 W m^{-2} for each of the effects).

The partitioning of the total indirect radiative forcing between the first and second effect is uncertain. *Jones et al*. [1999] found that the ratio between their best estimates of the first and second indirect effects, taken separately, was 1.38, while *Lohmann et al*. [2000] predicted a ratio of 0.71 (for sulphate and carbonaceous aerosols taken together). In a set of independent simulations, *Rotstayn* [1999] estimated with his GCM that the radiative impact of the two effects considered together was similar or slightly larger than the sum of the two effects considered separately, depending on the versions of the model being used. In contrast, *Jones et al*. [1999] found that the combined radiative impact (-1.18 W m^{-2}) was less than the sum of the two effects computed separately (estimated as -0.91 and -0.66 W m^{-2}, respectively, corresponding to a total of -1.57 W m^{-2}). This nonadditivity of the radiative impacts implies that some sort of interactions between the two effects are occurring, at least in the model of Jones et al. This suggests that the change in top-of-atmosphere fluxes

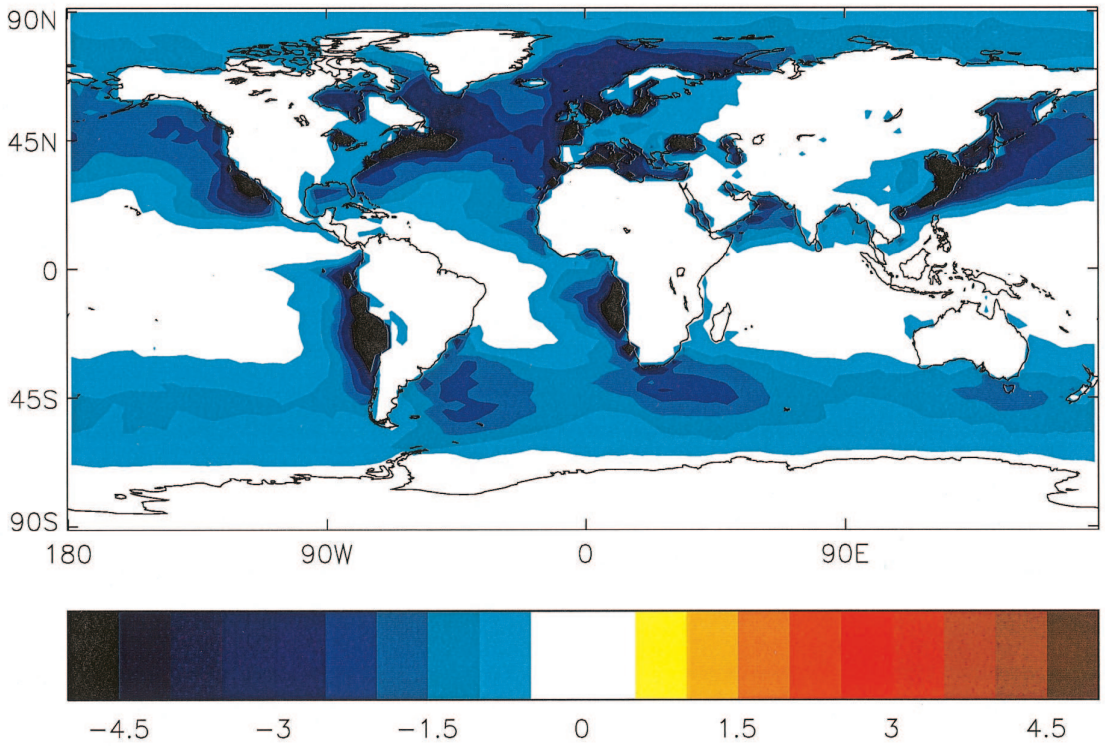

Plate 3. Example of the radiative forcing (W m^{-2}) due to the "first" indirect effect of sulphate aerosol [*Jones and Slingo*, 1997].

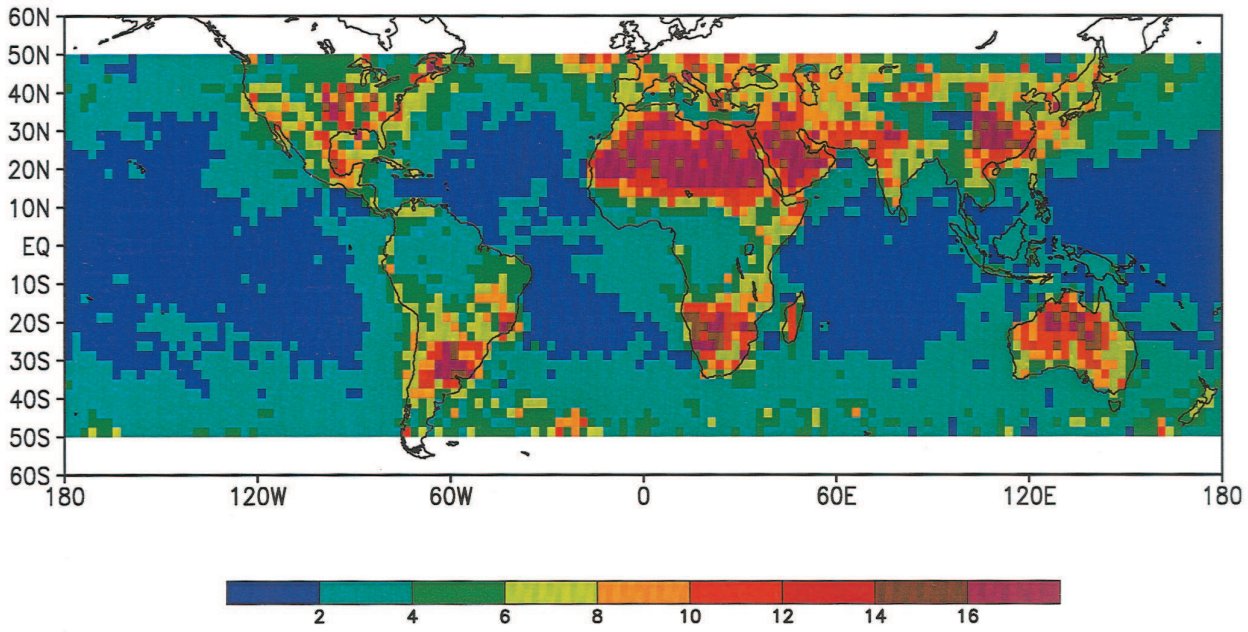

Plate 4. Annual mean cloud column droplet concentration (10^6 cm^{-2}) retrieved from advanced very high resolution radiometer data. Adapted from *Han et al.* [1998b].

between two independent simulations with and without the effects of anthropogenic aerosols constitutes an imperfect quantity in representing the aerosol indirect effect. However, it is recognized that the impact of the second indirect aerosol effect could be a major factor of climate change.

3.1.3. Model evaluation. To date, there is no method for a direct validation of GCM estimates of the aerosol indirect forcing against observations. Nevertheless, global satellite retrievals of various cloud parameters provide indirect means for evaluating and validating the GCM predictions. The simulated cloud droplet effective radii [*Jones et al*., 1994; *Boucher and Lohmann*, 1995; *Jones and Slingo*, 1996; *Chuang et al*., 1997; *Jones and Slingo*, 1997; *Roelofs et al*., 1998; *Rotstayn*, 1999; *Kiehl et al*., 2000; *Ghan et al*., 2000b] have been compared with those retrieved from satellite data [*Han et al*., 1994]. The observed hemispheric and land/ocean contrasts in cloud droplet size are generally simulated by the models, at least qualitatively, the detailed comparison being more or less conclusive depending on the models. It would certainly be appropriate to validate also the horizontal and vertical distribution of the cloud droplet number concentration. This is not yet possible because a global-scale climatology of this parameter does not exist. However, *Han et al*. [1998b] produced a climatology of the column cloud droplet concentration from AVHRR data (Plate 4), which may prove very helpful for model validation. General circulation models with a predictive treatment of the cloud droplet number concentration [*Ghan et al*., 1997, 2000b; *Lohmann et al*., 1999a] tend to produce reasonable results.

3.1.4. Further discussion of uncertainties. Some authors have argued that sea-salt particles may compete with sulphate aerosols as cloud condensation nuclei, thereby reducing the importance of anthropogenic sulphate in droplet nucleation [*O'Dowd et al*., 1999; *Ghan et al*., 1998]. While this process is accounted for in some of the above mentioned estimates, validation of its parameterizations against observations remains difficult, which adds further uncertainty. Considerable sensitivity is found to the parameterization of the autoconversion process [*Boucher et al*., 1995; *Lohmann and Feichter*, 1997; *Jones et al*., 1999], which complicates matters because there is a need to "tune" the autoconversion onset in GCMs [*Boucher et al*., 1995; *Fowler et al*., 1996; *Rotstayn*, 1999] to which the indirect aerosol forcing is sensitive [*Rotstayn*, 1999; *Jones et al*., 1999; *Ghan et al.,* 2000a]. The indirect aerosol forcing is also sensitive to the treatment of the preindustrial aerosol concentrations and properties [*Jones et al*., 1999; *Lohmann et al*., 2000], which remains poorly characterized, the representation of the microphysics of midlevel clouds [*Lohmann et al*., 2000], the representation of aerosol size distribution [*Ghan et al*., 2000a], the parameterization of subgrid-scale clouds [*Ghan and Easter*, 1998], and the ability of GCMs to simulate the stratus and stratocumulus cloud fields. Also, it should be noted that all the studies discussed above cannot be considered as truly "independent" because many of them (with the exception of those of *Lohmann et al*. [2000] and *Ghan et al*. [2000a]) use similar methodologies and similar relationships between sulphate mass and cloud droplet number concentration. Therefore the range of results does not encompass the total range of uncertainties.

3.2. Other Aerosol Species

3.2.1. Carbonaceous aerosols. In this section, carbonaceous aerosols refer to the mixture (internal or external) of OC and BC aerosols. *Novakov and Penner* [1993] and *Novakov and Corrigan* [1996] have suggested that organic aerosols may act as efficient cloud condensation nuclei. There have been few GCM studies estimating the indirect forcing from carbonaceous aerosols. *Penner et al*. [1996] reported a range of forcing from -2.5 to -4.5 W m^{-2} (not reported in Table 4), which may be too large because of low natural emissions of organic aerosols and neglect of absorption of solar absorption by black carbon within the cloud. *Lohmann et al*. [2000] predicted a radiative impact for the combined effect (i.e., first and second effects) of -1.3 and -0.9 W m^{-2} for externally and internally mixed carbonaceous aerosols, respectively. These estimates do not include the effects of secondary organic aerosols or the effects of absorption of solar radiation by black carbon within the cloud.

3.2.2. Combination of sulphate and carbonaceous aerosols. *Lohmann et al*. [2000] found that the radiative impact of sulphate and carbonaceous aerosols considered simultaneously (-1.1 W m^{-2} for the internally mixed assumptions) is comparable to the sum of the radiative impacts calculated separately (-0.4 and -0.9 W m^{-2} for sulphate and carbonaceous aerosols, respectively). This finding is to be related to the fact that sulphate production does not form new particles in their model. Therefore this result probably does not hold for the other studies, and it is likely that the indirect radiative forcings by sulphate and carbonaceous aerosols computed independently do not add linearly. In fact, most of the GCM studies of the indirect aerosol effect used sulphate as a surrogate for the total anthropogenic fraction of the aerosol [e.g., *Boucher and Lohmann*, 1995; *Feichter et al*., 1997; *Lohmann and Feichter*, 1997]. In this case the computed forcings incorporate the effects of other aerosol types that have a spatial distribution similar to sulphate aerosols, such as nitrate aerosols or carbonaceous aerosols from fossil fuel combustion. It does not include, however, the effects of biomass-burning aerosols, which have a spatial distribution different from sulphate aerosols.

Another issue is the potential for light-absorbing aerosols to increase in-cloud absorption of solar radiation (and correspondingly decrease the cloud albedo) when incorporated inside cloud droplets. This effect is generally not considered in the GCM studies, where the

black carbon is included as interstitial particles within the cloudy areas. *Twohy et al*. [1989] concluded from measurements off the coast of California and from simple radiative calculations that the observed levels of soot would not lead to a significant impact on the cloud albedo. *Chýlek et al*. [1996a] estimated an upper bound for increased absorption of solar radiation of 1–3 W m^{-2} (global and annual average) for a black carbon concentration of 0.5 μg m^{-3}. Considering the modeled atmospheric concentrations of soot (see sections 2.3.1 and 2.3.3) and the fact that only a small fraction of the soot is incorporated in the cloud droplets, the effect is probably smaller by 1–2 orders of magnitude. It remains, however, to be estimated properly. For instance, *Heintzenberg and Wendisch* [1996] showed that the decrease in radiative forcing due to a decrease in soot concentrations with increasing distance from the pollution sources could be compensated for by a concurrent increase in the fraction of soot which is incorporated in the cloud droplets.

3.2.3. Mineral dust aerosols. *Levin et al*. [1996] observed desert dust particles coated with sulphate. Such particles may originate from in-cloud scavenging of interstitial dust particles followed by evaporation of the cloud droplets (see also sections 2.6 and 2.8 for the direct effect). The presence of soluble material (which may be of anthropogenic origin) on the desert dust particles converts them into large and effective CCN, which may affect the cloud microphysics. Whether this effect results in a significant climate forcing has not been investigated and cannot presently be quantified.

3.2.4. Effect of gas phase nitric acid. *Kulmala et al*. [1993, 1995] argued that enhanced concentrations of condensable vapors (such as HNO_3 and HCl) in the atmosphere could affect cloud properties by facilitating the activation of cloud condensation nuclei. The impact of such an effect on the planetary cloud albedo has not been assessed.

3.3. Other Methods for Estimating the Indirect Aerosol Effect

3.3.1. The "missing" climate forcing. Hansen and colleagues have used two alternative approaches to characterize and quantify any "missing" climate forcings besides those due to greenhouse gases, solar constant, ozone, and aerosol direct effect. *Hansen et al*. [1995] used a simplified GCM to investigate the impact of various climate forcings on the diurnal cycle of surface air temperature. They found that although the aerosol direct effect or an increase in continental cloud albedo could contribute to damp the surface temperature diurnal cycle, only an increase in continental cloud cover would be consistent with observations [*Karl et al*., 1993]. The required cloud increase depends on cloud height and would be of the order of 1% global coverage for low clouds (i.e., 2–5% over land). We cannot rule out that such a change is an unidentified cloud feedback rather than a forcing. *Hansen et al*. [1997b] also argued that agreement between observed and computed temperature trends requires the presence of another forcing of at least -1 W m^{-2}. However, this method assumes that the observed change in surface temperature since the preindustrial times is entirely a response to anthropogenic forcings, that all the other anthropogenic forcings are well quantified, and that the climate sensitivity parameter (see section 1) predicted by the GCM is correct. As outlined by *Rodhe et al*. [2000], there is also a risk of circular reasoning in estimating the indirect radiative forcing of aerosols in this manner. Therefore it may simply be a coincidence that such an estimate is consistent with the GCM estimates discussed above.

3.3.2. Remote sensing of the indirect effects of aerosols. Because of their global coverage, satellite observations are very useful to evaluate the results of general circulation models. They also provide some insights on the detection and quantification of the indirect radiative effects of aerosols on clouds. *Han et al*. [1994] analyzed AVHRR satellite radiances to retrieve the cloud droplet size of low-level clouds. They reported significant interhemispheric differences for both maritime and continental clouds. *Boucher* [1995] showed that if this difference is to be attributed to anthropogenic aerosols, it implied a differential forcing of about -1 W m^{-2} between the two hemispheres. Assuming a NH:SH ratio of 2:1 for the aerosol indirect effect, this would imply a globally averaged forcing of -1.5 W m^{-2}. Using an independent technique for retrieving cloud droplet size, *Bréon and Goloub* [1998] and *Bréon et al*. [1999] confirmed the smaller size of cloud droplets in the Northern Hemisphere compared with the Southern Hemisphere. They also noted smaller cloud droplet sizes downstream from the source regions of anthropogenic aerosols. The technique of *Bréon and Goloub* [1998] is based on the polarization signature of cloud droplets in the rainbow scattering angle, which requires specific conditions of observations and applies only to homogeneous cloud fields; therefore it is currently difficult to extrapolate these results to the global scale. In a recent analysis of the International Satellite Cloud Climatology Programme (ISCCP) data, *Han et al*. [1998a] revealed a more complicated picture. They found that the cloud albedo increases with decreasing cloud droplet size for most continental clouds and for all optically thick clouds. However, the cloud albedo is observed to decrease with decreasing droplet size for the optically thinner clouds over the oceans. Correlations between cloud albedo and cloud droplet size (or similarly, aerosol optical depth) are in fact not meaningful if they are not made for clouds that are comparable with respect to their other macroscopic properties such as geometrical thickness. In particular, this study underlines the limitations in using the hemispheric contrast in droplet size as an indicator of the aerosol indirect forcing, as was done by *Boucher* [1995]. In this context the positive correlation between aerosol optical depth and cloud optical depth and the

negative correlation between aerosol optical depth and cloud droplet size found by *Wetzel and Stowe* [1999] for stratus clouds have to be interpreted with caution.

Kaufman and Nakajima [1993] used AVHRR data to analyze bright warm clouds over Brazil during the biomass-burning season. While they found a decrease in the cloud droplet size, they also found a decrease in the cloud reflectance when the smoke optical thickness increased and accredited this to the effects of absorbing graphitic carbon particles within the cloud. *Kaufman and Fraser* [1997] used a similar approach to observe thinner and less reflective clouds. They showed that smoke reduced the cloud droplet size and increased the cloud reflectance for smoke optical depth up to 0.8. They estimated the indirect radiative forcing by smoke to be -2 W m^{-2} over this region for the 3 months of biomass burning, which would suggest a much smaller global average. However, using a combination of satellite observations and a global chemistry model, *Remer et al*. [1999] estimate that 50% of the cumulative biomass-burning aerosol indirect forcing occurs for smoke optical depth smaller than 0.1, that is, well away from the source regions.

Rosenfeld [1999, 2000] used a combination of AVHRR and Tropical Rainfall Measuring Mission (TRMM) satellite observations to investigate precipitation formation in clouds. He gave evidence for a suppression of precipitation in clouds locally affected by high levels of pollution from biomass burning or industrial aerosols. However, it seems to be currently difficult to quantify the cloud lifetime effect on the global scale from satellite measurements.

3.4. Aerosol Indirect Effect on Ice Clouds

3.4.1. Contrails and contrail-induced cloudiness. Contrails are ice clouds that form under some thermodynamical conditions after aircraft have passed in the upper troposphere. Their radiative effect is similar to that of thin cirrus clouds. Line-shaped contrails can be identified in satellite data, either from visual inspection [*Bakan et al*., 1994] or through some automatic detection scheme [*Mannstein et al*., 1999]. These studies indicate that line-shaped contrails have an average cover of between 0.5 and 2% in some parts of Europe and the eastern North Atlantic. Using meteorological and air traffic data scaled to regional observations of contrail cover, *Sausen et al*. [1998] estimated the present-day global mean cover by line-shaped contrails to be about 0.1%. This results in a global- and annual-mean radiative forcing by line-shaped contrails of 0.02 W m^{-2} [*Minnis et al*., 1999], subject to an uncertainty factor of about 4, due to uncertainties in the contrail cover, optical depth, ice particle size, and shape [*Meerkötter et al*., 1999].

When the ambient relative humidity exceeds ice saturation, contrails can evolve into extended cirrus clouds. *Boucher* [1999] and *Fahey et al*. [1999] have shown evidence that cirrus occurrence and coverage may have increased in regions of high air traffic compared with the rest of the globe. The trends in cirrus clouds could not be established with accuracy because of quantitative differences between the ground-based and satellite observations. *Smith et al*. [1998] reported the existence of nearly invisible layers of small ice crystals, which cause absorption of infrared radiation and could be due to remnant contrail particles. From consideration of the spatial distribution of cirrus trends during the last 25 years, *Fahey et al*. [1999] gave a range of 0 to 0.04 W m^{-2} for the radiative forcing due to aviation-induced cirrus. The available information on cirrus clouds was deemed insufficient to determine a single best estimate or an uncertainty range.

3.4.2. Impact of aircraft exhaust on cirrus cloud microphysics. Measurements by *Ström and Ohlsson* [1998] in a region of high air traffic revealed higher crystal number concentrations in areas of the cloud affected by soot emissions from aircraft. If the observed enhancement in crystal number density (which is about a factor of 2) is associated with a reduction in the mean crystal size, a change in cloud radiative forcing may result. *Wyser and Ström* [1998] estimated the forcing, although with considerable uncertainty, to be of the order of 0.3 W m^{-2} in regions of dense air traffic under the assumption of a 20% decrease of the mean crystal size. No estimate of the globally averaged radiative forcing is available.

Sedimentation of ice particles from contrails may remove water vapor from the upper troposphere. This effect is expected to be more important in strongly supersaturated air when ice particles can fall without evaporating [*Fahey et al*., 1999]. The impacts of such an effect on cirrus formation, vertical profile of humidity, and the subsequent radiative forcing have not been assessed.

3.4.3. Effect of anthropogenic aerosols emitted at the surface on ice clouds. Aerosols also serve as ice nuclei, although it is well recognized that there are fewer ice nuclei than cloud condensation nuclei. It is conceivable that anthropogenic aerosols emitted at the surface and transported to the upper troposphere affect the formation and properties of ice clouds.

Jensen and Toon [1997] suggested that insoluble particles from the surface or soot particles emitted by aircraft, if sufficiently effective ice nuclei, can result in an increase in cirrus cloud coverage. *Laaksonen et al*. [1997] argued that nitric acid pollution is able to cause an increase in supercooled cirrus cloud droplet concentrations and thereby influence climate. Such effects, if significant at all, are not quantified at present.

4. SUMMARY AND CONCLUSION

Table 5 shows a summary of the range of radiative forcings for the direct and indirect effect of aerosols that

TABLE 5. A Summary of the Range of Radiative Forcings Discussed in the Text

Forcing Mechanism	*Aerosol Species*	*IPCC [1996], W m^{-2}*	*Range Discussed in the Text, W m^{-2}*	*Remarks*
Direct effect	sulphate aerosol	−0.2 to −0.8	−0.26 to −0.82	main uncertainties in column burden and effects of relative humidity and cloud
	fossil fuel BC	+0.03 to +0.3	+0.16 to +0.42	smallest estimates for an external mixture, largest estimates for an internal mixture
	fossil fuel OC	NA	−0.02 to −0.04	likely to be a lower limit due to the effects of mixing and unresolved hygroscopicity
	biomass-burning BC + OC	−0.07 to −0.6	−0.14 to −0.74	highest estimate has larger atmospheric burden and specific extinction coefficient
	mineral dust	NA	−0.46 to +0.09	significant positive terrestrial and negative solar radiative forcing lead to uncertainties in the sign of the radiative forcing
	nitrate aerosol	NA	−0.03	only one very tentative estimate available
Indirect effect	cloud albedo effect	−0 to −1.5	−0.3 to −1.8	this range for sulphate aerosols only
	cloud lifetime effect	NE	−0.4 to −2.3	this range for sulphate aerosols only[a]
	contrails	NA	0.005 to 0.06	this estimate based on *IPCC* [1999]
	aviation-induced cirrus	NA	0.04	this estimate based on *IPCC* [1999]; no range given

The range of radiative forcings from *IPCC* [1996] is included where appropriate. NA indicates that *IPCC* [1996] did not consider this forcing mechanism. NE indicates that *IPCC* [1996] did not give any estimate.

[a]GCM estimates cannot be strictly considered as radiative forcing calculations (see text).

have become available in the literature since *IPCC* [1996]. For sulphate aerosol the direct radiative forcing ranges from −0.26 W m^{-2} [*Graf et al*., 1997] to −0.82 W m^{-2} [*Haywood and Ramaswamy*, 1998] and depends not just on the column burden determined by the chemical transport models, but also on the treatment of relative humidity and cloud. For fossil fuel BC aerosol the direct radiative forcing ranges from +0.16 to +0.42 W m^{-2} [*Myhre et al*., 1998], the major factor influencing the radiative forcing being the degree of internal mixing. The two studies that have examined the radiative forcing due to fossil fuel OC lead to radiative forcings of −0.02 W m^{-2} [*Cooke et al*., 1999] and −0.04 W m^{-2} [*Penner et al*., 1998], although the forcing may be stronger if the effects of mixing and relative humidity are considered. Estimates of the radiative forcing due to OC and BC from biomass burning range from −0.14 W m^{-2} [*Penner et al*., 1998] to −0.74 W m^{-2} [*Iacobellis et al*., 1999]; the main uncertainties appear to be in the emission factors that subsequently affect the atmospheric burden of aerosol and the assumed optical parameters. For mineral dust, even the sign of the radiative forcing is in doubt due to the competing nature of the (negative) solar radiative forcing and (positive) terrestrial radiative forcing. Estimates of the radiative forcing due to mineral dust range from −0.46 W m^{-2} [*Sokolik and Toon*, 1996] to +0.09 W m^{-2} [*Tegen et al*., 1996]. Areas of uncertainty in determining the radiative forcing due to mineral dust lie in determining the fraction that is of anthropogenic origin and determining the optical characteristics. Only one tentative estimate of the radiative forcing due to nitrate aerosol is available at −0.03 W m^{-2}. It should be noted that the overall direct effect of anthropogenic aerosols is unlikely to equal simply the sum of all of the individual radiative forcing components due to the complexities of internal mixing. Additionally, the range in the estimates in the literature makes it difficult to quantify the overall direct radiative forcing of aerosols. Satellite retrievals of aerosol radiative effects have made considerable progress in determining the radiative effects of aerosols over ocean regions provided they are carefully calibrated against field measurements. Satellite retrievals of the radiative effects over land currently remain problematic, as does determining the anthropogenic component of aerosols from satellite data.

For the indirect effect of aerosols, only GCM estimates of the cloud albedo effect computed in a diagnostic manner can be strictly compared against estimates of the radiative forcing by other agents (e.g., greenhouse gases). The GCM studies dedicated to the cloud lifetime effect (or second indirect effect) usually approximate its radiative impact as the change in top-of-atmosphere fluxes between two independent experiments (with and without aerosols), which may allow feedbacks on the hydrological cycle and the dynamics of the atmosphere to develop. The second indirect effect is therefore difficult to define and quantify in the context of current evaluations of radiative forcing of climate change and current model simulations. Nevertheless, available GCM simulations suggest a radiative flux perturbation for the second aerosol indirect effect of a magnitude similar to that for the first effect. Published GCM estimates of the radiative forcing for the cloud albedo effect by sulphate aerosols range from −0.3 to −1.8 W m^{-2}. GCM estimates of the radiative impact of the second indirect effect by sulphate aerosols range from −0.4 to −2.3 W

m^{-2}. Only one reliable GCM estimate of the effect of carbonaceous aerosols indicates a radiative impact of -0.9 W m^{-2} for the combined (first and second) effects. The aerosol indirect radiative forcing due to all aerosols differs significantly from the sum of the radiative forcings by the individual components. In particular, the indirect effects of sulphate and carbonaceous aerosols cannot be added up because of internal mixing and because the different aerosol species compete with each other to form cloud droplets. It is argued that present estimates of the indirect aerosol effects are subject to large uncertainties and that the present range of estimates does not necessarily reflect the actual uncertainty range because most GCMs use similar assumptions. Also, absorption of solar radiation by black carbon aerosols incorporated into the cloud droplets, although probably a second-order effect, is generally not considered in the GCM studies. Recent field campaigns (e.g., ACE 2) provided useful insights into the chemistry and physics of the aerosol indirect effects. It will be fruitful to "scale up" the observations at the local scale to the larger scale of the GCMs in order to evaluate and improve the parameterizations. Combined satellite retrievals of aerosol and cloud parameters are becoming useful tools to diagnose the radiative impact of the first indirect effect but require a careful interpretation. Global-scale satellite observations of cloud microphysical properties will also help to validate the GCM simulations of the aerosol indirect effects. Clearly, more research is needed regarding the indirect effects of aerosols, especially as far as middle- and high-level clouds are concerned.

These estimates for the aerosol direct and indirect effects derived from the published literature can be compared against a radiative forcing for well-mixed greenhouse gases of $+2.45$ W m^{-2} [*IPCC*, 1996]. We believe that the effects of aerosols continue to represent one of the largest uncertainties in the detection and prediction of climate change.

ACKNOWLEDGMENTS. C. Chuang, R. van Dorland, J. Feichter, H.-F. Graf, K. E. Grant, J. Hansen, J. Kiehl, Z. Kogan, G. Myhre, K. Restad, H. Rodhe, J. Roeckner, and L. Rotstayn are thanked for making their model results available. Special thanks are extended to Q. Han, S. Ghan, A. Jones, U. Lohmann, J. Penner, and I. Tegen for providing the data used in the figures. The authors are grateful to V. Ramaswamy and S. Solomon for encouragement in writing this review. This manuscript benefited from constructive comments by reviewers and D. L. Roberts.

Michael Coffey was the Editor responsible for this paper. He thanks J. Kiehl and an anonymous reviewer for the technical reviews and B. Scanlon for the cross-disciplinary review.

REFERENCES

Ackerman, S. A., Remote sensing aerosols using satellite infrared observations, *J. Geophys. Res.*, *102*, 17,069–17,079, 1997.

Ackerman, S. A., and H. Chung, Radiative effects of airborne dust on regional energy budgets at the top of the atmosphere, *J. Appl. Meteorol.*, *31*, 223–233, 1992.

Adams, P. J., J. H. Seinfeld, and D. M. Koch, Global concentrations of tropospheric sulfate, nitrate, and ammonium aerosol simulated in a general circulation model, *J. Geophys. Res.*, *104*, 13,791–13,823, 1999.

Albrecht, B. A., Aerosols, cloud microphysics, and fractional cloudiness, *Science*, *245*, 1227–1230, 1989.

Bakan, S., M. Betancor, V. Gayler, and H. Grassl, Contrail frequency over Europe from NOAA-satellite images, *Ann. Geophys.*, *12*, 962–968, 1994.

Barth, M. C., P. J. Rasch, J. T. Kiehl, C. M. Benkovitz, and S. E. Schwartz, Sulfur chemistry in the National Center for Atmospheric Research Community Climate Model: Description, evaluation, features, and sensitivity to aqueous chemistry, *J. Geophys. Res.*, *105*, 1387–1415, 2000.

Benkovitz, C. M., M. T. Scholtz, J. Pacyna, L. Tarrason, J. Dignon, E. C. Voldner, P. A. Spiro, J. A. Logan, and T. E. Graedel, Global gridded inventories of anthropogenic emissions of sulfur and nitrogen, *J. Geophys. Res.*, *101*, 29,239–29,253, 1996.

Boucher, O., GCM estimate of the indirect aerosol forcing using satellite-retrieved cloud effective droplet radii, *J. Clim.*, *8*, 1403–1409, 1995.

Boucher, O., Aircraft can increase cirrus cloudiness, *Nature*, *397*, 30–31, 1999.

Boucher, O., and T. L. Anderson, General circulation model assessment of the sensitivity of direct climate forcing by anthropogenic sulfate aerosols to aerosol size and chemistry, *J. Geophys. Res.*, *100*, 26,117–26,134, 1995.

Boucher, O., and U. Lohmann, The sulfate-CCN-cloud albedo effect: A sensitivity study using two general circulation models, *Tellus*, *Ser. B*, *47*, 281–300, 1995.

Boucher, O., and H. Rodhe, The sulfate-CCN-cloud albedo effect: A sensitivity study, *Rep. CM-83*, 20 pp., Dep. of Meteorol., Stockholm Univ., Stockholm, 1994.

Boucher, O., and D. Tanré, Estimation of the aerosol perturbation to the Earth's radiative budget over the oceans using POLDER satellite aerosol retrievals, *Geophys. Res. Lett.*, *27*, 1103–1106, 2000.

Boucher, O., H. Le Treut, and M. B. Baker, Precipitation and radiation modeling in a general circulation model: Introduction of cloud microphysics, *J. Geophys. Res.*, *100*, 16,395–16,414, 1995.

Boucher, O., et al., Intercomparison of models representing direct shortwave radiative forcing by sulfate aerosols, *J. Geophys. Res.*, *103*, 16,979–16,998, 1998.

Brenguier, J.-L., P. Y. Chuang, Y. Fouquart, D. W. Johnson, F. Parol, H. Pawlowska, J. Pelon, L. Schüller, F. Schröder, and J. Snider, An overview of the ACE-2 CloudyColumn Closure Experiment, *Tellus*, *Ser. B*, *52*, 815–827, 2000a.

Brenguier, J.-L., H. Pawlowska, L. Schüller, R. Preusker, J. Fischer, and Y. Fouquart, Radiative properties of boundary layer clouds: Droplet effective radius versus number concentration, *J. Atmos. Sci.*, *57*, 803–821, 2000b.

Bréon, F.-M., and P. Goloub, Cloud droplet effective radius from spaceborne polarization measurements, *Geophys. Res. Lett.*, *25*, 1879–1882, 1998.

Bréon, F.-M., S. Colzy, and P. Goloub, Global distribution of cloud droplet radius from POLDER polarization measurements, in *Proceedings of the ALPS99 International Conference, 18–22 January 1999, Méribel, France*, pp. WK1 and WK2/O/08/1–4, Cent. Natl. des Etudes Spatiales, Toulouse, France, 1999.

Capaldo, K., J. J. Corbett, P. Kasibhatla, P. Fischbeck, and S. N. Pandis, Effects of ship emissions on sulphur cycling and radiative climate forcing over the ocean, *Nature*, *400*, 743–746, 1999.

Charlson, R. J., S. E. Schwartz, J. M. Hales, R. D. Cess, J. A. Coakley, J. E. Hansen, and D. J. Hofmann, Climate forcing by anthropogenic aerosols, *Science*, *255*, 423–430, 1992.

Charlson, R. J., T. L. Anderson, and H. Rodhe, Direct climate forcing by anthropogenic aerosols: Quantifying the link between sulfate and radiation, *Contrib. Atmos. Phys*., *72*, 79–94, 1999.

Chin, M., and D. J. Jacob, Anthropogenic and natural contributions to tropospheric sulfate: A global model analysis, *J. Geophys. Res*., *101*, 18,691–18,699, 1996.

Chuang, C. C., J. E. Penner, K. E. Taylor, and J. J. Walton, Climate effects of anthropogenic sulfate: Simulation from a coupled chemistry/climate model, in *Preprints of the AMS Conference on Atmospheric Chemistry*, pp. 170–174, Am. Meteorol. Soc., Boston, Mass., 1994.

Chuang, C. C., J. E. Penner, K. E. Taylor, A. S. Grossman, and J. J. Walton, An assessment of the radiative effects of anthropogenic sulfate, *J. Geophys. Res*., *102*, 3761–3778, 1997.

Chýlek, P., and J. Wong, Effect of absorbing aerosols on global radiation budget, *Geophys. Res. Lett*., *22*, 929–931, 1995.

Chýlek, P., G. Videen, and D. Ngo, Effect of black carbon on the optical properties and climate forcing of sulfate aerosols, *J. Geophys. Res*., *100*, 16,325–16,332, 1995.

Chýlek, P., C. M. Banic, B. Johnson, P. A. Damiano, G. A. Isaac, W. R. Leaitch, P. S. K. Liu, F. S. Boudala, B. Winter, and D. Ngo, Black carbon: Atmospheric concentrations and cloud water content measurements over southern Nova Scotia, *J. Geophys. Res*., *101*, 29,105–29,110, 1996a.

Chýlek, P., G. B. Lesins, G. Videen, J. G. D. Wong, R. G. Pinnick, D. Ngo, and J. D. Klett, Black carbon and absorption of solar radiation by clouds, *J. Geophys. Res*., *101*, 23,365–23,371, 1996b.

Claquin, T., M. Schulz, Y. Balkanski, and O. Boucher, Uncertainties in assessing radiative forcing by mineral dust, *Tellus*, *Ser. B*, *50*, 491–505, 1998.

Claquin, T., M. Schulz, and Y. Balkanski, Modeling the mineralogy of atmospheric dust sources, *J. Geophys. Res*., *104*, 22,243–22,256, 1999.

Coakley, J. A., Jr., R. L. Bernstein, and P. A. Durkee, Effect of ship-stack effluents on cloud reflectivity, *Science*, *237*, 1020–1022, 1987.

Cooke, W. F., and J. J. N. Wilson, A global black carbon model, *J. Geophys. Res*., *101*, 19,395–19,409, 1996.

Cooke, W. F., C. Liousse, H. Cachier, and J. Feichter, Construction of a 1° × 1° fossil fuel emission data set for carbonaceous aerosol and implementation and radiative impact in the ECHAM4 model, *J. Geophys. Res*., *104*, 22,137–22,162, 1999.

Cox, S. J., W.-C. Wang, and S. E. Schwartz, Climate response to radiative forcings by aerosols and greenhouse gases, *Geophys. Res. Lett*., *22*, 2509–2512, 1995.

Cusack, S., A. Slingo, J. M. Edwards, and M. Wild, The radiative impact of a simple aerosol climatology on the Hadley Centre atmospheric GCM, *Q. J. R. Meteorol. Soc*., *124*, 2517–2526, 1998.

Dentener, F. J., G. R. Carmichael, Y. Zhang, J. Lelieveld, and P. Crutzen, Role of mineral aerosol as a reactive surface in the global troposphere, *J. Geophys. Res*., *101*, 22,869–22,889, 1996.

Deuzé, J.-L., M. Herman, P. Goloub, D. Tanré, and A. Marchand, Characterization of aerosols over the ocean from POLDER/ADEOS-1, *Geophys. Res. Lett*., *26*, 1421–1424, 1999.

Dubovik, O., B. N. Holben, Y. N. Kaufman, M. Yamasoe, A. Smirnov, D. Tanré, and I. Slutsker, Single-scattering albedo of smoke retrieved from the sky radiance and solar transmittance measured from ground, *J. Geophys. Res*., *103*, 31,903–31923, 1998.

Eck, T. F., B. N. Holben, I. Slutsker, and A. Setzer, Measurements of irradiance attenuation and estimation of aerosol single scattering albedo for biomass burning aerosols in Amazonia, *J. Geophys. Res*., *103*, 31,865–31,878, 1998.

Fahey, D. W., U. Schumann, S. Ackerman, P. Artaxo, O. Boucher, M. Y. Danilin, B. Kärcher, P. Minnis, T. Nakajima, and O. B. Toon, Aviation-produced aerosols and cloudiness, in *Aviation and the Global Atmosphere*, edited by J. E. Penner et al., chap. 3, pp. 65–120, Cambridge Univ. Press, New York, 1999.

Feichter, J., U. Lohmann, and I. Schult, The atmospheric sulfur cycle in ECHAM-4 and its impact on the shortwave radiation, *Clim. Dyn*., *13*, 235–246, 1997.

Flowerdew, R. J., and J. D. Haigh, Retrieval of aerosol optical thickness over land using the ATSR-2 dual-look satellite radiometer, *Geophys. Res. Lett*., *23*, 351–354, 1996.

Fowler, L. D., D. A. Randall, and S. A. Rutledge, Liquid and ice cloud microphysics in the CSU general circulation model, part I, Model description and simulated microphysical processes, *J. Clim*., *9*, 489–529, 1996.

Francis, P. N., P. Hignett, and J. P. Taylor, Aircraft observations and modeling of sky radiance distributions from aerosol during TARFOX, *J. Geophys. Res*., *104*, 2309–2319, 1999.

Ghan, S., and R. Easter, Comment on "A limited-area-model case study of the effects of sub-grid scale variations in relative humidity and cloud upon the direct radiative forcing of sulfate aerosol" by Haywood et al., *Geophys. Res. Lett*., *25*, 1039–1040, 1998.

Ghan, S. J., and J. E. Penner, Smoke: Effects on climate, in *Encyclopedia of Earth System Science*, vol. 4, edited by W. A. Nierenberg, pp. 191–198, Academic, San Diego, Calif., 1992.

Ghan, S. J., L. R. Leung, R. C. Easter, and H. Abdul-Razzak, Prediction of cloud droplet number in a general circulation model, *J. Geophys. Res*., *102*, 21,777–21,794, 1997.

Ghan, S. J., G. Guzman, and H. Abdul-Razzak, Competition between sea salt and sulfate particles as cloud condensation nuclei, *J. Atmos. Sci*., *55*, 3340–3347, 1998.

Ghan, S. J., R. C. Easter, E. Chapman, H. Abdul-Razzak, Y. Zhang, R. Leung, N. Laulainen, R. Saylor, and R. Zaveri, A physically based estimate of radiative forcing by anthropogenic sulfate aerosol, *J. Geophys. Res.*, in press, 2000a.

Ghan, S. J., N. Laulainen, R. Easter, R. Wagener, S. Nemesure, E. Chapman, Y. Zhang, and R. Leung, Evaluation of aerosol indirect radiative forcing in MIRAGE, *J. Geophys. Res.,* in press, 2000b.

Goloub, P., D. Tanré, J.-L. Deuzé, M. Herman, A. Marchand, and F.-M. Bréon, Validation of the first algorithm applied for deriving the aerosol properties over the ocean using the POLDER/ADEOS measurements, *IEEE Trans. Geosci. Remote Sens*., *37*, 1586–1596, 1999.

Graf, H.-F., J. Feichter, and B. Langmann, Volcanic sulfur emissions: Estimates of source strength and its contribution to the global sulfate distribution, *J. Geophys. Res*., *102*, 10,727–10,738, 1997.

Grant, K. E., C. C. Chuang, A. S. Grossman, and J. E. Penner, Modeling the spectral optical properties of ammonium sulfate and biomass burning aerosols: Parameterization of relative humidity effects and model results, *Atmos. Environ*., *33*, 2603–2620, 1999.

Han, Q., W. B. Rossow, and A. A. Lacis, Near-global survey of effective droplet radii in liquid water clouds using ISCCP data, *J. Clim*., *7*, 465–497, 1994.

Han, Q., W. B. Rossow, J. Chou, and R. M. Welch, Global survey of the relationships of cloud albedo and liquid water path with droplet size using ISCCP, *J. Clim*., *11*, 1516–1528, 1998a.

Han, Q., W. B. Rossow, J. Chou, and R. M. Welch, Global

variation of column droplet concentration in low-level clouds, *Geophys. Res. Lett*., *25*, 1419–1422, 1998b.

Hansen, J., D. Johnson, A. Lacis, S. Lebedeff, P. Lee, D. Rind, and G. Russell, Climate impact of increasing atmospheric carbon dioxide, *Science*, *213*, 957–966, 1981.

Hansen, J. E., M. Sato, and R. Ruedy, Long-term changes of the diurnal temperature cycle: Implications about mechanisms of global climate change, *Atmos. Res*., *37*, 175–209, 1995.

Hansen, J., M. Sato, A. Lacis, and R. Ruedy, The missing climate forcing, *Philos. Trans. R. Soc. London*, *Ser. B*, *352*, 231–240, 1997a.

Hansen, J., M. Sato, and R. Ruedy, Radiative forcing and climate response, *J. Geophys. Res*., *102*, 6831–6864, 1997b.

Hansen, J., M. Sato, A. Lacis, R. Ruedy, I. Tegen, and E. Matthews, Climate forcings in the industrial era, *Proc. Natl. Acad. Sci*., *95*, 12,753–12,758, 1998.

Haywood, J. M., and V. Ramaswamy, Global sensitivity studies of the direct radiative forcing due to anthropogenic sulfate and black carbon aerosols, *J. Geophys. Res*., *103*, 6043–6058, 1998.

Haywood, J. M., and K. P. Shine, The effect of anthropogenic sulfate and soot on the clear-sky planetary radiation budget, *Geophys. Res. Lett*., *22*, 603–606, 1995.

Haywood, J. M., and K. P. Shine, Multi-spectral calculations of the radiative forcing of tropospheric sulphate and soot aerosols using a column model, *Q. J. R. Meteorol. Soc*., *123*, 1907–1930, 1997.

Haywood, J. M., D. L. Roberts, A. Slingo, J. M. Edwards, and K. P. Shine, General circulation model calculations of the direct radiative forcing by anthropogenic sulphate and fossil-fuel soot aerosol, *J. Clim*., *10*, 1562–1577, 1997a.

Haywood, J. M., V. Ramaswamy, and L. J. Donner, A limited-area-model case study of the effects of sub-grid scale variations in relative humidity and cloud upon the direct radiative forcing of sulfate aerosol, *Geophys. Res. Lett*., *24*, 143–146, 1997b.

Haywood, J. M., V. Ramaswamy, and L. J. Donner, Reply, *Geophys. Res. Lett*., *25*, 1041, 1998.

Haywood, J. M., V. Ramaswamy, and B. J. Soden, Tropospheric aerosol climate forcing in clear-sky satellite observations over the oceans, *Science*, *283*, 1299–1303, 1999.

Haywood, J. M., P. N. Francis, M. D. Glew, and J. P. Taylor, Optical properties and direct radiative effect of Saharan dust: A case study of two Saharan dust outbreaks using data from the U.K. Meteorological Office C-130, *J. Geophys. Res*., in press, 2000.

Hegg, D. A., R. J. Ferek, and P. V. Hobbs, Light scattering and cloud condensation nucleus activity of sulfate aerosol measured over the northeastern Atlantic Ocean, *J. Geophys. Res*., *98*, 14,887–14,894, 1993.

Hegg, D. A., J. Livingston, P. V. Hobbs, T. Novakov, and P. Russell, Chemical apportionment of aerosol column optical depth off the mid-Atlantic coast of the United States, *J. Geophys. Res*., *102*, 25,293–25,303, 1997.

Heintzenberg, J., and M. Wendisch, On the sensitivity of cloud albedo to the partitioning of particulate absorbers in cloudy air, *Contrib. Atmos. Phys*., *69*, 491–499, 1996.

Herman, J. R., P. K. Barthia, O. Torres, C. Hsu, C. Seftor, and E. Celarier, Global distribution of UV-absorbing aerosols from NIMBUS-7/TOMS data, *J. Geophys. Res*., *102*, 16,911–16,922, 1997.

Herman, M., J.-L. Deuzé, C. Devaux, P. Goloub, F.-M. Bréon, and D. Tanré, Remote sensing of aerosols over land surfaces including polarization measurements and application to POLDER measurements, *J. Geophys. Res*., *102*, 17,039–17,049, 1997.

Hignett, P., J. T. Taylor, P. N. Francis, and M. D. Glew, Comparison of observed and modeled direct aerosol forcing during TARFOX, *J. Geophys. Res*., *104*, 2279–2287, 1999.

Higurashi, A., and T. Nakajima, Development of a two-channel aerosol retrieval algorithm on global scale using NOAA/AVHRR, *J. Atmos. Sci*., *56*, 924–941, 1999.

Hobbs, P. V., J. S. Reid, R. A. Kotchenruther, R. J. Ferek, and R. Weiss, Direct radiative forcing by smoke from biomass burning, *Science*, *275*, 1776–1778, 1997.

Holben, B. N., et al., AERONET: A federated instrument network and data archive for aerosol characterization, *Remote Sens. Environ*., *66*, 1–16, 1998.

Horvath, H., Atmospheric light absorption—A review, *Atmos. Environ*., *Part A*, *27*, 293–317, 1993.

Husar, R. B., J. M. Prospero, and L. L. Stowe, Characterization of tropospheric aerosols over the oceans with the NOAA advanced very high resolution radiometer optical thickness operational product, *J. Geophys. Res*., *102*, 16,889–16,909, 1997.

Iacobellis, S. F., R. Frouin, and R. C. J. Somerville, Direct climate forcing by biomass-burning aerosols: Impact of correlations between controlling variables, *J. Geophys. Res*., *104*, 12,031–12,045, 1999.

Intergovernmental Panel on Climate Change, *Climate Change 1994*: *Radiative Forcing of Climate Change and an Evaluation of the IPCC IS92 Emission Scenarios*, edited by J. T. Houghton et al., Cambridge Univ. Press, New York, 1994.

Intergovernmental Panel on Climate Change, *Climate Change 1995*: *The Science of Climate Change, The Contribution of Working Group I to the Second Assessment Report of the IPCC*, edited by J. T. Houghton et al., 572 pp., Cambridge Univ. Press, New York, 1996.

Intergovernmental Panel on Climate Change, *Aviation and the Global Atmosphere*, edited by J. E. Penner et al., 373 pp., Cambridge Univ. Press, New York, 1999.

Jankowiak, I., and D. Tanré, Satellite climatology of Saharan dust outbreaks: Method and preliminary results, *J. Clim*., *5*, 646–656, 1992.

Jensen, E. J., and O. B. Toon, The potential impact of soot from aircraft exhaust on cirrus clouds, *Geophys. Res. Lett*., *24*, 249–252, 1997.

Jones, A., and A. Slingo, Predicting cloud-droplet effective radius and indirect sulphate aerosol forcing using a general circulation model, *Q. J. R. Meteorol. Soc*., *122*, 1573–1595, 1996.

Jones, A., and A. Slingo, Climate model studies of sulphate aerosols and clouds, *Philos. Trans. R. Soc. London*, *Ser. B*, *352*, 221–229, 1997.

Jones, A., D. L. Roberts, and A. Slingo, A climate model study of the indirect radiative forcing by anthropogenic sulphate aerosols, *Nature*, *370*, 450–453, 1994.

Jones, A., D. L. Roberts, and M. J. Woodage, The indirect effects of anthropogenic sulphate aerosol simulated using a climate model with an interactive sulphur cycle, *Tech. Note 14*, 38 pp., Hadley Cent., U.K. Meteorol. Off., Bracknell, England, 1999.

Karl, T. R., P. D. Jones, R. W. Knight, G. Kukla, N. Plummer, V. Razuvayev, K. P. Gallo, J. Lindseay, R. J. Charlson, and T. C. Peterson, A new perspective on recent global warming: Asymmetric trends of daily maximum and minimum temperature, *Bull. Am. Meteorol. Soc*., *74*, 1007–1023, 1993.

Kasibhatla, P., W. L. Chameides, and J. St. John, A three-dimensional global model investigation of the seasonal variation in the atmospheric burden of anthropogenic sulfate aerosols, *J. Geophys. Res*., *102*, 3737–3759, 1997.

Kattenberg, A., F. Giorgi, H. Grassl, G. A. Meehl, J. F. B. Mitchell, R. J. Stouffer, T. Tokioka, A. J. Weaver, and T. M. L. Wigley, Climate Models—Projections of Future Climate, in *Climate Change 1995: The Science of Climate Change, The Contribution of Working Group I to the Second*

Assessment Report of the IPCC, edited by J. T. Houghton et al., pp. 285–357, Cambridge Univ. Press, New York, 1996.

Kaufman, Y. J., Satellite sensing of aerosol absorption, *J. Geophys. Res.*, *92*, 4307–4317, 1987.

Kaufman, Y. J., and R. S. Fraser, Control of the effect of smoke particles on clouds and climate by water vapor, *Science*, *277*, 1636–1639, 1997.

Kaufman, Y. J., and T. Nakajima, Effect of Amazon smoke on cloud microphysics and albedo—Analysis from satellite imagery, *J. Appl. Meteorol.*, *32*, 729–744, 1993.

Kaufman, Y. J., D. Tanré, L. Remer, E. Vermote, A. Chu, and B. N. Holben, Operational remote sensing of tropospheric aerosol over land from EOS moderate resolution imaging spectroradiometer, *J. Geophys. Res.*, *102*, 17,051–17,067, 1997.

Kiehl, J. T., and B. P. Briegleb, The relative roles of sulfate aerosols and greenhouse gases in climate forcing, *Science*, *260*, 311–314, 1993.

Kiehl, J. T., and H. Rodhe, Modeling geographical and seasonal forcing due to aerosols, in *Aerosol Forcing of Climate*, pp. 281–296, edited by R. J. Charlson and J. Heintzenberg, John Wiley, New York, 1995.

Kiehl, J. T., T. L. Schneider, P. J. Rasch, M. C. Barth, and J. Wong, Radiative forcing due to sulfate aerosols from simulations with the National Center for Atmospheric Research Community Climate Model, Version 3, *J. Geophys. Res.*, *105*, 1441–1457, 2000.

King, M. D., Y. J. Kaufman, W. P. Menzel, and D. Tanré, Remote sensing of cloud, aerosol, and water vapor properties from the moderate resolution imaging spectrometer (MODIS), *IEEE Trans. Geosci. Remote Sens.*, *30*, 2–27, 1992.

King, M. D., Y. J. Kaufman, D. Tanré, and T. Nakajima, Remote sensing of tropospheric aerosols: Past, present, and future, *Bull. Am. Meteorol. Soc.*, *80*, 2229–2259, 1999.

Kirkevåg, A., T. Iversen, and A. Dahlback, On radiative effects of black carbon and sulphate aerosols, *Atmos. Environ.*, *33*, 2621–2635, 1999.

Koch, D., D. Jacob, I. Tegen, D. Rind, and M. Chin, Tropospheric sulfur simulation and sulfate direct radiative forcing in the Goddard Institute for Space Studies general circulation model, *J. Geophys. Res.*, *104*, 23,799–23,822, 1999.

Kogan, Z. N., Y. L. Kogan, and D. K. Lilly, Evaluation of sulfate aerosols indirect effect in marine stratocumulus clouds using observation-derived cloud climatology, *Geophys. Res. Lett.*, *23*, 1937–1940, 1996.

Kogan, Z. N., Y. L. Kogan, and D. K. Lilly, Cloud factor and seasonality of the indirect effect of anthropogenic sulfate aerosols, *J. Geophys. Res.*, *102*, 25,927–25,939, 1997.

Kotchenruther, R. A., P. V. Hobbs, and D. A. Hegg, Humidification factors for atmospheric aerosols off the mid-Atlantic coast of the United States, *J. Geophys. Res.*, *104*, 2239–2251, 1999.

Kulmala, M., A. Laaksonen, P. Korhonen, T. Vesala, and T. Ahonen, The effect of atmospheric nitric acid vapor on cloud condensation nucleus activation, *J. Geophys. Res.*, *98*, 22,949–22,958, 1993.

Kulmala, M., P. Korhonen, A. Laaksonen, and T. Vesala, Changes in cloud properties due to NO_x emissions, *Geophys. Res. Lett.*, *22*, 239–242, 1995.

Laaksonen, A., J. Hienola, M. Kulmala, and F. Arnold, Supercooled cirrus cloud formation modified by nitric acid pollution of the upper troposphere, *Geophys. Res. Lett.*, *24*, 3009–3012, 1997.

Langner, J., and H. Rodhe, A global three-dimensional model of the tropospheric sulfur cycle, *J. Atmos. Chem.*, *13*, 225–263, 1991.

Leaitch, W. R., G. A. Isaac, J. W. Strapp, C. M. Banic, and H. A. Wiebe, The relationship between cloud droplet number concentrations and anthropogenic pollution: Observations and climatic implications, *J. Geophys. Res.*, *97*, 2463–2474, 1992.

Legrand, M., J.-J. Bertrand, M. Desbois, L. Menenger, and Y. Fouquart, The potential of infrared satellite data for the retrieval of Saharan dust optical depth over Africa, *J. Appl. Meteorol.*, *28*, 309–318, 1989.

Leroy, M., J.-L. Deuzé, F.-M. Bréon, O. Hautecoeur, M. Herman, J.-C. Buriez, D. Tanré, S. Bouffiès, P. Chazette, and J. L. Roujean, Retrieval of atmospheric properties and surface bidirectional reflectances over land from POLDER/ADEOS, *J. Geophys. Res.*, *102*, 17,023–17,037, 1997.

Le Treut, H., M. Forichon, O. Boucher, and Z. X. Li, Sulfate aerosol indirect effect and CO_2 greenhouse forcing: Equilibrium response of the LMD GCM and associated cloud feedbacks, *J. Clim.*, *11*, 1673–1684, 1998.

Levin, Z., E. Ganor, and V. Gladstein, The effects of desert particles coated with sulfate on rain formation in the eastern Mediterranean, *J. Appl. Meteorol.*, *35*, 1511–1523, 1996.

Li, Z., and L. Kou, The direct radiative effect of smoke aerosols on atmospheric absorption of visible light, *Tellus*, *Ser. B*, *50*, 543–554, 1998.

Liao, H., and J. H. Seinfeld, Effect of clouds on direct radiative forcing of climate, *J. Geophys. Res.*, *103*, 3781–3788, 1998.

Liousse, C., H. Cachier, and S. G. Jennings, Optical and thermal measurements of black carbon content in different environments: Variation of specific attenuation cross-section, σ, *Atmos. Environ.*, *Part A*, *27*, 1203–1211, 1993.

Liousse, C., J. E. Penner, C. C. Chuang, J. J. Walton, and H. Eddleman, A global three-dimensional model study of carbonaceous aerosols, *J. Geophys. Res.*, *101*, 19,411–19,432, 1996.

Lohmann, U., and J. Feichter, Impact of sulfate aerosols on albedo and lifetime of clouds: A sensitivity study with the ECHAM4 general circulation model, *J. Geophys. Res.*, *102*, 13,685–13,700, 1997.

Lohmann, U., J. Feichter, C. C. Chuang, and J. E. Penner, Prediction of the number of cloud droplets in the ECHAM general circulation model, *J. Geophys. Res.*, *104*, 9169–9198, 1999a. (Correction, *J. Geophys. Res.*, *104*, 24,557–24,563, 1999.)

Lohmann, U., K. von Salzen, N. McFarlane, H. G. Leighton, and J. Feichter, Tropospheric sulfur cycle in the Canadian general circulation model, *J. Geophys. Res.*, *104*, 26,833–26,858, 1999b.

Lohmann, U., J. Feichter, J. Penner, and R. Leaitch, Indirect effect of sulfate and carbonaceous aerosols: A mechanistic treatment, *J. Geophys. Res.*, *105*, 12,193–12,206, 2000.

Manabe, S., and R. T. Wetherald, Thermal equilibrium of the atmosphere with a given distribution of relative humidity, *J. Atmos. Sci.*, *24*, 241–259, 1967.

Mannstein, H., R. Meyer, and P. Wendling, Operational detection of contrails from NOAA-AVHRR data, *Int. J. Remote Sens.*, *20*, 1641–1660, 1999.

Martin, G. M., D. W. Johnson, and A. Spice, The measurement and parameterization of effective radius of droplets in warm stratiform clouds, *J. Atmos. Sci.*, *51*, 1823–1842, 1994.

Martins, J. V., P. V. Hobbs, R. E. Weiss, and P. Artaxo, Sphericity and morphology of smoke particles from biomass burning in Brazil, *J. Geophys. Res.*, *103*, 32,051–32,067, 1998.

McInnes, L. M., M. H. Bergin, J. A. Ogren, and S. Schwartz, Apportionment of light scattering and hygroscopic growth to aerosol composition, *Geophys. Res. Lett.*, *25*, 513–516, 1998.

Meerkötter, R., U. Schumann, D. R. Doelling, P. Minnis, T. Nakajima, and Y. Tsushima, Radiative forcing by contrails, *Ann. Geophys.*, *17*, 1080–1094, 1999.

Miller, R., and I. Tegen, Climate response to soil dust aerosols, *J. Clim.*, *11*, 3247–3267, 1998.

Miller, R., and I. Tegen, Radiative forcing of a tropical direct circulation by soil dust aerosols, *J. Atmos. Sci.*, *56*, 2403–2433, 1999.

Minnis, P., U. Schumann, D. R. Doelling, K. M. Gierens, and D. W. Fahey, Global distribution of contrail radiative forcing, *Geophys. Res. Lett.*, *26*, 1853–1856, 1999.

Mishchenko, M. I., L. D. Travis, R. A. Kahn, and R. A. West, Modeling phase functions for dustlike tropospheric aerosols using a shape mixture of randomly orientated polydisperse spheroids, *J. Geophys. Res.*, *102*, 16,831–16,847, 1997.

Moulin, C., F. Guillard, F. Dulac, and C. E. Lambert, Long-term daily monitoring of Saharan dust load over ocean using Meteosat ISCCP-B2 data, 1, Methodology and preliminary results for 1983–1994 in the Mediterranean, *J. Geophys. Res.*, *102*, 16,947–16,958, 1997.

Murphy, D. M., J. R. Anderson, P. K. Quinn, L. M. McInnes, M. Posfai, D. S. Thomson, and P. R. Buseck, Influence of sea-salt on aerosol radiative properties in the Southern Ocean marine boundary layer, *Nature*, *392*, 62–65, 1998.

Myhre, G., and F. Stordal, Global sensitivity experiments of the radiative forcing due to mineral aerosols, *J. Geophys. Res.*, in press, 2000.

Myhre, G., F. Stordal, K. Restad, and I. Isaksen, Estimates of the direct radiative forcing due to sulfate and soot aerosols, *Tellus*, *Ser. B*, *50*, 463–477, 1998.

Nakajima, T., and A. Higurashi, A use of two-channel radiances for aerosol characterization from space, *Geophys. Res. Lett.*, *25*, 3815–3818, 1998.

Nakajima, T., A. Higurashi, K. Aoki, T. Endoh, H. Fukushima, M. Toranti, Y. Mitomi, B. G. Mitchell, and R. Frouin, Early phase analysis of OCTS radiance data for aerosol remote sensing, *IEEE Trans. Geosci. Remote Sens.*, *37*, 1575–1585, 1999.

Nemesure, S., R. Wagener, and S. E. Schwartz, Direct shortwave forcing of climate by anthropogenic sulfate aerosol: Sensitivity to particle size, composition, and relative humidity, *J. Geophys. Res.*, *100*, 26,105–26,116, 1995.

Novakov, T., and C. E. Corrigan, Cloud condensation nucleus activity of the organic component of biomass smoke particles, *Geophys. Res. Lett.*, *23*, 2141–2144, 1996.

Novakov, T., and J. E. Penner, Large contribution of organic aerosols to cloud-condensation-nuclei concentrations, *Nature*, *365*, 823–826, 1993.

Novakov, T., C. Rivera-Carpio, J. E. Penner, and C. F. Rogers, The effect of anthropogenic sulfate aerosols on marine cloud droplet concentrations, *Tellus*, *Ser. B*, *46*, 132–141, 1994.

Novakov, T., D. A. Hegg, and P. V. Hobbs, Airborne measurements of carbonaceous aerosols during TARFOX, *J. Geophys. Res.*, *102*, 30,023–30,030, 1997.

O'Dowd, D., J. A. Lowe, and M. H. Smith, Coupling sea-salt and sulphate interactions and its impact on cloud droplet concentration predictions, *Geophys. Res. Lett.*, *26*, 1311–1314, 1999.

Pan, W., M. A. Tatang, G. J. McRae, and R. T. G. Prinn, Uncertainty analysis of the direct radiative forcing by anthropogenic sulfate aerosols, *J. Geophys. Res.*, *102*, 21,915–21,924, 1997.

Penner, J. E., R. E. Dickinson, and C. A. O'Neill, Effects of aerosol from biomass burning on the global radiation budget, *Science*, *256*, 1432–1434, 1992.

Penner, J. E., H. Eddleman, and T. Novakov, Towards the development of a global inventory for black carbon emissions, *Atmos. Environ.*, *Part A*, *27*, 1277–1295, 1993.

Penner, J. E., R. J. Charlson, J. M. Hales, N. S. Laulainen, R. Leifer, T. Novakov, J. Ogren, L. F. Radke, S. E. Schwartz, and L. Travis, Quantifying and minimising uncertainty of climate forcing by anthropogenic aerosols, *Bull. Am. Meteorol. Soc.*, *75*, 375–400, 1994.

Penner, J. E., C. C. Chuang, and C. Liousse, The contribution of carbonaceous aerosols to climate change, in *Nucleation and Atmospheric Aerosols*, edited by M. Kulmala and P. E. Wagner, pp. 759–769, Elsevier Sci., New York, 1996.

Penner, J. E., C. C. Chuang, and K. Grant, Climate forcing by carbonaceous and sulfate aerosols, *Clim. Dyn.*, *14*, 839–851, 1998.

Pham, M., J.-F. Muller, G. Brasseur, C. Granier, and G. Mégie, A three-dimensional study of the tropospheric sulfur cycle, *J. Geophys. Res.*, *100*, 26,061–26,092, 1995.

Pilinis, C., S. N. Pandis, and J. H. Seinfeld, Sensitivity of direct climate forcing by atmospheric aerosols to aerosol size and composition, *J. Geophys. Res.*, *100*, 18,739–18,754, 1995.

Pincus, R., and M. Baker, Precipitation, solar absorption, and albedo susceptibility in marine boundary layer clouds, *Nature*, *372*, 250–252, 1994.

Platnick, S., and S. Twomey, Determining the susceptibility of cloud albedo to changes in droplet concentration with the advanced very high resolution radiometer, *J. Appl. Meteorol.*, *33*, 334–347, 1994.

Podgorny, I. A., W. Conant, V. Ramanathan, and S. K. Satheesh, Aerosol modulation of atmospheric and surface solar heating over the tropical Indian Ocean, *Tellus*, *Ser. B*, *52*, 947–958, 2000.

Radke, L. F., J. A. Coakley, Jr., and M. D. King, Direct and remote sensing observations of the effects of ships on clouds, *Science*, *246*, 1146–1149, 1989.

Ramanathan, V., and J. A. Coakley, Climate modeling through radiative-convective models, *Rev. Geophys.*, *16*, 465–489, 1978.

Ramaswamy, V., and C.-T. Chen, Climate forcing-response relationships for greenhouse and shortwave radiative perturbations, *Geophys. Res. Lett.*, *24*, 667–670, 1997.

Reader, M. C., I. Fung, and N. McFarlane, The mineral dust aerosol cycle during the Last Glacial Maximum, *J. Geophys. Res.*, *104*, 9381–9398, 1999.

Remer, L. A., Y. J. Kaufman, B. N. Holben, A. M. Thompson, and D. McNamara, Biomass burning aerosol size distribution and modeled optical properties, *J. Geophys. Res.*, *103*, 31,879–31,891, 1998.

Remer, L. A., Y. J. Kaufman, D. Tanré, Z. Levin, and D. A. Chu, Principles in remote sensing of aerosol from MODIS over land and ocean, in *Proceedings of the ALPS99 International Conference, 18–22 January 1999, Méribel, France*, pp. WK1/O/05/1–4, Cent. Natl. des Etudes Spatiales, Toulouse, France, 1999.

Restad, K., I. Isaksen, and T. K. Berntsen, Global distribution of sulfate in the troposphere, A three-dimensional model study, *Atmos. Environ.*, *32*, 3593–3609, 1998.

Rodhe, H., R. J. Charlson, and T. L. Anderson, Avoiding circular logic in climate modeling, *Clim. Change*, *44*, 419–422, 2000.

Roelofs, G.-J., J. Lelieveld, and L. Ganzeveld, Simulation of global sulfate distribution and the influence on effective cloud drop radii with a coupled photochemistry-sulfur cycle model, *Tellus*, *Ser. B*, *50*, 224–242, 1998.

Rosenfeld, D., TRMM observed first direct evidence of smoke from forest fires inhibiting rainfall, *Geophys. Res. Lett.*, *26*, 3105–3108, 1999.

Rosenfeld, D., Suppression of rain and snow by urban and industrial air pollution, *Science*, *287*, 1793–1796, 2000.

Ross, J. L., P. V. Hobbs, and B. Holben, Radiative characteristics of regional hazes dominated by smoke from biomass burning in Brazil: Closure tests and direct radiative forcing, *J. Geophys. Res.*, *103*, 31,925–31,941, 1998.

Rotstayn, L., Indirect forcing by anthropogenic aerosols: A general circulation model calculation of the effective-radius

and cloud lifetime effects, *J. Geophys. Res.*, *104*, 9369–9380, 1999.

Russell, P. B., and J. Heintzenberg, An overview of the ACE-2 Clear Sky Column Closure Experiment (CLEARCOLUMN), *Tellus*, *Ser. B*, *52*, 463–483, 2000.

Russell, P. B., J. M. Livingston, P. Hignett, S. Kinne, J. Wong, A. Chien, R. Bergstrom, P. Durkee, and P. V. Hobbs, Aerosol-induced radiative flux changes off the United States mid-Atlantic coast: Comparison of values calculated from Sun-photometer and in situ data with those measured by airborne pyranometer, *J. Geophys. Res.*, *104*, 2289–2307, 1999.

Satheesh, S. K., V. Ramanathan, X. Li-Jones, J. M. Lobert, I. A. Podgorny, J. M. Prospero, B. N. Holben, and N. G. Loeb, A model for the natural and anthropogenic aerosols over the tropical Indian Ocean derived from Indian Ocean Experiment data, *J. Geophys. Res.*, *104*, 27,421–27,440, 1999.

Sausen, R., K. Gierens, M. Ponater, and U. Schumann, A diagnostic study of the global distribution of contrails, part I, Present-day climate, *Theor. Appl. Climatol.*, *61*, 127–141, 1998.

Schmid, B., et al., Clear-sky closure studies of lower tropospheric aerosol and water vapor during ACE-2 using airborne sunphotometer, airborne in situ, space-borne, and ground-based measurements, *Tellus*, *Ser. B*, 52, 568–593, 2000.

Schult, I., J. Feichter, and W. F. Cooke, Effect of black carbon and sulfate aerosols on the global radiation budget, *J. Geophys. Res.*, *102*, 30,107–30,117, 1997.

Schwartz, S. E., and A. Slingo, Enhanced shortwave cloud radiative forcing due to anthropogenic aerosols, in *Clouds, Chemistry, and Climate*, *Global Environ. Change*, vol. 35, edited by P. J. Crutzen and V. Ramanathan, *NATO ASI Ser. I*, pp. 191–235, Springer-Verlag, New York, 1995.

Shine, K. P., and P. M. de F. Forster, The effects of human activity on radiative forcing of climate change: A review of recent developments, *Global Planet. Change*, *20*, 205–225, 1999.

Shine, K. P., Y. Fouquart, V. Ramaswamy, S. Solomon, and J. Srinivasan, Radiative forcing of climate change, in *Climate Change 1995: The Science of Climate Change, The Contribution of Working Group I to the Second Assessment Report of the IPCC*, edited by J. T. Houghton et al., chap. 2.4, pp. 108–118, Cambridge Univ. Press, New York, 1996.

Smith, W. L., S. Ackerman, H. Revercomb, H. Huang, D. H. DeSlover, W. Feltz, L. Gumley, and A. Collard, Infrared spectral absorption of nearly invisible cirrus clouds, *Geophys. Res. Lett.*, *25*, 1137–1140, 1998.

Sokolik, I. N., and O. B. Toon, Direct radiative forcing by anthropogenic airborne mineral aerosols, *Nature*, *381*, 681–683, 1996.

Sokolik, I. N., and O. B. Toon, Incorporation of mineralogical composition into models of the radiative properties of mineral aerosol from UV to IR wavelengths, *J. Geophys. Res.*, *104*, 9423–9444, 1999.

Sokolik, I. N., A. Andronova, and T. C. Johnson, Complex refractive index of atmospheric dust aerosols, *Atmos. Environ.*, *Part A*, *27*, 2495–2502, 1993.

Sokolik, I. N., O. B. Toon, and R. W. Bergstrom, Modeling the direct radiative characteristics of airborne mineral aerosols at infrared wavelengths, *J. Geophys. Res.*, *103*, 8813–8826, 1998.

Soufflet, V., D. Tanré, A. Royer, and N. T. O'Neill, Remote sensing of aerosols over boreal forest and lake water from AVHRR data, *Remote Sens. Environ.*, *60*, 22–34, 1997.

Ström, J., and S. Ohlsson, In situ measurements of enhanced crystal number densities in cirrus clouds caused by aircraft exhaust, *J. Geophys. Res.*, *103*, 11,355–11,361, 1998.

Swap, R., S. Ulanski, M. Cobbett, and M. Garstang, Temporal and spatial characteristics of Saharan dust outbreaks, *J. Geophys. Res.*, *101*, 4205–4220, 1996.

Tanré, D., Y. J. Kaufman, M. Herman, and S. Mattoo, Remote sensing of aerosol properties over oceans using the MODIS/EOS spectral radiances, *J. Geophys. Res.*, *102*, 16,971–16,988, 1997.

Tanré, D., L. A. Remer, Y. J. Kaufman, S. Mattoo, P. V. Hobbs, J. M. Livingston, P. B. Russell, and A. Smirnov, Retrieval of aerosol optical thickness and size distribution over ocean from the MODIS airborne simulator during TARFOX, *J. Geophys. Res.*, *104*, 2261–2278, 1999.

Taylor, J. P., and A. McHaffie, Measurements of cloud susceptibility, *J. Atmos. Sci.*, *51*, 1298–1306, 1994.

Tegen, I., and I. Fung, Contribution to the atmospheric mineral aerosol load from land surface modification, *J. Geophys. Res.*, *100*, 18,707–18,726, 1995.

Tegen, I., and A. Lacis, Modeling of particle size distribution and its influence on the radiative properties of mineral dust, *J. Geophys. Res.*, *101*, 19,237–19,244, 1996.

Tegen, I., A. Lacis, and I. Fung, The influence of mineral aerosols from disturbed soils on climate forcing, *Nature*, *380*, 419–422, 1996.

Tegen, I., P. Hollrigl, M. Chin, I. Fung, D. Jacob, and J. E. Penner, Contribution of different aerosol species to the global aerosol extinction optical thickness: Estimates from model results, *J. Geophys. Res.*, *102*, 23,895–23,915, 1997.

ten Brink, H. M., C. Kruisz, G. P. A. Kos, and A. Berner, Composition/size of the light-scattering aerosol in the Netherlands, *Atmos. Environ.*, *31*, 3955–3962, 1997.

Twohy, C. H., A. D. Clarke, S. G. Warren, L. F. Radke, and R. J. Charlson, Light-absorbing material extracted from cloud droplets and its effect on cloud albedo, *J. Geophys. Res.*, *94*, 8623–8631, 1989.

Twomey, S., Pollution and the planetary albedo, *Atmos. Environ.*, *8*, 1251–1256, 1974.

van Dorland, R., F. J. Dentener, and J. Lelieveld, Radiative forcing due to tropospheric ozone and sulfate aerosols, *J. Geophys. Res.*, *102*, 28,079–28,100, 1997.

Veefkind, J. P., J. C. H. van der Hage, and H. M. ten Brink, Nephelometer derived and directly measured aerosol optical depth of the atmospheric boundary layer, *Atmos. Res.*, *41*, 217–228, 1996.

Veefkind, J. P., G. de Leeuw, and P. A. Durkee, Retrieval of aerosol optical depth over land using two-angle view satellite radiometry during TARFOX, *Geophys. Res. Lett.*, *25*, 3135–3138, 1998.

Veefkind, J. P., G. de Leeuw, P. A. Durkee, P. B. Russell, P. V. Hobbs, and J. M. Livingston, Aerosol optical depth retrieval using ATSR-2 and AVHRR data during TARFOX, *J. Geophys. Res.*, *104*, 2253–2260, 1999.

von Hoyningen-Huene, W., K. Wenzel, and S. Schienbein, Radiative properties of desert dust and its effect on radiative balance, *J. Aerosol Sci.*, *30*, 489–502, 1999.

Wanner, W., A. H. Srahler, B. Hu, P. Lewis, J.-P. Muller, X. Li, C. L. Barker Schaaf, and M. J. Barnsley, Global retrieval of bidirectional reflectance and albedo over land from EOS MODIS and MISR data: Theory and algorithm, *J. Geophys. Res.*, *102*, 17,143–17,161, 1997.

Warren, S. G., C. J. Hahn, J. London, R. M. Chervin, and R. L. Jenne, Global distribution of total cloud cover and cloud type amounts over the ocean, *NCAR Tech. Note TN-317+STR*, 42 pp. + 170 maps, 1998.

West, J. J., C. Pilinis, A. Nenes, and S. N. Pandis, Marginal direct climate forcing by atmospheric aerosols, *Atmos. Environ.*, *32*, 2531–2542, 1998.

Wetzel, M., and L. L. Stowe, Satellite-observed patterns in stratus microphysics, aerosol optical thickness, and shortwave radiative forcing, *J. Geophys. Res.*, *104*, 31,287–31,299, 1999.

Wyser, K., and J. Ström, A possible change in cloud radiative forcing due to aircraft exhaust, *Geophys. Res. Lett*., *25*, 1673–1676, 1998.

Yamasoe, M. A., Y. J. Kaufman, O. Dubovik, L. A. Remer, B. N. Holben, and P. Artaxo, Retrieval of the real part of the refractive index of smoke particles from Sun/sky measurements during SCAR-B, *J. Geophys. Res*., *103*, 31,893–31,902, 1998.

O. Boucher, Laboratoire d'Optique Atmosphérique, UFR de Physique, Bâtiment P5, Université des Sciences et Technologies de Lille, 59655 Villeneuve d'Ascq Cedex, France. (boucher@loa.univ-lille1.fr)

J. Haywood, Meteorological Research Flight, U.K. Meteorological Office, DERA, Farnborough, Hampshire, GU14 0LX, England. (jmhaywood@meto.gov.uk)

Annexe B

Une nouvelle vue des aérosols depuis l'espace

Nous reproduisons ici l'article de Kaufman et al. publié en 2002 dans la revue *Nature*.

A satellite view of aerosols in the climate system

Yoram J. Kaufman*, Didier Tanré† & Olivier Boucher†

*NASA/Goddard Space Flight Center, Greenbelt, Maryland 20771, USA (e-mail: kaufman@climate.gsfc.nasa.gov)
†Laboratoire d'Optique Atmosphérique, Université de Lille/CNRS, Villeneuve d'Ascq, France

Anthropogenic aerosols are intricately linked to the climate system and to the hydrologic cycle. The net effect of aerosols is to cool the climate system by reflecting sunlight. Depending on their composition, aerosols can also absorb sunlight in the atmosphere, further cooling the surface but warming the atmosphere in the process. These effects of aerosols on the temperature profile, along with the role of aerosols as cloud condensation nuclei, impact the hydrologic cycle, through changes in cloud cover, cloud properties and precipitation. Unravelling these feedbacks is particularly difficult because aerosols take a multitude of shapes and forms, ranging from desert dust to urban pollution, and because aerosol concentrations vary strongly over time and space. To accurately study aerosol distribution and composition therefore requires continuous observations from satellites, networks of ground-based instruments and dedicated field experiments. Increases in aerosol concentration and changes in their composition, driven by industrialization and an expanding population, may adversely affect the Earth's climate and water supply.

During the last century, the Earth's surface temperature increased by 0.6 °C, reaching the highest levels in the last millennium[1]. This rapid temperature change is attributed to a shift of less than 1% (ref. 2) in the energy balance between absorption of incoming solar radiation and emission of thermal radiation from the Earth system. Among the different agents of climate change, anthropogenic greenhouse gases and aerosols have the larger roles[1]. Whereas greenhouse gases reduce the emission of thermal radiation to space, thereby warming the surface, aerosols mainly reflect and absorb solar radiation (the aerosol direct effect) and modify cloud properties (the aerosol indirect effect), cooling the surface. These impacts on the radiation balance are very different and therefore require different research approaches.

Greenhouse gases, such as carbon dioxide and methane, have a lifetime of up to 100 years in the atmosphere and a rather homogeneous distribution around the globe; this is in contrast to the heterogeneous spatial and temporal distribution of tropospheric aerosols, which results from their short lifetime of about a week[1,3]. As a consequence, the global increase in the CO_2 concentration of 1–2 p.p.m. per year was measured half a century ago using a single ground-based instrument[4], while daily satellite observations[5,6] and continuous *in situ* measurements[7,8] are needed to observe the emission and transport of dense aerosol plumes downwind of populated and polluted regions (urban haze), regions with vegetation fires (smoke), and deserts (dust). The effect of greenhouse gases on the energy budget occurs everywhere around the globe. Aerosols have both regional and global impacts on the energy budget, requiring frequent global measurements tied to elaborate models that provide realistic representations of the atmospheric aerosols[3,9,10].

Aerosol effects on climate differ from those of greenhouse gases in two additional ways. Because most aerosols are highly reflective, they raise our planet's albedo, thereby cooling the surface and effectively offsetting greenhouse gas warming by anywhere from 25 to 50% (refs 1, 9–11). However, aerosols containing black graphitic and tarry carbon particles (present in smoke and urban haze) are dark and therefore strongly absorb incoming sunlight. The effects of this type of aerosol are twofold, both warming the atmosphere and cooling the surface before a redistribution of the energy occurs in the column. During periods of heavy aerosol concentrations over the Indian Ocean[12] and Amazon Basin[13], for example, measurements revealed that the black carbon aerosol warmed the lowest 2–4 km of the atmosphere while reducing by 15% the amount of sunlight reaching the surface. Heating the atmosphere and cooling the surface below reduces the atmosphere's vertical temperature gradient and therefore is expected to cause a decline in evaporation and cloud formation[14,15].

The second way in which aerosols differ from greenhouse gases is through the aerosol effect on clouds and precipitation. In polluted regions, the numerous aerosol particles share the condensed water during cloud formation, therefore reducing cloud droplet size by 20–30%, causing an increase in cloud reflectance of sunlight by up to 25% (refs. 2, 16–19), and cooling the Earth's surface. The smaller, polluted cloud droplets are inefficient in producing precipitation[20,21], so they may ultimately modify precipitation patterns in populated regions that are adapted to present precipitation rates. The cooling effect due to polluted clouds is still poorly characterized with an uncertainty 5 to 10 times larger than the uncertainty in the predicted warming effect of greenhouse gases[1,22]. The effect of aerosols on precipitation is even less well understood.

To assess the aerosol effect on climate we first need to distinguish natural from anthropogenic aerosols. Satellite data and aerosol transport models show that plumes of smoke and regional pollution have distinguishably large concentrations of aerosols in particular of fine (submicron) size. In contrast, natural aerosol layers may have concentrated coarse dust particles and only widespread fine aerosols from oceanic and continental sources[23]. The ability of satellites to observe the spatial distribution of aerosols[24–28], and to distinguish fine from coarse particles, can be exploited to separate natural from anthropogenic aerosols. *In situ* measurements of aerosol composition[29,30] and size, models that assimilate

the measurements and information on population density and economic activities are needed to further quantify the anthropogenic aerosol component, and to relate it to specific sources.

Aerosol research is in transition from an exploratory phase to a global quantitative phase. The exploratory phase is dominated by the discovery of new aerosol-related processes. For example, the large concentration of black carbon emitted from vegetation fires and found in regional pollution in the tropics[31–33] and its effect on slowing down the hydrologic cycle[2,34]; or the effect of aerosol on reducing precipitation efficiency[20,21,35,36] and counteracting regionally the greenhouse warming[9,10,17]. In this phase, models are used to assess the potential of aerosol processes to affect the global climate[10,37]. Because aerosols vary widely from region to region, a multiple-measurement approach is necessary to assess their impacts on global climate. Specifically, we require the use of long-term, detailed global measurements from satellites[17,23,38–40], distributed networks of ground-based instruments[29,41,42], and comprehensive regional experiments in clean[43] and polluted[31,32] environments, that feed global aerosol and climate models[14,23,44].

Regional variability of aerosols

Most aerosols are regional in nature owing to their short lifetime, the regional distribution of sources, and the variability in their properties. Seasonal meteorological conditions determine how far aerosols are transported from their sources as well as how distributed they are vertically through the atmosphere. Elevated aerosol layers can be picked up by strong winds and transported from Africa or Asia to America and from America to Europe[7,8]. Aerosol properties are modified during the transport by dry or wet deposition, in-cloud processes, and atmospheric chemical reactions.

Aerosol optical thickness (AOT) describes attenuation of sunlight by a column of aerosol, and thus serves as a measure of aerosol column concentration. In Fig. 1a,b, AOT is shown separately for fine and coarse aerosol for September 2000, using satellite techniques discussed in Box 1; several typical regional aerosols are distinguished (see also Table 1).

Urban and industrial regional pollution (urban haze)

These mainly fine hygroscopic particles are found downwind of populated regions[5] (regions a, c and e in Fig. 1a) in air polluted, for example, by car engines, industry, cooking and fireplaces. In China, economic growth and population expansion increased AOT from 0.38 in 1960 to 0.47 in 1990 (ref. 45). Pollution aerosol was modelled first as sulphates only[11], but new chemical measurements[46] show that downwind of the eastern United States[47] the contribution of carbonaceous material to AOT (30%) is double that of sulphates (16%), with water intake (48%) and black carbon (6%) accounting for the rest. Black carbon describes the effective fraction of elemental carbon that accounts for the absorption properties of the aerosol. Emission of black carbon is lower for newer engine technology so that black carbon contributes generally more to AOT in south and east Asia and Central America[32,33] (11%). Absorption by black carbon is not only related to its concentration, but also depends on its location in the aerosol particle — absorption can be two to three times stronger if the black carbon is located inside the scattering particle[48–51].

Smoke from vegetation fires

Smoke from vegetation fires is dominated by fine organic particles with varying concentrations of light-absorbing black carbon (regions b and d in Fig. 1a) emitted in the hot, flaming stage of the fire. In forest fires the flaming stage is followed by a long, cooler smouldering stage in which the thicker wood, not completely consumed, emits smoke (composed of organic particles without black carbon) in much greater quantities than during the flaming stage. Conversely, thin African grasses burn quickly in strong flaming fires, emitting large quantities of black carbon, without a smouldering stage. On average, 12% of African smoke AOT is due to absorption by black

Table 1 **Climatology of ambient aerosol properties averaged on the atmospheric column**

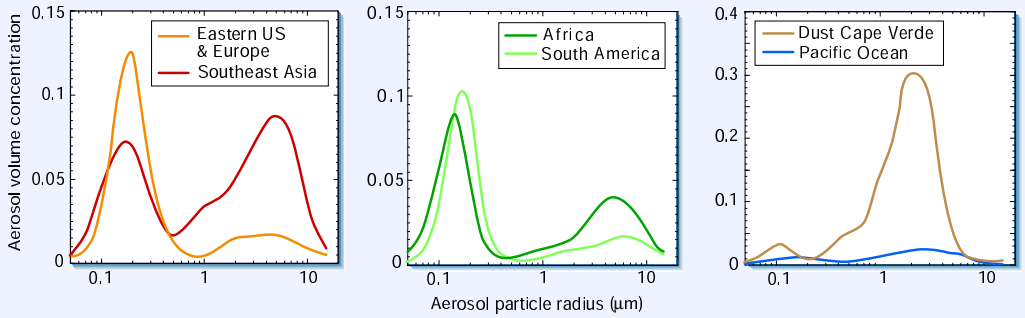

Analysis\Aerosol type	Regional pollution aerosol				Biomass burning			Dust	Oceanic
AERONET analysis	East. US	Europe	SE Asia	Cen. Am.	Boreal forest	Trop. forest	Savanna Africa–S.A.	Sahara–Saudi Arabia	Pacific Ocean
Time of the year	Jun–Sep		Jan–Apl	Jan–Dec		Jun–Nov		Jan–Dec	Jan–Dec
Average AOT	0.20		0.20	0.30	0.25–0.45		0.25–0.5	0.2–0.4	0.06
AOT_f	94%		95%	90%	95%		92%	25%	67%
% absorption of AOT	3%	6%	12%		7%		12%	5%	2%
MODIS analysis	North Atlantic 60–105° W 20–45° N		SE Asia 70–140° E 5–40° N		South Africa 15° W–30° E 0–20° S			West Africa 15–50° W 10–25° N	
Average AOT	0.18		0.24		0.31			0.30	
AOT_f	41%		44%		66%			33%	
ΔF_{TOA} (W m^{-2})	–8		–10		–10			–17	
ΔF_{SUR} (W m^{-2})	–10		–23		–30			–23	

The aerosol properties presented are based on two types of analysis. The top part of the table shows systematic multi-year measurements by the Aerosol Robotic Network (AERONET)[33,41] and *in situ* measurements[47,87,88], whereas data in the bottom part of the table are based on analysis of Moderate-resolution Imaging Spectroradiometer (MODIS) satellite data for September 2000. In the AERONET analysis, aerosol optical thickness (AOT) is a measure of the aerosol column concentration and is given at a wavelength of 0.55 μm. Four aerosol types are shown with a representative size distribution (in units of μm^3 per μm^2): (1) pollution from eastern United States (Greenbelt, Maryland) and Europe (Venice and Paris), southeast Asia (Maldives-INDOEX) and Central America (Mexico City); (2) biomass burning from Africa and South America; (3) dust over the Atlantic Ocean (Cape Verde); and (4) maritime aerosol over the Pacific Ocean (Lanai). The uncertainty in AOT is ±0.01; contribution of the fine mode to AOT (AOT_f) is given over the land with uncertainty of ±2%. In the MODIS data the uncertainty in AOT ranges from ±0.03 to ±0.06. The reflection of sunlight to space (ΔF_{TOA}) and reduction of surface illumination (ΔF_{SUR}) are based on the AERONET and MODIS data, using the radiative transfer code of Chou[89].

carbon[52], in contrast to 5% for Boreal fires[33]. Smoke is less hygroscopic than regional pollution aerosol, with only 10–20% of smoke AOT being associated with water for typical relative humidities of 80–85% in South America and Africa[53], compared with 50% for regional pollution aerosol[1]. Dense smoke plumes are found annually downwind of fires in South America (August–October), Central America (April and May), Southern Africa (July–September) and Central Africa (January–March)[5,6,54].

Dust

Dust is emitted from dry lakebeds in the Sahara, east Asia and the Saudi Arabian deserts[5,6] (regions a and c in Fig. 1b) that were flooded

Box 1

How do satellites observe aerosols?

Radiant energy reflected and emitted by the Earth carries with it a signature of the atmospheric and surface properties. By measuring the wavelength, angular and polarization properties of this energy, satellite sensors can quantify several atmospheric and surface properties. (Polarization is the degree of organization of the electric field of the scattered solar radiation into a given direction.)

The human eye is sensitive to a narrow spectral range of the solar spectrum, with spectral receptors for blue, green and red light. Depth perception is provided by our eyes having slightly different angles of observation. By analogy, aerosol remote sensing — for example, AVHRR (Advanced Very High Resolution Radiometer), METEOSAT and GOES (Geostationary Operational Environmental Satellite) — developed from using a single wavelength[5,91] and single angle of observation, like a colour-blind person with one eye. The TOMS instruments (for Total Ozone Mapping Spectrometer), flown since 1978, have two channels sensitive to ultraviolet light that were discovered to be excellent for observations[92,93] of elevated smoke or dust layers above scattering atmosphere (Box Fig. 1).

The first instrument designed for aerosol measurements, POLDER (Polarization and Directionality of the Earth's Reflectances)[26,38,40], uses a combination of spectral channels in a range wider than that of human vision (0.44–0.86 μm). The instrument comprises a wide-angle camera that observes the same target on the Earth at several different angles, up to zenith angle of 65°. POLDER also measures light polarization to detect fine aerosols over the land, taking advantage of the difference between the spectrally neutral polarized light reflected from the Earth's surface and the spectrally decreasing polarized light reflected by fine aerosols (see Fig. 4).

Two instruments, MODIS (Moderate-resolution Imaging Spectroradiometer) and MISR (Multi-angle Imaging Spectroradiometer), on the Terra satellite measure global aerosol concentrations and properties since 2000. Over the ocean, MODIS uses the aerosol spectral signature in a wide range (0.47–2.1 μm) to distinguish small pollution particles from coarse sea-salt and dust[25] (Box Fig. 2). MODIS measures aerosol optical thickness (AOT) with an estimated error of $\pm 0.05 \pm 0.20$AOT over the land[94] and $\pm 0.03 \pm 0.05$AOT over the ocean[95] (note that 0.03 is an offset due to uncertainty in the ocean state and 0.05AOT is due to uncertainty in aerosol properties). Over land, MODIS uses the 2.1-μm channel to observe surface-cover properties, estimate surface reflectance at visible wavelengths, and derive AOT[96] from the residual reflectance at the top of the atmosphere.

The amount of light escaping the top of the atmosphere is affected by the angle at which the light was reflected by the surface or atmosphere. MISR[27] takes advantage of this fact by detecting the reflected light at different viewing angles (nadir to 70° forward and backward) along the satellite's track in a narrower spectral range (0.44–0.86 μm). It is thus able to separate the aerosol signal from that of surface reflectance, and determine the aerosol properties. A mixed approach using two viewing directions but a wider spectral range (0.55–1.65 μm) is used by ATSR (Along Track Scanning Radiometer)[28] to derive the aerosol concentration and type.

Over bright desert the magnitude of dust absorption determines if dust brightens or darkens the image[82,97], and this property is used for its estimation. Such satellite measurements, in agreement with *in situ*[8], aircraft[98] and radiation-network[33] measurements of dust absorption, helped resolve a long-standing uncertainty in desert-dust absorption of sunlight[56].

The realization that aerosols affect surface temperature and precipitation patterns creates a demand for more informative spaceborne observations. We foresee several improvements in this respect. First, spaceborne instruments are being considered that combine a wide spectral and viewing-angle range[99] with polarization. Such instruments are expected to improve derivation of fine and coarse aerosols, including their sizes and refractive index (refractive index, an optical property, is sensitive to the aerosol composition and water intake[100]). Second, derivation of aerosol absorption over the oceans will be achieved by measuring the aerosol spectral attenuation of the bright glint.

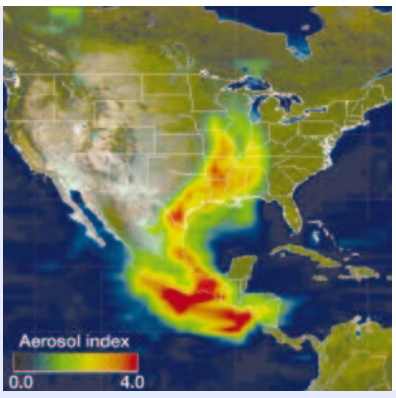

Box Figure 1 TOMS image showing heavy smoke aerosol transported to North America from large wild fires in Mexico on 15 May 1998. (Image courtesy of J. Herman, NASA/GSFC; see http://toms.gsfc.nasa.gov/aerosols/aerosols.html for additional images.)

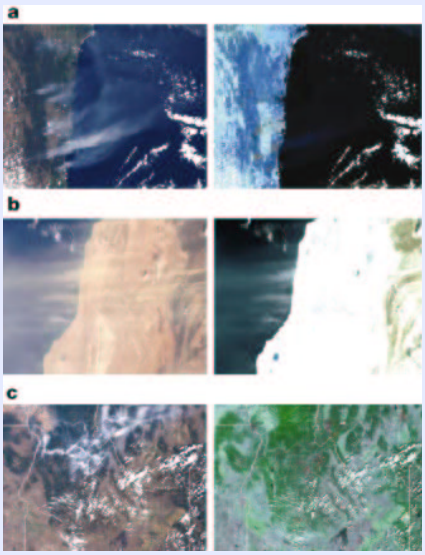

Box Figure 2 Spectral aerosol reflectance measured by MODIS. Panels in the left column show colour composites of channels in the visible spectrum and those on the right show composites in the near infrared spectrum. **a**, Fine smoke particles from fires in Australia (25 December 2001), which are invisible over the ocean in the near infrared[24]. **b**, Coarse dust particles emitted from West Africa (7 January 2002), which are visible in both panels over the ocean. **c**, Smoke in Idaho and Montana invisible in the mid-infrared over the land. The spectral measurements are used to detect smoke over land[31,95,96] and distinguish smoke from dust over the ocean.

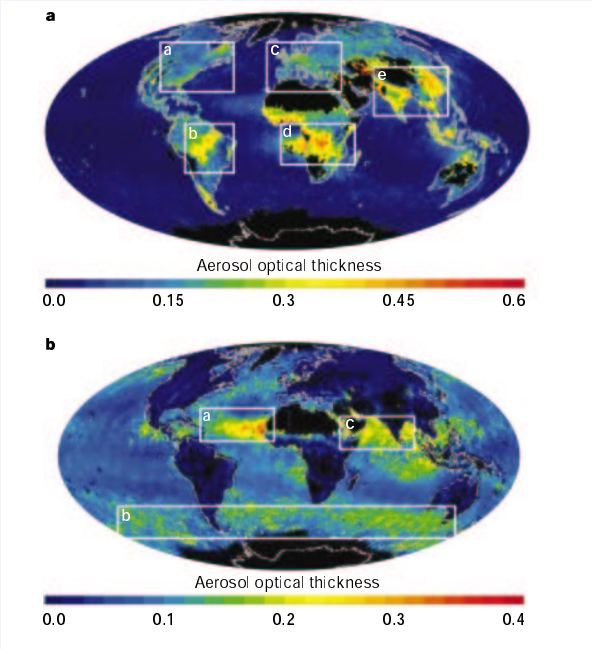

Figure 1 Global distribution of fine and coarse aerosol optical thickness (AOT) derived from MODIS measurements on the NASA Terra spacecraft for September 2000. AOT is a measure of the aerosol column concentration and is represented by the colour scale at a wavelength of 0.55 μm. Black regions have surface properties inappropriate for MODIS aerosol retrievals or very low solar elevations. The white boxes indicate regions with high aerosol concentrations. **a**, Distribution of fine AOT. The image shows fine particles in pollution from North America and Europe (regions a and c), vegetation fires in South America and southern Africa (regions b and d) and pollution in south and east Asia (region e). **b**, Distribution of coarse AOT. Coarse dust from Africa (region a), salt particles in the windy Southern Hemisphere (region b) and desert dust (region c).

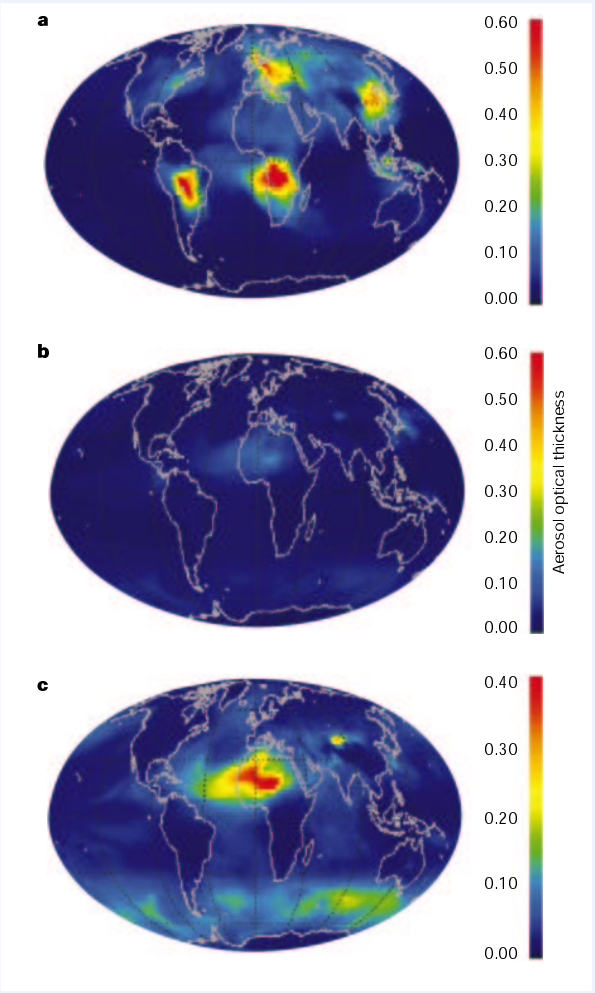

Figure 2 Model results of Chin *et al.*[23] that correspond to the MODIS data of September 2000. **a**, Anthropogenic fine aerosols; **b**, natural fine aerosols; and **c**, coarse aerosols composed of natural dust and salt.

in the Pleistocene era[55]. Almost no dust is observed from Australia[5], where the topography is mostly flat, because the arid regions are old and highly weathered[55]. An unknown amount of dust is emitted from disturbed soils in Africa and east Asia. A previous estimate that 30–50% (ref. 56) of African dust results from human impact is questioned by new satellite observations using the ultraviolet part of the solar spectrum[6] (Box 1); these show that African dust originates mostly from uninhabited regions north of 15° N (ref. 55). Dust emission from Africa is influenced by large-scale air circulation[57], which affects flow from the continent, and drought conditions. The highest dust production matches drought conditions in the strongest El Niño year of 1983 (ref. 7).

Dust AOT is dominated by coarse particles[58] with varying concentrations of iron oxide (rust) that absorbs light in the blue and ultraviolet wavelengths. However, African dust transported to Florida contains high concentrations of fine particles (10–100 $\mu g\ m^{-3}$) during the summer months and exceeds local pollution standards on particulate matter[42]. Dust from east Asia, from both natural sources and land use, is elevated to a height of 3–5 km with a pollution layer under it at 0–2 km (ref. 59), and is transported during April and May to North America. In April 2001 such a dust storm generated hazy conditions (AOT of 0.4) as far away as Boulder, Colorado (G. Feingold personal communication). On its way to North America, dust deposited in the Atlantic and Pacific Oceans provides key nutrients such as iron to oceanic phytoplankton[60].

Oceanic aerosol

Oceanic aerosol is shown in the blue regions of Fig. 1b and the elevated green values at latitudes south of 40° S (region b in Fig. 1b). It is composed of coarse salt particles emitted from bursting sea foam in windy conditions and fine sulphate particles from oceanic emissions[61]. Oceanic aerosol generally absorbs very little sunlight[33,62] — its AOT is estimated to average 0.07 in most regions[32,62], but increases in the windy region south of 40° S to 0.2 (ref. 23).

Anthropogenic component

It is difficult to distinguish anthropogenic from natural aerosols as even individual particles can have both natural and anthropogenic components[30,32,63]. Precise description of aerosol composition requires *in situ* chemical measurements that are restricted in time and location. However, it is possible to estimate the anthropogenic part of aerosols using a combination of satellite data, aerosol models[23,24,44] and information on urban and agricultural activities and fire practices. For example, in Fig. 1 we see that anthropogenic aerosols downwind from vegetation fires and regions of industrial pollution are characterized by high concentration of fine particles. Aerosol models[23] confirm this finding, and further show that natural fine aerosols emitted from large-area oceanic and land sources exhibit much smaller spatial variability (Fig. 2). An example of daily satellite data and model calculations (Fig. 3) shows clear distinction between dust plume (coarse particles) and the regional pollution (fine particles). The model simulations confirm this distinction.

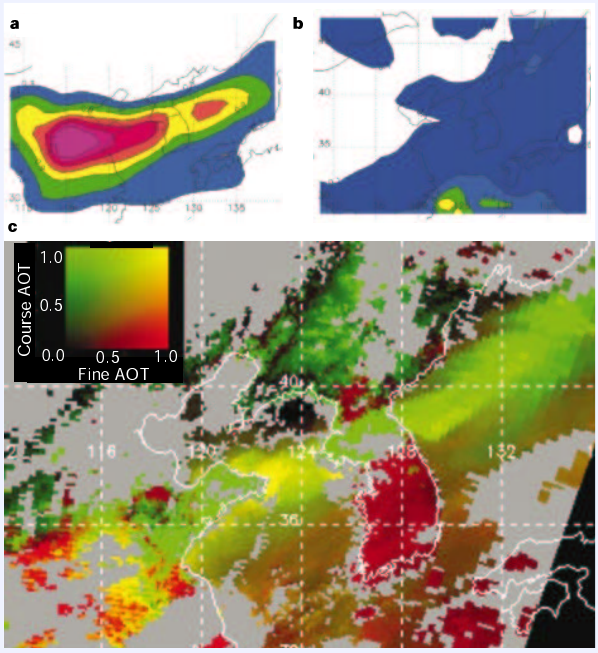

Figure 3 Satellite data and model calculations for a dust episode in east Asia advected over a pollution layer on 20 March 2001. **a**, **b**, NAAPS aerosol model simulation[90] of the optical thickness of the coarse dust particles (**a**) and the fine sulphate particles (**b**); the optical thickness varies from 0.3 for the blue to 1.5 for the red. **c**, Optical thickness of fine particles (red) associated with air pollution and the coarse dust (green) derived from the MODIS data on the Terra satellite.

An example of the relationship between population density and pollution concentration is shown in Fig. 4. Proximity of dust to desert or agricultural area can be used as an indicator for natural desert dust. Continued improvements in the models, constrained by new, detailed global measurements, will enable us to isolate the anthropogenic aerosol component.

In the Indian Ocean Experiment, chemical separation of aerosols into natural and anthropogenic components[32] shows that the natural aerosol AOT is 0.07, with an additional 0.2–0.6 over the Bay of Bengal resulting from anthropogenic activity[64]. But pinpointing the anthropogenic source is proving difficult. Aerosol chemical composition can be used as a 'fingerprint' of the source, and a ratio of 1:2 between black carbon and total carbonaceous aerosol or sulphates suggests that the aerosol is emitted primarily from fossil fuel consumption[32]. But aerosol concentration varies through the year, whereas the relatively steady use of fossil fuel in the tropics, with its small variation of energy use from winter to summer[64], would suggest a stable aerosol concentration. A correlation between aerosol concentration and number of fires in India[64] suggests a large contribution of biomass burning. Analysis of aerosols and trace gases (CO and SO_2) suggests a mixed origin, both from fossil fuel and bio-fuel burning in the same proximity[65].

Aerosol direct forcing

The climate system varies naturally, through the dynamic interplay between atmospheric, oceanic and terrestrial moisture and energy. However, the radiative effects resulting from an increase in the concentration of anthropogenic aerosol or greenhouse gases, called radiative forcing, cause a net change in the Earth's absorbed and emitted solar and thermal energy and therefore are the basic ingredients of climate change[1].

A negative radiative forcing indicates that the Earth–atmosphere system loses radiant energy, resulting in cooling. Models of the climate system[1] show a direct relationship between radiative forcing and average global surface temperature, which rises 0.4–1.2 °C for every 1 W m^{-2} of forcing. However, this relationship may break down for strongly absorbing aerosols[12,14,15].

Dust and smoke serve as an example of weakly and strongly absorbing aerosols (see Table 1). Absorption accounts for 5% and 12% of AOT for Saharan Desert dust and for aerosols in south and east Asia, respectively[33]. In September 2000, dust reflected 17 W m^{-2} of sunlight to space, thus reducing by an equivalent amount the energy available to heat the Earth–atmosphere system. At the same time, the dust reduced surface illumination by 23 W m^{-2}; the difference (6 W m^{-2}) is due to the absorption of sunlight. The aerosols in south and east Asia also reduced surface illumination by 23 W m^{-2}, but absorbed 13 W m^{-2}, reflecting only 10 W m^{-2} to space[32]. Figure 5 shows the large regional extent of the aerosol radiative effects for these two aerosol types.

Another example of the radiative effects of weakly or strongly absorbing aerosol occurs over the Atlantic Ocean. Absorbing smoke is transported from Africa across the Southern Atlantic and less absorbing pollution aerosol is transported from North America in the Northern Atlantic (Fig. 1). In September 2000, aerosols found in these two

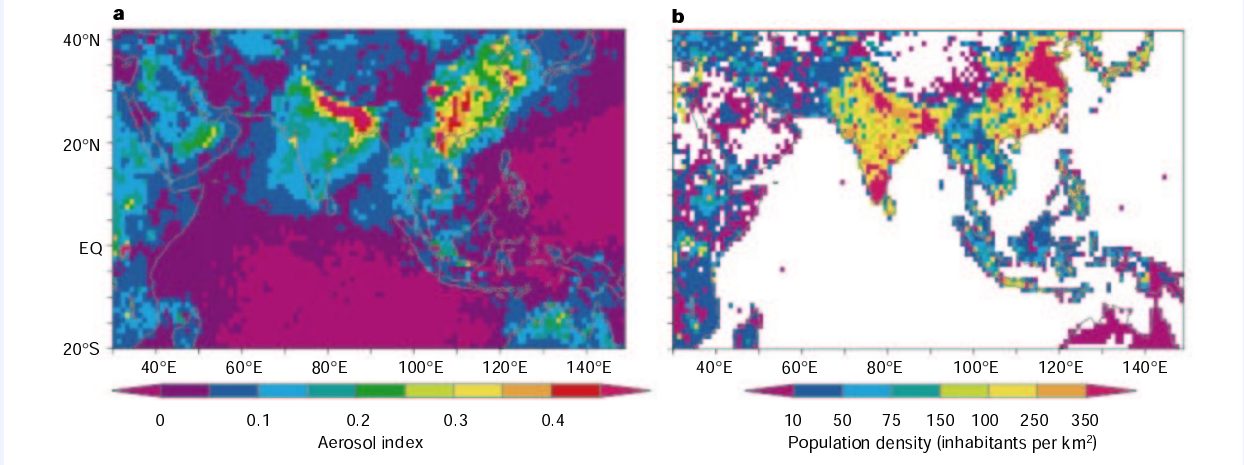

Figure 4 Comparison between concentration of anthropogenic aerosol and population density. **a**, Aerosol polarization index derived from the data of the POLDER instrument flown on ADEOS-1 in February 1997. The index is derived from measurements of polarization of scattered solar light and is sensitive only to the presence of fine aerosol particles that in high concentration originate from anthropogenic sources. **b**, Population density map (inhabitants per square kilometre).

regions reflected 10 and 8 W m^{-2}, respectively, of sunlight to space. But the impact on surface illumination is three times larger for the smoke than for the pollution aerosol (30 W m^{-2} versus 10 W m^{-2}). Model calculations show that such strong aerosol absorption occurring in the lower troposphere heats the air layer, reducing its relative humidity and temperature gradients[32], and increasing atmospheric stability. This decreases cloudiness[15] and possibly reduces or prevents precipitation[20] that could have washed the aerosols from the atmosphere.

The results in Fig. 5 and Table 1 were computed for cloud-free oceanic regions. In cloudy conditions, the aerosol radiative effect depends on the fraction of absorbing aerosol located above clouds[14], where the particles can absorb up to three times more sunlight than aerosol in cloud-free conditions[66]. Absorbing aerosols may even have a positive (warming) rather than negative (cooling) radiative impact. Over dark oceans (albedo of 6%) the aerosol absorption has to be as high as 15% of AOT to result in warming, but 10% is enough over the brighter land (albedo of 20%), and only 5% if the aerosol layer is above boundary-layer clouds[14].

Knowledge of the vertical distribution of aerosols and clouds is therefore needed to calculate the impact of aerosol radiative effects. Elevated aerosol plumes occur during long-range transport of aerosols. For example, smoke from forest fires in Canada was found over Greece at 2–3 km altitude[67], above the local boundary-layer clouds; Saharan dust is transported over Europe at 3–10 km elevation[68]; and smoke intrusions from fires in Mexico[69] and northeast Canada are transported across North America at altitudes of 3–5 km. With the launch of space lidars[70] in the next few years we will begin to make the global measurements of the aerosol and cloud profiles needed to assess aerosol radiative forcing.

Aerosol modification of clouds and precipitation

Each cloud drop requires an aerosol particle to condense upon; clouds could not form otherwise. Thus the concentration, size and composition of the aerosols that can act as cloud condensation nuclei (CCN) determine the cloud properties[9,17,18], evolution and development of precipitation[20]. However, availability of moisture, updrafts and cloud formation are influenced mainly by large-scale dynamic processes. Although natural aerosols are needed to form clouds, it seems that urban haze and smoke aerosols take every opportunity to reduce formation of precipitation and affect cloud radiative properties at the same time (Fig. 6).

Cloud base

Aircraft measurements show that in polluted air a sixfold increase in the number of fine aerosols per unit volume of air produces a three- to fivefold increase in the droplet concentration[2,71]. Analysis of global satellite data shows that such a change in aerosol concentration corresponds to 10–25% smaller cloud droplets[17,38] (Fig. 7), because the condensed water is divided into more numerous droplets. Clouds with smaller, more numerous droplets have a larger surface area and a corresponding increase in reflectivity of up to 30% (ref. 17). This increase in the reflection of sunlight to space, called the first aerosol indirect effect, was proposed by Twomey, based on two decades of aircraft sampling, to possibly rival the greenhouse forcing[9]. If these global cloud modifications can be attributed to anthropogenic effects[72], they would translate into a solar radiative forcing of –0.5 to –1.5 W m^{-2} (refs 17, 73).

The actual effect of aerosols on cloud droplets, as inferred from global measurements from aircraft[2] and satellites[17,38], is 1.5–3 times smaller than that expected by Twomey for constant liquid water content[9]. In polluted air, above a given threshold of CCN concentration, the concentration of cloud droplets does not increase further; this results from competition between the more numerous CCN for water vapour[2], and it may explain the smaller global effect. The threshold depends on cloud dynamics, availability of moisture, aerosol size distribution and chemical properties. The larger and more hygroscopic the particles, the greater their ability to

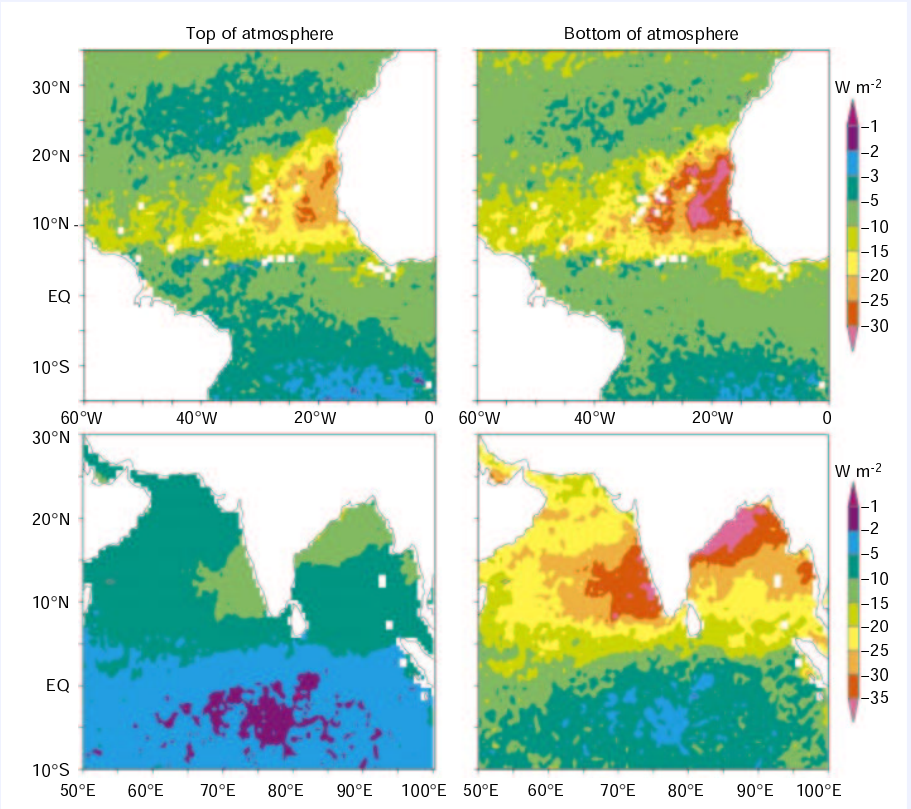

Figure 5 Solar radiative perturbation at the top of the atmosphere and the surface for the tropical Atlantic and Indian Ocean. Top of the atmosphere (left parts) and surface (right parts) solar radiative perturbation (W m^{-2}) in clear sky is shown for the tropical Atlantic Ocean in May 1997 (upper parts) and the Indian Ocean in March 1997 (lower parts). The radiative perturbation is derived from the POLDER daily analysis of the aerosol optical depth combined with aerosol models modified to reproduce the aerosol absorption of Table 1. Over the Indian Ocean the perturbation is three times larger at the surface than at the top of atmosphere, as the aerosol-absorbed sunlight does not reach the surface.

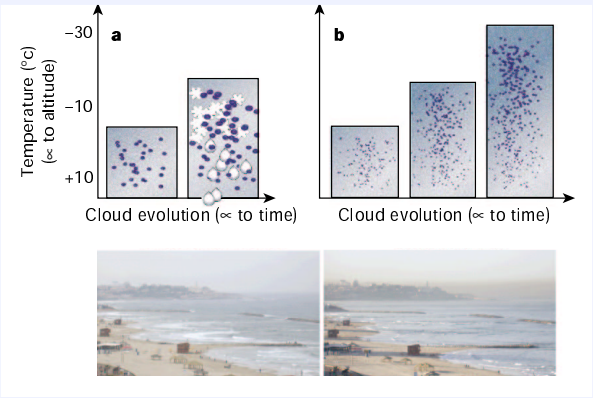

Figure 6 Schematic diagram of cloud formation in a clean and polluted atmosphere. **a**, In a clean atmosphere, the cloud droplet size increases with cloud development until liquid precipitation or glaciation and precipitation take place. **b**, In polluted clouds, the availability of cloud condensation nuclei decreases cloud droplet development. In clouds with strong updrafts the developed cloud can be supercooled with no glaciation down to −37.5 °C. The filled circles show the location of droplets of varying size, the asterisks show the location of ice crystals, and the oval shapes indicate rain drops.

compete at a given cloud updraft speed[74]. The presence of even a few supermicron CCN particles per litre, such as sea salt or dust particles coated with sulphates[63], may reduce the indirect effect of pollution aerosol and produce precipitation[75].

Additional aerosol processes have to be considered, such as the possibility that water-soluble organic compounds present in the particle and the presence of soluble gases (HNO_3) in the atmosphere help the aerosols to take up water vapour and further increase the concentration of cloud droplets and the indirect forcing[76]. A contrary effect can take place from organic films that retard droplet growth and reduce drop concentration[77].

Cloud development

In clean conditions the cloud droplet size increases as the cloud develops and extends in the vertical direction until the droplet reaches a critical radius of ~15 μm (ref. 36) for the onset of liquid precipitation. Alternatively, the droplet may freeze if the cloud top temperature reaches −10 °C. In pollution plumes over Australia and Canada, and smoke plumes over Indonesia, satellite data show not only smaller droplets at the cloud base (5–8 μm radius compared with 10–15 μm in clean conditions), but also a lack of increase in droplet size as the cloud develops, rising through the atmosphere and accumulating water vapour. Consequently, precipitation does not occur or is delayed in polluted water clouds[20,21]. In the same regions, non-polluted cloud droplets grow to 20–30 μm and precipitation occurs. This suppression of precipitation was also observed for stratiform clouds polluted by emissions from ship stacks[36] and for polluted cumulus clouds in the Indian Ocean[71].

The high concentration of aerosol supplies new CCN to condense the excess water vapour as the cloud cools down. The result is an increase in the cloud liquid water content, cloud lifetime and area of coverage — called the second aerosol indirect effect. The global importance of this effect is still not clear. Analysis of changes in cloud fraction and precipitation throughout the last century suggests that more clouds are needed for the same amount of precipitation, as would be expected given the inhibitory effect of pollution on precipitation (D. Rosenfeld personal communication, from data in ref. 1).

Ice crystals

Water clouds that cannot precipitate owing to the high concentration of aerosols could still precipitate once the droplets freeze.

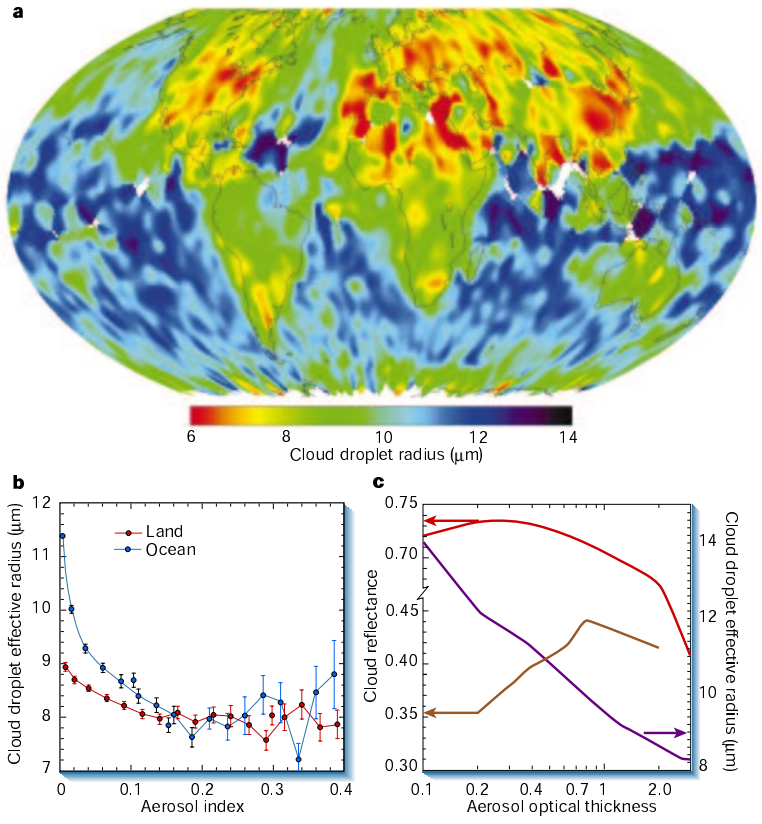

Figure 7 Effect of aerosol on cloud droplet and reflectance derived from POLDER and AVHRR spaceborne measurements. **a**, Seasonal (March–May 1997) average droplet size in liquid water clouds estimated from the POLDER measurements[31]. **b**, The dependence of the droplet size on the aerosol index, also derived from POLDER over land (red) and ocean (blue). **c**, Analysis of AVHRR data for the dependence of the droplet size (purple) and cloud reflectance (brown and red) on aerosol optical thickness over the Amazon Basin during the dry burning season of 1987 (refs 16, 19). The reflectance of low-level clouds (brown) with reflectance of 0.35 increases with the aerosol concentration and the reflectance of bright clouds (red) decreases.

However, measurements in a deep convective cloud with a strong updraft show that the freezing process is postponed until the cloud reaches temperatures of –37.5 °C. Strong updrafts and condensation lead to a high concentration of small cloud droplets. These droplets do not collide efficiently to form raindrops, nor do they freeze at –10 °C. The result is a supercooled water cloud, thus eliminating an alternative way for clouds to precipitate[78]. Model simulations suggest that this process requires the presence of high CCN concentrations (1,260 cm^{-3}) and vigorous updrafts[79].

Cloud formation

The presence of light-absorbing black carbon in aerosols can also affect cloud properties. Models show that heating of the lower troposphere by aerosol absorption reduces cloud formation[15], an effect referred to as the semi-direct effect[14]. There are no direct measurements of this effect, but analysis of satellite data of clouds embedded in varying concentrations of smoke from fires in the Amazon basin[19] shows that for the thicker clouds an increase in the smoke AOT from 0.2 to 3 raises the cloud-top temperature by 4 °C, decreases the cloud reflectance by 0.13, while still reducing the droplet size by 40% (Fig. 7c). The simultaneous rise in the cloud-top temperature and reduction in reflectance — more than black carbon absorption itself can explain[19] — indicates the possibility of a reduction in convection, thereby causing a decrease in the updraft speed and in the amount of liquid water available to form the cloud[19].

The effect of aerosols on cloud droplet size is better understood than their effect on precipitation. Additional studies are needed to quantify the indirect effect of aerosols on climate, but the potential for a significant cooling in most regions is indicated. The reduction of the precipitation efficiency by anthropogenic aerosols has the potential to shift precipitation away from polluted regions[34]. Because the continents are more polluted than the ocean, this can cause a loss of fresh water over the continents, and in particular around populated regions. However, long-term regional studies that can measure the significance of this effect are still not available.

Aerosols in climate change

The cooling influence of aerosols on climate, directly through the reflection of sunlight to space[10] and indirectly through changes in cloud properties[9], has been appreciated for over a decade, and has triggered a large number of observations, simulations and analyses. The effect of anthropogenic aerosols is not limited to cooling by sulphates. Instead, carbonaceous compounds that include light-absorbing black carbon can be an important warming agent, and the sign of the temperature change from aerosols[80] can vary depending on the aerosols' radiative properties[81,82] and their distribution over the dark ocean and reflective land. The cooling of the Earth's surface from absorbing aerosols (compared with the top of the atmosphere) and consequential warming of the atmosphere causes a flattened vertical temperature profile in the troposphere, which is expected to slow the hydrologic cycle[2], reduce evaporation from the surface and reduce cloud formation[14,15]. It has also been suggested that as aerosols tend to reduce cloud droplet sizes[17,38], and hence precipitation[20], rain and snow may be shifted from highly polluted populated areas to the more pristine oceanic regions[34]. This raises the question of whether there has been or will be a change in the availability of fresh water due to aerosols.

Future research will need to unravel the magnitude of the aerosol effect on clouds and precipitation, on regional and global scales, and its sensitivity to aerosol chemistry and cloud dynamics. Given the importance of the absorption of sunlight by black carbon[12], a quantitative assessment of black carbon sources[83], its lifetime in the atmosphere, its distribution around the globe[54] and its impact on the hydrologic cycle[2] will need to be explored.

To associate the aerosol impact with human activity, we need to distinguish natural from anthropogenic aerosols. By measuring separately fine and coarse particles, remote sensors distinguish the emission and transport of dust (mostly from natural sources) from pollution and smoke aerosols (mostly anthropogenic) around the planet. Remote sensors also map the distribution and properties of clouds[17,24,38,72], precipitation[20,21] and the Earth's reflected solar and emitted thermal energy to space[39,84,85], as these atmospheric constituents are impacted by the aerosol. These global data and source characterization[83] feed aerosol models[11,23,86] to show us an increasingly realistic picture of aerosols around the world and their impact on the environment. To achieve these ends, ground-based and *in situ* measurements, models and satellite observation have to be each improved and integrated. □

doi:10.1038/nature01091

1. Intergovernmental Panel on Climate Change. *Climate Change 2001—The Scientific Basis* (contribution of working group I to the Third Assessment Report of the Intergovernmental Panel on Climate Change) (Cambridge Univ. Press, Cambridge, 2001).
2. Ramanathan, V. *et al.* Aerosols, climate, and the hydrological cycle. *Science* **294,** 2119–2124 (2001).
3. Andreae, M. O. *et al.* External mixture of sea salt, silicates, and excess sulfate in marine aerosols. *Science* **232,** 1620–1623 (1986).
4. Keeling, C. D. The concentration and isotopic abundances of carbon dioxide in the atmosphere. *Tellus* **12,** 200–203 (1960).
5. Husar, R. B., Prospero, J. & Stowe, L. L. Characterization of tropospheric aerosols over the oceans with the NOAA AVHRR optical thickness operational product. *J. Geophys. Res.* **102,** 16889–16909 (1997).
6. Herman, J. R. *et al.* Global distribution of UV-absorbing aerosol from Nimbus-7/TOMS data. *J. Geophys. Res.* **102,** 16911–16922 (1997).
7. Prospero, J. M. & Nees, R. T. Impact of the North African drought and El Niño on mineral dust in the Barbados trade wind. *Nature* **320,** 735–738 (1986).
8. Clarke, A. D. & Charlson, R. J. Radiative properties of the background aerosol: absorption component of extinction. *Science* **229,** 263–265 (1985).
9. Twomey, S. A., Piepgrass, M. & Wolfe, T. L. An assessment of the impact of pollution on the global albedo. *Tellus* **36B,** 356–366 (1984).
10. Charlson, R. J. *et al.* Climate forcing of anthropogenic aerosols. *Science* **255,** 423–430 (1992).
11. Kiehl, J. T. & Briegleb, B. P. The relative roles of sulfate aerosols and greenhouse gases in climate forcing. *Science* **260,** 311–314 (1993).
12. Satheesh, S. K. & Ramanathan, V. Large differences in tropical aerosol forcing at the top of the atmosphere and Earth's surface. *Nature* **405,** 60–63 (2000).
13. Eck, T. F. *et al.* Measurements of irradiance attenuation and estimation of the aerosol single scattering albedo for biomass burning in Amazonia. *J. Geophys. Res.* **103,** 31865–31878 (1998).
14. Hansen, J., Sato, M. & Ruedy, R. Radiative forcing and climate response. *J. Geophys. Res.* **102,** 6831–6864 (1997).
15. Ackerman, A. S. *et al.* Reduction of tropical cloudiness by soot. *Science* **288,** 1042–1047 (2000).
16. Kaufman, Y. J. & Fraser, R. S. Confirmation of the smoke particles effect on clouds and climate. *Science* **277,** 1636–1639 (1997).
17. Nakajima, T. *et al.* A possible correlation between satellite-derived cloud and aerosol microphysical parameters. *Geophys. Res. Lett.* **28,** 1171–1174 (2001).
18. Coakley, J. A. Jr, Bernstein, R. L. & Durkee, P. A. Effect of ship stack effluents on cloud reflectance. *Science* **237,** 953–956 (1987).
19. Kaufman, Y. J. & Nakajima, T. Effect of Amazon smoke on cloud microphysics and albedo. *J. Appl. Meteorol.* **32,** 729–744 (1993).
20. Rosenfeld, D. TRMM observed first direct evidence of smoke from forest fires inhibiting rainfall. *Geophys. Res. Lett.* **26,** 3105–3108 (1999).
21. Rosenfeld, D. Suppression of rain and snow by urban and industrial air pollution. *Science* **287,** 1793–1796 (2000).
22. Boucher, O. & Haywood, J. On summing the components of radiative forcing of climate change. *Clim. Dynam.* **18,** 297–302 (2001).
23. Chin, M *et al.* Tropospheric aerosol optical thickness from the GOCART model and comparisons with satellite and Sun photometer measurements. *J. Atmos. Sci.* **59,** 461–483 (2002).
24. King, M. D. *et al.* Remote sensing of tropospheric aerosols from space: past, present and future. *Bull. Am. Meteorol. Soc.* **80,** 2229–2259 (1999).
25. Tanré, D. *et al.* Remote sensing of aerosol over oceans from EOS-MODIS. *J. Geophys. Res.* **102,** 16971–16988 (1997).
26. Deuzé, J.-L. *et al.* Estimate of the aerosol properties over the ocean with POLDER. *J. Geophys. Res.* **105,** 15329–15346 (2000).
27. Diner, D. J. *et al.* MISR aerosol optical depth retrievals over southern Africa during the SAFARI-2000 dry season campaign. *Geophys. Res. Lett.* **28,** 3127–3130 (2001).
28. Veefkind, J. P., de Leeuw, G. & Durkee, P. A. Retrieval of aerosol optical depth over land using two-angle view satellite radiometry during TARFOX. *Geophys. Res. Lett.* **25,** 3135–3138 (1998).
29. Delene, D. J. & Ogren, J. A. Variability of aerosol optical properties at four North American surface monitoring sites. *J. Atmos. Sci.* **59,** 1135–1150 (2002).
30. Artaxo, P. *et al.* Large scale aerosol source apportionment in Amazonia. *J. Geophys. Res.* **103,** 31837–31847 (1998).
31. Kaufman, Y. J. *et al.* The Smoke, Clouds and Radiation experiment in Brazil (SCAR-B). *J. Geophys. Res.* **103,** 31783–31808 (1998).
32. Ramanathan, V. *et al.* The Indian Ocean Experiment: an integrated analysis of the climate forcing and effects of the great Indo-Asian haze. *J. Geophys. Res.* **106,** 28371–28398 (2001).
33. Dubovik, O. *et al.* Variability of absorption and optical properties of key aerosol types observed in worldwide locations. *J. Atmos. Sci.* **59,** 590–608 (2002).
34. Rotstayn, L. D., Ryan, B. F. & Penner, J. E. Precipitation changes in a GCM resulting from the indirect effects of anthropogenic aerosols. *Geophys. Res. Lett.* **27,** 3045–3048 (2000).
35. Lohmann, U. & Feichter, J. Impact of sulfate aerosols on albedo and lifetime of clouds: a sensitivity study with the ECHAM4 GCM. *J. Geophys. Res. Atmos.* **102,** 13685–13700 (1997).

36. Albrecht B. A. Aerosols, cloud microphysics, and fractional cloudiness. *Science* **245,** 1227–1230 (1989).
37. Penner, J. E., Dickinson, R. E. & O'Neill, C. A. Effects of aerosol from biomass burning on the global radiation budget. *Science* **256,** 1432–1433 (1992).
38. Bréon, F.-M., Tanré, D. & Generoso, S. Aerosol effect on cloud droplet size monitored from satellite. *Science* **295,** 834–838 (2002).
39. Wielicki, B. A. *et al.* Clouds and the earth's radiant energy system (CERES): an earth observing system experiment. *Bull. Am. Meteorol. Soc.* **77,** 853–868 (1996).
40. Herman, M. *et al.* Remote sensing of aerosol over land surfaces including polarization measurements and application to POLDER measurements. *J. Geophys. Res.* **102,** 17039–17049 (1997).
41. Holben, B. N. *et al.* An emerging ground based aerosol climatology: aerosol optical depth from AERONET. *J. Geophys. Res.* **106,** 12067–12097 (2001).
42. Prospero, J. M. Long term measurements of the transport of African mineral dust to the Southern US: implications for regional air quality. *J. Geophys. Res.* **104,** 15917–15927 (1999).
43. Bates T. S. *et al.* International Global Atmospheric Chemistry (IGAC) project's first aerosol characterization experiment ACE-1: overview. *J. Geophys. Res.* **103,** 16297–16318 (1998).
44. Takemura, T. *et al.* Single-scattering albedo and radiative forcing of various aerosol species with a global three-dimensional model. *J. Clim.* **15,** 333–352 (2002).
45. Luo Y. F. *et al.* Characteristics of the spatial distribution and yearly variation of aerosol optical depth over China in last 30 years. *J. Geophys. Res.* **106,** 14501–14513 (2001).
46. Novakov, T., Hegg, D. A. & Hobbs, P. V. Airborne measurements of carbonaceous aerosols on the East Coast of the United States. *J. Geophys. Res.* **102,** 30023–30030 (1997).
47. Hegg, D. A. *et al.* Chemical apportionment of aerosol column optical depth off the mid-Atlantic coast of the United States. *J. Geophys. Res.* **102,** 25293–25303 (1997).
48. Ackerman, T. P. & Toon, O. B. Absorption of visible radiation in atmosphere containing mixtures of absorbing and non-absorbing particles. *Appl. Opt.* **20,** 3661–3668 (1981).
49. Martins, J. V. *et al.* Effects of black carbon content, particle size, and mixing on light absorption by aerosol particles from biomass burning in Brazil. *J. Geophys. Res.* **103,** 32041–32050 (1998).
50. Haywood, J. & Boucher, O. Estimates of the direct and indirect radiative forcing due to tropospheric aerosols: a review. *Rev. Geophys.* **38,** 513–543 (2000).
51. Jacobson, M. Z. Strong radiative heating due to the mixing state of black carbon in atmospheric aerosols. *Nature* **409,** 695–697 (2001).
52. Eck, T. F. *et al.* Characterization of the optical properties of biomass burning aerosols in Zambia during the 1997 ZIBBEE field campaign. *J. Geophys. Res.* **106,** 3425–3448 (2001).
53. Ross, J. L., Hobbs, P. V. & Holben, B. Radiative characteristics of regional hazes dominated by smoke from biomass burning in Brazil: closure tests and direct radiative forcing. *J. Geophys. Res.* **103,** 31925–31941 (1998).
54. Liousse, C. *et al.* A Three-dimensional model study of carbonaceous aerosols. *J. Geophys. Res.* **101,** 19411–19432 (1996).
55. Prospero, J. M. *et al.* Environmental characterization of global sources of atmospheric soil dust identified with the NIMBUS-7 TOMS absorbing aerosol product. *Geophys. Rev.* (in the press).
56. Sokolik, I. N. & Toon, O. B. Direct radiative forcing by anthropogenic airborne mineral aerosol. *Nature* **381,** 681–683 (1996).
57. Moulin, C. *et al.* Control of atmospheric export of dust from North Africa by the North Atlantic oscillation. *Nature* **387,** 691–694 (1997).
58. Tanré, D. *et al.* Climatology of dust aerosol size distribution and optical properties derived from remotely sensed data in the solar spectrum. *J. Geophys. Res.* **106,** 18205–18218 (2001).
59. Clarke, A. D. & Kapustin, V. N. A Pacific aerosol survey, part 1: a decade of data on particle formation, transport, evolution, and mixing in the troposphere. *J. Atmos. Sci.* **59,** 363–382 (2002).
60. Gao, Y. *et al.* Seasonal distribution of Aeolian iron fluxes to the global ocean. *Geophys. Res. Lett.* **28,** 29–33 (2001).
61. Hoppel, W. A. *et al.* Aerosol size distribution and optical properties found in the marine boundary layer over the Atlantic Ocean. *J. Geophys. Res.* **95,** 3659–3686 (1990).
62. Smirnov, A. *et al.* Optical properties of atmospheric aerosol in maritime environments. *J. Atmos. Sci.* **59,** 501–523 (2002).
63. Levin, Z., Ganor, E. & Gladstein, V. The effects of desert particles coated with sulfate on rain formation in the Eastern Mediterranean. *J. Appl. Meteorol.* **35,** 1511–1523 (1996).
64. Leon, J. F. *et al.* Large-scale advection of continental aerosols during INDOEX. *J. Geophys. Res.* **106,** 28427–28439 (2001).
65. Reiner T. *et al.* Chemical characterization of pollution layers over the tropical Indian Ocean: signatures of emissions from biomass and fossil fuel burning. *J. Geophys. Res.* **106,** 28497–28510 (2001).
66. Liao, H. & Seinfeld, J. H. Effect of clouds on direct aerosol radiative forcing of climate. *J. Geophys. Res.* **103,** 3781–3788 (1998).
67. Formenti, P. *et al.* Aerosol optical properties and large-scale transport of air masses: observations at a coastal and a semiarid site in the eastern Mediterranean during summer 1998. *J. Geophys. Res.* **106,** 9807–9826 (2001).
68. Gobbi, G. P. *et al.* Altitude-resolved properties of a Saharan dust event over the Mediterranean. *Atmos. Environ.* **34,** 5119–5127 (2000).
69. Kreidenweis, S. M. *et al.* Smoke aerosol from biomass burning in Mexico: hygroscopic smoke optical model. *J. Geophys. Res.* **106,** 4831–4844 (2001).
70. Winker, D. M., Couch, R. H. & McCormick, M. P. An overview of LITE: NASA's lidar in-space technology experiment. *Proc. IEEE* **84,** 164–180 (1996).
71. Heymsfield A. J. & McFarquhar, G. M. Microphysics of INDOEX clean and polluted trade cumulus clouds. *J. Geophys. Res.* **106,** 28653–28674 (2001).
72. Han, Q., Rossow, W. B. & Lacis, A. A. Near global survey of effective droplet radii in liquid water clouds using ISCCP data. *J. Clim.* **7,** 465–496 (1994).
73. Boucher, O. GCM estimate of the indirect aerosol forcing using satellite-retrieved cloud droplet effective radii. *J. Clim.* **8,** 1403–1409 (1995).
74. Feingold, G. *et al.* Analysis of smoke impact on clouds in Brazilian biomass burning regions: an extension of Twomey's approach. *J. Geophys. Res.* **106,** 22907–22922 (2001).
75. Feingold, G. *et al.* The impact of giant cloud condensation nuclei on drizzle formation in stratocumulus: implications for cloud radiative properties. *J. Atmos. Sci.* **56,** 4100–4117 (1999).
76. Charlson, R. J. *et al.* Reshaping the theory of cloud formation. *Science* **292,** 2025–2026 (2001).
77. Feingold, G. & Chuang, P. Y. Analysis of the influence of film-forming compounds on droplet growth: implications for cloud microphysical processes and climate. *J. Atmos. Sci,* **59,** 2006–2018 (2002).
78. Rosenfeld, D. & Woodley, W. L. K. Deep convective clouds with sustained supercooled liquid water down to –37.5 °C. *Nature* **405,** 440–442 (2001).
79. Khain, A. P., Rosenfeld, D. & Pokrovsky, A. Simulating convective clouds with sustained supercooled liquid water down to –37.5 °C using a spectral microphysics model. *Geophys. Res. Lett.* **28,** 3887–3890 (2001).
80. Alpert, P. *et al.* Quantification of dust-forced heating of the lower troposphere. *Nature* **395,** 367–370 (1998).
81. Claquin, T. *et al.* Uncertainties in assessing radiative forcing by mineral dust. *Tellus* **50B,** 491–505 (1998).
82. Kaufman, Y. J. *et al.* Satellite and ground-based radiometers reveal much lower dust absorption of sunlight than used in climate models. *Geophys. Res. Lett.* **28,** 1479–1483 (2001).
83. Bond, T. C., Charlson, R. J. & Heintzenberg, J. Quantifying the emission of light-absorbing particles: measurements tailored to climate studies. *Geophys. Res. Lett.* **25,** 337–340 (1998).
84. Christopher, S. A. *et al.* First estimates of the radiative forcing of aerosol generated from biomass burning using satellite data. *J. Geophys. Res.* **101,** 21265–21273 (1996).
85. Li, Z. & Kou, L. Atmospheric direct radiative forcing by smoke aerosols determined from satellite and surface measurements. *Tellus* **50B,** 543–554 (1998).
86. Collins, W. D. *et al.* Simulating aerosols using a chemical transport model with assimilation of satellite aerosol retrievals: methodology for INDOEX. *J. Geophys. Res.* **106,** 7313–7336 (2001).
87. Satheesh, S. K. *et al.* A model for the natural and anthropogenic aerosols over the tropical Indian Ocean derived from Indian Ocean Experiment data. *J. Geophys. Res.* **104,** 27421–27440 (1999).
88. Remer, L. A. *et al.* Urban/industrial aerosol: ground based sun/sky radiometer and airborne in situ measurements. *J. Geophys. Res.* **102,** 16849–16859 (1997).
89. Chou, M. D. A solar-radiation model for use in climate studies. *J. Atmos. Sci.* **49,** 762–772 (1992).
90. Liu M., & Westphal, D. L. A study of the sensitivity of simulated mineral dust production to model resolution. *J. Geophys. Res.* **106,** 18099–18112 (2001).
91. Fraser, R. S., Kaufman, Y. J. & Mahoney, R. L. Satellite measurements of aerosol mass and transport. *Atmos. Environ.* **18,** 2577–2584 (1984).
92. Hsu, N. C., Herman, J. R. & Weaver, C. Determination of radiative forcing of Saharan dust using combined TOMS and ERBE. *J. Geophys. Res.* **105,** 20649–20661 (2000).
93. Torres O. *et al.* A long-term record of aerosol optical depth from TOMS observations and comparison to AERONET measurements. *J. Atmos. Sci.* **59,** 398–413 (2002).
94. Chu, D. A. *et al.* Validation of MODIS aerosol optical depth retrieval over land. *Geophys. Res. Lett.* (in the press).
95. Remer, L. A. *et al.* Validation of MODIS aerosol retrieval over ocean. *Geophys. Res. Lett.* (in the press).
96. Kaufman, Y. J. *et al.* Remote sensing of tropospheric aerosol from EOS-MODIS over the land using dark targets and dynamic aerosol models. *J. Geophys. Res.* **102,** 17051–17067 (1997).
97. Fraser, R. S. & Kaufman, Y. J. The relative importance of aerosol scattering and absorption in remote sensing. *IEEE J. Geosci. Rem. Sens.* **GE-23,** 525–633 (1985).
98. Fouquart, Y. *et al.* Observations of Saharan aerosols: results of ECLATS field experiment. II: Broadband radiative characteristics of the aerosols and vertical radiative flux divergence. *J. Clim. Appl. Meteorol.* **25,** 28–37 (1986).
99. Mishchenko, M. I. & Travis, L. D. Satellite retrieval of aerosol properties over the ocean using polarization as well as intensity of reflected sunlight. *J. Geophys. Res.* **102,** 16989–17013 (1997).
100. Chowdhary, J., Cairns, B. & Travis, L. D. Case studies of aerosol retrieval over the ocean from multiangle, multispectral photopolarimetric remote sensing data. *J. Atmos. Sci.* **59,** 383–397 (2002).

Acknowledgements

We thank F. M. Bréon, M. Chin, O. Dubovik, G. Feingold, P. Formenti, M. Herman, D. Herring, B. N. Holben, S. Mattoo, L. Remer and D. Rosenfeld for measurements and calculations used in this paper and for editorial comments. POLDER was a CNES/NASDA project; TOMS and MODIS are NASA projects.